



**HAL**  
open science

# Nano-ions in interaction with non-ionic surfactant self-assemblies

Max Hohenschutz

► **To cite this version:**

Max Hohenschutz. Nano-ions in interaction with non-ionic surfactant self-assemblies. Theoretical and/or physical chemistry. Université Montpellier, 2020. English. NNT : 2020MONT064 . tel-03173636

**HAL Id: tel-03173636**

**<https://theses.hal.science/tel-03173636v1>**

Submitted on 18 Mar 2021

**HAL** is a multi-disciplinary open access archive for the deposit and dissemination of scientific research documents, whether they are published or not. The documents may come from teaching and research institutions in France or abroad, or from public or private research centers.

L'archive ouverte pluridisciplinaire **HAL**, est destinée au dépôt et à la diffusion de documents scientifiques de niveau recherche, publiés ou non, émanant des établissements d'enseignement et de recherche français ou étrangers, des laboratoires publics ou privés.

# THÈSE POUR OBTENIR LE GRADE DE DOCTEUR DE L'UNIVERSITÉ DE MONTPELLIER

En Chimie Physique

Au sein de l'École Doctorale Sciences Chimiques Balard (ED 459)  
Préparé à l'Institut de Chimie Séparative de Marcoule (UMR 5257)

## Nano-ions in interaction with non-ionic surfactant self-assemblies

Présentée par Max HOHENSCHUTZ  
Le 15/12/2020

Sous la direction de Dr. Olivier DIAT  
et Dr. Pierre BAUDUIN

Devant le jury composé de

M Werner NAU, Pr., Jacobs Universität Bremen, Allemagne	Rapporteur
Mme Cécile MONTEUX, Dr. Directrice de Recherche, ESPCI, France	Rapporteuse
M Pascal HERVE, Dr., Solvay, France	Examineur
M Jordi FARAUDO, Dr., ICMAB, Espagne	Examineur
Mme Laurence RAMOS, Dr. Directrice de Recherche, Université de Montpellier, France	Examinatrice, Présidente de Jury
M Dominik HORINEK, Pr., Universität Regensburg, Allemagne	Invité
M Mathieu GRAS, Dr., Extractive, France	Invité
M Pierre BAUDUIN, Dr., ICSM CEA Marcoule, France	Co-directeur de thèse
M Olivier DIAT, Dr. Directeur de Recherche, ICSM CEA Marcoule, France	Directeur de thèse



UNIVERSITÉ  
DE MONTPELLIER



## *Acknowledgements*

After three short years, this thesis work is coming to an end. Achieving this would not have been possible without many people that supported me until the end, to whom I want to express my sincerest gratitude in the following.

First and foremost, I want to thank my thesis supervisors Olivier Diat and Pierre Bauduin. Their perpetual advice and support on the matter discussed herein constitute a crucial part of this PhD. Olivier with his enthusiastic directness and pragmatism and Pierre with his calm meticulousness and patience they have both equally made me learn and grow tremendously towards becoming a more independent researcher. The familial environment they have created in the L2IA has made me feel warmly welcome and animated strongly the work put into this thesis. It was a delight to work closely with these two over the last three years and I could not have imagined any better supervisors. Thank you!

I would like to thank Extractive Cie and Region Occitanie for financing this thesis. Correspondingly, I would like to thank Frédéric Goettmann, Quentin Ricoux and Matthieu Gras from Extractive for fruitful discussions.

I would like to thank Luc and (again) Pierre for welcoming me in their office, for creating a stimulating and prosperous work environment and for responding patiently to my questions whenever they arose. Also, I would like to thank Alban for his reliability concerning the order of lab materials, the scientific discussions and for the shared beers. Many thanks go out to my fellow PhD-students at the L2IA: Tania, Edward, Jing, Ioanna and Klaudia for the positive environment in the lab and the activities outside work. Furthermore, throughout this thesis, I had the pleasure to supervise the internships of Imane Sayah, Steven Paulet and Reymoana Frogier. I would like to thank these three for contributing to parts of my thesis with their diligent lab work.

There are many more people at the ICSM that made this thesis period very pleasant. Thus, I want to thank Toni, Philipp, Remi, Elisa, Robert, Markus, Zijie, Zijun, Jun, Mohan, Ruwaid, Patricio, Michael, Ludovic, Ali, David, Ran, Theo and Marin for the lunches in the canteen and the numerous fun activities outside of work. Also, I want to express my gratitude to the secretaries of the ICSM Vainina, Aurélie and Alice for taking care of all the administrative

procedures throughout my thesis. The upbeat atmosphere around these three, especially around Vainina was fantastic as a reception at the ICSM in the beginning and stayed a place of comfort throughout the whole thesis period.

I made many scientific acquaintances through this thesis, to whom I'd like to express my gratitude for the collaborations and discussions. Thus, I would like to thank the beam line contacts Isabelle Grillo (ILL) and Sebastian Busch (MLZ) for their unlimited availability, whenever the slightest problem in a SANS-experiment arose. I thank Emanuel Schneck, Gerald Brezesinski, Regine von Klitzing, Larissa Braun, Thomas Zemb and Pratap Bahadur for fruitful discussions. I'd like to thank Clara Vinãs and Francesc Teixidor, and Clément Falaise and Emmanuel Cadot for kindly synthesizing and providing some chemicals used in this thesis. Also, I would like to thank Loïc Desbordes, Sylvain Faure and Fabien Frances for allowing me to use their FOAMSCAN-setup. Furthermore, I was permitted to follow the meetings of the FOAMEX ANR project. I am grateful for the insights into this project and would like to thank all the members.

I want to thank my family and friends for their infinite support, the visits and the distraction when needed. My mom Inge deserves a special mention owing to her limitless life advice and moral support. Also, I would like to thank my best friend Quirin for the countless phone calls and shared long-distance beers.

*Thank you all!*

## Abbreviations

ABC	-	anionic boron cluster
BW	-	borotungstate ( $\text{BW}_{12}\text{O}_{40}^{5-}$ )
cac	-	critical aggregation concentration
CEA	-	Commissariat à l'Énergie Atomique et aux énergies alternatives
$\text{C}_i\text{E}_j$	-	denotes ethoxylated non-ionic surfactant
cmc	-	critical micellar concentration
COSAN	-	Cobalta-bis-dicarbollide
CP	-	Cloud Point
Cryo-TEM	-	Cryogenic Transmission Electron Microscopy
DLS	-	Dynamic Light Scattering
DSC	-	Differential Scanning Calorimetry
$\gamma$ -CD	-	$\gamma$ -Cyclodextrin
(H)MSA	-	(Hayter) Mean Spherical Approximation
HSiW	-	silicotungstic acid ( $\text{H}_4\text{SiW}_{12}\text{O}_{40}$ )
HPW	-	phosphotungstic acid ( $\text{H}_3\text{PW}_{12}\text{O}_{40}$ )
ICSM	-	Institut de Chimie Séparative de Marcoule
ILL	-	Institut Laue-Langevin
KBW	-	potassium borotungstate ( $\text{K}_5\text{BW}_{12}\text{O}_{40}$ )
L2IA	-	Laboratoire des Ions aux Interfaces Actives
mM	-	mmol/l
M	-	mol/l
MD	-	Molecular Dynamics
MLZ	-	Heinz Maier-Leibniz Zentrum
MW	-	metatungstate ( $\text{H}_2\text{W}_{12}\text{O}_{40}^{6-}$ )
$\text{NH}_4\text{MW}$	-	ammonium metatungstate ( $(\text{NH}_4)_6\text{H}_2\text{W}_{12}\text{O}_{40}$ )
NMR	-	Nuclear Magnetic Resonance
PEG	-	Polyethyleneglycol
PNIPAM	-	Poly N-isopropylamide
POM	-	Polyoxometalate
PW	-	phosphotungstate ( $\text{PW}_{12}\text{O}_{40}^{3-}$ )
SANS	-	Small Angle Neutron Scattering
SDS	-	Sodium dodecylsulfate

SiW	-	silicotungstate ( $\text{SiW}_{12}\text{O}_{40}^{4-}$ )
SLD	-	Scattering Length Density
S(W)AXS	-	Small (and Wide) Angle X-ray Scattering
vdW	-	van der Waals (-interactions)

# Table of Contents

Abstract .....	i
Abstract en francais .....	iii
Introduction .....	1
1. State of the art .....	5
1.1. Specific ion effects .....	5
1.2. The extension to superchaotropic ions .....	9
1.2.1. Boron clusters and their superchaotropic behavior .....	10
1.2.2. Polyoxometalates and their superchaotropic behavior .....	14
1.2.3. Hydrophobic ions .....	18
2. Nano-ions in interaction with non-ionic surfactant micelles.....	21
2.1. Non-ionic surfactant phases as probes for superchaotropic ions.....	21
2.2. C <sub>8</sub> E <sub>4</sub> in water in the presence of classical salts and SDS .....	25
2.3. Keggin-POMs in C <sub>8</sub> E <sub>4</sub> .....	33
2.3.1. The importance of the POM's counter-ion.....	39
2.3.2. Quantifying superchaotropic adsorption .....	43
2.3.3. Changing C <sub>8</sub> E <sub>4</sub> -concentration.....	49
2.3.4. The thermodynamics of superchaotropic adsorption.....	51
2.3.5. Beyond the electrostatics of SiW-decorated micelles .....	58
2.3.6. Addendum – Chaotropic POMs in C <sub>8</sub> E <sub>4</sub> .....	67
2.4. Dodecaborates in C <sub>8</sub> E <sub>4</sub> .....	70
2.4.1. Addendum – Chaotropic dodecaborates in C <sub>8</sub> E <sub>4</sub> .....	84
2.5. Disruptive ions (BPh <sub>4</sub> <sup>-</sup> , COSAN, PW <sub>12</sub> O <sub>40</sub> <sup>3-</sup> ) in C <sub>8</sub> E <sub>4</sub> .....	85
2.6. Classification of the nano-ions .....	91
2.6.1. Addendum – Classification of the nano-ions .....	97
2.7. Chapter summary.....	98



---

2.8. Résumé du chapitre en français .....	101
2.9. SAXS- and SANS-fit parameters used in this chapter .....	104
3. How nano-ions act like ionic surfactants .....	109
3.1. C <sub>12</sub> E <sub>5</sub> in dilute aqueous solutions .....	110
3.2. Nano-ions in dilute C <sub>12</sub> E <sub>5</sub> .....	112
3.3. Comparison of the nano-ions.....	121
3.4. Changing C <sub>12</sub> E <sub>5</sub> -concentration .....	124
3.5. Remarks on vesicle stability .....	126
3.6. Chapter summary.....	128
3.7. Résumé en français .....	130
3.8. Appendix .....	132
3.8.1. Remaining SANS-spectra.....	132
3.8.2. Flexible vs rigid cylindrical micelles (form factor fits).....	134
3.8.3. Repelling cylindrical and spherical micelles (form and structure factor fits) .....	135
3.8.4. Ellipsoidal fits of SAXS and SANS upon heating .....	137
3.8.5. Vesicles (form factor fit) .....	139
3.8.6. DLS of SANS samples .....	140
3.8.7. NMR: C <sub>12</sub> E <sub>5</sub> -stability.....	142
3.8.8. Vesicles of another non-ionic surfactant - BrijO10.....	143
4. Nano-ions in non-ionic surfactant foams .....	145
4.1. Introduction to foams.....	146
4.1.1. Thin foam films .....	148
4.1.2. Aging phenomena in foams .....	152
4.2. Non-ionic foam films subjected to superchaotropic ions .....	153
4.3. Appendix .....	163
4.3.1. Quasi-stationary foams .....	163
4.3.2. Micelles in the foams.....	166

---

4.3.3. Delayed injection of SiW into the foam .....	168
4.3.4. The effect of electrolyte in non-ionic BrijO10-foams .....	169
4.4. Lifetime of non-ionic surfactant foams in the presence of superchaotropic ions.....	170
4.4.1. Appendix .....	179
4.5. Chapter summary .....	180
4.6. Résumé en francais .....	183
5. Conclusions .....	186
6. Perspectives .....	188
7. Materials and methods .....	191
7.1. Chemicals .....	191
7.2. Visual methods: Cloud points and phase diagrams .....	192
7.3. Small angle x-ray (or neutron) scattering (SAXS or SANS).....	193
7.3.1. Worked fitting example SANS .....	200
7.3.2. Worked fitting example SAXS (supported by SANS) .....	204
7.3.3. List of used form and structure factors .....	209
7.3.4. SAXS-Experimental .....	211
7.3.5. SANS-Experimental ILL .....	212
7.3.6. SANS-Experimental MLZ.....	213
7.4. Dynamic Light Scattering.....	214
7.4.1. DLS-Experimental.....	216
7.5. FOAMSCAN .....	217
7.5.1. FOAMSCAN Experimental .....	218
7.6. NMR-Experimental .....	218
7.7. Surface tension experimental.....	219
Bibliography.....	221



## Abstract

Nanometer-sized ions (nano-ions), such as ionic boron clusters, polyoxometalates (POMs) and large organic ions, have spawned remarkable interest in recent years due to their ability to adsorb or bind to electrically neutral chemical systems, such as macrocyclic host molecules, colloidal nanoparticles, surfactants and polymers etc. The underlying adsorption or binding processes were shown to be driven by a solvent-mediated phenomenon, the chaotropic effect, which drives the nano-ion from the water bulk towards an interface. Thus, hydration water of the ion and the interface is released into the bulk resulting in a bulk water structure recovery. This effect is particularly strong for nano-ions. Therefore, they were termed superchaotropic or hydrophobic ions as an extension to classical (weakly) chaotropic ions such as  $\text{SCN}^-$ . All commonly studied superchaotropes, though chemically diverse, share physical characteristics such as low charge density and high polarizability. Herein, the effects of nano-ions on ethoxylated non-ionic surfactant self-assemblies, micellar and bilayer phases, are elucidated to draw conclusions on their chaotropic and/or hydrophobic nature. By combining small angle scattering of neutrons and x-rays (SANS and SAXS), and phase diagrams, non-ionic surfactant/nano-ion systems are examined and compared, from the nanometer to the macroscopic scale. Thus, all studied nano-ions are found to induce a charging of the surfactant assemblies along with a dehydration of the non-ionic surfactant head groups. Furthermore, chaotropic and hydrophobic ions differ in their effects on the micellar shape. Superchaotropic ions drive the elongated non-ionic surfactant micelles towards spherical micelles (increase in curvature), whereas hydrophobic ions cause a transition towards bilayer phases (decrease in curvature). It is concluded that superchaotropic nano-ions act like ionic surfactants because their addition to non-ionic surfactant systems causes a charging effect. However, nano-ions and ionic surfactants are fundamentally different by their association with the non-ionic surfactant assembly. The nano-ion adsorbs to the non-ionic surfactant heads by the chaotropic effect, while the ionic surfactant anchors into the micelles between the non-ionic surfactant tails by the hydrophobic effect. The comparison of the effects of adding nano-ions or ionic surfactant to non-ionic surfactant was further investigated on foams. The foams were investigated regarding foam film thickness, drainage over time and stability, respectively using SANS, image analysis and conductometry. The tested superchaotropic POM ( $\text{SiW}_{12}\text{O}_{40}^{4-}$ , SiW) does not foam in water in contrast to the classical ionic surfactant SDS. Nevertheless, addition of small amounts of SiW or SDS to a non-ionic surfactant foaming solution resulted in wetter

foams with longer lifetimes. Meanwhile, the foam film thickness (determined in SANS) is increased due to the electric charging of the non-ionic surfactant monolayers in the foam film. It is concluded that the remarkable behavior of nano-ions – herein on non-ionic surfactant systems – can be extended to colloidal systems, such as foams, polymers, proteins or nanoparticles. This thesis demonstrates that the superchaotropic behavior of nano-ions is a versatile tool to be used in novel formulations of soft matter materials and applications.

## Abstract en français

Les ions de taille nanométrique (nano-ions), tels que les clusters ioniques de bore, les polyoxométalates (POM) et les grands ions organiques, ont suscité un intérêt remarquable ces dernières années en raison de leur capacité à s'adsorber ou se lier à des systèmes chimiques électriquement neutres, tels que les molécules hôtes macrocycliques, les nanoparticules, les tensioactifs et les polymères, etc. Il a été démontré que ces processus d'adsorption ou de liaison sont induits par un phénomène médié par solvant, l'effet chaotropique, qui pousse le nano-ion de la masse d'eau vers une interface. Ainsi, l'eau d'hydratation de l'ion et de l'interface est libérée dans la masse d'eau, ce qui entraîne une restitution de la structure intrinsèque de l'eau. Cet effet est particulièrement fort pour les nano-ions. Ils sont par conséquent appelés ions superchaotropiques ou hydrophobes dans le prolongement des ions classiques (faiblement) chaotropiques tels que le  $\text{SCN}^-$ . Tous les superchaotropes couramment étudiés, bien que chimiquement divers, partagent des caractéristiques physiques telles qu'une faible densité de charge et une grande polarisabilité. Les effets des nano-ions sur les auto-assemblages de tensioactifs non ioniques éthoxylés, les phases micellaires et bicouches, sont ici élucidés pour tirer des conclusions sur leur nature chaotropique et/ou hydrophobe. En combinant la diffusion aux petits angles des neutrons et des rayons X (SANS et SAXS), et les diagrammes de phase, les systèmes tensioactifs non ioniques/nano-ion sont examinés et comparés, du nanomètre à l'échelle macroscopique. Ainsi, il est montré que tous les nano-ions étudiés induisent un chargement électrique des assemblages de tensioactifs ainsi qu'une déshydratation des têtes de tensioactif non-ionique. En outre, les ions chaotropiques ou hydrophobes diffèrent dans leurs effets sur la forme micellaire. Les ions chaotropiques entraînent les micelles allongées de tensioactif non-ionique vers les micelles sphériques (augmentation de la courbure), tandis que les ions hydrophobes provoquent une transition vers les phases bicouches (diminution de la courbure). Il est conclu que les nano-ions superchaotropiques agissent comme des tensioactifs ioniques car leur ajout à des systèmes de tensioactifs non ioniques provoque un effet de charge. Cependant, les nano-ions et les tensioactifs ioniques sont fondamentalement différents par leur association avec l'ensemble des tensioactifs non ioniques. Le nano-ion s'adsorbe sur les têtes des tensioactifs non ioniques par effet chaotropique, tandis que le tensioactif ionique s'ancre dans les micelles entre les queues des tensioactifs non ioniques par effet hydrophobe. La comparaison des effets de l'ajout de nano-ions ou de tensioactifs ioniques à des tensioactifs non ioniques a été approfondie sur les mousses. Les mousses ont été étudiées en ce qui concerne l'épaisseur du film de mousse, le drainage dans le temps et la stabilité, respectivement en

utilisant la SANS, l'analyse d'image et la conductométrie. Le POM superchaotropique testé ( $\text{SiW}_{12}\text{O}_{40}^{4-}$ , SiW) ne mousse pas dans l'eau contrairement au SDS classique de tensioactif ionique. Néanmoins, l'ajout de petites quantités de SiW ou de SDS à une solution moussante de tensioactif non ionique a permis d'obtenir des mousses plus humides avec une durée de vie plus longue. Entre-temps, l'épaisseur du film de mousse (déterminée en SANS) est augmentée en raison de la charge électrique des monocouches de tensioactifs non ioniques dans le film de mousse. Il est conclu que le comportement remarquable des nano-ions - ici sur les systèmes tensioactifs non ioniques - peut être étendu aux systèmes colloïdaux, tels que les mousses, les polymères, les protéines ou les nanoparticules. Cette thèse démontre que le comportement superchaotropique des nano-ions est un outil polyvalent qui peut être utilisé dans de nouvelles formulations de matériaux et d'applications de la matière molle.





# Introduction

Molecular assembly lies at the bottom of chemistry and is the mere reason why life could spawn on planet earth. For instance, for the emergence of life-inspiring molecules on a yet young, abiotic Earth (besides other viable theories) a peculiar driving force of molecular assembly is surmised to have played an important role: The chaotropic effect.<sup>1</sup> In the theory, it is hypothesized that the nitrogen and sulfur rich atmosphere in prehistoric times gave rise to thiocyanate,  $\text{SCN}^-$ , a particularly ‘soft’ and weakly hydrated ion, also known as a chaotrope. Its sparse hydration shell facilitates self-assembly of  $\text{SCN}^-$ -ions, which is known to appear at high  $\text{SCN}^-$ -concentrations.<sup>2</sup> As  $\text{SCN}^-$  and water,  $\text{H}_2\text{O}$ , contain all constituent atoms of amino acids and proteins, such  $\text{SCN}^-$ -aggregates present a potential origin of biological molecules, especially under the extreme conditions that took effect in the primordial soup.<sup>1</sup>

In modern day science, though classical salts like  $\text{CaCO}_3$ ,  $\text{NaCl}$ ,  $\text{Na}_2\text{SO}_4$ ,  $\text{NaSCN}$  or  $\text{KI}$  are common in all life sciences, specific ion phenomena arising from fundamental differences of the individual ions are often neglected as the observed effects in dilute saline media are small. However, in 2015 and 2016, large ionic species were discovered to exhibit the chaotropic effect to unparalleled extents.<sup>3-5</sup> The underlying driving force was termed superchaotropic effect and superchaotropy emerged as a general property of nanometer-sized weakly charged ionic species and is best described as the tendency of such nano-ions to be drawn to and to adsorb to electrically neutral soft matter surfaces. The discovery of superchaotropy has since spurred copious studies on the effects of such nano-ions on various soft matter systems, has opened new pathways for material synthesis and nano-ion focused research has become a flourishing field with high interdisciplinarity.

Owing to the fast growth and the broadness of the field, resulting studies are often hardly comparable making it difficult to set effects appearing in the diverse systems on the same footing. This thesis aims to form a link between the existing studies by providing an overview of the commonly used superchaotropic ions and their behavior on various non-ionic surfactant self-assemblies in aqueous solution and at the air/water interface on the example of foams.

This thesis was prepared at the *Laboratoire des Ions aux Interfaces Actives* (L2IA, laboratory of ions at active interfaces) at the *Institut de Chimie Séparative de Marcoule* (ICSM, institute of separation chemistry at CEA Marcoule). Research topics within this lab revolve around the physico-chemical behavior of ions at any kind of interface set into the context of metal

extraction, formulation or biologically relevant systems. The interface here might be i) buried in solution, such as in soft matter dispersions, or ii) a macroscopic interface, e.g. water/air or water/oil. Classical (metal) ions do not exhibit a marked propensity to interact with bare liquid interfaces. Thus, in the context of ion extraction, generally surface-active agents functionalized with a complexing group are used to fix ions at the interface and then extraction can be done for example via a flotation process, where the large surfactant-covered water/air interface in a surfactant foam serves as the extracting phase. However, over the last five years, the L2IA-group has revealed that some specific ions have the property to strongly interact with soft matter - buried in water or at any aqueous phase border - without necessitating ionic complexing moieties. This novel ionic behavior was found most pronounced for nanometer-sized ionic species and is understood as a result of a solvent-mediated phenomenon, the so-called chaotropic effect, causing an energetically favorable minimization of water/ion contacts, which drives the ion to less polar environments than water (soft matter interfaces). The discovery of this peculiar ionic behavior spawned a new field of research around these so-called nano-ions, which was brought forward besides the L2IA by research groups such as Nau et al, Matejcek et al, Bastos-Gonzalez et al and Cadot et al among others. Overall, a plethora of (super-) chaotropic nano-ions (polyoxometalates, metal clusters, ionic boron clusters, hydrophobic ions) were investigated in studies regarding supramolecular chemistry, colloidal nanoparticles and soft matter dispersions of polymers, surfactant or lipids. While there is consensus that all nano-ions are similar in their pronounced propensity to interact with interfaces, there is a debate on whether these ions are chaotropic (hydrophilic) or hydrophobic entities or exhibit simultaneously both traits, mostly because a general overview is lacking as the respective ions are usually studied individually with specific or given chemical systems or interfaces. Attempting to remedy, the present thesis performs a quantitative comparison of the most studied nano-ions in interaction with non-ionic surfactant self-assemblies pointing out the nano-ions' similarities and differences. The high responsiveness and deformability of these non-ionic surfactant assemblies to external stimuli such as nano-ion adsorption will serve as a sensitive indicator for the nano-ion behavior in the presence of non-ionic soft matter. Thus, after reviewing the current state-of-the-art on specific ion effects and nano-ions in chapter 1, the nano-ions will be examined on a model micellar non-ionic surfactant system based on tetraethyleneglycol mono-octylether ( $C_8E_4$ ), in chapter 2.  $C_8E_4$  is an interesting system as it shows, in water, a simple phase behavior, forming only micelles and no lyotropic phases, such as hexagonal or lamellar phases. The effects of the nano-ions on the  $C_8E_4$ -micelles are determined macroscopically by establishing phase diagrams and on the nanometer-length scale

using small angle scattering of neutrons and x-rays (SANS and SAXS). This combined approach captures the behavior of the nano-ion (in SAXS) and of  $C_8E_4$  (in SANS) allowing for a total description of the system via a global fitting procedure using mathematical models. The gathered results will be discussed firstly separately for each chemical class of nano-ions (polyoxometalates, boron clusters and hydrophobic ions) and secondly overall, comparing all nano-ions with each other. Using the same experimental strategy in chapter 3, the effects of the different nano-ions are investigated on a more complex surfactant system, pentaethyleneglycol monododecyl ether ( $C_{12}E_5$ ).  $C_{12}E_5$  displays a richer phase behavior in water forming (elongated) micellar as well as lyotropic (lamellar) phases. This enables to extend the investigation of the effect of nano-ions on phase boundaries. Moreover, a focus was made on the comparison between the effect of anionic surfactants and nano-ions on the  $C_{12}E_5$  system. To compare further inorganic globular nano-ions and organic, amphipathic ionic surfactants, their effects on a non-ionic surfactant foam are examined in chapter 5. Therein, foams were analyzed in a quasi-stationary dry state (under continuous foam generation) using SANS as well as under free drainage conditions (foam generation halted) using conductometry and image analysis. Thus, microscopic effects on foam film thickness (from SANS) and macroscopic effects on foam generation, drainage and stability (from conductometry and image analysis) are revealed for foams that contain nano-ions or in the presence of an ionic surfactant.

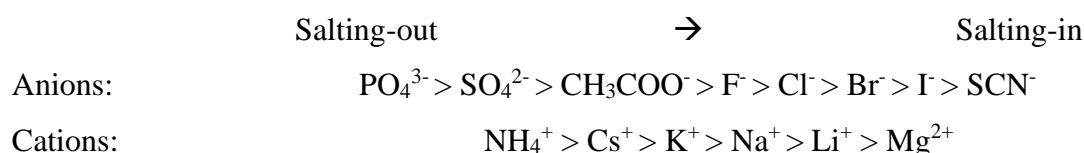


# 1.State of the art

First the current state of the art will be discussed. For this purpose, specific ion effects and nano-ion related research are reviewed in the following.

## 1.1. Specific ion effects

The discovery of specific ion effects dates back to 1887 when Franz Hofmeister first reported on the precipitation of various proteins as a function of salt type and salt concentration.<sup>6,7</sup> He fixed the cation and altered the anionic species and vice versa with the result of two separate series, one for the anions and one for the cations. These series are famously known today as the Hofmeister series of cations and anions. An extended version of the Hofmeister series is shown below.



Considering the series of anions, phosphate is most efficient at inducing protein precipitation, meaning that comparably low concentrations of  $\text{PO}_4^{3-}$  are necessary, while for example  $\text{SCN}^-$  is relatively inefficient, as it needs to be added in much higher concentrations. The series for anions, thus, reaches from highly charged small, to weakly charged large anions. In comparison, the effects of cations were less pronounced and showed the opposite ordering, that is, from weakly charged large ions to strongly charged small ions.

Since Hofmeister's pioneering work these series were rediscovered in many different systems reaching far beyond processes concerning proteins, involving Hofmeister effects on water surface tension<sup>8-10</sup>, on various surfactant phenomena including cloud points, Krafft points, cmcs and others<sup>11,12</sup>, in supramolecular binding phenomena<sup>13</sup>, colloidal stability<sup>14</sup>, bacterial growth<sup>15</sup>, bubble-bubble coalescence<sup>16,17</sup> and in many other diverse systems.<sup>11</sup> Furthermore, the salt effects depend on the concentration of the salt, in some cases pH (especially in systems containing proteins) and the choice of the solvent<sup>18</sup>. Notably, also reversed order and partially reversed Hofmeister series were commonly observed.<sup>19,20</sup> This vast variety of Hofmeister phenomena displays the seemingly endless scope of the Hofmeister series.

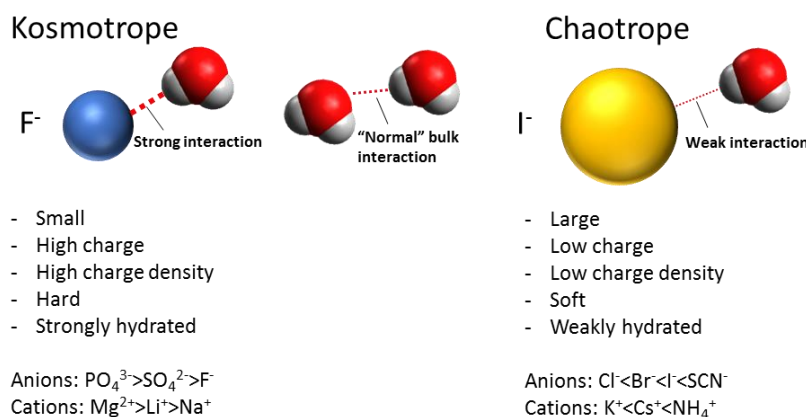


Figure 1: Kosmotropes and chaotropes with corresponding characteristics and interaction (H-bonding) with water. Kosmotropes bind water more strongly than water binds itself and chaotropes bind water more weakly than water binds itself. The sizes of the water molecules and ions are up to scale.

Originally, these salt effects were interpreted in terms of the water-absorbing capacity of ions<sup>6,7</sup>, which was later framed into the theory of water structure making and breaking. Highly charged, weakly polarizable (hard) ions were expected to induce order (kosmos) to the surrounding water molecules and were termed kosmotropes. Such kosmotropic ions would withdraw water molecules from the solute (protein) lowering its solubility and cause a salting-out effect. Weakly charged, strongly polarizable (soft) ions, in return, were expected to create disorder (chaos) in the water bulk and loosen the water molecules in the rigid scaffold of bulk water. Thus, chaotropic ions would provide more water molecules for additional solute hydration, which leads to an increase in the solute's solubility, inducing a salting-in effect. This theory of water structuring and breaking has turned into what we consider today hydration and activity of an ion.<sup>21</sup> Notably, it was shown that the water bulk structure was shown to remain unaffected beyond the first two water layers around the ion (distance to ion  $< 5 \text{ \AA}$ ).<sup>22,23</sup> The terms chaotrope and kosmotrope, however, remained and describe respectively weakly hydrated and strongly hydrated ions relative to water-water binding in the bulk, see Figure 1. Their differently strong interactions with water are clearly reflected in the thermodynamic solvation signatures of the ions: Upon solvation of a kosmotrope, an entropic penalty has to be paid owing to resulting low water dynamics in the strongly bound hydration shell (compared to the bulk), while hydration of a chaotrope is entropically favorable due to high water dynamics in their loose hydration shell.<sup>24–26</sup> However, the motional freedom of water molecules in the hydration shells depends on ion concentration and is reduced at high salt concentrations for both chaotropic and kosmotropic ions.<sup>26</sup> Furthermore, owing to the asymmetric distribution of charge in the water molecule (water is a protic dipolar solvent), anions are usually more strongly hydrated than cations, which is due to: (i) Hydrogen-bonding with anions is stronger than the interaction of

the electronegative oxygen atom with cations, (ii) the electron withdrawing power of the oxygen favors binding to anions and (iii) geometrical reasons, as cations are much smaller than anions and can subsequently fit fewer water molecules into their hydration sphere.<sup>23,27,28</sup> These three factors entail that, for instance, the ions  $K^+$  and  $F^-$ , with identical radii of  $r=1.2 \text{ \AA}$  (and same, but opposite charge) are classified differently as, respectively, cationic chaotrope and anionic kosmotrope, and explain why the effects of cations are generally weaker than the effects of anions.<sup>23</sup>

However, Hofmeister series reversals as well as, for instance, the salting-out effect of the chaotropic cations in Hofmeister's protein systems, see the series above, cannot be explained by mere effects of ions on bulk water as initially proposed. Rather a wholistic picture considering the entire respective system including specific ion effects in the bulk and at interfaces is needed.

In the context of proteins, this was elegantly demonstrated by Jungwirth et al. using a combination of experimental techniques and molecular dynamics simulations. His group showed that the electrically neutral protein backbone as well as charged moieties in a protein respectively interact specifically with ions, where each interaction site on the protein gives rise to a respective specific Hofmeister ordering, according to the nature of the moiety.<sup>29,30</sup> The overall observed salt effect (salting-in or salting-out) would thus be the summed outcome of all ion specific effects along the entire protein plus the effects of the ions on the water bulk.

To conceptualize interactions between ionic species in aqueous solution, Kim Collins developed a simple, yet potent principle to assess whether oppositely charged ions tend to form contact ion pairs in solution or not. His so-called concept of matching water affinities<sup>28,31</sup> predicts that ions of opposite charge with similar hydration spheres will spontaneously form contact ion pairs, whereas ions with differing hydration will not. Implied to Hofmeister termination this means that a kosmotrope is attracted by an oppositely charged kosmotrope and a chaotrope is attracted by an oppositely charged chaotrope, while kosmotrope-chaotrope pairs will always stay separated by their hydration shells in aqueous solution. Collins' concept is a variant of the prominent like-seeks-like rule in chemistry and serves as a rule of thumb when it comes to interaction of ionic species in solution. As a follow-up, Vlachy et al. have shown that Collins' concept can be extended to interfaces containing ionic groups as demonstrated for adsorption of Hofmeister ions to ionic surfactant micelles with differing ionic head groups.<sup>32,33</sup> However, some Hofmeister phenomena cannot be conceived with simple electrostatics, such as the interaction of Hofmeister ions with the electrically neutral protein backbone, the air-water

interface or with electrically neutral soft matter assemblies of non-ionic surfactants or zwitterionic lipids, all of which can be united under the umbrella term of Hofmeister ions at electrically neutral polar hydrated interfaces. For instance, upon investigating a non-ionic surfactant monolayer, respectively at high concentrations, kosmotropic anions were found to dehydrate the monolayer without direct interaction whereas chaotropic anions weakly adsorbed to it.<sup>12</sup> Similar observations were made on zwitterionic surfactant micelles<sup>34</sup> and lipid assemblies. Chaotropic anions thus exhibit a weak propensity to adsorb to neutral soft matter surfaces, which is often regarded as a solvent-mediated effect and, in the case of classical chaotropic ions, effects become significant at high concentrations ( $c > 0.1$  M). In the context of lipids, Leontidis et al. framed this adsorption phenomenon as a result of a competition for hydration water and interfacial sites in the lipid self-assembly between the ion and the lipid.<sup>35</sup> Interestingly, Collins' concept in this non-electrostatic situation seems again valid as common soft matter interfaces like on non-ionic micelles are less polar than water and, thus, carry a rather soft hydration shell similar to chaotropes, which can be easily shed off and allows for direct contact between the interface and the chaotrope but prohibits adsorption of strongly hydrated kosmotropic ions.



## 1.2. The extension to superchaotropic ions

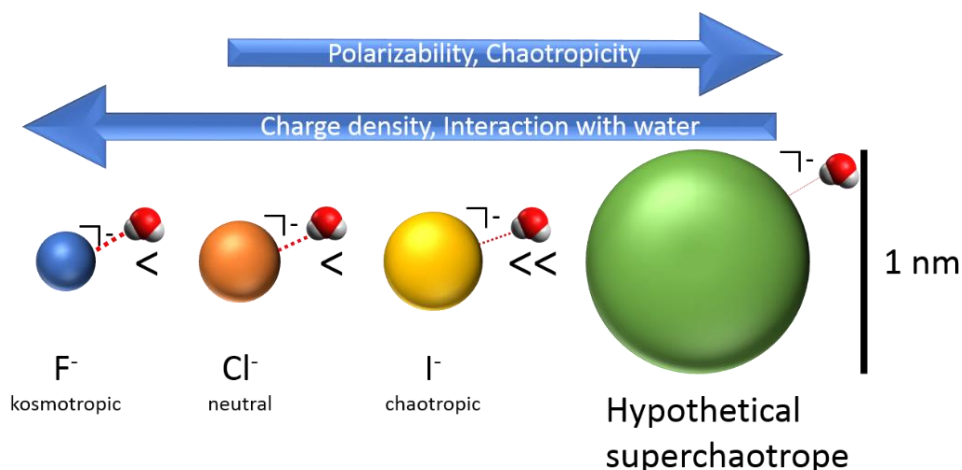


Figure 2: Transition from kosmotropic over chaotropic to superchaotropic ions upon increase of the ion volume. The ion-water interaction becomes weaker with ion size. The size of the water molecules and the ionic radii of the halides are up to scale and the diameter of the hypothetical superchaotropic ion was arbitrarily set to 1 nm. The less-than signs hint at the propensity of the ions to adsorb to neutral polar surfaces.

Classical Hofmeister ions range from highly charged, small, strongly hydrated kosmotropic ions to less charged, larger, weakly hydrated chaotropic ions. These ions are characterized by their respective charge densities and polarizabilities. Thus, if it were possible to increase the size of a kosmotropic ion, without affecting its charge, this hypothetical ion would gradually lose its kosmotropic character and become more and more chaotropic, which can be exemplified upon comparison of the halide anions  $F^-$ ,  $Cl^-$  and  $I^-$ , see Figure 2. Consequently upon further increase of the ionic volume a very chaotropic species would result (and at even higher ionic volumes and even lower charge densities, ionic properties will fade, and the ion will behave like a hydrophobic colloid without direct interaction with water.) In reality, such a strongly chaotropic ion, due to its large nanometer size needs to be a multiatomic molecule with few and delocalized charges, and subsequently very low charge density and high polarizability. Indeed, in recent years several such nano-ions of organic (hydrophobic ions such as  $BPh_4^-$  by the group of Bastos-Gonzalez and Faraudo<sup>5</sup>) as well as of inorganic origin (polyoxometalates by the group of Bauduin and Diat<sup>4</sup> and boron clusters by Nau and co-workers<sup>3</sup>) were unveiled to exhibit strongly chaotropic, so-called superchaotropic, behavior as they were found to non-specifically and strongly adsorb to neutral interfaces at low ( $\mu M$ - $mM$ ) concentrations.

These discoveries spawned substantial research interest on the fundamental behavior of these nano-ions and their potential for application and since then, the understanding of the chaotropic effect as an assembly motif has seen tremendous progress and has been reviewed.<sup>36,37</sup> Figure 3

depicts the nano-ions that can be considered as extensions to the chaotropic side of the Hofmeister series. The corresponding literature is summarized in the following.

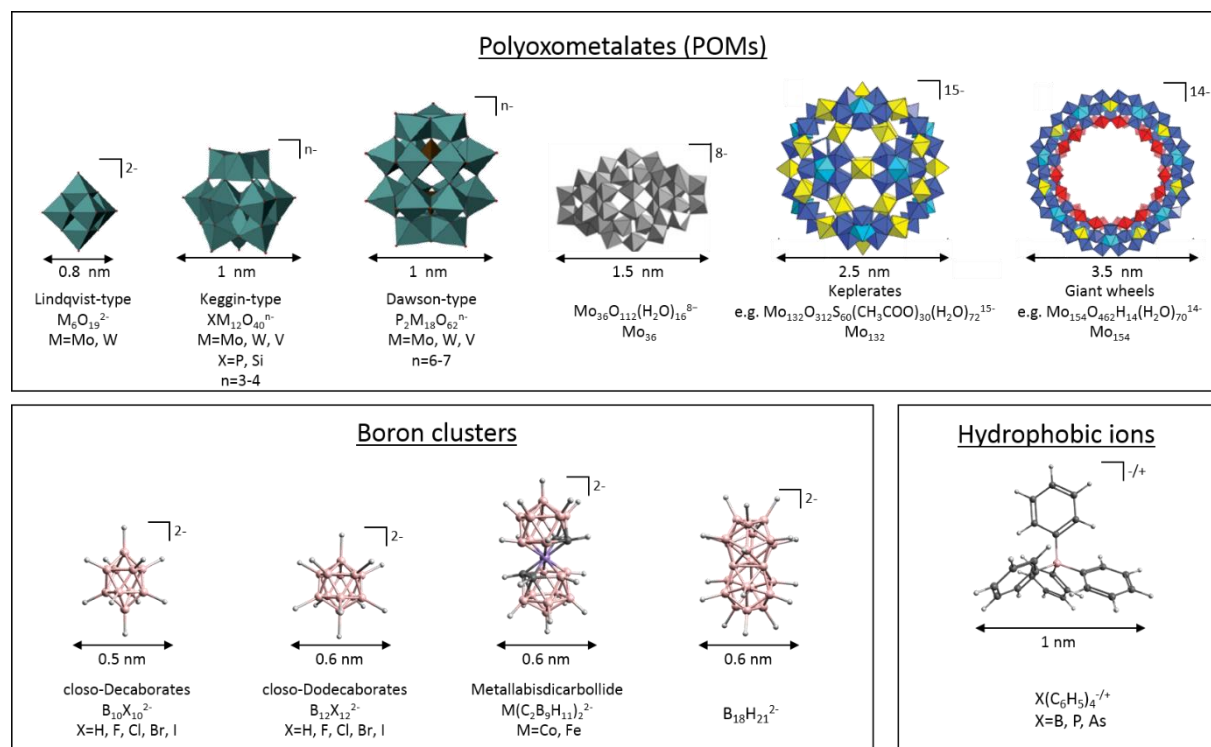


Figure 3: Nano-ions that are considered within the framework of superchaotropic ions, including polyoxometalates (POMs), boron clusters and hydrophobic ions with respective sizes. The POMs are presented with polyhedral structures, e.g. an octahedron contains a metal with 6 coordinated oxygens, i.e.  $MO_6$ . The list is not exhaustive and only presents the architectures that will be discussed within the scope of this thesis. Polyhedral representations adapted from Rompel 2015<sup>38</sup>, Kögerler 2012<sup>39</sup> (with permission from RSC) and Falaise 2018<sup>40</sup> (with permission from ACS). Boron cluster and hydrophobic ion structures were drawn and simulated using Avogadro software.

### 1.2.1. Boron clusters and their superchaotropic behavior

Boron has the ability to catenate and form molecules of unlimited size, which due to the three electrons in boron's valence shell, take forms of highly symmetric polyhedra, e.g. decaborate,  $B_{10}H_{10}^{2-}$ , and dodecaborate,  $B_{12}H_{12}^{2-}$ , see Figure 3, that cannot be obtained in carbon-based organic chemistry. Their discovery dates back to the work of Alfred Stock in the beginning of the 1900s<sup>41,42</sup> and since then tremendous progress was made in the field of boron cluster chemistry owing to the discoveries of a vast variety of architectures of non-ionic as well as ionic boranes and their derivatives that incorporate heteroatoms, such as carbon (then called carboranes), and metals (then called metallaboranes), or both (called metallacarboranes, example metallabisdicarbollide in Figure 3) in their structures. The ionic as well as the non-ionic plenary boron clusters and metallabisdicarbollides exhibit 3D-aromaticity, which equips them with exceptional thermal and chemical stabilities.<sup>43,44</sup> Due to their inertness and low toxicity in humans, such boron-rich clusters find application as boron carriers in boron neutron

capture therapy<sup>44,45</sup> and as carriers of chemo-therapy drugs<sup>46</sup>. Further, they can be used as active components in photoluminescent materials<sup>47</sup>, as building blocks in material science<sup>44,48,49</sup>, as non-coordinating anions in ion-selective electrodes<sup>44,50</sup>, in metal extraction<sup>44</sup>, in hydrogen storage<sup>51</sup> and in catalysis<sup>52</sup>.

For the purpose of this work, the focus is set on plenary nanometer-sized anionic boron clusters (ABCs) with delocalized charges as these belong to the chaotropic end of the Hofmeister series. The different boron cluster architectures, which shall be discussed in this context are the quasi-spherical *closo*-decaborates,  $B_{10}X_{10}^{2-}$ , and *closo*-dodecaborates,  $B_{12}X_{12}^{2-}$  with respectively  $X=H, F, Cl, Br, I$  and the theta-shaped metallabisdicarbollides,  $M(C_2B_9H_{11})_2^-$  with  $M=Co, Fe$  and  $B_{18}H_{21}^{2-}$ , all depicted in Figure 3. Metallabisdicarbollide can be best described as a sandwich complex of  $M^{3+}$  in between two open *nido*-carborane ( $C_2B_9H_{11}^{2-}$ ) domes with the most prominent and widely studied one being the COSAN anion  $Co(C_2B_9H_{11})_2^-$ .

In aqueous solution, all mentioned ABCs are expected to bind water weakly due to their low charge densities and their characteristic molecular inability to make classical hydrogen-bonds ( $H_2O^{\delta-} \cdots H^{\delta+} - X^{\delta-}$ ) with surrounding water molecules arising from the delta-negative partial charge on the hydrogen in the  $B^{\delta+} - H^{\delta-}$  bond. Instead, the comparably weaker dihydrogen bonds ( $O^{\delta-} - H^{\delta+} \cdots H^{\delta-} - B^{\delta+}$ ) are formed with water in the borate's first hydration shell.<sup>53</sup> Upon solvation in water these ABCs exhibit the classical thermodynamic fingerprint of chaotropic ions.<sup>36</sup> Furthermore, decaborates, dodecaborates and metallabisdicarbollides are known to adsorb to the air-water interface inducing a decrease of the surface tension and to show self-aggregation in aqueous solution.<sup>54</sup> The onset concentration of the aggregation/surface adsorption is inversely proportional with their low respective charge densities and can be ascribed to at least a partial intrinsic hydrophobic character of these ions.<sup>54</sup> Thus, decaborate and dodecaborate show a weak tendency to aggregate at high concentrations ( $c > 0.1$  M), whereas metallabisdicarbollides, remarkably, self-assemble strongly in a fashion very similar to classical amphiphilic surfactants. For instance, COSAN, was shown to exhibit numerous classical characteristics of surfactants including self-assembly into micelles and vesicles at low concentrations, into lyotropic lamellar phases at high concentrations and even foaming.<sup>55-58</sup> Such self-assembly behavior of boron clusters is exceptional because their symmetrical structure lacks typical hydrophobic and hydrophilic structure motifs of classical surfactants. Rather, ABCs seem to exhibit a certain intrinsic amphiphilicity and may be referred to as stealth amphiphiles.<sup>54</sup> For COSAN, which is not entirely symmetrical, its peculiar aggregation behavior might arise from an interplay of inter-COSAN  $C^{\delta+} - H^{\delta-} \cdots H^{\delta+} - B^{\delta-}$  dihydrogen bonding<sup>59</sup>, an anisotropic distribution of charge between the C- and B-atoms<sup>60</sup> and short-range

COSAN<sup>-</sup>...COSAN<sup>-</sup>-attraction.<sup>59</sup> Interestingly, the micellization of COSAN is driven by enthalpy and not by entropy, a thermodynamic aggregation fingerprint, which cannot be assigned to the classical hydrophobic effect and was also observed upon binding with macromolecular host molecules as outlined in the following.

Thus, decaborates, dodecaborate and its perhalogenated derivatives, COSAN and B<sub>18</sub>H<sub>21</sub><sup>-</sup>, all show strong binding to the hydrophobic cavities of macrocyclic host molecules such as cyclodextrins both in the gas phase (B<sub>12</sub>X<sub>12</sub><sup>2-</sup> <sup>61</sup>, B<sub>18</sub>H<sub>21</sub><sup>-</sup> <sup>62</sup>) and in aqueous solution (B<sub>10</sub>H<sub>10</sub><sup>2-</sup> <sup>63,64</sup>, B<sub>12</sub>X<sub>12</sub><sup>2-</sup> <sup>3,65</sup>, B<sub>18</sub>H<sub>21</sub><sup>-</sup> <sup>66</sup>, COSAN <sup>67</sup>). The thermodynamic fingerprint of the binding process in aqueous solution is characterized for all these ABCs by a highly favorable enthalpic gain and an unfavorable entropic cost, which was traced back to a shedding of the weakly bound hydration shell of the ABCs consonant with a release of water-molecules from the cavity that results in a bulk water structure recovery.<sup>3</sup> These binding phenomena were concluded to arise as a result of the chaotropic effect. Because the observed binding constants exceeded largely the weak binding of common classical chaotropic ions these ABCs were termed superchaotropic ions.<sup>3,66,67</sup> It should be noted that all such supramolecular binding phenomena are always subject to geometric requirements. For example, Nau et al. observed the following ordering of binding constants of the dodecaborates with  $\gamma$ -cyclodextrin: B<sub>12</sub>H<sub>12</sub><sup>2-</sup> < B<sub>12</sub>Cl<sub>12</sub><sup>2-</sup> < B<sub>12</sub>I<sub>12</sub><sup>2-</sup> < B<sub>12</sub>Br<sub>12</sub><sup>2-</sup>. It was concluded that B<sub>12</sub>Br<sub>12</sub><sup>2-</sup> had the best geometrical fit with the hydrophobic pocket of  $\gamma$ -cyclodextrin, while its larger derivative B<sub>12</sub>I<sub>12</sub><sup>2-</sup> had a worse match with the cavity leading to a lower binding constant despite its presumably more chaotropic nature.<sup>3</sup>

In accordance with the supramolecular binding of ABCs, it was shown that classical chaotropic ions bind to hydrophobic pockets within proteins with the same thermodynamic signature.<sup>68</sup> Subsequently, upon investigating bovine serum albumin protein by means of fluorescence quenching and light scattering techniques, it was concluded that COSAN and its derivatives bind specifically and strongly (at low concentrations) to hydrophobic pockets within the protein, whereas the specific binding did not occur for the smaller B<sub>12</sub>H<sub>12</sub><sup>2-</sup>-dodecaborate. Additionally, non-specific binding to the protein surface was observed to be strong for COSAN and weak (at high concentrations) for B<sub>12</sub>H<sub>12</sub><sup>2-</sup>.<sup>69</sup> Similarly, per-halogenated decaborates and dodecaborates were shown to interact with hydrophobic moieties in human serum albumin. The extent of interaction increased with size of the borates from hydrogenated to iodinated.<sup>70,71</sup>

Further, a few studies demonstrated strong non-specific interaction of COSAN with non-ionic polymers and block co-polymers, inducing either precipitation or nanoparticle formation of the

formed COSAN/polymer composite.<sup>72-75</sup> Additionally, COSAN was shown to be able to rapidly cross lipid assemblies<sup>67,76</sup>, while  $B_{12}H_{12}^{2-}$  did not.<sup>67</sup>

To conclude, all mentioned ABCs seem to have dual characters including both hydrophobic as well as chaotropic traits. In the quasi-spherical decaborates and dodecaborates, hydrophobicity seems to be less pronounced because they tend to aggregate and affect the surface tension of water only at high concentrations. Their interaction with neutral soft matter interfaces, for example proteins, polymers and macromolecular cavities, is expected to be strong and mostly driven by the chaotropic effect, where a release of hydration water of the interface and the ion into the bulk serves as the driving force, see Figure 4. In comparison, COSAN seems to differ significantly. It displays strong surface activity and can easily cross lipid membranes, both clear signs of a substantial hydrophobic or lipophilic character. However, as it is weakly hydrated in aqueous solution it additionally exhibits classical chaotropic traits as indicated for instance by its thermodynamic signature upon micellization or upon binding to cyclodextrin.

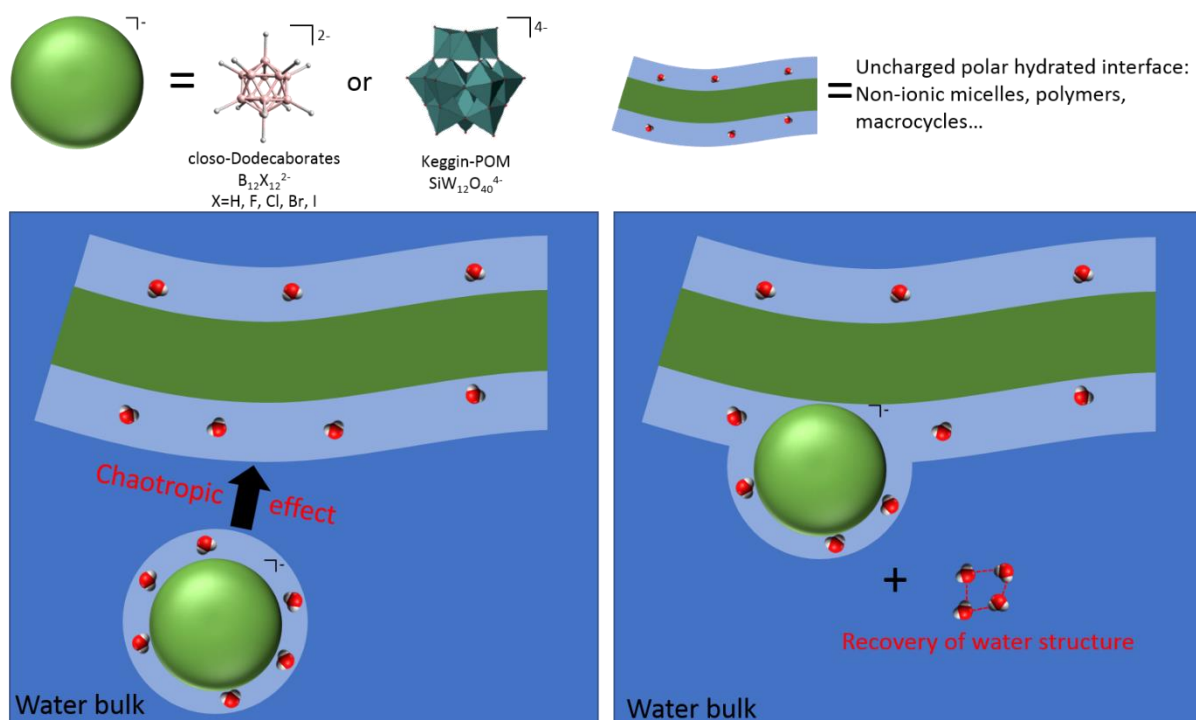


Figure 4: Adsorption of a superchaotropic ion to an uncharged hydrated polar interface leading to water structure recovery. Only hydration water molecules are shown.

### 1.2.2. Polyoxometalates and their superchaotropic behavior

Polyoxometalates (POMs) are anionic discrete metal oxide clusters of early transition metals in their highest oxidation states, such as vanadium (VI), molybdenum (VI) and tungsten (VI). If they contain central heteroatoms (e.g. P, Si, As) they are referred to as heteropolyanions, if not they are called homopolyanions.

After the first POM-synthesis by Berzelius in 1826<sup>77</sup> ( $\text{PMo}_{12}\text{O}_{40}^{3-}$ ) and the first structure resolution by Keggin in 1933<sup>78</sup> ( $\text{PW}_{12}\text{O}_{40}^{3-}$ , Keggin structure), many more POMs and respective structural archetypes were discovered that can involve hundreds of metal centers in just one structure, like Keplertes<sup>79</sup> and giant wheels<sup>80</sup>. For a selection of different POM-types, see Figure 3. The vast structural and electronic diversity<sup>81</sup> of POMs implies diverse and tunable chemical and physical properties, which has led to applications involving POMs in many different fields. Accordingly, POMs find uses as oxidation and acid (photo-) catalysts<sup>81,82</sup>, in analytical chemistry for element determination<sup>81,83</sup> and as sensors<sup>84</sup>, in medicine owing to their antitumoral and antiviral activity<sup>81,82,85</sup>, in materials exploiting their magnetic<sup>86</sup> and redox-properties<sup>82,87,88</sup>, as building blocks in hybrid organic-inorganic materials<sup>89</sup> and as crystallizing agents for proteins<sup>38</sup>.

In respect to their size, many POMs, e.g. the Keggin-POMs  $\text{SiW}_{12}\text{O}_{40}^{4-}$  (SiW) and  $\text{PW}_{12}\text{O}_{40}^{3-}$  (PW) hold only few and delocalized<sup>88,90</sup> charges (3D-aromaticity), which gives rise to very low charge densities compared to classical anions, such as  $\text{Cl}^-$  and  $\text{I}^-$ , see the following table.

Table 1: Comparison of volume charge densities of the classical halide anions  $\text{Cl}^-$  (neutral ion) and  $\text{I}^-$  (chaotropic ion) with the two Keggin-POMs  $\text{SiW}_{12}\text{O}_{40}^{4-}$  and  $\text{PW}_{12}\text{O}_{40}^{3-}$ .

Ion	Ionic radius [nm]	V [nm <sup>3</sup> ]	Charge, $q_e$	Charge density [q <sub>e</sub> /nm <sup>3</sup> ]	Classification
$\text{Cl}^-$	0.18 <sup>1</sup>	0.02	1	40	neutral
$\text{I}^-$	0.22 <sup>1</sup>	0.04	1	22.4	chaotropic
$\text{SiW}_{12}\text{O}_{40}^{4-}$	0.48 <sup>2</sup>	0.46 <sup>1</sup>	4	8.7	superchaotropic
$\text{PW}_{12}\text{O}_{40}^{3-}$	0.48 <sup>2</sup>	0.46 <sup>1</sup>	3	6.5	superchaotropic

<sup>1</sup>taken from Marcus.<sup>91</sup>

<sup>2</sup>POM-dimensions taken from Buchecker et al.<sup>92</sup> POMs are considered as spheres.

In water, these Keggin-POMs are thus very weakly hydrated<sup>93,94</sup> and expected to have the classical thermodynamic solvation fingerprint of chaotropic ions (shown by extrapolation from classical ions and their sizes)<sup>36</sup>. Further, due to their large size (d=1 nm), Keggin-POMs lie at the border to the colloidal regime and are best characterized with a dual behavior comprising colloidal and ionic properties.<sup>95,96</sup> Thus, for instance,  $\text{PW}(3-)$ -molecules in aqueous solution interact with each other by short-range attraction and long-range repulsion forces, a common

feature of charged colloids, such as proteins.<sup>97</sup> This behavior arises from the very low charge densities and high polarizabilities of the Keggin-POMs in respect to their size and entails that PW-ions tends to self-aggregate at high concentrations ( $c > 0.1$  M) as shown experimentally and by MD-simulations.<sup>97-99</sup> Notably, other Keggin-ions with higher charge, such as SiW(4-), do not exhibit the short-range attractive force and corresponding self-aggregation ability as electrostatic POM-POM repulsions are too strong.<sup>97,98</sup> Additionally, a similar phenomenon was observed at the air-water interface, as PW accumulated close to it, while SiW did not.<sup>97</sup> Remarkably, despite the accumulation of PW at the air-water interface, the surface tension was shown to remain unaffected. Moreover, for larger, so-called giant POMs such as Keplerates and giant wheels, see Figure 3, in aqueous solution aggregation behavior is more pronounced, especially because counter-ion condensation to surface patches with high charge density (so-called Manning condensation, again a colloidal property exhibited by highly charge colloids such as ionic micelles) takes place, which allows for counter-ion bridging between POMs and induces self-assembly.<sup>100-103</sup>

The behavior of POMs in aqueous solution was shown to substantially change in the presence of polar (uncharged) entities: Thus, it was highlighted for Keggin-POMs by Naskar et al. that these nano-ions adsorb to hydrated polar interfaces driven by the chaotropic effect and with much higher extents compared to classical chaotropic ions.<sup>4</sup> Therein, both, SiW and PW were classified as superchaotropic ions because they adsorbed strongly at millimolar concentrations to or in between the hydrated polar head groups in non-ionic (sugar-head and ethoxylated) surfactant assemblies including micelles and foams as concluded from SAXS, flotation and cloud point measurements. A favorable release of water-molecules from the hydration shell of the surfactant assemblies and the ion upon adsorption of the Keggin-POMs was proposed to be at the origin of this chaotropic adsorption phenomenon.<sup>4</sup> Naskar's pivotal paper provided the foundation for numerous follow-up studies of superchaotropes at hydrated polar soft matter interfaces. Thus, shortly after, Dawson-POMs were assessed as superchaotropic ions, as they adsorbed to non-ionic ethoxylated micelles and in doing so a general method to assess the superchaotropicity of ions by means of cloud point and SAXS-measurement was presented by Buchecker et al.<sup>92</sup> The same author further highlighted the strong superchaotropic adsorption of Keggin-POMs PW, SiW and PMo ( $\text{PMo}_{12}\text{O}_{40}^{3-}$ ) to the biomimetic poly N-isopropyl amide polymer (PNIPAM) inducing strong structuration into PNIPAM globules and sheets concluded from SAXS, SANS and cryo-TEM.<sup>104</sup> Additionally, it was shown by DSC-measurement on the example of PW that adsorption of nano-ions causes a dehydration of the PNIPAM-polymer. Notably, PW had the strongest structuring effect related to its strongest superchaotropic

character among the used POMs arising from its low charge density and high polarizability. Moreover, the Keggin-POMs were also found to interact strongly with smaller hydrated molecules that do not provide discrete interfaces. Thus, for example, interaction of SiW and PW with non-ionic surfactant monomers (ethoxylated and sugar-based) can lead to an increase of the surfactant's cmc as it may be preferable over the interaction with the entire micelle depending on the specific surfactant.<sup>105</sup> These interactions are expected to happen at the hydrated moieties of the surfactant, for instance ethylene glycol groups and accordingly polyethylene glycol (PEG) oligomers were found to interact strongly with the Keggin-POM PW in aqueous solution forming PW-PEG nano-assemblies.<sup>106</sup> Upon addition of NaCl to screen interactions between the PW-PEG self-assemblies, precipitation and crystal formation was induced with an unexpected specificity for crystals containing 5-6 ethylene glycol groups excluding longer and shorter PEG oligomers. Similarly, polyethylene glycol polymers and PPO-PEO-PPO pluronics were found to form inclusion crystals with the Keggin-POM SiW<sup>107</sup> and coacervate formation of PEG with the Keggin-POM MW ( $\text{H}_2\text{W}_{12}\text{O}_{40}^{6-}$ ) was observed<sup>108</sup>. A special class of non-charged polar hydrated molecules are macrocycles, for example the sugar-based cyclodextrins that contain a central hydrophobic cavity. Classically, hydrophobic molecules bind to these cavities to avoid unfavorable interaction with bulk-water entailing a favorable recovery of water structure. However, various POMs and other nanometric metal clusters were found to bind to the cavities of cyclodextrins despite them being generally considered as hydrophilic ions due to their high solubilities in water, including the Keggin-ion  $\text{PMo}_{12}\text{O}_{40}^{3-}$ <sup>109</sup>, the Dawson-POM  $\text{P}_2\text{W}_{18}\text{O}_{62}^{6-}$ <sup>110,111</sup>, the cationic  $\text{Ta}_6\text{Br}_{12}(\text{H}_2\text{O})_6^{2+}$ <sup>111</sup> and the anionic  $\text{Re}_6\text{X}_8(\text{CN})_6^{4-}$  with X=S, Se, Te.<sup>112-114</sup> For the latter cluster, it was shown that oxidation to  $\text{Re}_6\text{S}_8(\text{CN})_6^{3-}$  causes a strong increase in the binding constant related to the lower charge density and resulting stronger chaotropic character.<sup>114</sup> Interestingly, the central cavity in giant wheel type  $\text{Mo}_{154}$  POMs was even found to serve as a host for a Dawson-POM-cyclodextrin complex.<sup>110</sup> Further, it was shown that the presence of a cyclodextrin changed substantially the speciation of  $\text{MoO}_4^{2-}$  in aqueous solution as the  $\text{Mo}_{36}$ -species (Figure 3 for the structures), present at low pH and unable to bind to cyclodextrins cavity due to its large size, turned into the smaller Lindqvist-ion  $\text{Mo}_6\text{O}_{19}^{2-}$  (structure shown in Figure 3) stabilized by complexation in the cyclodextrin cavity, which was thus far never observed in aqueous solution.<sup>40</sup> The transformation of  $\text{Mo}_{36}$  to  $\text{Mo}_6$  in the presence of cyclodextrin as well as the other mentioned POM-host binding phenomena can be assigned to a good geometric match between host and guest, which in turn allows for a large release of water molecules that provides the characteristic chaotropic driving force.



Besides, POMs are known to interact strongly with biological molecules, such as proteins arising from a variety of interactions such as covalent and H-bonding, as well as electrostatic and vdW-interactions<sup>38</sup>, but also from superchaotropic adsorption onto non-charged polar moieties.<sup>104,115</sup> Accordingly, by measuring Langmuir isotherms it was shown that Keggin-ions interact electrostatically with condensed cationic lipid monolayers leading to a decrease of the area per cationic headgroup as MW (6-) had the strongest effect followed by SiW (4-) and PW (3-).<sup>116</sup> A condensed anionic lipid monolayer was affected by the ions as well due to a suspected hydrophobic character of the Keggin-ions, however, no specific ordering was observed. Last, the head group area of a condensed zwitterionic lipid monolayer was increased in the presence of Keggin-ions due to ion adsorption and induced electrostatic repulsion following the chaotropic ordering of the POMs, that is PW had the strongest effects followed by SiW and MW.<sup>116</sup>

Furthermore, Bastos-Gonzaléz et al. demonstrated that the Keggin-POM PW adsorbs to cationic and anionic colloidal particles regardless of the hydrophilic or hydrophobic nature of the particles and concluded that the adsorption arises exclusively from the colloidal character of PW and is not driven by the chaotropic effect.<sup>96</sup>

In conclusion, the adsorption of low-charge density (small) POMs onto polar surfaces seems to be a non-specific and general phenomenon, which is attributed in most cases to the workings of the chaotropic effect. Upon adsorption, the hydrated interface as well as the superchaotropic ion shed at least a part of their hydration shell, which leads to a thermodynamically favored water structure recovery in the bulk, as shown in Figure 4. However, with increasing size and decreasing charge density of the POM, colloidal as well as hydrophobic behavior arises, which starts to appear for the Keggin-POM PW and is most pronounced for giant POMs.

### 1.2.3. Hydrophobic ions

Hydrophobic ions are generally ionic molecules that contain large organic groups, which shield the hydrophilic charge from direct contact with water, such as alkylated ammonium, phosphonium or borate ions. Leontidis et al. discussed the position of particularly large organic hydrophobic ions to lie beyond the chaotropic end of the Hofmeister scale on the example of the nanometric hydrophobic ion  $\text{BPh}_4^-$  (see Figure 3), as it was found to interfere strongly with phospholipid monolayers and micelles. Unlike classical chaotropic ions, which only adsorb weakly and cause negligible alterations to such polar soft matter interfaces, hydrophobic ions, like  $\text{BPh}_4^-$  adsorbed strongly to (at mM concentrations) and also intercalated into the lipid interface inducing strong alterations to the lipid packing and affecting micellar shape and size.<sup>34,35</sup> Thus, the hydrophobic ion  $\text{BPh}_4^-$  was termed a soft matter disruptor as an extension to classical chaotropes.<sup>35</sup> With the arrival of superchaotropic ions in the scientific literature obvious parallels of hydrophobic ions with the superchaotropic boron clusters and POMs, discussed in the preceding sections, were observed. Thus, Bastos-Gonzalez et al. concluded from stability experiments of charged colloidal latex particles as a function of ion type and concentration, that the hydrophobic ion  $\text{BPh}_4^-$  and its cationic analogue  $\text{AsPh}_4^+$  belong to the group of superchaotropic ions owing to their more pronounced hydrophobic characters compared to classical chaotropic ions.<sup>5</sup>

However, hydrophobic ions and (super)chaotropic ions can be clearly distinguished by comparing their interaction with water. (Super)chaotropic ions interact favorably with water as reflected by negative Gibbs free energies of solvation (entailing high solubility), while hydrophobic ions do not interact favorably with water (entailing very limited solubility), therefore, display positive solvation free energies and are only “held” in aqueous solution owing to a favorable solvation of their hydrophilic counter-ions.<sup>36,91</sup> Similarly, the structural entropy of water molecules around hydrophobic ions, such as  $\text{BPh}_4^-$  is negative<sup>91</sup> as the ion-surrounding water-molecules are highly structured arising from the attempt of water to maximize hydrogen-bonding around the hydrophobic molecule at the expense of motional freedom.<sup>117</sup> This lies in direct contrast to superchaotropic ions, which exhibit highly negative structural entropies and high dynamics in their hydration shells.<sup>26,91</sup> For these reasons, hydrophobic ions, such as  $\text{AsPh}_4^+$  and  $\text{BPh}_4^-$ , are referred to specifically as hydrophobic and not as superchaotropic ions in this thesis.

Due to their intrinsic hydrophobicity,  $\text{PPh}_4^+$ <sup>118</sup> and  $\text{BPh}_4^-$  adsorb to the air/water interface causing a strong decrease in surface tension at  $c(\text{hydrophobic ion}) > 0.01 \text{ M}$ . Accordingly, such

hydrophobic ions (e.g.  $\text{BPh}_4^-$ ) prefer solvation in organic media whereas their hydrophilic counter-ions (e.g.  $\text{Na}^+$ ) prefer the aqueous environment. As a result, in mixed organic/aqueous systems these so-called antagonistic salts exhibit surfactant-like behavior as the ions respectively self-organize along organic/aqueous interfaces inducing structuration and stabilization of otherwise insoluble organic solvent droplets.<sup>119–121</sup>

Furthermore,  $\text{BPh}_4^+$  and  $\text{AsPh}_4^+$  were shown to interact strongly with PNiPAM polymer (poly *n*-isopropyl amide) inducing precipitation at millimolar concentrations driven by the hydrophobic effect.<sup>122</sup> At concentrations inferior to the precipitation limit, the effects of the hydrophobic ions on the lower critical solution temperature were investigated and compared to classical ions. Despite the evidently strong interaction, the salting-in effects of  $\text{BPh}_4^-$  and  $\text{AsPh}_4^+$  were surprisingly small, notably weaker than the effect of  $\text{SCN}^-$ , and were accompanied by a formation of PNiPAM/hydrophobic ion nanoparticles at  $T > \text{LCST}$ , which was not observed with classical ions.<sup>122</sup> Further, strong interaction between these hydrophobic ions and proteins takes place, especially with more hydrophobic proteins that contain many hydrophobic amino acids<sup>123</sup> and strong binding to the hydrophobic cavities of cyclodextrins has been observed.<sup>124</sup> All these phenomena result from the hydrophobic effect. Essentially, a favorable minimization of ion/water contacts drives the hydrophobic ions out of the aqueous bulk towards all kinds of unpolar (weakly hydrated) or hydrophobic environments. Notably, as with the chaotropic effect a bulk water structure recovery also results from the hydrophobic effect. Both chaotropic and hydrophobic binding processes are driven by an enthalpically favorable recovery of hydrogen bonds in the water bulk. The structural entropic term, however, is opposite in the two cases as release of water molecules from the hydration sphere of chaotropic ions entails a decrease in water dynamics (entropically unfavorable), whereas water molecules around hydrophobic ions regain motional freedom upon release into the bulk (entropically favorable).<sup>3</sup>



## 2. Nano-ions in interaction with non-ionic surfactant micelles

### 2.1. Non-ionic surfactant phases as probes for superchaotropic ions

Non-ionic surfactants represent a large group of amphiphilic molecules, among which polyethoxylated surfactants ( $\text{H}(\text{CH}_2)_i(\text{OCH}_2\text{CH}_2)_j\text{OH}$ , abbreviated  $\text{C}_i\text{E}_j$ ) are the most common ones. They are composed of an aliphatic carbon chain ( $\text{H}(\text{CH}_2)_i$ ), constituting the hydrophobic tail, end-linked with a hydrophilic polyethoxy ( $(\text{OCH}_2\text{CH}_2)_j\text{OH}$ ) head. Two example surfactants,  $\text{C}_{12}\text{E}_5$  and  $\text{C}_8\text{E}_4$  are shown in Figure 5a. Due to their amphiphilic nature they can self-assemble into different morphologies, where the hydrophilic polyethoxy heads point outwards into the aqueous phase, while the hydrophobic chains point into the center of the self-assembly. Depending on the surfactant and conditions used, the underlying molecular surfactant geometry changes and drives the formation of, for example, micellar, lamellar and sponge phases. Classically, the geometric requirement of the individual surfactant molecules inside such self-assemblies is described by the molecular packing parameter  $N_S$ , which is the ratio of the end area of the hydrophobic tail  $a_T$  to the effective area of the hydrophilic head  $a_H$ , shown in Figure 5a.<sup>125</sup>

$$N_S = \frac{a_T}{a_H} = \frac{V_T}{a_H * l_T}$$

with the length  $l_T$  and the molecular volume  $V_T$  of the hydrophobic tail. Thus, spherical micelles form at low packing parameters of  $N_S < 1/3$  and turn into cylindrical micelles up to  $N_S = 1/2$ , followed by bilayer phases up to  $N_S = 1$ . For schematic depictions of the mentioned phases, see Figure 5b and c. There exist also other non-ionic surfactant phases, such as hexagonal and cubic and inverted phases, which appear at high surfactant concentrations (above 10 wt-%). However, these surfactant phases are irrelevant in this thesis as the surfactants were always used in rather dilute solutions and will therefore not be further discussed. Additionally, the lyotropic bilayer phases will be set into focus later, in chapter 3. Here, we shall concentrate on micellar phases.

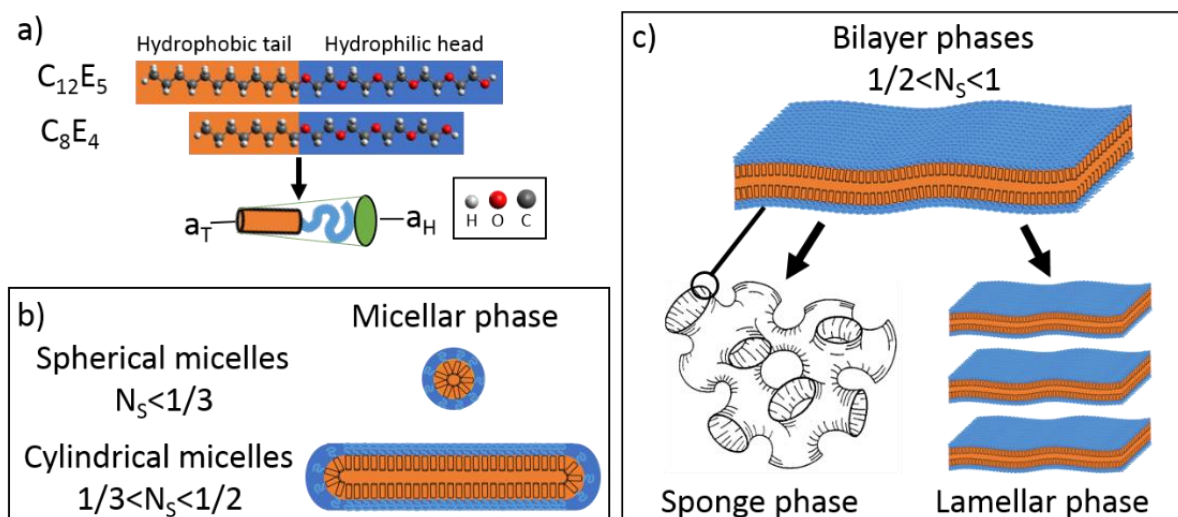


Figure 5: a) Non-ionic surfactants  $C_8E_4$  and  $C_{12}E_5$  with their respective hydrophobic and hydrophilic parts. b) Schematic self-assemblies of non-ionic surfactants into spherical and cylindrical micelles. c) Surfactant self-assemblies into bilayer phases such as sponge phases and lamellar phases.

Thus, at low temperatures and at surfactant concentrations not too far above the critical micellar concentration (cmc), which is characteristic to each surfactant, micelles form spontaneously in water. Generally, ethoxylated non-ionic surfactant self-assemblies exhibit characteristic heat-sensitivity. In particular, the hydration shell around the hydrophilic PEO-headgroups is weakly bound and is gradually shed off into the water bulk upon heating.<sup>126,127</sup> Thus, micelles become more hydrophobic with temperature as the effective head group area per surfactant molecule decreases. The geometry of the individual surfactant molecules thus changes and manifests as an elongation of the micelles up to a critical temperature<sup>128,129</sup>, the so-called cloud point, CP. At the CP, the elongated micelles interact attractively and aggregate, which causes a destabilization of the micellar phase causing phase separation (turbid solution) into a concentrated and a dilute micellar phase, see Figure 6.

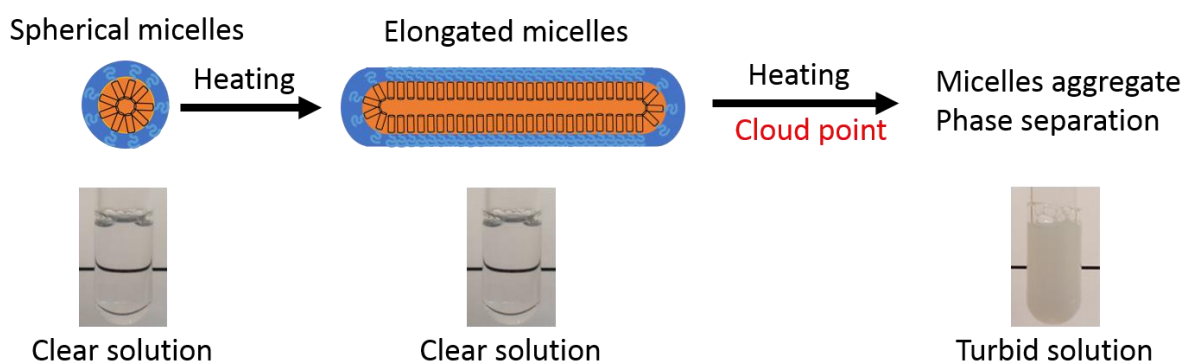
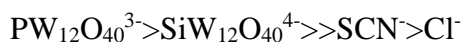


Figure 6: Elongation of non-ionic surfactant micelles upon heating to the cloud point. Additionally, images of the resulting phases are shown.

This phase separation temperature is sensitive to external stimuli such as the addition of salt. Classical ions do not interact with the hydrophobic micellar core and may interact weakly with

the hydrophilic headgroups of the non-ionic surfactant depending on the nature of the ion. Kosmotropic ions, on the one hand, bind water strongly in their own hydration shells and effectively withdraw water molecules from the hydrophilic surfactant head groups. Consequently, as micelles become less hydrated and slightly more hydrophobic, the cloud point shifts to lower temperatures. On the other hand, chaotropic ions weakly adsorb to the hydrated surfactant head groups. This leads to an increase of the cloud point as the micelles acquire minuscule surface charges that inhibit the aggregation of the micelles and, consequently, shift the CP to higher temperatures. Overall, the prominent Hofmeister series of ions results from CP-measurements in the presence of classical salts.<sup>12,130,131</sup>

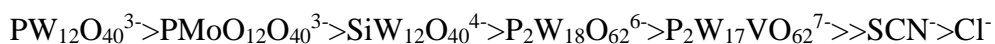
This simple, yet powerful concept was used recently to assess the chaotropicity of POMs by Naskar et al.<sup>4</sup>: Upon investigation of the CP of the dilute non-ionic surfactant C<sub>8</sub>E<sub>4</sub> (60 mM, 1.8 wt-%) in water as a function of salt (POM) concentration, it was observed that the Keggin-POMs silicotungstate (SiW<sub>12</sub>O<sub>40</sub><sup>4-</sup>, SiW) and phosphotungstate (PW<sub>12</sub>O<sub>40</sub><sup>3-</sup>, PW) induced a tremendous CP-increase in the millimolar range. PW induced a more pronounced CP-increase than SiW, and both largely exceeded the effects of classical chaotropic ions such as SCN<sup>-</sup>. The CP-increase followed the inverse ordering of charge densities:



Consonantly, small angle x-ray scattering (SAXS) revealed that PW and SiW adsorb strongly to all kinds of non-ionic surfactant micelles including ethoxylated (C<sub>8</sub>E<sub>4</sub>), sugar based (octylglucoside, C<sub>8</sub>G<sub>1</sub>) and commercial carboxyl surfactants (C<sub>18:1</sub>E<sub>8-10</sub>COOH, at pH < pK<sub>a</sub>). For all used surfactants, spherical, electrostatically repulsive, POM- (and, hence charge-) decorated micelles were formed. For C<sub>8</sub>G<sub>1</sub>-micelles specifically, PW was found to penetrate deeper in between the glucose headgroups compared to SiW. Upon addition of the electrolyte NaCl, electrostatics between the decorated micelles were screened while the spherical micellar shape remained. The electrostatic intermicellar repulsion between these POM-decorated micelles was inferred to be at the origin of the strong cloud point increase in the presence of the two POMs and, in conclusion of the article, SiW and PW were classified as superchaotropic anions.

Buchecker et al.<sup>92</sup> then developed the CP-method further and expanded it to other POM architectures, including Keggin type (XM<sub>12</sub>O<sub>40</sub><sup>n-</sup>, here X=Si, P and M=W, Mo and n=3-4) as well as Dawson type POMs (X<sub>2</sub>M<sub>18</sub>O<sub>62</sub><sup>n-</sup>, here X=P, and M=W, V and n=6-7). The ordering according to the respective CP-increase (again of dilute C<sub>8</sub>E<sub>4</sub>) corresponded to the inverse ordering of the charge density of the used POMs, while the polarizability of the POMs seemed to be of less importance. To assess the CP-evolutions, an adapted Langmuir model, commonly used to assess salt effects in clouding phenomena<sup>29,132</sup>, was used to condense the curves into

two parameters. This fitting procedure proved reliable and provided an automated method to interpret the acquired CP-evolutions. In addition, SAXS was again employed to confirm the adsorption of all used POMs to the C<sub>8</sub>E<sub>4</sub> micelles. As a result, an extension of the Hofmeister series towards more superchaotropic ions was established including Keggin and Dawson type POMs:



Moreover, Buchecker et al. demonstrated that changing the counter-cation of P<sub>2</sub>W<sub>18</sub>O<sub>62</sub><sup>6-</sup> from H<sup>+</sup> to K<sup>+</sup> had a negligible effect on the CP-evolution. Thus, at the used conditions, counter-ion binding as well as pH effects were excluded to significantly affect POM-adsorption and the CP-phenomenon.

The present chapter intends to quantify and understand more deeply the interaction of superchaotropic nano-ions with C<sub>8</sub>E<sub>4</sub>-micelles. The established concepts are applied and expanded to more diverse classes of nano-ions including POMs, boron clusters and hydrophobic ions. The nano-ions are first examined within each individual group and then in totality in order to establish a nano-ion scale from chaotropic over superchaotropic to hydrophobic. To do so, the sodium salts of SCN<sup>-</sup> and Cl<sup>-</sup> are used to provide the reference effects of a classical chaotropic and a “neutral” ion in Hofmeister terms. Furthermore, the effects of the (inorganic) nano-ions are juxtaposed with the effect of the (organic) ionic surfactant sodium dodecylsulfate (SDS) to highlight the remarkable similarities of these two very dissimilar chemical classes. For each nano-ion and for SDS, a parametric study was performed combining the macroscopic method of CP-measurement with small angle neutron (performed at SANS-1 at MLZ in Garching, Munich) and x-ray scattering (SWAXS lab setup at the ICSM) at selected compositions, in the presence of electrolyte and as a function of temperature. In doing so, morphological changes of the C<sub>8</sub>E<sub>4</sub>-micelles and adsorption ratios are quantified to pinpoint the effects of nano-ions on the non-ionic surfactant micelles and understand the superchaotropic adsorption process and its impact more deeply.

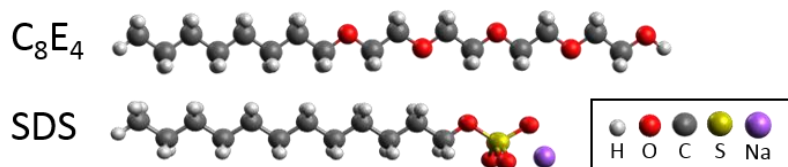
The study is organized systematically for each nano-ion class (or SDS) to elucidate:

- the effect of nano-ion (or SDS) concentration
- the effect of temperature
- the effect of electrolyte (NaCl)-concentration on electrically charged decorated (or mixed surfactant) micelles
- the effect of surfactant (C<sub>8</sub>E<sub>4</sub>) concentration



## 2.2. C<sub>8</sub>E<sub>4</sub> in water in the presence of classical salts and SDS

Tetraethylene glycol mono-octyl ether (C<sub>8</sub>H<sub>17</sub>(OC<sub>2</sub>H<sub>4</sub>)<sub>4</sub>OH), C<sub>8</sub>E<sub>4</sub>, is a polyethoxylated non-ionic surfactant, see Scheme 1 for its chemical structure.



Scheme 1: Molecular structures of the nonionic surfactant C<sub>8</sub>E<sub>4</sub> and of the ionic surfactant SDS.

Above its critical micellar concentration at 8 mM<sup>133</sup>, C<sub>8</sub>E<sub>4</sub> forms a micellar phase in water that phase-separates into a concentrated and a dilute micellar phase at its characteristic cloud point (CP) temperature.<sup>134</sup> Thus, an aqueous solution containing 60 mM C<sub>8</sub>E<sub>4</sub> ( $\cong$  1.8 wt-%) exhibits a CP at 41°C, see Figure 7, in agreement with literature.<sup>133</sup> Upon addition of classical salts the CP of C<sub>8</sub>E<sub>4</sub> either decreases or increases monotonically depending on the natures of the corresponding dissociated ions in solution. All used salts contained Na<sup>+</sup> as the cation, which is known to act as a neutral ion without pronounced chaotropic or kosmotropic character.<sup>23</sup> Additionally, as generally the Hofmeister effects of cations are smaller compared to anions, the anions are expected to affect predominantly the CP-evolution. Overall, the classical Hofmeister series of anions results from the CP-evolutions in Figure 7: SO<sub>4</sub><sup>2-</sup> < F<sup>-</sup> < Cl<sup>-</sup> < I<sup>-</sup> < SCN<sup>-</sup>. SO<sub>4</sub><sup>2-</sup> shows the most pronounced kosmotropic character as it caused the biggest CP-decrease, while SCN<sup>-</sup> exhibits the most pronounced chaotropic character as it caused the biggest CP-increase. In addition, NaCl exhibits an almost neutral character as it has the weakest effect on the CP. Overall, these effects are linked to the ability of the kosmotropic and chaotropic ions, for the former, to dehydrate and for the latter to adsorb to and charge the C<sub>8</sub>E<sub>4</sub>-micelles. Notably, these classic salt effects become significant at concentrations above 50 mM as the cloud point determinations using this surfactant generally feature error bars of  $\pm 1^\circ\text{C}$ .

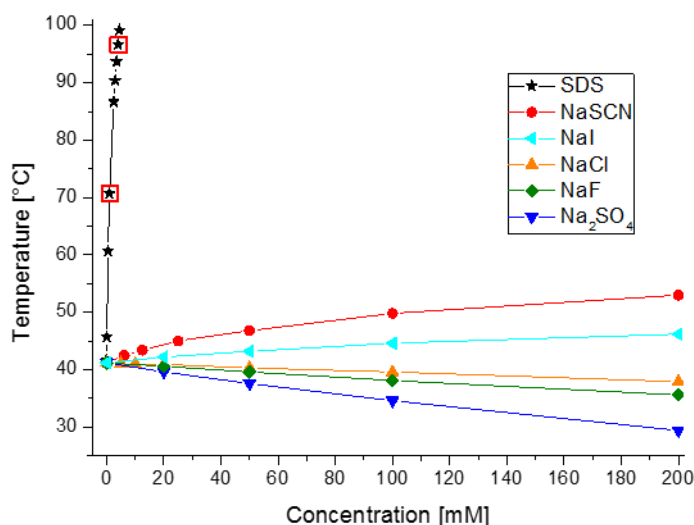


Figure 7: Cloud point evolution of 60 mM  $C_8E_4$  (1.8 wt-%) as a function of the concentration of the ionic surfactant sodium dodecylsulfate, SDS and the classical salts  $Na_2SO_4$ , NaF, NaCl, NaI and NaSCN. The two data points of SDS at 1 mM and 4 mM are framed in red to indicate that they are the same as the framed points in Figure 8.

As chaotropic ions bring an electric charge to the non-ionic micelle upon adsorption it seems adequate to provide a reference, which pinpoints the effect of charge without any ion specific contributions. For this purpose, the ionic surfactant sodium dodecylsulfate ( $C_{12}H_{25}SO_4Na$ , SDS,  $cmc=8.2$  mM at 25 °C), see Scheme 1 for its chemical structure, is used in comparison to the classical salts. Driven by the hydrophobic effect on its aliphatic  $C_{12}$ -chain and a favorable entropy of mixing, SDS anchors spontaneously into  $C_8E_4$ -micelles resulting in electrically charged mixed SDS/ $C_8E_4$ -micelles. The emergent intermicellar repulsion entails a tremendous increase in the cloud point at low millimolar SDS-concentrations, see Figure 7. Thus, for 60 mM  $C_8E_4$ , addition of only 5 mM SDS shifts the CP above 100°C. It must be emphasized that this effect of SDS is not a salt effect as the mixed micelle formation and the resulting CP-increase are consequences of the hydrophobic effect on the aliphatic  $C_{12}$ -chain of SDS. Furthermore, the enormous difference between SDS and the classical salts in the concentration ranges and the respective extents of the CP-increase provide a hint of the weak adsorption (and charging) that occurs with classical chaotropic ions, such as  $SCN^-$ .

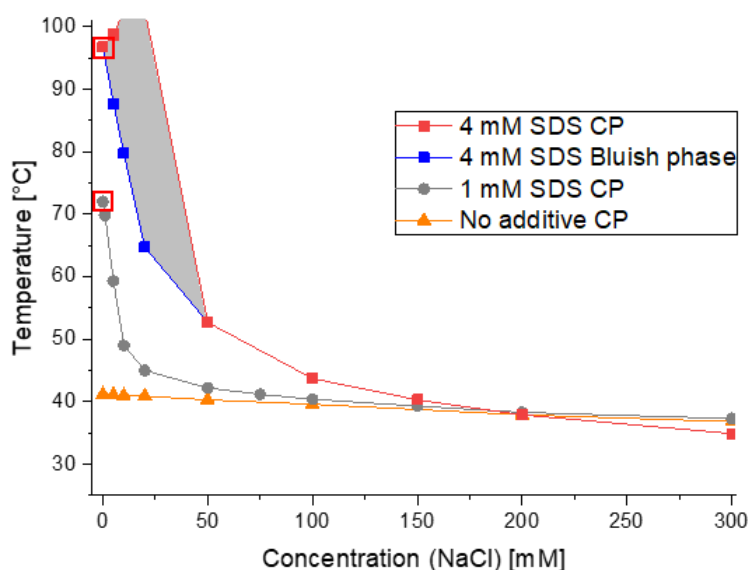


Figure 8: Cloud point evolution of 60 mM  $C_8E_4$  in the presence of 1 mM SDS and 4 mM SDS as a function of NaCl concentration. With 4 mM SDS a bluish opalescent, streaming birefringent phase was observed before the appearance of the CP as indicated with the grey region. The no additive curve is identical to the CP of 60 mM  $C_8E_4$  as a function of NaCl-concentration in Figure 7. The two data points framed in red squares are the same compositions as the framed data points in Figure 7.

To test whether the observed effects are of purely electrostatic nature or cause more profound alterations to the micelles, the CPs of mixed SDS/ $C_8E_4$  in the presence of a screening electrolyte were measured. For this purpose, the mixtures of 1 mM SDS or 4 mM SDS in 60 mM  $C_8E_4$  were chosen to trace the CP-evolution as a function of NaCl concentration, see Figure 8. NaCl was selected deliberately as it exhibits the most neutral character of all tested salts and is expected to cause charge screening without significant secondary ion specific effects. Thus, with 1 mM SDS and at  $[NaCl] < 10$  mM, the CP of 60 mM  $C_8E_4$  decreases sharply and at  $[NaCl] > 50$  mM the curve of the mixed micelles levels off and then converges precisely with the CP reference curve of just NaCl. This is a common observation at such low ionic surfactant and salt contents<sup>135–137</sup> and as the CP of a non-ionic surfactant is a measure of intermicellar interactions, here, the mixed micelles of 60 mM  $C_8E_4$  + 1 mM SDS in the presence of large enough amounts of NaCl seem to behave exactly like 60 mM  $C_8E_4$ -micelles in water. However, at higher SDS concentrations the situation is significantly different as is shown for 4 mM SDS. Thus, at  $[NaCl] < 20$  mM, the CP unexpectedly increases as it is preceded by a bluish opalescent phase, which showed birefringence under agitation. Up to  $[NaCl] < 50$  mM, the onset of this bluish phase as well as the CP first drop significantly to then level off at high NaCl concentrations. For this sample, at  $[NaCl] > 300$  mM the CP even drops slightly below the reference value of just  $C_8E_4$ +NaCl. Notably, this pronounced CP-decrease is a thoroughly

documented phenomenon, which appears especially at high NaCl or ionic surfactant concentrations linked with a strong viscosity increase.<sup>138–140</sup> Furthermore, the appearance of this bluish opalescent phase is unexpected because bare  $C_8E_4$  classically only forms micelles in solution and cannot form lyotropic phases. Notably, SDS may form lyotropic phases at high concentrations over 30 wt-%, though not in dilute solution.<sup>141</sup> Here, the peculiar combination of adding SDS and low amounts of electrolyte (NaCl) to 60 mM  $C_8E_4$  seems to give rise to a lyotropic phase at high temperatures. This phase behavior was not further investigated as we are primarily interested in the electrostatic effect of SDS on the  $C_8E_4$ -micelles. For this purpose, the sample with 1 mM SDS seems more feasible and was further investigated by small angle neutron scattering (SANS) as is outlined in the following.

$D_2O$  was employed as the solvent (instead of  $H_2O$ ) to give rise to high neutron contrast with the hydrogenated  $C_8E_4$ - or mixed  $C_8E_4$ /SDS-micelles. From the resulting scattering spectra, interactions between micelles as well as micellar shapes can be directly inferred and quantified. Thus, SANS was employed to pinpoint the effects of 1 mM SDS on the micellar shape and size and to evaluate the arising intermicellar electrostatic repulsion. For this purpose, SANS-spectra of 60 mM  $C_8E_4$  were recorded at room temperature in the presence of SDS as well as NaCl, see Figure 9.

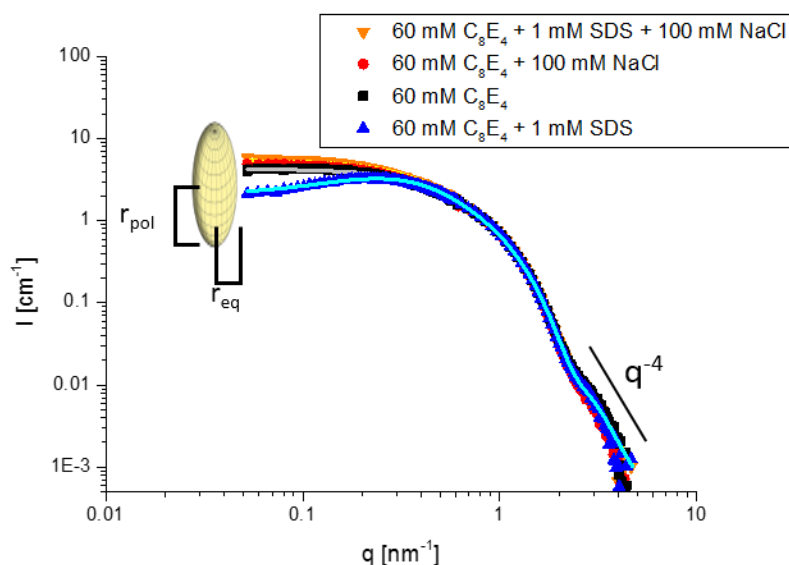


Figure 9: SANS-spectra of 60 mM  $C_8E_4$  with 1 mM SDS and 100 mM NaCl in  $D_2O$  at 20°C. The intensity is in absolute scale and the solvent was subtracted from the spectra. The lines are fits using a prolate ellipsoid model as indicated with the scheme and a Hayter-MSA structure factor for 60 mM  $C_8E_4$ +1 mM SDS. Corresponding fit parameters are listed in section 2.9. The spectra were measured at MLZ.

Micelles of 60 mM  $C_8E_4$  in  $D_2O$  show significant scattering in the probed  $q$ -range, see the black curve in Figure 9. At high  $q$ , a characteristic  $q^{-4}$ -dependence is observed hinting at the specific surface of the scatterer. Towards lower  $q$ , the scattering intensity of the  $C_8E_4$ -micelle increases

and reaches a plateau that indicates that the non-ionic micelles are non-interacting. Fitting of the experimental spectrum worked best using an ellipsoid form factor<sup>1</sup> (grey line in Figure 9) with an equatorial radius of 1.6 nm and a polar radius of 6 nm. The C<sub>8</sub>E<sub>4</sub>-micelles in water at 20°C are thus rather short and of ellipsoidal (cylinder-like) shape, which is a common result for non-ionic surfactant micelles below the CP. Addition of 100 mM NaCl to 60 mM C<sub>8</sub>E<sub>4</sub> caused only minuscule changes to the spectrum and resulted in a slight increase in the polar radius to 6.8 nm of the ellipsoidal micelles. This is an expected result, as NaCl should not strongly interact with the C<sub>8</sub>E<sub>4</sub>-micelles as concluded previously from the CP-evolutions.

Upon addition of 1 mM SDS to 60 mM C<sub>8</sub>E<sub>4</sub>, the spectrum remains unchanged at high  $q$ , while a significant decrease in the scattering intensity is observed at low  $q$ . This indicates that the shape of the micelle remains unaffected while intermicellar repulsion induces long-range order, which is expected for the formed mixed SDS/C<sub>8</sub>E<sub>4</sub>-micelles and rationalizes the rising CP upon addition of SDS. Fitting showed that these mixed micelles are ellipsoids with an equatorial radius of 1.6 nm and a polar radius of 6.7 nm that carry 3.9 charges. Thus, compared to the C<sub>8</sub>E<sub>4</sub>-micelles, the mixed SDS/C<sub>8</sub>E<sub>4</sub>-micelles are electrically charged and slightly longer. Adding 100 mM NaCl screened fully the intermicellar repulsion as again a plateau at low  $q$  emerges, which explains the sharp CP-decrease upon electrolyte addition. By fitting, here, ellipsoidal micellar dimensions of  $r_{eq}=1.6$  nm and  $r_{pol}=7.4$  nm were determined. As an overview, the micellar dimensions of the mentioned compositions are summarized in the following table together with calculated aggregation numbers and SDS/micelle ratios.

Table 2: Micellar equatorial and polar radii of the ellipsoids and charges with calculated aggregation numbers of 60 mM C<sub>8</sub>E<sub>4</sub> in the presence of 1 mM SDS, 100 mM NaCl or both.

Sample compositions			Micellar dimensions		Micellar charges from structure factor, $q_e$	Micellar aggregation number, $N_{Agg}^1$	SDS/micelle <sup>2</sup>
			$r_{eq}$ [nm]	$r_{pol}$ [nm]			
[C <sub>8</sub> E <sub>4</sub> ]	[SDS]	[NaCl]					
60 mM	-	-	1.6	6.0	-	126	-
60 mM	-	100 mM	1.6	6.8	-	143	-
60 mM	1 mM	-	1.6	6.7	3.9	141	2.7
60 mM	1 mM	100 mM	1.6	7.4	-	156	3

<sup>1</sup>calculated by using  $cmc(C_8E_4)=8$  mM<sup>133</sup>

<sup>2</sup>estimated from the fits by assuming that 100 % of SDS is found on the micelles.  $SDS/micelle=N_{Agg}/52$  Where 52 is  $c(SDS)/(c(C_8E_4)-cmc(C_8E_4))$

Overall, the effect of such small concentrations of SDS (1 mM) on the shape and size of C<sub>8</sub>E<sub>4</sub>-micelles (3 SDS per C<sub>8</sub>E<sub>4</sub>-micelle for 60 mM C<sub>8</sub>E<sub>4</sub>) at room temperature is expectedly small as

<sup>1</sup> A cylinder form factor model gave good fits to the data as well. The theoretical cylinder for 60 mM C<sub>8</sub>E<sub>4</sub> had a radius of 1.55 nm and a length of 8.5 nm, giving rise to similar dimensions compared to the ellipsoid. However, for reasons of fit quality and comparability, the ellipsoid model is maintained throughout this chapter.

micellar sizes increase only slightly in absence as well as in presence of NaCl. Thus, by addition of such small concentrations of SDS to  $C_8E_4$ -micelles predominantly the effect of the induced micellar surface charge is observed, while effects on micellar shape and size are of second order and small. These secondary effects might arise due to packing constraints originating from the differences in hydrophobic chain length of  $C_8E_4$  ( $C_8$ ) and SDS ( $C_{12}$ ). Generally, upon increasing the ionic/non-ionic surfactant ratio the micelles shrink as the non-ionic micelles with relatively high aggregation numbers turn into ionic micelles with commonly comparably lower aggregation numbers.<sup>142,143</sup> To observe this phenomenon, however, high ionic/non-ionic surfactant ratios must be attained. Here, at a low SDS/ $C_8E_4$ -ratios (1 mM SDS to 60 mM  $C_8E_4$ ) charged  $C_8E_4$ -micelles are formed that are not significantly altered in shape and, thus, allow for a dissection of the effect of charge on the non-ionic surfactant system. This notion was further investigated with SANS as a function of temperature as shown in Figure 10.

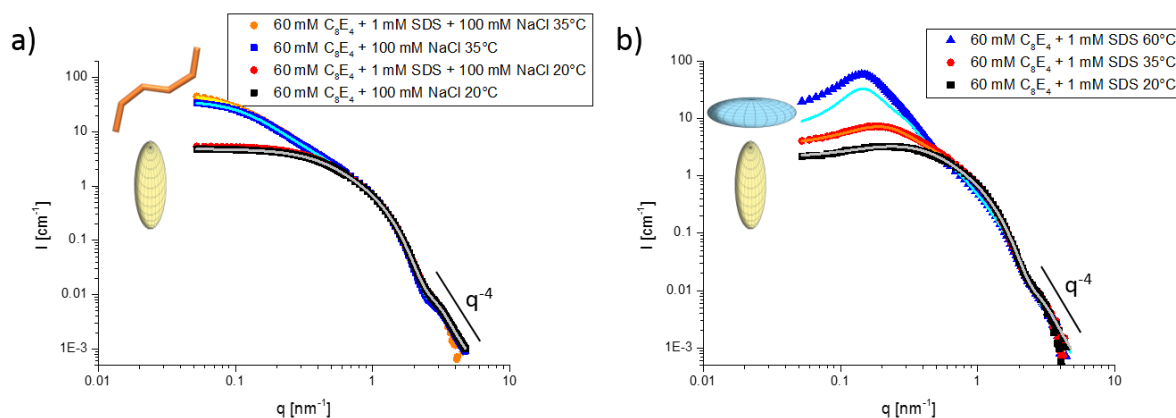


Figure 10: SANS-spectra of 60 mM  $C_8E_4$  in  $D_2O$  as a function of temperature a) at 100 mM NaCl (CP=39.6°C) without and with 1 mM SDS (CP=40.4°C) and b) at 1 mM SDS (CP=70°C). The intensity is in absolute scale and the solvent was respectively subtracted from the spectra. The lines are fits using oblate and prolate ellipsoid and flexible cylinder form factor models as indicated with the schemes. Corresponding fit parameters are listed in section 2.9. In Figure 10b, a Hayter-MSA structure factor was used to model the repulsion. The spectra were measured at MLZ.

In presence, as well as in absence of salt, respectively Figure 10a and b, the micelles grow with increasing temperature as indicated by the increasing intensities at low  $q$ . With 100 mM NaCl, see Figure 10a, in the high  $q$ -region a perfect overlap of the experimental curves without and with 1 mM SDS is observed. This indicates that the basic shape of the micelles is unaffected upon approach of the CP at 40°C. At low  $q$ , however, the samples at 35°C show a tremendous increase in scattering intensity, which hints at a growth of the micelles. Fitting of the experimental spectra revealed that the short ellipsoidal  $C_8E_4$  micelles at 20°C (discussed above) grow into elongated flexible cylinders at 35°C, see orange scheme in Figure 10a, with respective radii of 1.58 nm and lengths of 90 nm (without SDS) and 113 nm (with 1 mM SDS). Being only 5°C below the respective cloud points, these compositions thus show the classical

morphological evolution before phase separation takes place, that is one-dimensional micellar growth.<sup>128</sup>

When heating mixed micelles of 1 mM SDS/60 mM C<sub>8</sub>E<sub>4</sub> without NaCl, see Figure 10b, the situation is somewhat different. Here, the samples at 20°C and at 35°C overlap at high  $q$ , while the sample at 60°C shows a significantly steeper slope. Thus, a morphological change takes place between 35°C and 60°C. At low  $q$ , it is observed that the structure factor peak becomes more intense and moves to lower  $q$ -values with increasing temperature. This indicates that the micelles become larger and more repelling as the number of SDS-molecules and thus the charge per micelle is increased. Fitting of the experimental spectra showed that the prolate ellipsoid at 20°C with  $r_{eq}=1.6$  nm and  $r_{pol}=6.7$  nm grows to  $r_{eq}=1.7$  nm and  $r_{pol}=16.5$  nm at 35°C. The spectrum collected at 60°C could not be fitted well with any models (flexible cylinders, prolate ellipsoids). The best result was obtained by using a repulsive oblate ellipsoid with  $r_{eq}=11.5$  nm and  $r_{pol}=1.3$  nm, which assumes the shape of a small disk-like object. Thus, for the mixed SDS/C<sub>8</sub>E<sub>4</sub>-micelles in absence of electrolyte, the cloud point seems to be approached by a non-classical route, as the short ellipsoidal micelles seem to grow in length first and then transition into disks before clouding at 70°C. Possibly, such disk-like aggregates might be precursors of a lyotropic phase.

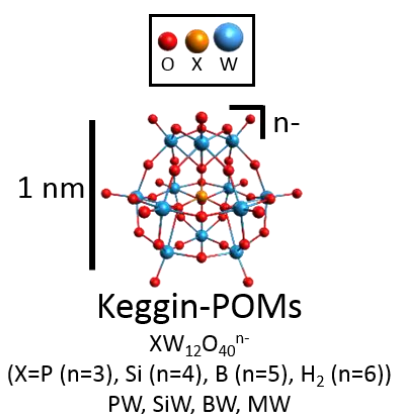
It was shown here that non-ionic C<sub>8</sub>E<sub>4</sub>-micelles constitute an adequate system to investigate and evaluate salt effects as cloud point measurement resulted in the classical Hofmeister series of anions. In addition, the effect of the ionic surfactant SDS on these non-ionic micelles was elucidated. Driven by the hydrophobic effect on its C<sub>12</sub>-chain, SDS spontaneously anchors into C<sub>8</sub>E<sub>4</sub>-micelles resulting in micellar electric charge equal the number of SDS per micelle at the used compositions. The exerted intermicellar repulsion entails a tremendous increase in the cloud point of C<sub>8</sub>E<sub>4</sub> and manifests in SANS as a structure factor peak. Upon addition of NaCl to such charged mixed micelles, electrostatics are screened, and the cloud point drops. For mixed micelles of 60 mM C<sub>8</sub>E<sub>4</sub> and 1 mM SDS screening reveals that the system behaves like C<sub>8</sub>E<sub>4</sub> without SDS as the micellar properties such as size and shape as well as the cloud points are alike for the mixed and purely non-ionic system. Thus, here the effect of charge was isolated and secondary effects of SDS on the C<sub>8</sub>E<sub>4</sub>-micelles are negligible. At higher concentrations of SDS, that is at 4 mM SDS, the mixed micelles were found to behave differently to the bare C<sub>8</sub>E<sub>4</sub>-micelles in the presence of electrolyte. More specifically, at low salt contents a lyotropic phase emerged before the CP and at high salt content the CP drops below the reference temperature of bare C<sub>8</sub>E<sub>4</sub>, a phenomenon linked to an increase in viscosity thoroughly documented in the literature.<sup>138–140</sup>

The induced behavior by SDS and the effect of charge on the micelles will serve as a reference in the upcoming sections to dissect the effects of the nano-ions on C<sub>8</sub>E<sub>4</sub> beyond expected electrostatics.



### 2.3. Keggin-POMs in C<sub>8</sub>E<sub>4</sub>

Polyoxometalates (POMs) are discrete metal oxide clusters of early transition metals in their highest oxidation state, such as tungsten (VI). Owing to their vast structural and electronic diversity they find applications for example as catalysts<sup>81,82</sup>, and in materials that exploit their redox<sup>82,87,88</sup> and magnetic<sup>86</sup> properties. Keggin-types,  $XM_{12}O_{40}^{n-}$  (with M=Mo or W), are among the most common and widely used POM-architectures, see Scheme 2 for the four polyoxotungstates  $PW_{12}O_{40}^{3-}$  (PW),  $SiW_{12}O_{40}^{4-}$  (SiW),  $BW_{12}O_{40}^{5-}$  (BW) and  $H_2W_{12}O_{40}^{6-}$  (MW) that were investigated in this chapter. These Keggin-POMs are quasi-spherical nanometric ions with delocalized charges. Though they lack a classical amphiphilic structure, they show surface activity at millimolar concentrations, as is reflected in surface tension at the air/water interface as shown below.



Scheme 2: Molecular structure of the Keggin-POMs  $PW_{12}O_{40}^{3-}$  (PW),  $SiW_{12}O_{40}^{4-}$  (SiW),  $BW_{12}O_{40}^{5-}$  (BW) and  $H_2W_{12}O_{40}^{6-}$  (MW).

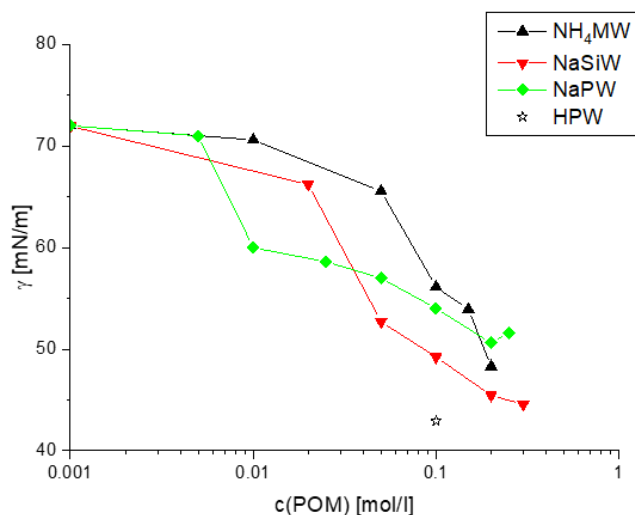


Figure 11: Surface tension  $\gamma$  at the air/water interface as a function of the Keggin-ion concentration for  $NH_4MW$  ( $(NH_4)_6H_2W_{12}O_{40}$ ),  $NaSiW$  ( $Na_4SiW_{12}O_{40}$ ) and  $NaPW$  ( $Na_3PW_{12}O_{40}$ ). Equilibration times were slow, and, in some cases, equilibrium was not reached. The corresponding surface tension vs time curves for each data point are shown in Figure 27 in the addendum.

The surface tensions were determined by drop shape analysis on emergent air bubbles submerged in the aqueous POM-solutions. In some cases bubbles ripped off the capillary before equilibrium surface tension was reached as it took up to a few hours for the bubbles to equilibrate, see the surface tension vs time curves in Figure 27 in the addendum on page 67. The data shown in Figure 11 therefore represent preliminary results. Nevertheless, it is clear that the three used POMs PW, SiW and MW are surface active though to differing extents. The initial drop in surface tension correlates inversely with the charge of the POM, i.e. PW (3-) causes a significant decrease in surface tension at 10 mM to 60 mN/m, while for SiW (4-) and MW (6-) respectively 20 mM and 50 mM are necessary to cause surface tensions below 70 mN/m. At high POM-concentrations, the surface tension continues to decrease prohibiting the determination of a CAC (critical aggregation concentration) in the probed concentration range. Similarly, surface activity (and self-association in water) was observed for other globular nano-ions such as the boron clusters  $B_{12}H_{12}^{2-}$  and  $B_{10}H_{10}^{2-}$  at molar concentrations, where the surface activity was expounded to arise from a non-classical hydrophobic effect.<sup>54</sup> Furthermore, Bera and Antonio demonstrated that PW in its acid form self-aggregates in solution and at the air/water interface, however without a change in water/air surface tension.<sup>144</sup> In contrast to Bera's results, it is shown here that PW (NaPW as well as HPW) and also the other two POMs SiW and MW decrease the water/air surface tension. In comparison to classical salts that may cause a surface tension change of  $\pm 1$  mN/m at 1 mol/L<sup>10,11</sup>, the effects on surface tension of the POMs are tremendous hinting at the strong difference to classical ions regarding their behavior in water.

Furthermore, the two Keggin-ions silicotungstate ( $SiW_{12}O_{40}^{4-}$ , SiW) and phosphotungstate ( $PW_{12}O_{40}^{3-}$ , PW) were classified as superchaotropic ions as they were found to adsorb strongly to polar non-ionic surfactant interfaces in extension to classical chaotropic ions such as  $SCN^-$  that show rather weak adsorption.<sup>4,92</sup> For the POMs, their superchaotropic character seems linked to their exceptionally low charge densities and, hence, weak solvation in water.<sup>4,92</sup> Here, the two superchaotropic Keggin-POMs SiW and PW are compared with borotungstate ( $BW_{12}O_{40}^{5-}$ , BW) and metatungstate ( $H_2W_{12}O_{40}^{6-}$ , MW) to exemplify and test the previously established concept:

*The lower the charge density of an ion the more pronounced is its chaotropic character.*<sup>4,92</sup>

The four used POMs MW, BW, SiW and PW have identical molecular structure and size and only differ in their charges, which correspond to -3, -4, -5 and -6 depending on their central

atoms, respectively  $P^{5+}$ ,  $Si^{4+}$ ,  $B^{3+}$  and  $H_2^{2+}$ . Additionally, the contact surface with the solvent is chemically identical for all Keggin-ions as the central atoms are shielded from solvent contact by the surrounding polyoxotungstate skeleton. Thus, these Keggin-ions are an ideal system to vary systematically the volume charge density and pinpoint its impact on the superchaotropic adsorption phenomenon. The corresponding charge densities that arise from the volume and the charge of each Keggin-POM are shown in Table 3.

Table 3: The three Keggin anions MW ( $H_2W_{12}O_{40}^{6-}$ ), SiW ( $SiW_{12}O_{40}^{4-}$ ), PW ( $PW_{12}O_{40}^{3-}$ ) with ionic charges, molecular volumes and charge densities.

	SCN <sup>-</sup>	$H_2W_{12}O_{40}^{6-}$	$BW_{12}O_{40}^{5-}$	$SiW_{12}O_{40}^{4-}$	$PW_{12}O_{40}^{3-}$
Charge, $q_e$	1	6	5	4	3
Molecular volume [nm <sup>3</sup> ]	0.07 <sup>1</sup>	0.46 <sup>2</sup>	0.46 <sup>2</sup>	0.46 <sup>2</sup>	0.46 <sup>2</sup>
Charge density [ $q_e/nm^3$ ]	14.1	13.0	10.9	8.7	6.5

<sup>1</sup> taken from Marcus<sup>91</sup>

<sup>2</sup> taken from Buchecker et al.<sup>92</sup>

To compare the chaotropic characters of the POMs MW, BW, SiW and PW the evolution of the cloud point of 60 mM  $C_8E_4$  as a function of POM-concentration was measured and is shown in Figure 12 in comparison with the references SDS, NaCl and NaSCN. PW and SiW were used in their sodium ( $Na^+$ ) forms, BW in its potassium ( $K^+$ ) form and MW in its ammonium ( $NH_4^+$ ) form. Generally, the effects of cations on the CP are small and should be negligible compared to the effect of the anion.<sup>92</sup>

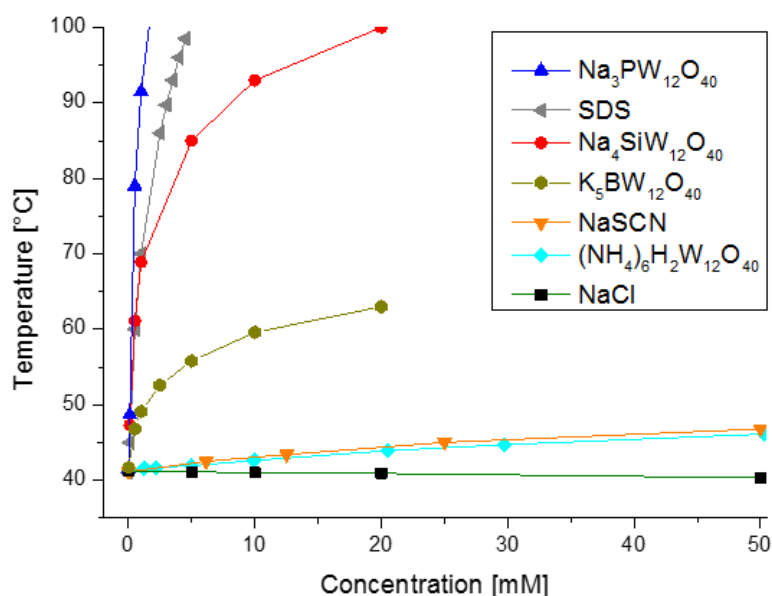


Figure 12: Cloud point evolution of 60 mM  $C_8E_4$  as a function of the concentration of the three Keggin-POMs NaPW ( $Na_3PW_{12}O_{40}$ ), NaSiW ( $Na_4SiW_{12}O_{40}$ ), KBW ( $K_5BW_{12}O_{40}$ ) and  $NH_4MW$  ( $(NH_4)_6H_2W_{12}O_{40}$ ) compared with the references SDS, NaSCN and NaCl. The lines are guides to the eye. For NaPW bluish opalescent phases were observed before the CP and will be discussed later in section 2.5.

The CP-evolutions in Figure 12 show that all four POMs MW, BW, SiW and PW stabilize the C<sub>8</sub>E<sub>4</sub>-micellar phase as they all cause an increase in the CP. The extent of the effect, however, varies tremendously between the Keggin-ions. PW and SiW increase strongly the CP to above 100°C at 5 mM and 20 mM respectively, while BW and MW induce much weaker effects. This trend can be assigned to the more pronounced superchaotropic character of PW compared to SiW, BW and MW, which leads to a more complete adsorption of PW to the C<sub>8</sub>E<sub>4</sub>-micelles and a resulting higher micellar charge. Interestingly, NaPW even exceeds significantly the effect of SDS, which seems linked to the fact that one PW-molecule carries 3 negative charges to the micelle compared to just 1 per SDS-molecule. Thus, at the tested millimolar concentrations PW is expected to adsorb most strongly to the C<sub>8</sub>E<sub>4</sub>-micelles, while SiW and, even more so, BW and MW exhibit weaker interaction. Furthermore, NaSCN induced a similar CP-increase as NH<sub>4</sub>MW. Therefore, MW behaves rather like a classical chaotropic ion and does not exhibit a superchaotropic character. Overall, the CP-evolutions of SiW and PW are in good agreement with the CP-evolutions reported by Naskar and Buchecker et al.<sup>4,92</sup> and the predicted ordering of POMs is observed: The lower the charge density of the POM, the higher is the induced CP-increase and the strength of interaction with C<sub>8</sub>E<sub>4</sub>-micelles follows the sequence PW<sub>12</sub>O<sub>40</sub><sup>3-</sup> > SiW<sub>12</sub>O<sub>40</sub><sup>4-</sup> > BW<sub>12</sub>O<sub>40</sub><sup>5-</sup> > H<sub>2</sub>W<sub>12</sub>O<sub>40</sub><sup>6-</sup>.

To reinforce the results of the CP-measurements, small angle x-ray scattering (SAXS) was used. X-rays scatter due to electron density inhomogeneities within a sample. Therefore, Keggin-ions (e.g. SiW<sub>12</sub>O<sub>40</sub><sup>4-</sup>) have high contrast in water owing to their high electron density stemming mainly from the twelve tungsten atoms ( $Z=72$ ). Similarly, C<sub>8</sub>E<sub>4</sub> (and its micelles) provides very little contrast as its electron density approximates the one of water. Therefore, SAXS is a powerful technique to trace the behavior of POMs in aqueous solution. For the superchaotropic ions SiW and PW, it was shown by Naskar et al. that C<sub>8</sub>E<sub>4</sub>-micelles are spontaneously decorated by the POMs. Here, the adsorption of BW and MW is compared to the adsorption of SiW onto the micelles. Thus, SAXS was performed at room temperature on solutions containing 10 mM SiW, BW or MW in bare water and in the presence of 60 mM C<sub>8</sub>E<sub>4</sub>. The corresponding SAXS-spectra are shown in Figure 13.

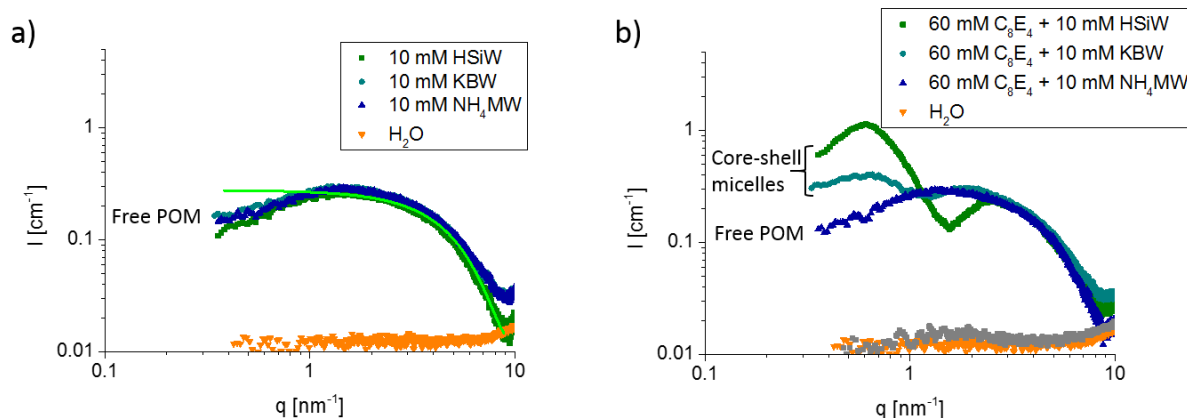


Figure 13: SAXS at room temperature of 10 mM of the Keggin-POMs HSiW ( $\text{H}_4\text{SiW}_{12}\text{O}_{40}$ ), KBW ( $\text{K}_5\text{BW}_{12}\text{O}_{40}$ ) and  $\text{NH}_4\text{MW}$  ( $(\text{NH}_4)_6\text{H}_2\text{W}_{12}\text{O}_{40}$ ) a) in water and b) in presence of 60 mM  $\text{C}_8\text{E}_4$ . The scattering contributions of 60 mM  $\text{C}_8\text{E}_4$  and of water are additionally shown. The background signal at  $q > 9 \text{ nm}^{-1}$  fluctuates slightly between the samples. The spectrum of 10 mM HSiW in water in a) was fitted using a spherical form factor with  $r=0.43 \text{ nm}$  coinciding well with the expected size of a POM ( $r=0.48 \text{ nm}^{92}$ ). Corresponding fit parameters are listed in section 2.9.

In the investigated  $q$ -region from  $0.3$  to  $8 \text{ nm}^{-1}$ , the scattering of water produces a weak and constant background signal. Upon addition of 60 mM  $\text{C}_8\text{E}_4$ , the scattering remains almost unchanged as the contrast between water and  $\text{C}_8\text{E}_4$  is too small to give rise to significant intensities when using the SAXS-setup at the ICSM. However, 10 mM of SiW, BW or MW in water produce significant excess scattering and perfectly overlap in the whole  $q$ -region owing to their identical contrast, size and shape. Their scattering intensity emerges from the background signal of water at  $q < 8 \text{ nm}^{-1}$ , passes through a maximum at  $q = 1.2 \text{ nm}^{-1}$  and then decreases towards lower  $q$ -values. This decrease hints at a structure factor contribution that arises from POM-POM repulsion due to the charges of 4-, 5- and 6- for SiW, BW and MW, respectively. These three spectra show the characteristic scattering signature of dispersed, repulsive spheres, which were fitted by using a spherical form factor with a radius of 0.43 nm that corresponds well to the expected size of a Keggin-POM ( $r = 0.48 \text{ nm}$ ), see the green line in Figure 13. However, the electrostatic repulsion between the POMs could not be modeled as the Hayter-MSA structure factor, which models electrostatic interscatterer forces, breaks down at the used low POM-concentrations and respective charges of -4, -5 and -6 for SiW, BW and MW.

Furthermore, in the presence of 60 mM  $\text{C}_8\text{E}_4$ , the spectra of 10 mM SiW, 10 mM BW and 10 mM MW strongly differ. The spectrum of 10 mM MW, regardless of the presence of  $\text{C}_8\text{E}_4$ -micelles, shows the same scattering as dispersed MW-molecules in water. Therefore, MW does not interact with or adsorb to the non-ionic  $\text{C}_8\text{E}_4$ -micelles explaining the weak effect of MW on the CP of  $\text{C}_8\text{E}_4$ . By contrast, the spectra of 10 mM BW and of 10 mM SiW with 60 mM  $\text{C}_8\text{E}_4$  contain large oscillations that emerge at  $q < 1 \text{ nm}^{-1}$  for BW and at  $q < 3 \text{ nm}^{-1}$  for SiW from

the signal of the POMs. This appearing pattern is characteristic of a POM-decorated micelle and the maximum intensity of the appearing oscillation is indicative of the number of adsorbed POM per micelle. Therefore, SiW adsorbs in higher numbers to the C<sub>8</sub>E<sub>4</sub>-micelles compared to BW, while MW does not show significant interaction.

The presented results recapitulate that both cloud point measurement as well as SAXS are powerful tools to examine the interaction of nanometric POMs with soft matter systems, as herein with C<sub>8</sub>E<sub>4</sub>-micelles. Thus, by testing the isostructural Keggin-ions H<sub>2</sub>W<sub>12</sub>O<sub>40</sub><sup>6-</sup>, BW<sub>12</sub>O<sub>40</sub><sup>5-</sup>, SiW<sub>12</sub>O<sub>40</sub><sup>4-</sup> and PW<sub>12</sub>O<sub>40</sub><sup>3-</sup> as to their superchaotropic characters, a clear effect of the charge of the ion was observed. It was shown that the highest charge Keggin-ion metatungstate (H<sub>2</sub>W<sub>12</sub>O<sub>42</sub><sup>6-</sup>) does not interact with the C<sub>8</sub>E<sub>4</sub>-micelles. However, with decreasing charge, the superchaotropic character of a Keggin-ion becomes more and more pronounced as the interaction with the C<sub>8</sub>E<sub>4</sub>-micelles becomes stronger from BW<sub>12</sub>O<sub>40</sub><sup>5-</sup> over SiW<sub>12</sub>O<sub>40</sub><sup>4-</sup> to PW<sub>12</sub>O<sub>40</sub><sup>3-</sup>. The extent of the superchaotropic nature of an ion seems to correlate well with the exceptionally low charge densities of the used Keggin-POMs in comparison to classical ions with high charge densities as was previously proposed by Naskar and Buchecker et al.<sup>4,92</sup> Consequently, the POM-adsorption to the non-ionic C<sub>8</sub>E<sub>4</sub>-micelles is a phenomenon of purely physical origin as chemical bonding and specific interaction of the external W-O bonds with the micellar ethoxy corona can be excluded because MW does not interact strongly with the C<sub>8</sub>E<sub>4</sub>-micelles in harsh contrast to the superchaotropic SiW and PW.

### 2.3.1. The importance of the POM's counter-ion

The interactions of counter-ions with POMs have profound effects on POM synthesis and crystallization and can direct POM self-assembly in solution.<sup>145,146</sup> Moreover, choosing the right counter-ion affects strongly the POM's properties in solution and tailors its feasibility for application. Here, the focus is set on the effects of counter-ions on superchaotropic Keggin-ions, which are highly symmetrical, 3D-aromatic compounds with delocalized charges<sup>90</sup> and, thus, do not provide a defined binding site for oppositely charged ions. As a result, Keggin-type POMs are generally considered as weakly coordinating ions as counter-ion binding is disfavored.<sup>50</sup> Nevertheless, when using chaotropic counter-cations the solubility of the Keggin-anions is known to decrease presumably due to the formation of insoluble chaotrope (POM<sup>n-</sup>)-chaotrope (e.g. Cs<sup>+</sup>) contact ion-pairs.<sup>145</sup> Here, such counter-ion effects are investigated first in bare water and then on the superchaotropic adsorption process by measuring the cloud point of 60 mM C<sub>8</sub>E<sub>4</sub> for the two most superchaotropic POMs PW and SiW with counter-ions H<sup>+</sup>, Na<sup>+</sup>, K<sup>+</sup> and Cs<sup>+</sup>. Classified by the strength of interaction with water, Na<sup>+</sup> is weakly kosmotropic, K<sup>+</sup> is weakly chaotropic and Cs<sup>+</sup> is a chaotropic cation.<sup>23,28</sup> The proton (H<sup>+</sup>) is generally considered apart as it is incorporated in the water network and is much more dynamic in water compared to classical Hofmeister ions.<sup>147,148</sup> Moreover, there is still an ongoing debate on which form the proton assumes in aqueous solution as it may exist as species of the types H<sub>3</sub>O<sup>+</sup>, H<sub>5</sub>O<sub>2</sub><sup>+</sup> or H<sub>13</sub>O<sub>6</sub><sup>+</sup>.<sup>147</sup> As a consequence, the proton H<sup>+</sup> is generally excluded from the Hofmeister-series and needs to be considered as a special case.

In the first step, solubilities of the Keggin-ions SiW and PW in water were determined for the four different cations. Here, disregarding cation combinations, POMs with a single cation type were produced by titration of the acidic HPW and HSiW with the respective base (NaOH, KOH or CsOH in water) except NaPW, which was purchased from Sigma Aldrich. As a result, the Na<sup>+</sup>- and H<sup>+</sup>- forms of PW and SiW were found to be soluble in water (solubilities > 100 mM) as well as the K<sup>+</sup>-form of SiW. However, the K<sup>+</sup>-form of PW was insoluble as were the Cs<sup>+</sup>-forms of SiW and PW (solubilities < 0.1 mM). Table 4 provides an overview of the solubility trend in water of all tested POM-cation pairs.

Table 4: Solubilities in water of the respective POM-cation pairs of  $\text{PW}_{12}\text{O}_{40}^{3-}$  and  $\text{SiW}_{12}\text{O}_{40}^{4-}$  with  $\text{H}^+$ ,  $\text{Na}^+$ ,  $\text{K}^+$  and  $\text{Cs}^+$ .

		$\text{H}^+$	Weakly kosmotropic $\text{Na}^+$	Weakly chaotropic $\text{K}^+$	More chaotropic $\text{Cs}^+$
Superchaotropic	$\text{SiW}_{12}\text{O}_{40}^{4-}$	Soluble	Soluble	Soluble	Insoluble
More superchaotropic	$\text{PW}_{12}\text{O}_{40}^{3-}$	Soluble	Soluble	Insoluble	Insoluble

Overall, the expected solubility trend is observed showing a sharp drop in solubility when the counterion becomes more chaotropic, presumably due to chaotrope (cation)/superchaotrope (POM) ion-pair formation.

The POM-cation pairs were then further investigated in aqueous solution in the presence of 60 mM of the non-ionic surfactant  $\text{C}_8\text{E}_4$ . Thus, it was observed that the solubility of the insoluble KPW (insoluble in water) is significantly increased in the presence of  $\text{C}_8\text{E}_4$  under formation of a bluish opalescent phase, see Figure 14. Notably, similar solubilization effects were also observed for  $\text{CsSiW}$  and  $\text{CsPW}$  but to lesser extents.

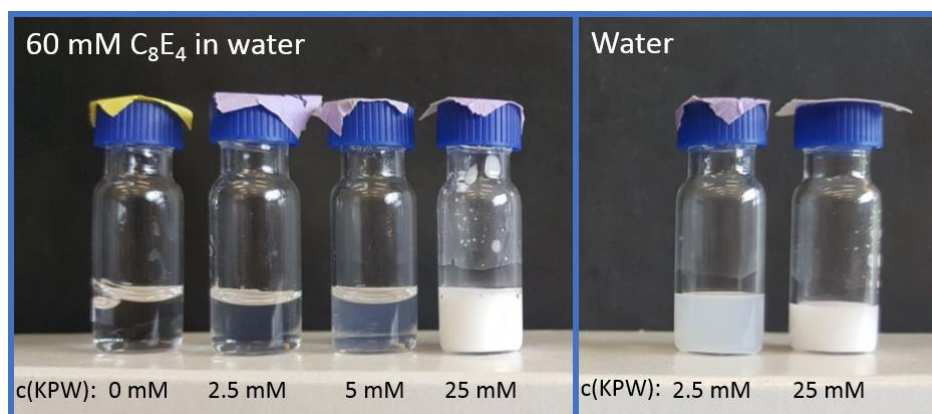


Figure 14: Solubilization effect of 60 mM  $\text{C}_8\text{E}_4$  on KPW ( $\text{K}_3\text{PW}_{12}\text{O}_{40}$ ) under the formation of a bluish opalescent (non-birefringent) phase at 2.5 and 5 mM KPW (left) and insoluble turbid KBW samples in water (right).

Neither  $\text{K}^+$  nor  $\text{PW}_{12}\text{O}_{40}^{3-}$  are hydrophobic and cannot be classically solubilized in the hydrophobic core of the  $\text{C}_8\text{E}_4$ -micelles. Therefore, this solubility increase arises from the preferred interaction of PW with the ethoxylated surfactant heads of  $\text{C}_8\text{E}_4$ . Thus, here the thermodynamic equilibrium between insoluble and soluble KPW is strongly shifted by the chaotropic effect operating as a so far unconsidered solubilization force.

While this is an interesting discovery, the focus shall be set here on water-soluble POM-cation pairs in order to classify eventual differences in their superchaotropicity depending on the counterion. Thus far, the literature concerning the effects of counter-ions on the superchaotropic adsorption process is limited to one CP-measurement (of 60 mM  $\text{C}_8\text{E}_4$ ) by Buchecker et al., where it was shown that changing the counter-ion from  $\text{H}^+$  to  $\text{K}^+$  for the Dawson-POM



$P_2W_{18}O_{62}^{6-}$  induced a slight increase in the CP at high Dawson-POM concentrations.<sup>92</sup> Here, using the same method, the effects of the cations are investigated by measuring the CP-evolutions of 60 mM  $C_8E_4$  in the presence of PW ( $H^+$ - and  $Na^+$ -forms) and SiW ( $H^+$ -,  $K^+$ - and  $Na^+$ -forms). The corresponding CP-curves are shown in Figure 15. Technically, measurement of the CP in the presence of KPW is also possible due to the occurring solubilization in the presence of  $C_8E_4$  as outlined above. However, the appearing bluish opalescent phase affected strongly the determination and evolution of the CP. Therefore, KPW is omitted in Figure 15.

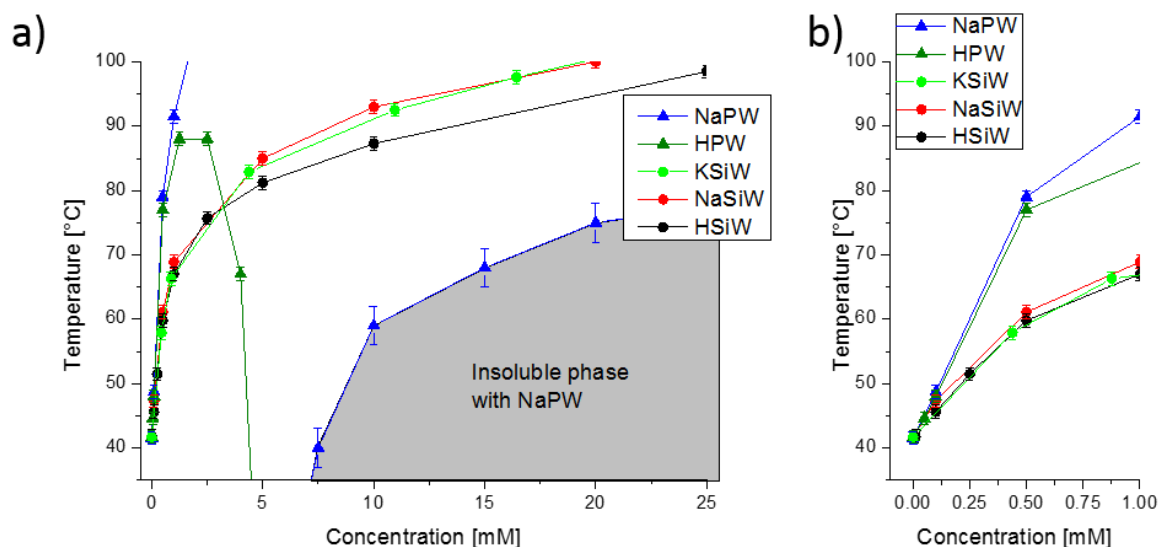


Figure 15: CP-evolutions with SiW ( $SiW_{12}O_{40}^{4-}$ ) and PW ( $PW_{12}O_{40}^{3-}$ ) using different counter-ions  $K^+$ ,  $Na^+$  and  $H^+$  a) full concentration range and b) zoom on 0-1 mM. Addition of more than 4 mM HPW led to a drop of the cloud point and more than 5 mM NaPW caused the appearance of a turbid phase. Estimated error bars of the phase transition temperatures are included.

For PW and SiW, regardless of the used cation, the CP is shifted tremendously to higher temperatures. More specifically, at  $[PW] < 1$  mM and  $[SiW] < 2.5$  mM counter-ion effects can be neglected as the CP-curves overlap perfectly. At further increased POM-concentrations, for SiW, the  $K^+$ - and  $Na^+$ -forms produce well overlapping CP-curves, while the acid form shows a weaker CP-increase similarly to the observation by Buchecker et al.<sup>92</sup> However, for PW, the difference between the  $Na^+$ - and the  $H^+$ - form is quite marked as NaPW causes a monotonous CP-increase, whereas the CP with HPW reaches a maximum CP at 2.5 mM followed by a sharp drop in the CP down to 0°C. Thus, at 2.5 mM HPW the micellar phase of  $C_8E_4$  is destabilized and micellar aggregation becomes favorable upon addition of more HPW. Overall, the use of the halide counter-ions  $K^+$  and  $Na^+$  proved indifferent to the CP-increase as observed for SiW. However, the choice of  $H^+$  as the counter-ion seems to affect the CP-evolution at high POM-concentrations, where adsorbed POMs (on the  $C_8E_4$ -micelles) might come into close contact, while at low POM-concentrations the effect of  $H^+$  can be disregarded. Notably, this peculiarity

of  $H^+$  manifests only weakly for SiW, yet strongly for PW. Interestingly, such specificities of the  $H^+$ -form of PW compared to other Keggin-ions seem to be rather common. For example, a similar increase with subsequent decrease of the lower critical solution temperature of the polymer PNiPAM was observed by Buchecker et al upon adding HPW (but not with  $H_4SiW_{12}O_{40}$  or  $H_3PMO_{12}O_{40}$ ).<sup>104</sup> Additionally, it was shown by Antonio et al. that PW is the only Keggin-ion (compared to  $H_4SiW_{12}O_{40}$  and  $H_5AlW_{12}O_{40}$ ) that can self-aggregate in water. The authors claim that this aggregation is moderated by  $H^+$ -counterions (under the form of  $H_5O_2^+$ ), that bridge in between neighboring PW-molecules at high HPW-concentrations.<sup>97,98</sup> Thus, it can be speculated that such  $H^+$ -moderated aggregation might contribute in the occurring CP-drop as the local PW-concentration on the  $C_8E_4$ -micelle is expectedly high, which could allow for similar HPW-aggregation along the  $C_8E_4$ -micelles. Furthermore, at high concentrations of NaPW a turbid phase was observed, which could be entirely solubilized upon heating. Such turbid phase formation did not occur with SiW and seems to be another result of the particularly strong interaction of PW with  $C_8E_4$ -micelles owing to its strongly superchaotropic character.

To conclude, the choice of the cation to the Keggin-POMs SiW and PW has significant effects on their solubilities in water as usage of chaotropic counterions causes a tremendous solubility decrease. For instance, KPW and CsPW are insoluble in water as well as CsSiW, which can be surmised to arise from insoluble ion-pair formation of the respective counter-ions with the superchaotropic POM. Furthermore, classical halide cations like  $Na^+$  or  $K^+$  do not interfere with the superchaotropic adsorption process as was shown by CP-measurements for the Keggin-ion SiW. By contrast, employment of the Keggin-ions in their  $H^+$ -forms had a slight hampering effect on the CP-increase caused by SiW, while  $H^+$  induced significant effects for PW even causing a sharp CP-decrease at high HPW-concentrations.

### 2.3.2. Quantifying superchaotropic adsorption

In the previous sections, the adsorption of POMs to C<sub>8</sub>E<sub>4</sub>-micelles was qualitatively evidenced. Here, a quantitative approach is used to examine the properties of the decorated C<sub>8</sub>E<sub>4</sub>-micelles as a function of POM-concentration. To this end, the focus is set on the POM SiW (SiW<sub>12</sub>O<sub>40</sub><sup>4-</sup>), as it is a strong superchaotrope, yet can be added in high amounts (over 100 mM) to 60 mM C<sub>8</sub>E<sub>4</sub> without causing precipitation unlike the more superchaotropic PW<sub>12</sub>O<sub>40</sub><sup>3-</sup>. In particular, the H<sup>+</sup>-form of SiW was used as counter-ion effects for SiW are slight as shown in the previous section and usage of the acid forms guarantees for an acidic environment, which averts decomposition of the Keggin structure at pH > 7.<sup>149,150</sup> Thus, SANS and SAXS of 60 mM C<sub>8</sub>E<sub>4</sub> were measured in the presence of increasing concentrations of SiW at 20°C. The corresponding spectra are shown in Figure 16. As SANS and SAXS fundamentally differ by their contrasts, different features of identical samples are probed with the two techniques. Neutrons, on the one hand, reveal exclusively the hydrogenated C<sub>8</sub>E<sub>4</sub>-micelles in D<sub>2</sub>O whereas the POM SiW is transparent. On the other hand, x-rays are especially sensitive to the high electron density of SiW and therefore, reveal exclusively the behavior of the POM in solution and adsorbed on the micelles. Thus, these two techniques complement each other perfectly, which allows for a quantification of the entire C<sub>8</sub>E<sub>4</sub>/SiW-system including micellar size, shape, aggregation numbers and POM-adsorption ratios.

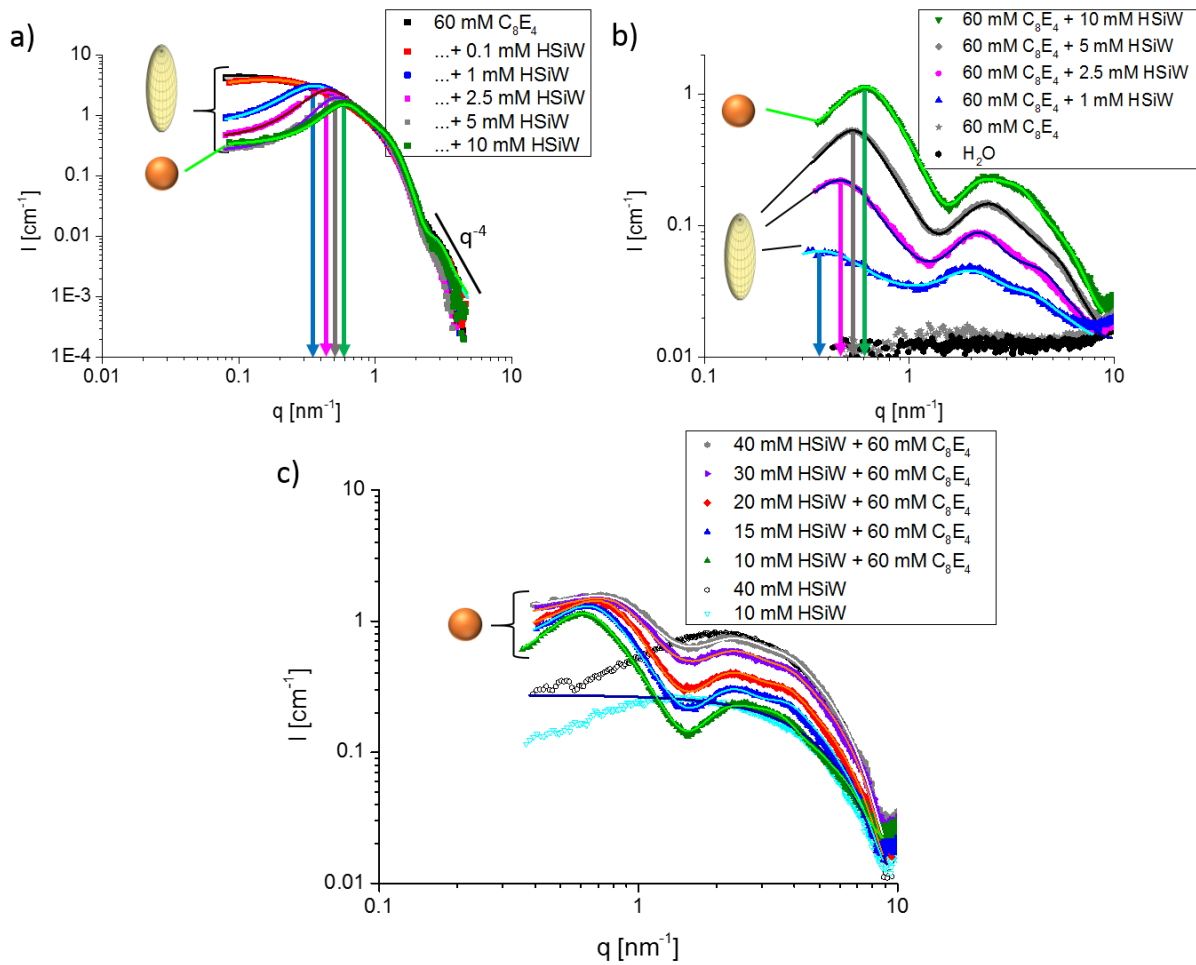


Figure 16: a) SANS-spectra of 60 mM  $C_8E_4$  in  $D_2O$  at increasing HSiW ( $H_4SiW_{12}O_{40}$ )-concentrations measured at  $20^\circ C$  and b) SAXS-spectra of 60 mM  $C_8E_4$  in  $H_2O$  from 1 mM to 10 mM HSiW and with the individual contributions  $C_8E_4$  in water. The structure factor peaks measured with the two techniques are at the same positions as indicated with the arrows. c) SAXS-spectra of 60 mM  $C_8E_4$  in  $H_2O$  from 10 mM HSiW to 40 mM HSiW. Additionally, the individual contributions of 10 mM HSiW and 40 mM HSiW in water are shown. The spectra are in absolute scale and the lines represent fits using ellipsoidal or spherical form factor models for SANS and corresponding core-shells for SAXS or a sphere for 10 mM HSiW in c). Corresponding fit parameters are listed in section 2.9. SAXS-spectra were measured at the ICSM and SANS-spectra of 60 mM  $C_8E_4$  and ... + 1 mM HSiW were measured at MLZ, ... + 0.1 mM HSiW and ... + 10 mM HSiW were measured at ILL, and ... + 2.5 mM HSiW and ... + 5 mM HSiW were kindly measured and provided by Lionel Porcar at ILL.

The SANS-spectrum of bare 60 mM  $C_8E_4$  in water was discussed in detail in section 2.2 establishing that short non-interacting ellipsoidal micelles are formed at  $20^\circ C$ . Here, upon addition of SiW, the scattering of the  $C_8E_4$ -micelles remains practically unchanged at high  $q$  and decreases towards low  $q$ , see Figure 16a, which evokes a structure factor peak and indicates that intermicellar repulsion arises and grows as SiW adsorbs and charges the micelles. The samples containing 1 mM HSiW and 10 mM HSiW also provide sufficient excess scattering in SAXS and feature in the presence of 60 mM  $C_8E_4$  the characteristic core-shell pattern of decorated micelles, see Figure 16b. The structure factor peaks for the sample containing 60 mM  $C_8E_4$  with 1 mM or 10 mM HSiW appear at identical positions in SAXS and SANS confirming the identity of the samples regardless of the use of  $D_2O$  or  $H_2O$  as the solvent in SANS or

SAXS, respectively. In order to quantify this system adequate mathematical models were employed to fit the experimental spectra. As the SANS-spectra contain only the signal of one species, that is the C<sub>8</sub>E<sub>4</sub>-micelles (SiW is transparent), fitting was easily done using spherical or ellipsoidal form factors. The acquired parameters such as the number of micelles and the micellar dimensions were then further used in the fitting procedure of the SAXS-spectra, which are a superposition of the scattering of the individual SiW-molecules as well as of the SiW-decorated micelles. The signal of SiW-molecules was fitted using a spherical form factor with a hard sphere structure factor, while the signal of the decorated micelle was accounted for by spherical or ellipsoidal core-shell form factors.<sup>2</sup> Hayter-MSA structure factors fitted well the structure factor peak of the decorated micelles and were used with identical parameters for the same sample measured with either technique. All fitting parameters are listed in section 2.9 and an elaboration of the fitting procedure can be found in section 7.3.2. Thus, micellar shapes and sizes, and SiW-adsorption ratios were determined and are shown in table 5.

Table 5: Form factor shapes with corresponding dimensions and aggregation numbers from SANS, SiW-adsorption number and ratios from SAXS, and respective charges and salt content received from the structure factors.

Sample compositions	Form factor shape	Micellar dimensions (from SANS)			SiW-shell (from SAXS)		Structure factor HMSA SAXS and SANS	
		r_eq [nm]	r_pol [nm]	N <sub>Agg</sub>	SiW per micelle	SiW adsorption ratio R <sup>a</sup>	Charge, q <sub>e</sub>	Salt [M]
60 mM C <sub>8</sub> E <sub>4</sub> -	Ellipsoid	1.6	6.0	126	0	-	-	-
60 mM C <sub>8</sub> E <sub>4</sub> 0.1 mM HSiW	Ellipsoid	1.6	7.8	164	0.3	-	2 <sup>c</sup>	0.0001 <sup>c</sup>
60 mM C <sub>8</sub> E <sub>4</sub> 1 mM HSiW	Ellipsoid	1.6	6.6	142	1.81	0.66	8	0.0001
60 mM C <sub>8</sub> E <sub>4</sub> 2.5 mM HSiW	Ellipsoid	1.8	4.5	102	3.22	0.66	14	0.001
60 mM C <sub>8</sub> E <sub>4</sub> 5 mM HSiW	Ellipsoid	1.6	3.0	63	4.07	0.57	16	0.001
60 mM C <sub>8</sub> E <sub>4</sub> 10 mM HSiW	Sphere	1.7	1.7	43	4.9	0.59	20	0.006
60 mM C <sub>8</sub> E <sub>4</sub> 15 mM HSiW	Sphere	n.a. <sup>d</sup>	n.a.	n.a.	5.35	0.43	22	0.013
60 mM C <sub>8</sub> E <sub>4</sub> 20 mM HSiW	Sphere	n.a. <sup>d</sup>	n.a.	n.a.	5.71	0.34	24	0.035
60 mM C <sub>8</sub> E <sub>4</sub> 30 mM HSiW	Sphere	n.a. <sup>d</sup>	n.a.	n.a.	5.82	0.23	25	0.04
60 mM C <sub>8</sub> E <sub>4</sub> 40 mM HSiW	Sphere	n.a. <sup>d</sup>	n.a.	n.a.	5.82	0.18	25	0.05

<sup>a</sup> adsorption ratio  $R = \frac{[POM]_{adsorbed}}{[POM]_{total}}$

<sup>b</sup> 0.3 POMs/micelle is an estimated value for 100 % adsorption using  $N(POM)/N(\text{micelles})$  with  $N(\text{micelles})$  from SANS.

<sup>c</sup> only determined in SANS as signal is too weak in SAXS.

<sup>d</sup> not measured in SANS. Micellar dimensions from SANS with 10 mM HSiW were taken for the fitting of the SAXS-spectra at  $[HSiW] > 10$  mM.

The SANS-fits reveal that the ellipsoidal C<sub>8</sub>E<sub>4</sub>-micelles of 60 mM C<sub>8</sub>E<sub>4</sub> grow slightly in polar radius from 6.0 nm to 7.8 nm upon addition of 0.1 mM SiW. Further increase of SiW-

<sup>2</sup> Scattering spectra are ambiguous, and the choice of the model can have significant impact on the result. For the decorated micelles of SiW/C<sub>8</sub>E<sub>4</sub>, in the fitting procedure core-shell form factors proved superior to spherical form factors (no shell). Using a spherical form factor here would imply a penetration of SiW into the micellar core and a hydrophobic nature of SiW, which would contradict its commonly evidenced superchaotropic nature in the literature. Therefore, and owing to the better fit quality and because the micelles did not grow or get disrupted with SiW-concentration (SANS, see Figure 16a) core-shell form factors were systematically used to model the micelles in the SiW/C<sub>8</sub>E<sub>4</sub>-system.

concentration induces a gradual shortening of the micelles into spheres with a radius of 1.7 nm at 10 mM SiW. Note that this radius is a so-called dry radius because hydration water between the ethoxylated headgroups was disregarded in the SANS fitting procedure resulting in an underestimate of the micellar size. Generally, the extended length of a C<sub>8</sub>E<sub>4</sub>-molecule is 2.6 nm corresponding to a more realistic radius of a spherical C<sub>8</sub>E<sub>4</sub>-micelle. Nevertheless, SANS allows for a reliable determination of the micellar number densities, dimensions and shapes from SANS that are recycled into the fitting of the SAXS-spectra, which revealed that SiW-molecules populate the space between the surfactant head groups. More specifically, the high electron-density shell of adsorbed SiW was found to be located about 0.9 nm deep into the micelle at all HSiW-concentrations, which corresponds to the extended length of 2.4 ethyleneglycol units or the size of one SiW-molecule. SiW therefore forms a monolayer on the C<sub>8</sub>E<sub>4</sub>-micelle. Additionally, the number of POMs per micelle were determined and found to increase monotonically and strongly up to 5.8 SiW-molecules per micelle at 20 mM SiW, where the number of POM per micelle saturates indicating a full occupancy of the micellar surface. At saturation, there are 6.5 C<sub>8</sub>E<sub>4</sub>-molecules per SiW-molecule on the decorated micelles. Interestingly a plot of the number of adsorbed SiW against the SiW-concentration describes a Langmuir shape, see Figure 17a. In a similar fashion, the corresponding adsorption ratios are maximal (around 0.66) at low HSiW-concentrations from 0.1 mM-5 mM implying that 66% of all SiW is adsorbed on the micelles. At high HSiW-concentration larger than 5 mM, the adsorption ratio R is found to decrease monotonically to 0.18 at 40 mM HSiW because the micelles are fully covered, and SiW-ions are forced into the water bulk. Furthermore, the micellar charges were extracted from the structure factor fits (Hayter mean spherical approximation, HMSA) and coincide well with the expected charges that arise from adsorbed SiW: 2 charges/micelle at 0.1 mM SiW to 8 and 20 charges/micelle at 1 mM and 10 mM SiW. At even higher HSiW-concentration, the micellar charge seems to saturate at around 25 charges, while also increasing salt contents had to be plugged in to account for free unadsorbed SiW in solution. It is interesting to note here that the HMSA-structure factor considers an electrolyte of monovalent ions (e.g. NaCl, 1 Na<sup>+</sup> and 1 Cl<sup>-</sup>). However, technically H<sub>4</sub>SiW<sub>12</sub>O<sub>40</sub> is a quadrivalent electrolyte (1 SiW<sub>12</sub>O<sub>40</sub><sup>4-</sup> and 4 H<sup>+</sup>), which at same concentrations would provide ten times the ionic strength of a monovalent electrolyte. Nevertheless, the plugged-in salt contents remained close to the bulk-concentration of HSiW (at 30 mM HSiW, 23 mM of SiW are in the bulk and 7 mM SiW are adsorbed). As a consequence, the screening of micellar charges is only weakly governed by SiW<sub>12</sub>O<sub>40</sub><sup>4-</sup> and presumably arises mainly from H<sup>+</sup> in the bulk.

Furthermore, by using the micellar dimensions acquired in SANS to calculate the micellar surface area and the number of adsorbed SiW from SAXS an adsorption isotherm can be traced, see Figure 17b.

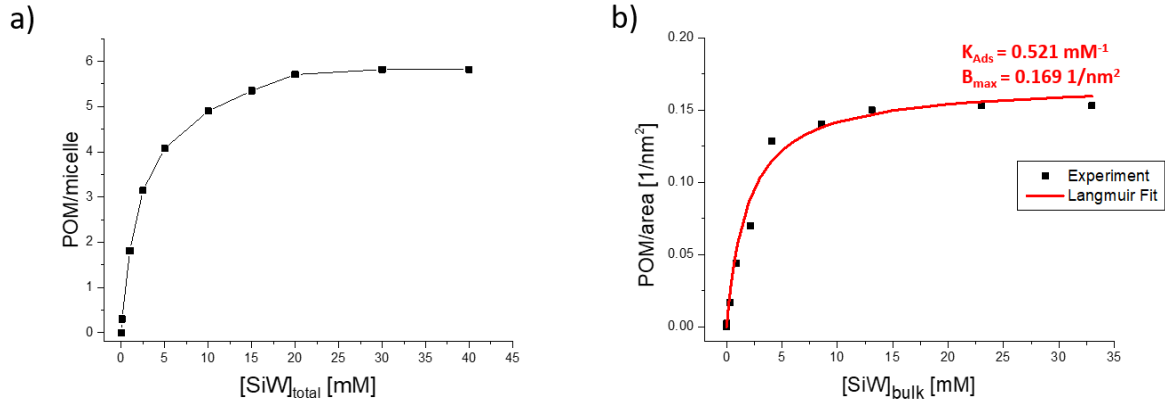


Figure 17: a) Number of POM per micelle against the total SiW-concentration. b) Adsorption isotherm of SiW on non-ionic micelles of 60 mM C<sub>8</sub>E<sub>4</sub>. The number of POM per micellar surface area was calculated by using the micellar dimensions from SANS and SiW-adsorption numbers from SAXS. [SiW]<sub>bulk</sub> was calculated from the adsorption ratios see text.

The experimental data in Figure 17b were fitted with a Langmuir adsorption isotherm described by

$$\frac{\text{POM}}{\text{area}} = \frac{B_{max} * K_{Ads} * [\text{SiW}]_{bulk}}{1 + K_{Ads} * [\text{SiW}]_{bulk}} \quad (3.1)$$

with  $B_{max}$  being the maximum occupancy on the C<sub>8</sub>E<sub>4</sub>-micelles at high HSiW-concentrations and  $K_{Ads}$  the equilibrium constant of the adsorption reaction, which in the Langmuir model is described as an complexation of an adsorbate in the bulk (SiW<sub>bulk</sub>) with a free adsorption site S on the adsorbent (here C<sub>8</sub>E<sub>4</sub>-micelles) resulting in the complex SiWS.



$$K_{Ads} = \frac{[\text{SiWS}]}{[\text{SiW}]_{bulk} * [\text{S}]} \quad (3.3)$$

Notably, the bulk concentration of SiW is linked to the adsorption ratio R obtained from the fits by this simple relation:

$$[\text{SiW}]_{bulk} = [\text{SiW}]_{total} * (1 - R) \quad (3.4)$$

With [SiW]<sub>total</sub> being the total concentration of HSiW in the sample.

This Langmuir model fitted well the experimental data providing a  $B_{max}$  value of 0.169 1/nm<sup>2</sup> along with a  $K_{Ads}$ -value of 0.521 mM<sup>-1</sup>. Furthermore, the isotherm shows a linear increase at [SiW]<sub>bulk</sub> < 4 mM corresponding to a total SiW-concentration of 10 mM. Therefore, at SiW-concentrations lower than 10 mM the amount of surface (and binding sites S) on the C<sub>8</sub>E<sub>4</sub>-

micelles can be completely neglected as saturation has not been reached. This understanding will prove useful in section 2.3.4. At saturation, that is at  $[\text{SiW}]_{\text{bulk}} > 10$  mM (or total SiW-concentrations higher than 20 mM) each SiW-molecule covers a square area with side length of 2.6 nm, which leaves a distance of 1.6 nm between adjacent SiW-molecules on the micellar surface. It should be noted here that the Langmuir model assumes non-interacting adsorbates, which does not apply to the electrostatically repelling SiW-ions. Furthermore, the number of free adsorption sites  $S$  on the  $\text{C}_8\text{E}_4$ -micelles is not constant as the micellar shape and surface area change with SiW-concentration. Nevertheless, the applicability of the Langmuir formalism to this system is an important result as it shows that the interaction of SiW with  $\text{C}_8\text{E}_4$ -micelles can be rationalized in the same lines as the classical sorption of solutes (or gases) to solid adsorbents. Furthermore, this behavior reveals that SiW is only governed by the chaotropic effect, which drives its adsorption to the  $\text{C}_8\text{E}_4$ -micelles, while SiW does not penetrate deeply into the  $\text{C}_8\text{E}_4$ -micelles. Additionally, the soft matter nature, namely the inherent dynamics of  $\text{C}_8\text{E}_4$ -micelles do not seem to impact the adsorption of SiW. Similar results are expected for other superchaotropic ions as well as other soft matter adsorbents such as other non-ionic surfactant micelles or polymers.

Overall, it was shown here that low amounts of SiW weakly affect the  $\text{C}_8\text{E}_4$ -micelles making them slightly longer, although the CP is increased (to 45°C at 0.1 mM SiW in comparison to 41°C for 60 mM  $\text{C}_8\text{E}_4$ ). This could indicate that SiW interacts faintly with the hydrophobic surfactant tails inside the  $\text{C}_8\text{E}_4$ -micelles affecting slightly the surfactant tail packing (increase in the packing parameter) while the micelles are simultaneously getting significantly charged. At higher concentrations, that is at  $[\text{SiW}] > 1$  mM, this phenomenon is inverted when more SiW adsorbs and the micelles shrink into spheres. Here, two factors might provide an explanation: i) Nano-ion adsorption causes an increase in the effective head group area as they intercalate between head groups, which pushes them apart and leads to a decrease in the molecular packing parameter causing the formation of spherical micelles. ii) Addition of superchaotropic ions drives a maximization of the area of the host-interface, which is achieved by shifting the geometry of the  $\text{C}_8\text{E}_4$ -micelles towards spheres. Furthermore, at  $[\text{SiW}] > 10$  mM, the micellar size and the number of SiW per micelle was found to saturate. The whole adsorption process of SiW to the  $\text{C}_8\text{E}_4$ -micelles was expressed as an adsorption isotherm, which could be fitted and rationalized using a Langmuir adsorption model. This understanding can be extended to all kinds of superchaotropic adsorption processes including other chaotropic ions as well as to other adsorbents such as polymers.



### 2.3.3. Changing C<sub>8</sub>E<sub>4</sub>-concentration

An increase in surfactant concentration generally leads to an increased number of micelles and to a smaller intermicellar distance. Consequently, the forces between strongly interacting micelles, such as charged POM-decorated C<sub>8</sub>E<sub>4</sub>-micelles, are tuned by surfactant concentration, which in turn might affect the extent of adsorption of POMs to the C<sub>8</sub>E<sub>4</sub>-micelles. To test this assumption CP-evolutions were measured for SiW and PW at different C<sub>8</sub>E<sub>4</sub>-concentrations. Notably, as PW tends to cause precipitation in C<sub>8</sub>E<sub>4</sub>-solutions only samples with [C<sub>8</sub>E<sub>4</sub>] ≤ 60 mM could be measured to avoid this experimental aspect.

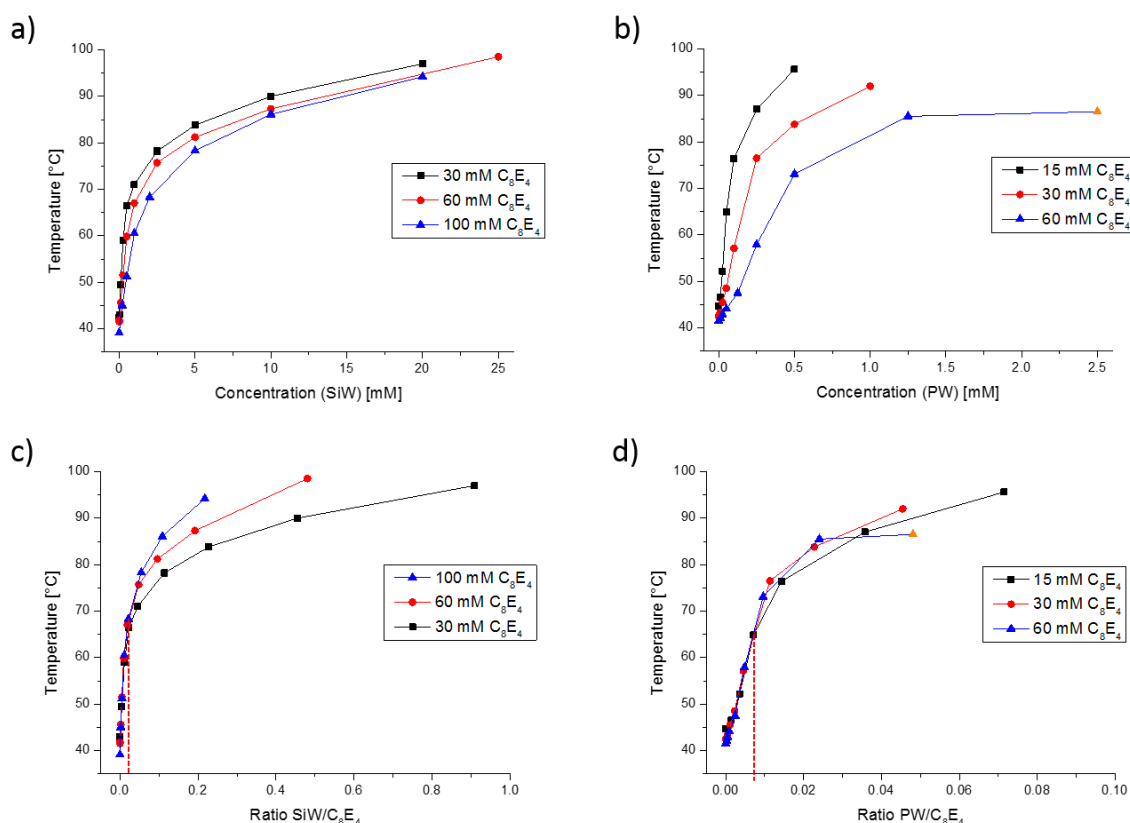


Figure 18: Cloud point evolution of different C<sub>8</sub>E<sub>4</sub>-concentrations as a function of a) SiW-concentration, b) PW-concentration, c) SiW/C<sub>8</sub>E<sub>4</sub>-ratio in the decorated micelles and d) PW/C<sub>8</sub>E<sub>4</sub>-ratio in the decorated micelles. The ratios were calculated assuming 100% adsorption by:  $POM/C_8E_4 = \frac{[POM]}{[C_8E_4] - cmc(C_8E_4)}$ . The cmc of C<sub>8</sub>E<sub>4</sub> was assumed constant at 8 mM.<sup>133</sup>

Expectedly, the cloud point evolution in the presence of either SiW or PW is shifted to lower temperatures upon increase of the C<sub>8</sub>E<sub>4</sub>-concentration, see Figure 18a, b. As the CP is a measure of intermicellar interactions, this trend can be linked to the number of adsorbed PW or SiW and the resulting charges per micelle, which are lower at high surfactant concentrations and results in weaker micellar charge/repulsion potentials and lower CPs. When tracing the cloud point temperatures as a function of the ratio of PW or SiW/C<sub>8</sub>E<sub>4</sub> in the formed decorated micelles

(considering 100% adsorption), interestingly, all CP-evolutions overlap at low POM/C<sub>8</sub>E<sub>4</sub>-ratios and split up at higher ratios, see Figure 18c, d. More specifically, this overlap holds up to a ratio of 0.02 for SiW and about 0.01 for PW, meaning one POM per 50 or per 100 C<sub>8</sub>E<sub>4</sub>-molecules, respectively.

### 2.3.4. The thermodynamics of superchaotropic adsorption

Thermodynamic considerations have proven very useful to identify and classify the chaotropic effect as a general and strong driving force.<sup>36,68</sup> In particular, Nau et al. have shown in a number of recent studies that nanometer-sized ionic borate clusters bind strongly to the hydrophobic cavities of macrocyclic host molecules such as cyclodextrins even exceeding the affinities of classical hydrophobic guest molecules like adamantane.<sup>3,65–67</sup> This binding phenomenon was shown to be characterized by a peculiar thermodynamic fingerprint comprising an enthalpic gain at the expense of an entropic penalty both arising from a water-structure recovery upon binding driven by the chaotropic effect.<sup>3,36</sup> Likewise, the adsorption of Keggin-POMs to non-charged polar soft-matter interfaces including non-ionic surfactant micelles and polymers was shown to arise from the same driving force as corroborated by Buchecker and Naskar et al.<sup>4,92,104</sup> However, an evaluation of the underlying adsorption thermodynamics has not been provided so far for these soft matter systems to allow for a comparison with the association phenomena of superchaotropic ions with macrocyclic host-molecules. Here, by investigating the non-ionic surfactant micellar phase of 60 mM C<sub>8</sub>E<sub>4</sub> in the presence of the Keggin-POM SiW (SiW<sub>12</sub>O<sub>40</sub><sup>4-</sup>) as a function of temperature, the thermodynamic signature of the superchaotropic adsorption process is established. Thus, the reaction of SiW-decorated C<sub>8</sub>E<sub>4</sub>-micelles to heating is discussed first qualitatively and quantified in terms of thermodynamics afterwards. As a premise it has to be stated that the reaction of (bare) non-ionic surfactant (e.g C<sub>8</sub>E<sub>4</sub>) micelles to heating is well understood as a process that involves head group dehydration with increasing temperature, which manifests as a one dimensional micellar growth before the appearance of the cloud point.<sup>128</sup> Here, the focus is set on the behavior of the SiW-shell that surrounds the C<sub>8</sub>E<sub>4</sub>-micelle at temperatures before the cloud point. To this end, SAXS of 60 mM C<sub>8</sub>E<sub>4</sub> + 10 mM HSiW was measured at temperatures between 20°C and 80°C. The corresponding spectra are shown in Figure 19.

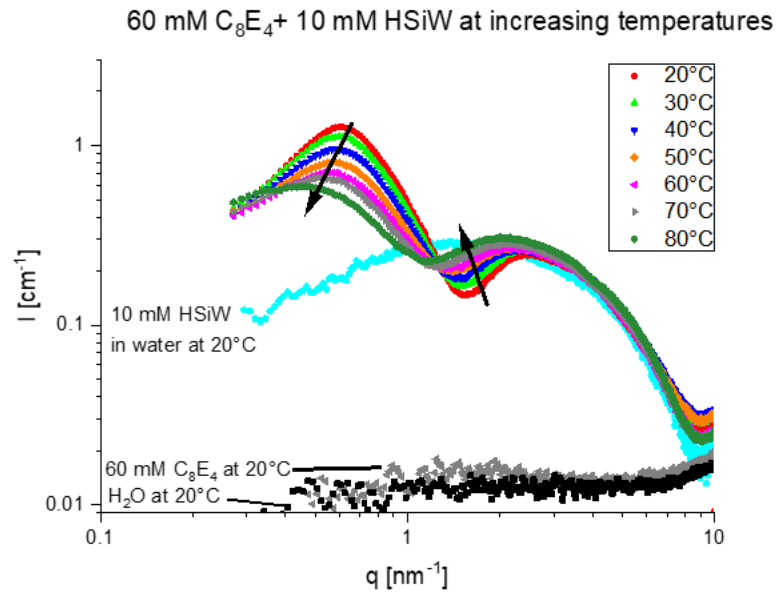


Figure 19: SAXS-spectra of 60 mM C<sub>8</sub>E<sub>4</sub> at different temperatures in the presence of 10 mM HSiW (H<sub>4</sub>SiW<sub>12</sub>O<sub>40</sub>). Additionally, the scattering contributions of water, 60 mM C<sub>8</sub>E<sub>4</sub> and of HSiW in water are shown. The CP lies at 87°C. Water was not subtracted. The spectra are in absolute scale.

At all temperatures, the classical core-shell pattern characteristic for decorated micelles is observed, which is a superposition of the signal of free SiW (2-10 nm<sup>-1</sup>) in water and the signal of the decorated micelles (0.2-2 nm<sup>-1</sup>) as was discussed in section 2.3. Upon heating, the scattering contribution of free SiW (cyan curve) in water remains constant, while the scattering intensity of the core-shell flattens out as displayed by an intensity increase at mid  $q$  and an intensity decrease at high  $q$ . As SAXS is only sensitive to SiW due to its high electron density compared to the rest of the sample (C<sub>8</sub>E<sub>4</sub> and H<sub>2</sub>O) this heat-induced flattening signifies that the adsorbed number of SiW on the C<sub>8</sub>E<sub>4</sub>-micelles decreases upon heating, which results in lower contrast and weaker scattering. Additionally, a change in shape of the micelles upon heating can be inferred as the slopes of the oscillation at mid  $q$  change significantly with temperature. Furthermore, the positive slope in the low- $q$  region, which is indicative of the electrostatic repulsion between the micelles, is levelling off with temperature indicating that electrostatics diminish, which again can be explained by a gradual desorption of SiW with rising temperature. At the highest temperature of 80°C – for reference the CP is at 87°C – the positive slope in the lowest  $q$ -region has almost disappeared indicating that the intermicellar repulsive forces diminish close to the CP. Thus, the CP of C<sub>8</sub>E<sub>4</sub> seems to appear only when the SiW-molecules are significantly desorbed, and the electric charges are sufficiently withdrawn from the micelles allowing for micellar approach and subsequent phase separation. Notably, desorbed SiW will have electrolytic effects and screen intermicellar repulsion and, thus, further facilitate the occurrence of the CP.

The same interpretation holds for the SAXS-spectra for samples containing 60 mM  $C_8E_4$  + 1 mM HSiW, see Figure 20b. However, for this sample additionally SANS-measurements were conducted, see Figure 20a for the spectra, which allows for a more quantitative evaluation of the effect of temperature via fitting according to the procedure described in section 7.3.2.

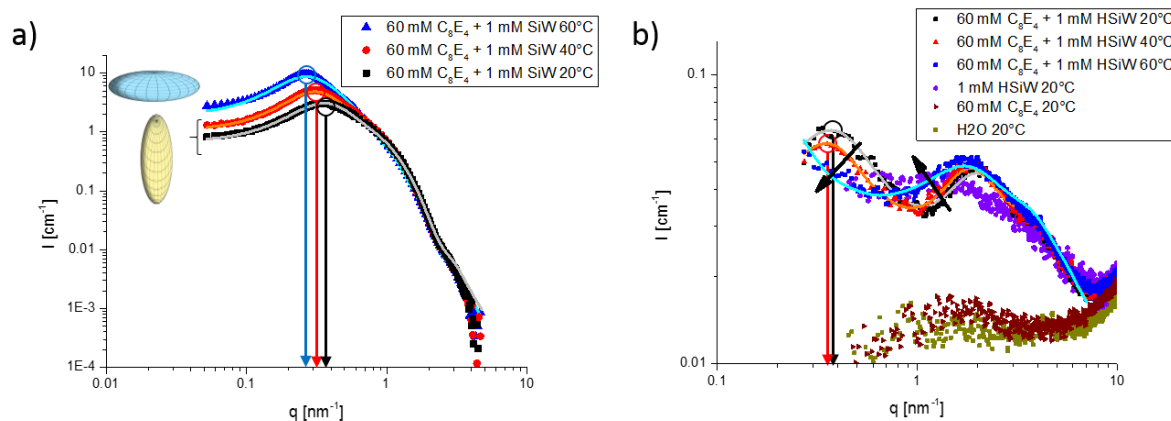


Figure 20: a) SANS- and b) SAXS-spectra of 60 mM  $C_8E_4$  in  $D_2O$  (or in  $H_2O$  in SAXS) in the presence of 1 mM HSiW ( $H_4SiW_{12}O_{40}$ ) measured at different temperatures. For reference, the CP lies at  $67^\circ C$ . The spectra are in absolute scale and the lines indicate theoretical fits using prolate ellipsoid form factors at  $20^\circ C$  and  $40^\circ C$  and an oblate ellipsoid form factor at  $60^\circ C$  as indicated with the schemes. The arrows indicate the positions of the structure factor maxima, appearing in SANS and in SAXS at the same  $q$ -values. Corresponding fit parameters are listed in section 2.9.

The SANS-spectra of 60 mM  $C_8E_4$  + 1 mM HSiW show a clear increase in intensity at low  $q$  upon heating, which displays the expected growth of the decorated  $C_8E_4$ -micelles upon approach of the CP. The corresponding micellar dimensions (from SANS) were extracted from the fits along with the parameters concerning the adsorbed SiW-shell (from SAXS), see Table 6. Thus, the commonly expected one-dimensional growth<sup>128</sup> of non-ionic micelles upon heating only holds at low temperatures from  $20$ - $40^\circ C$ , while towards higher temperatures ( $40^\circ C$ - $60^\circ C$ ) upon approach of the CP at  $67^\circ C$  a morphological change from elongated (prolate ellipsoids) to flat (oblate ellipsoids) micelles takes place. Thus, the cloud point of 60 mM  $C_8E_4$  is approached by a non-classical route in the presence of 1 mM SiW. It is noteworthy that the same observation was made for 60 mM  $C_8E_4$  + 1 mM SDS as was shown in section 2.2, Figure 10. Therefore, this pathway seems to manifest consistently when considering charged  $C_8E_4$ -micelles regardless of the origin of the charge be it the ionic surfactant SDS or the Keggin-POM HSiW.

Table 6: Fitting parameters of 60 mM C<sub>8</sub>E<sub>4</sub> + 1 mM HSiW at increased temperatures including form factor shapes with corresponding dimensions from SANS, SiW-adsorption number and ratios from SAXS, and respective charges and salt concentration from the structure factors.

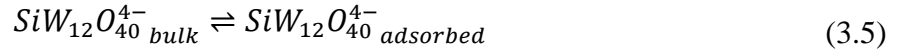
Temperature [°C]	Form factor shape	Micellar dimensions (from SANS)			SiW-shell (from SAXS)		Structure factor (SANS and SAXS)	
		r_eq [nm]	r_pol [nm]	N <sub>Agg</sub>	SiW per micelle	SiW adsorption ratio <sup>1</sup> , R	Charge, q <sub>e</sub>	Salt [M]
20	Prolate ellipsoid	1.6	6.6	142	1.81	0.66	8	0.0001
40	Prolate ellipsoid	1.7	8.4	211	1.96	0.49	11	0.0001
60	Oblate ellipsoid	5.7	1.6	421	1.63	0.20	11 <sup>2</sup>	0.0003 <sup>2</sup>

$$^1\text{adsorption ratio } R = \frac{[POM]_{\text{adsorbed}}}{[POM]_{\text{total}}}$$

<sup>2</sup>only determined in SANS as the structure factor peak lies below the investigated q-region in SAXS.

Moreover, SAXS further allowed for an evaluation of the adsorbed number of POMs per micelle amounting to 1.8, 1.96 and 1.63 SiW-molecules per C<sub>8</sub>E<sub>4</sub>-micelle respectively at 20°C, 40°C and 60°C. These numbers respectively correspond to decreasing adsorption ratios (as there are fewer micelles in solution) with temperature of 0.66 (66% of all SiW-molecules are adsorbed on micelles) at 20°C over 0.49 (49% SiW on micelles) at 40°C to 0.2 (20% SiW on micelles) at 60°C. This is an important result as it demonstrates the strong effect that temperature has on the superchaotropic adsorption phenomenon and it shows that as the cloud point occurs almost all SiW is desorbed from the micelle. Therefore, it is the responsiveness to heating of adsorbed SiW that allows for the appearance of the CP.

Furthermore, the adsorption ratios R can be used to determine the equilibrium constant K<sub>ads</sub> for the reaction between bulk and adsorbed SiW.



$$\text{with } K_{\text{Ads}} = \frac{[SiW_{12}O_{40}^{4-}]_{\text{adsorbed}}}{[SiW_{12}O_{40}^{4-}]_{\text{bulk}}} = \frac{[SiW_{12}O_{40}^{4-}]_{\text{total}} * R}{[SiW_{12}O_{40}^{4-}]_{\text{total}} * (1 - R)} \quad (3.6)$$

Application of eq. 3.5 neglects the limited number of adsorption sites on the C<sub>8</sub>E<sub>4</sub>-micelles and describes a linear adsorption isotherm (Henry isotherm), which only holds at [SiW]<10 mM as was shown in section 2.3.2. This concentration constraint provides the working range of the thermodynamic calculations made herein. The acquired equilibrium constant is in turn connected to the Gibbs free energy ΔG at a given temperature T in Kelvin by the van't Hoff-equation

$$\Delta G = -RT \ln(K_{\text{Ads}}) \quad (3.7)$$

with the gas constant  $R = 8.314 \frac{J}{K \cdot mol}$ . Combining eq. 3.7 with the definition of the Gibbs free energy

$$\Delta G = \Delta H - T \Delta S \quad (3.8)$$

couple the enthalpy ΔH and the entropy ΔS with the equilibrium constant K by a linear relation:

$$-\frac{\Delta H}{RT} + \frac{\Delta S}{R} = \ln K_{ads} \quad (3.9)$$

Thus, by using eq. 3.9, a plot of  $\ln(K)$  versus  $1/T$  makes accessible the standard enthalpy and entropy of the superchaotropic adsorption process. Figure 18 shows such a van't Hoff plot for an ensemble of three related samples:

1. 60 mM  $C_8E_4$  + 1 mM HSiW at different temperatures, present section (Figure 20 and Table 6)
2. 60 mM  $C_8E_4$  + 1 mM HSiW + 10 mM NaCl at different temperatures, see page 68 (Figure 28 and Table 9)
3. 25 mM  $C_{12}E_5$  + 2.5 mM HSiW as a function of temperature, see page 115 (Figure 50 and Table 18)

Samples 2 and 3 are included here because the thermodynamics of the superchaotropic adsorption process, for instance the equilibrium constants as a function of temperature were found to be independent of the addition of electrolyte (10 mM NaCl) as well as of the nature of the surfactant (comparison of  $C_8E_4$  with a closely related ethoxy surfactants  $C_{12}E_5$ ). The indifference to these slight systematic changes displays the robustness of this method.

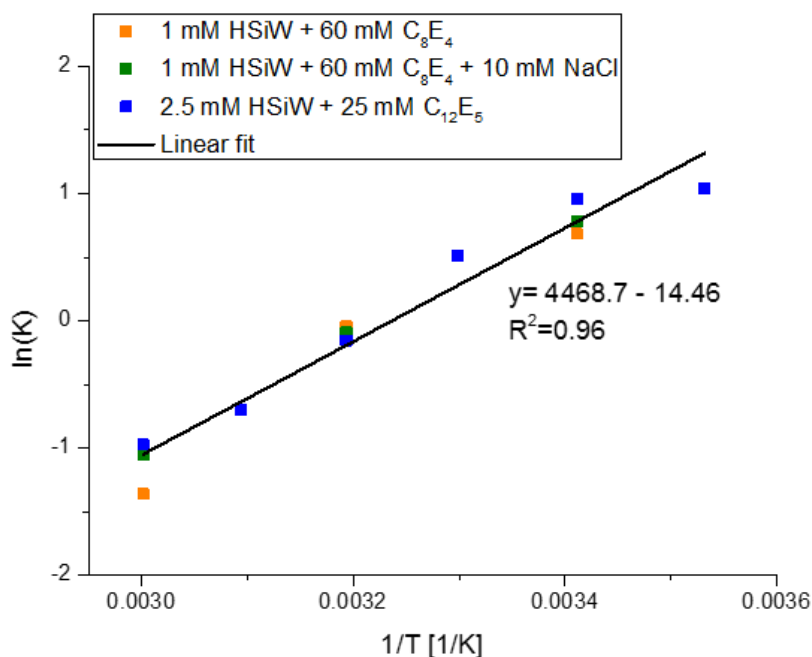


Figure 21: van't Hoff plot including the three aforementioned samples. A linear fit of all used data points is shown. Linear regression gave a good fit of the data with a  $R^2$  of 0.96.

Linear regression of the van't Hoff plot proved to fit the data well with  $R^2=0.96$ . The corresponding standard enthalpy and entropy of the adsorption process of SiW to ethoxylated micelles along with the corresponding Gibbs free energy at 293.15 K are listed in Table 7.

Table 7: Gibbs free energies along with standard enthalpic and entropic terms at 293.15 K arising from the adsorption equilibria of SiW on ethoxylated micelles C<sub>8</sub>E<sub>4</sub> and C<sub>12</sub>E<sub>5</sub>. The result is presented using different units. The errors were calculated by error propagation of the standard errors of the linear regression in Figure 21.

	$\Delta H$	$T\Delta S$	$\Delta G$
[kJ/mol]	$-37.2 \pm 2.4$	$-35.3 \pm 2.3$	$-1.9 \pm 4.7$
[kcal/mol]	$-8.9 \pm 0.6$	$-8.4 \pm 0.5$	$-0.5 \pm 1.1$

Thus, the thermodynamic fingerprint of the superchaotropic adsorption of SiW is characterized by an enthalpic driving force accompanied by an entropic penalty displaying the same signature as observed for guest-host binding of superchaotropic borate species to macrocyclic hosts.<sup>3,62,65–67</sup> Notably, the driving force here seems to be exceptionally weak as it amounts at 20°C to a Gibbs energy change of only -1.9 kJ/mol. By contrast, superchaotropic binding phenomena of boron clusters to  $\gamma$ -CD were shown to exhibit Gibbs free energies in the order of at least -15 kJ/mol. For a summary, of all published thermodynamic binding parameters of nano-ions to  $\gamma$ -CD, see Table 10 in the addendum on page 69. In a way the low binding constant for SiW on the C<sub>8</sub>E<sub>4</sub>-micelles is expected because SiW is only at 66% adsorbed to the micelle at 20°C corresponding to a low equilibrium constant of  $K=1.9$ , where  $K=1$  would correspond to 50% of SiW adsorbed to the micelles. As was established in section 2.3, the adsorption of SiW on C<sub>8</sub>E<sub>4</sub>-micelles is not due to chemical bonding at the contact interface between C<sub>8</sub>E<sub>4</sub> and SiW (SiW<sub>12</sub>O<sub>40</sub><sup>4-</sup>) because the isostructural metatungstate (H<sub>2</sub>W<sub>12</sub>O<sub>40</sub><sup>6-</sup>) did not show any interaction. Consequently, adsorption of a superchaotrope arises merely from a thermodynamically favored overlap of the hydration shells of the ion and the micelle causing a release of hydration water into the bulk. To rationalize the obtained thermodynamic signature, the energetic origin of the released water molecules has to be inferred and, to this end, both the adsorbate (SiW) and the adsorbent (C<sub>8</sub>E<sub>4</sub>-micelle) have to be individually considered in terms of their hydration. On the one hand, the Keggin-ion SiW is a superchaotropic species and consequently its hydration shell is highly dynamic (high positive structural entropy) and weakly bound (low negative enthalpy) in comparison to bulk water.<sup>26,36,91</sup> On the other hand, the hydration shell surrounding the ethylene glycol head groups of the C<sub>8</sub>E<sub>4</sub>-surfactant, is known to be shed off upon heating<sup>126,151–154</sup>, which suggests weakly bound water (low negative enthalpy) and a negative entropy of hydration. However, a direct determination of such thermodynamic parameters is lacking in the literature despite the plethora of studies that deals with the hydration of ethylene glycol either incorporated in surfactants<sup>151,155,156</sup> or as polymeric ethylene glycol (PEG)<sup>157,158</sup>. Nevertheless, Schrödle et al. concluded from dielectric relaxation spectroscopy experiments that the water molecules in the vicinity of the ethylene glycol heads of the surfactant C<sub>12</sub>E<sub>5</sub> are more weakly



bound compared to in the water bulk<sup>156</sup>, a notion reminiscent of the hydration of a chaotropic ion. Furthermore, Woutersen et al. and Kubarych et al. point out that the hydration water of PEG exhibits the same dynamics as bulk water.<sup>157,158</sup> Concluding from these studies, the hydration water that surrounds the ethylene glycol units in non-ionic ethoxylated surfactant is weakly bound or at least similarly as in bulk water and, thus, behaves somewhat similarly to the hydration water of a chaotrope (low negative enthalpy and high positive structural entropy<sup>91</sup>). Thus, as water is more strongly bound in the bulk and less dynamic than in the hydration shell of both SiW and C<sub>8</sub>E<sub>4</sub>, a water release upon adsorption will entail an enthalpic gain accompanied by an entropic penalty, which is indeed the observed result here, see Table 7. Notably, this interpretation is equivalent to the suggested water-structure recovery upon binding of a superchaotropic guest into macrocyclic hosts coined by Nau et al.<sup>3</sup>

To sum up, here by combination of SAXS and SANS at different temperatures of SiW-decorated micelles, we have shown that temperature has profound effects on the superchaotropic adsorption as was exemplified on the Keggin-ion SiW adsorbed on non-ionic surfactant micelles of the ethoxylated kind (C<sub>8</sub>E<sub>4</sub> and C<sub>12</sub>E<sub>5</sub>). With increasing temperature, the adsorption of SiW was found to become disfavored reflected in decreasing adsorption ratios. Derivation of the underlying adsorption equilibrium allowed for a calculation of the Gibbs free energy along with the standard enthalpy and entropy. Thus, the adsorption of SiW on C<sub>8</sub>E<sub>4</sub>-micelles was shown to be an enthalpically driven phenomenon, which is accompanied by an entropic penalty. This thermodynamic signature is a result of the chaotropic effect and can be linked to a recovery of bulk water structure upon adsorption arising from a release of hydration water from both the adsorbent (micelle) as well as the adsorbate (SiW). Interestingly, by evaluating the binding phenomenon of chaotropic borate clusters to macrocyclic host molecules, Nau et al. came to equivalent conclusions and observed the same thermodynamic signature.<sup>3,36</sup> Therefore, despite the principled difference between superchaotrope adsorption and binding, the chaotropic effect is shown to work as a general driving force in such association phenomena.

### 2.3.5. Beyond the electrostatics of SiW-decorated micelles

When a superchaotropic ion adsorbs to a non-ionic micelle it conveys its charge to the micelle, which has tremendous effects on the intermicellar interactions as can be inferred from cloud point experiments and SAXS. Here, an attempt is made to avoid the impact of electrostatics by working in electrolytic aqueous solution. By doing so, more subtle effects of the superchaotropic adsorption on the non-ionic surfactant micelles will be revealed. In this context, Naskar et al. pointed out by using SAXS that for a composition of 60 mM C<sub>8</sub>E<sub>4</sub> with 10 mM SiW adding 100 mM NaCl had a screening effect, while the micellar shape remained unaffected.<sup>4</sup> Here, a more complete picture concerning the effect of NaCl and other electrolytes shall be established. First, the cloud point of 60 mM C<sub>8</sub>E<sub>4</sub> with respectively 1 mM of the isostructural Keggin-POMs MW (H<sub>2</sub>W<sub>12</sub>O<sub>40</sub><sup>6-</sup>), BW (BW<sub>12</sub>O<sub>40</sub><sup>5-</sup>), SiW (SiW<sub>12</sub>O<sub>40</sub><sup>4-</sup>) and PW (PW<sub>12</sub>O<sub>40</sub><sup>3-</sup>) were measured as a function of NaCl concentration, see Figure 22a, and second the same experiment was performed at different SiW-concentrations, see Figure 22b. Notably, the choice of NaCl was made deliberately as it is considered a neutral salt (without kosmotropic or chaotropic character) and, thus, causes negligible effects on the CP of C<sub>8</sub>E<sub>4</sub> by itself, see reference curve in Figure 22a. Therefore, it is expected to induce only charge screening between charged micelles. This was previously shown in section 2.2 for mixed ionic/non-ionic surfactant micelles of 1 mM SDS/60 mM C<sub>8</sub>E<sub>4</sub>, where at low salt concentrations the CP drops and at higher concentration, that is, at [NaCl] > 50 mM, the CP-curve coincides with the reference curve, see SDS curve in Figure 22a.

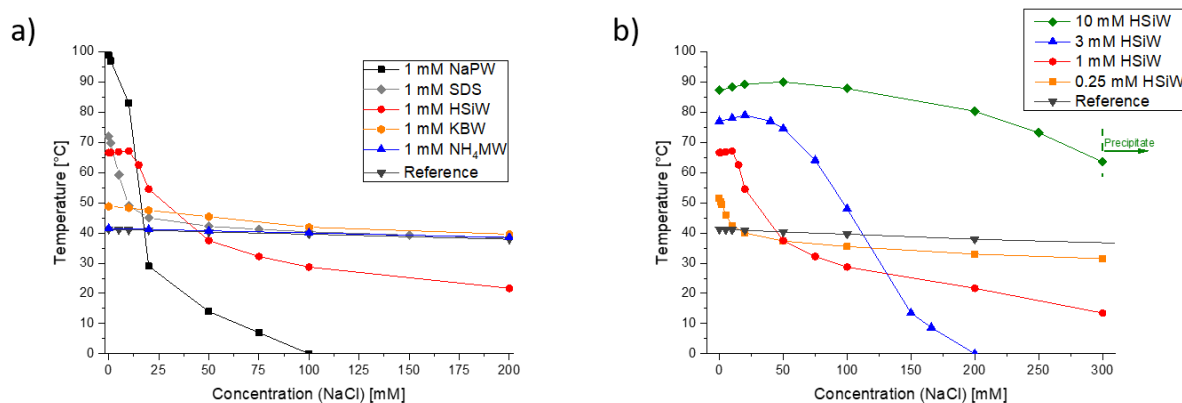


Figure 22: Cloud point evolutions of 60 mM C<sub>8</sub>E<sub>4</sub> as a function of the electrolyte NaCl (reference) a) in the presence of 1 mM HPW (H<sub>3</sub>PW<sub>12</sub>O<sub>40</sub>), HSiW (H<sub>4</sub>SiW<sub>12</sub>O<sub>40</sub>), KBW (K<sub>5</sub>BW<sub>12</sub>O<sub>40</sub>) and NH<sub>4</sub>MW ((NH<sub>4</sub>)<sub>6</sub>H<sub>2</sub>W<sub>12</sub>O<sub>40</sub>), respectively and b) at different concentrations of HSiW. The sample in a) containing 1 mM HPW precipitates at [NaCl] > 10 mM.

Similarly, for POM-decorated micelles of 1 mM POM/60 mM C<sub>8</sub>E<sub>4</sub> the CP drops as NaCl is added because the intermicellar repulsion is gradually screened, which allows for micellar

approach and facilitates the occurrence of the CP, see Figure 22a. However, expectedly the extent of the CP-drop in the presence of these Keggin-ions increases systematically from the weakest chaotropic POM  $\text{H}_2\text{W}_{12}\text{O}_{40}^{6-}$  over  $\text{BW}_{12}\text{O}_{40}^{5-}$  over  $\text{SiW}_{12}\text{O}_{40}^{4-}$  to the most superchaotropic  $\text{PW}_{12}\text{O}_{40}^{3-}$ . Notably, for PW extensive bluish phases were observed, which are omitted here and will be thoroughly discussed later in section 2.5. Here, for the weakest chaotropic POM MW ( $\text{H}_2\text{W}_{12}\text{O}_{40}^{6-}$ ) no difference with the reference curve is observed as it does not affect the CP or significantly adsorb to the  $\text{C}_8\text{E}_4$ -micelles at 1 mM MW. Further, in the presence of the more chaotropic BW ( $\text{BW}_{12}\text{O}_{40}^{5-}$ ), a monotonous decrease of the CP was observed upon addition of NaCl, which coincides with the reference curve at high NaCl-concentrations. However, for the superchaotropic SiW (and PW), at  $[\text{NaCl}] > 50$  mM (20 mM for PW) the CP drops even far below the reference curve unlike with the other POMs or for the mixed micelles of SDS/ $\text{C}_8\text{E}_4$ . At these high salt contents, the SiW-decorated micelles have thus become more hydrophobic than the micelles of 60 mM  $\text{C}_8\text{E}_4$  (with NaCl) and in such electrolytic solution addition of 1 mM SiW or PW has a significant salting-out effect. This reveals that, when the intermicellar electrostatic repulsion is screened, the SiW-decorated  $\text{C}_8\text{E}_4$ -micellar phase is less stable than bare  $\text{C}_8\text{E}_4$ -micelles in water, which shows that there are significant alterations to the  $\text{C}_8\text{E}_4$ -micelles upon SiW-adsorption that go beyond electrostatics and render the  $\text{C}_8\text{E}_4$ -micelles more hydrophobic.

Furthermore, Figure 22b shows that altering the SiW-concentration modulates strongly the effect of NaCl on the CP of 60 mM  $\text{C}_8\text{E}_4$ . Thus, at the lowest SiW-concentration of 0.25 mM a sharp decrease at low NaCl-concentrations is observed. However, starting at 1 mM SiW at very low NaCl-concentrations, unexpectedly, the CP even increases slightly before the CP-decrease sets in, giving rise to a plateau of slightly rising CP. This plateau is broadened at the higher SiW-concentrations. Thus, the higher the SiW-concentration the more NaCl is needed to cause a decrease in the CP. Further, the CP at high NaCl-concentrations drops to lower temperatures with increased SiW-concentration (compare 0, 0.25 mM, 1 mM and 3 mM SiW at 200 mM NaCl). The apparent salting-out is thus mediated simultaneously by SiW- and NaCl-concentrations. At the highest used concentration of 10 mM SiW, the effect of NaCl on the CP is comparably small as the plateau extends to  $[\text{NaCl}] = 100$  mM and decreases only slightly at higher NaCl-concentrations before precipitation occurred at  $[\text{NaCl}] > 300$  mM.

To investigate the effects of NaCl on the SiW-decorated  $\text{C}_8\text{E}_4$ -micelles on a microscopic level, SANS- and SAXS spectra were acquired at 20°C for 60 mM  $\text{C}_8\text{E}_4$ +1 mM SiW up to 100 mM NaCl, which are shown in Figure 23. Note that NaCl by itself has negligibly small effects on the size and shape of  $\text{C}_8\text{E}_4$ -micelles as was shown in section 2.2.

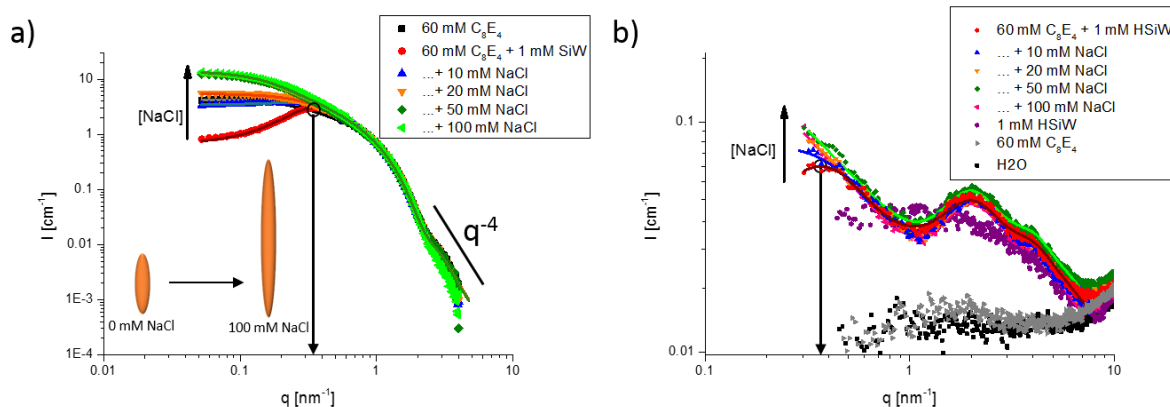


Figure 23: a) SANS- and b) SAXS-spectra of 60 mM  $C_8E_4$  in  $D_2O$  ( $H_2O$  in SAXS) in the presence of 1 mM SiW at different NaCl-concentrations. The spectra are in absolute scale and the lines indicate theoretical fits using ellipsoid models in SANS and equidimensional core-shell ellipsoid models in SAXS. The orange schemes in a) display the micellar shape at 0 and 100 mM, respectively acquired from fitting. Corresponding fit parameters are listed in section 2.9. SANS was measured at MLZ.

Figure 23a shows the SANS-spectra of the decorated micelles of 1 mM SiW/60 mM  $C_8E_4$  with increasing NaCl-concentrations. All spectra overlap perfectly in the high  $q$ -region, which is characteristic to the shape of the micelles and thus shows that the basic shape of the micelles remains unchanged upon addition of NaCl. By contrast, significant changes are observed at low  $q$  as (i) the positive slope arising from intermicellar repulsion turns into a plateau for  $[NaCl] = 20$  mM and (ii) at further elevated NaCl-concentrations the intensity of the plateau is increased. These two observations can be unambiguously assigned to a decrease of intermicellar repulsions and a significant growth of the micelles with increasing NaCl-concentration. Fitting of the SANS-spectra showed that the small prolate ellipsoidal micelles of 60 mM  $C_8E_4$  in the presence of 1 mM SiW with a polar radius  $r_{pol}=6.6$  nm grow consistently in the polar dimension to  $r_{pol}=17.3$  nm at 100 mM NaCl, whereas the equatorial radius of the ellipsoid stays at 1.6 nm at all NaCl-concentrations as indicated with the schemes. Thus, the micelles at 20°C grow expectedly larger as the distance to the CP decreases. For a listing of all micellar parameters including dimensions and SiW-adsorption numbers and ratios acquired from fitting of the SANS- and SAXS-spectra, see Table 8. Moreover, the SAXS-spectra of the same samples (60 mM  $C_8E_4$  + 1 mM HSiW + NaCl at 20°C) in Figure 23b all show the same overlapping classical core-shell pattern. Only at  $q < 0.4$  nm<sup>-1</sup>, differences emerge as the structure factor peak (without NaCl) disappears and steeper slopes emerge upon NaCl-addition hinting at the growth of the SiW-decorated micelles. By using the micellar dimensions acquired in SANS, the SAXS-spectra were fitted and the adsorbed number of SiW-molecules per micelle was determined and found to grow with micellar size from 2.4 at 0 mM NaCl to 6.8 at 100 mM NaCl. However, the corresponding adsorption ratios of SiW remained constant at around 0.9, meaning 90% of all SiW in solution is adsorbed on the micelles, regardless of NaCl-concentration. This is an

expected result as NaCl, due to its neutral character, should not affect the adsorption equilibrium and evidences that NaCl works as an ideal screening agent. Therefore, the micellar growth in NaCl-containing solution observed here arises exclusively from the adsorption of SiW. To rationalize this observation, considerations of the micellar packing parameter seem appealing, where an elongation of the micelle would arise from a decrease of the effective surfactant head group area. As SiW only interacts with the ethoxylated surfactant heads on the C<sub>8</sub>E<sub>4</sub>-micelles (and not with the C<sub>8</sub> micellar core) such micellar elongation can only appear if the hydration of the ethoxylated head groups is significantly decreased in the presence of adsorbed SiW. Equivalently, dehydration of the host surface upon superchaotropic binding to macrocycles or adsorption to micelles and polymers was also respectively proposed by Nau, Naskar and Buchecker et al.<sup>3,4,104</sup>

Table 8: Polar radii  $r_{\text{pol}}$ , equatorial radii  $r_{\text{eq}}$  and aggregation numbers  $N_{\text{Agg}}$  of the ellipsoidal micelles of 60 mM C<sub>8</sub>E<sub>4</sub>+1 mM SiW acquired by fitting of the SANS-spectra along with SiW-adsorption numbers and ratios from SAXS-fitting with corresponding NaCl-concentrations and cloud points.

		at 20°C				
c(NaCl)	Cloud point	$r_{\text{eq}}$ (micelle) from SANS	$r_{\text{pol}}$ (micelle) from SANS	$N_{\text{Agg}}$	SiW/micelle from SAXS	SiW adsorption ratio $R^1$ from SAXS
[mmol/L]	[°C]	[nm]	[nm]			
0	66.6	1.6	6.6	142	1.81	0.66
10	67.1	1.6	7.9	155	2.04	0.69
20	54.5	1.6	8.0	170	2.32	0.71
50	37.5	1.6	16.8	370	5.01	0.70
100	28.7	1.7	17.3	400	5.15	0.67

$$^1\text{adsorption ratio } R = \frac{[POM]_{\text{adsorbed}}}{[POM]_{\text{total}}}$$

Thus, by working in aqueous solution containing the (most) ideal electrolyte NaCl, a dehydration effect of the superchaotropic POM SiW on the C<sub>8</sub>E<sub>4</sub>-micelles seems to be the most compelling argument to rationalize both the CP-drop as well as the micellar elongation.

It is interesting to expand and apply this understanding to the effects of non-ideal electrolytes. For this purpose, the sodium salts of SO<sub>4</sub><sup>2-</sup>, F<sup>-</sup> and I<sup>-</sup> – arranged from kosmotropic to chaotropic anions – were examined as to their effects on the cloud point of decorated micelles of 1 mM HSiW/60 mM C<sub>8</sub>E<sub>4</sub> and set in comparison to the neutral Cl<sup>-</sup>, see Figure 24a. For reference, Figure 24b displays the effect of these classical Hofmeister-ions on the CP of bare 60 mM C<sub>8</sub>E<sub>4</sub>.

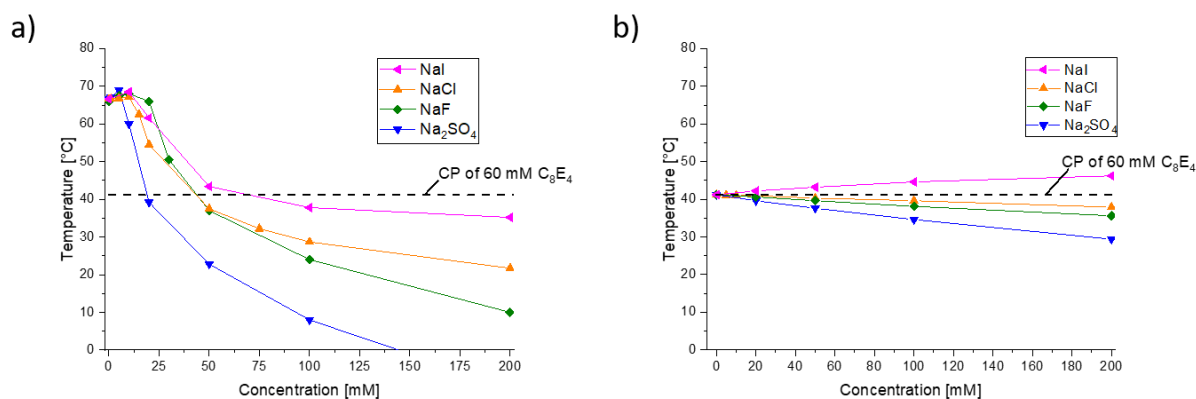


Figure 24: a) Cloud point evolutions of 60 mM C<sub>8</sub>E<sub>4</sub> in the presence of 1 mM HSiW (H<sub>4</sub>SiW<sub>12</sub>O<sub>40</sub>) as a function of the Hofmeister salts Na<sub>2</sub>SO<sub>4</sub>, NaF, NaCl and NaI. b) Cloud point evolutions of 60 mM C<sub>8</sub>E<sub>4</sub> as a function of the same salts (absence of SiW). Both figures contain a dotted reference line that indicates the CP of bare 60 mM C<sub>8</sub>E<sub>4</sub> in the absence of additives.

For all used salts, the CP drops strongly and below the reference curve of 60 mM C<sub>8</sub>E<sub>4</sub> owing to a predominant screening effect, which reveals the dehydration of the C<sub>8</sub>E<sub>4</sub>-micelles induced by adsorbed SiW. The onset of this drop follows the ordering  $\text{SO}_4^{2-} < \text{Cl}^- \approx \text{I}^- < \text{F}^-$ . Expectedly, the CP drops earliest with  $\text{SO}_4^{2-}$  as it is the only bivalent ion causing a three times higher ionic strength compared to the monovalent halide ions. Additionally, the onset of  $\text{F}^-$  is shifted to higher concentrations compared to  $\text{Cl}^-$  and  $\text{I}^-$ , which occurs here because the weak acid HF ( $\text{pK}_a=3.17$ ) forms spontaneously from NaF in the presence of 1 mM HSiW ( $[\text{H}^+]=4$  mM,  $\text{pH}\approx 2.3$ ). Therefore, at low NaF-concentrations and  $\text{pH}<3.17$ , HF is the major present species and the screening (CP-drop) onset is shifted to  $[\text{NaF}]>25$  mM, where the pH is sufficiently buffered prohibiting HF-formation. Furthermore, the extents of the CP-drop reveal the ion specific effects in this system, which are clearest at high electrolyte concentrations  $>50$  mM, where pH-effects for  $\text{F}^-$  become irrelevant. Thus, the classical Hofmeister ordering  $\text{SO}_4^{2-} > \text{F}^- > \text{Cl}^- > \text{I}^-$  is observed here as, in comparison to the neutral  $\text{Cl}^-$ , the kosmotropes  $\text{SO}_4^{2-}$  and  $\text{F}^-$  induce a stronger CP-drop and the chaotrope  $\text{I}^-$  has a weaker effect. At the lowest salt-concentrations (before the CP-drop), a plateau is observed, which even shows a small CP-increase upon addition of either of the sodium salts. It will be shown later that this slight, yet significant CP-increase arises mainly from a cation effect due to changing  $\text{H}^+$  to  $\text{Na}^+$ , see Figure 25. Nevertheless, to rationalize the ion-specific CP-decrease with the anions, the competition of the individual ionic species (SiW and the respective Hofmeister ions) for hydration water has to be considered. In this context, Collins demonstrated by using size exclusion chromatography (SEC) that the anions  $\text{SCN}^-$  (chaotrope),  $\text{Cl}^-$  (neutral) and  $\text{SO}_4^{2-}$  (kosmotrope) affect the hydrodynamic radius of a second radioactively marked ion ( $\text{SO}_4^{2-}$ ,  $\text{Cl}^-$  or  $\text{SCN}^-$ )

according to their Hofmeister characters. Addition of the chaotropic  $\text{SCN}^-$  caused an acceleration of the radioactive ion (regardless of it being  $\text{SCN}^-$ ,  $\text{Cl}^-$  or  $\text{SO}_4^{2-}$ ) in SEC owing to an increase in its hydrodynamic size and a competition for surface sites on the column, while adding  $\text{Cl}^-$  had negligible effects and adding the kosmotropic  $\text{SO}_4^{2-}$  induced a retardation due to a decrease of the radioactive ion's hydrodynamic size (and hydration).<sup>28</sup> This observation clearly shows that the individual ions manifest their natures and affect each other mutually in mixed salt solutions according to the Hofmeister-series, that is, salting-out (dehydration) by kosmotropes and salting-in by chaotropes. Van der Vegt et al. recently added to the matter and showed that in mixed salt solutions that contain ions of opposite Hofmeister character, for instance the kosmotropic  $\text{Na}_2\text{SO}_4$  and the chaotropic  $\text{NaI}$ , the observed salt effects on the phase transition of PNiPAM-polymer are concentration dependent and non-additive. Thus, in the presence of  $\text{SO}_4^{2-}$ , addition of the chaotropic  $\text{I}^-$  caused a salting-out of the PNiPAM-polymer followed by a salting-in at higher  $\text{I}^-$ -concentrations. The authors posit that the initial salting-out by  $\text{I}^-$  arises from a partition of the sodium counter-ions towards the counter-ion cloud of  $\text{SO}_4^{2-}$ , which leaves  $\text{I}^-$  more hydrated and kosmotropic. Only at higher  $\text{I}^-$ -concentrations,  $\text{I}^-$  regains its chaotropic nature and partitions towards the PNiPAM-polymer causing a salting-in effect boosted by the kosmotropic character of  $\text{SO}_4^{2-}$ .<sup>159,160</sup> Here, using SiW-decorated (charged)  $\text{C}_8\text{E}_4$ -micelles as a starting point to test the effects of the Hofmeister ions, we also find non-additive salt effects. Thus, at sufficiently high Hofmeister salt concentrations, the CP of the SiW-decorated  $\text{C}_8\text{E}_4$ -micelles drops, which can be attributed to a predominant screening of the intermicellar repulsion. At such high salt concentrations, the classical Hofmeister ordering occurs. In comparison to the effects of the classical Hofmeister salts  $\text{NaI}$ ,  $\text{NaCl}$ ,  $\text{NaF}$  and  $\text{Na}_2\text{SO}_4$  on bare  $\text{C}_8\text{E}_4$ -micelles, see Figure 24b, the CP-shifts of the same salts on the SiW-decorated micelles (Figure 24a) are much more distinct and seem to cause stronger effects in regard to the neutral  $\text{Cl}^-$ . Thus,  $\text{SO}_4^{2-}$  and  $\text{F}^-$  are most salting-out followed by the neutral  $\text{Cl}^-$  and the chaotropic  $\text{I}^-$ . Therefore, the presence of the superchaotropic SiW in solution seems to enhance the Hofmeister character of a second ion regardless of its kosmotropic or chaotropic nature.

To further investigate the origin of the initial CP-increase that appears at low electrolyte concentrations, CP-measurements were performed on 60 mM  $\text{C}_8\text{E}_4$ +10 mM HSiW or NaSiW as a function of salt concentration for  $\text{NaCl}$  and  $\text{Na}_2\text{SO}_4$  to study the effect of the counter-ion. The CP-curves are shown in Figure 25.

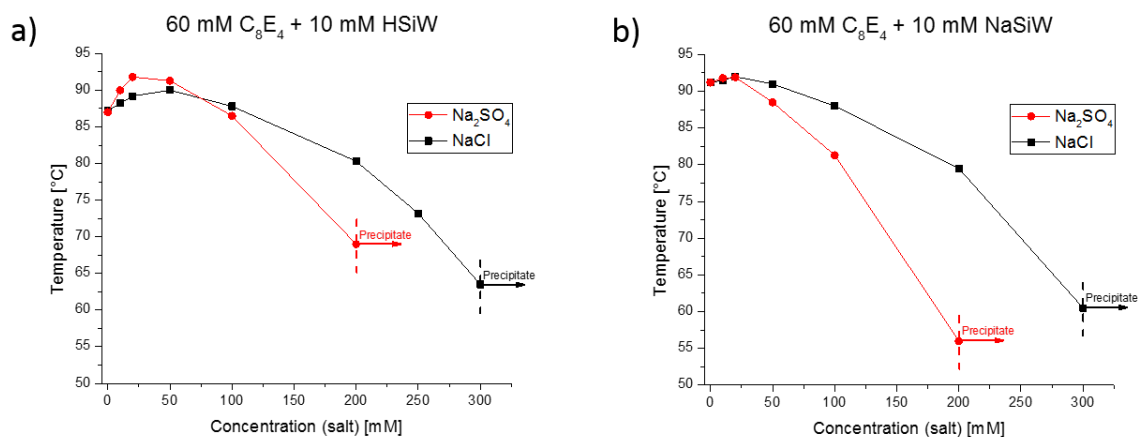


Figure 25: CP-evolutions of 60 mM C<sub>8</sub>E<sub>4</sub> + 10 mM SiW (SiW<sub>12</sub>O<sub>40</sub><sup>4-</sup>) as a function of NaCl and Na<sub>2</sub>SO<sub>4</sub> in its H<sup>+</sup>-form in a) and its Na<sup>+</sup>-form in b). At [Na<sub>2</sub>SO<sub>4</sub>] > 200 mM or [NaCl] > 300 mM a precipitate forms prohibiting CP-measurement.

When tracing the CP of 60 mM C<sub>8</sub>E<sub>4</sub> + 10 mM HSiW, Na<sub>2</sub>SO<sub>4</sub> and NaCl cause a slight increase in the CP at low salt concentrations, which is more pronounced for Na<sub>2</sub>SO<sub>4</sub> than for NaCl, see Figure 25a. Respectively, at [NaCl] > 50 mM and at [Na<sub>2</sub>SO<sub>4</sub>] > 20 mM the CP starts to drop. By conducting the same experiment for the Na<sup>+</sup>-form of SiW, see Figure 25b, this CP-increase is almost fully depressed and can therefore be mainly assigned to a counter-ion effect. Linked to this, it was shown in section 2.3.1 that NaSiW causes a slightly stronger CP-increase than HSiW, which is in agreement with the observed effect here. Furthermore, the CPs were found to drop more steeply for NaSiW.

To investigate the effects of SO<sub>4</sub><sup>2-</sup> and Cl<sup>-</sup> on the adsorption equilibrium of SiW, SAXS-spectra were acquired to observe eventual differences on the SiW-decorated C<sub>8</sub>E<sub>4</sub>-micelles. Thus, 60 mM C<sub>8</sub>E<sub>4</sub> + 10 mM HSiW was measured at 20, 50 and 80°C in the presence of Na<sub>2</sub>SO<sub>4</sub> and NaCl to trace the respective micellar evolution before the corresponding CPs, see Figure 26. The acquired spectra at 20°C and 50°C reveal no distinct difference between NaCl and Na<sub>2</sub>SO<sub>4</sub> as upon addition of either electrolyte, the classical core-shell pattern of the SiW-decorated C<sub>8</sub>E<sub>4</sub>-micelles remains unchanged at  $q > 0.8 \text{ nm}^{-1}$ , while the structure factor peak at  $0.6 \text{ nm}^{-1}$  levels off as the intermicellar charges are screened. Generally, at high electrolyte concentrations (or at high temperatures close to the CP), the plateau turns into a negative slope hinting at a change in the micellar shape and size that can be assigned to a growth of the decorated micelles as the distance to the CP decreases. Nevertheless, SAXS does not clarify any effects of NaCl or Na<sub>2</sub>SO<sub>4</sub> on the adsorbed number of SiW on the micelles, possibly because the effects are just too slight. Unfortunately, no further conclusions on the non-additive Hofmeister effects can be drawn.



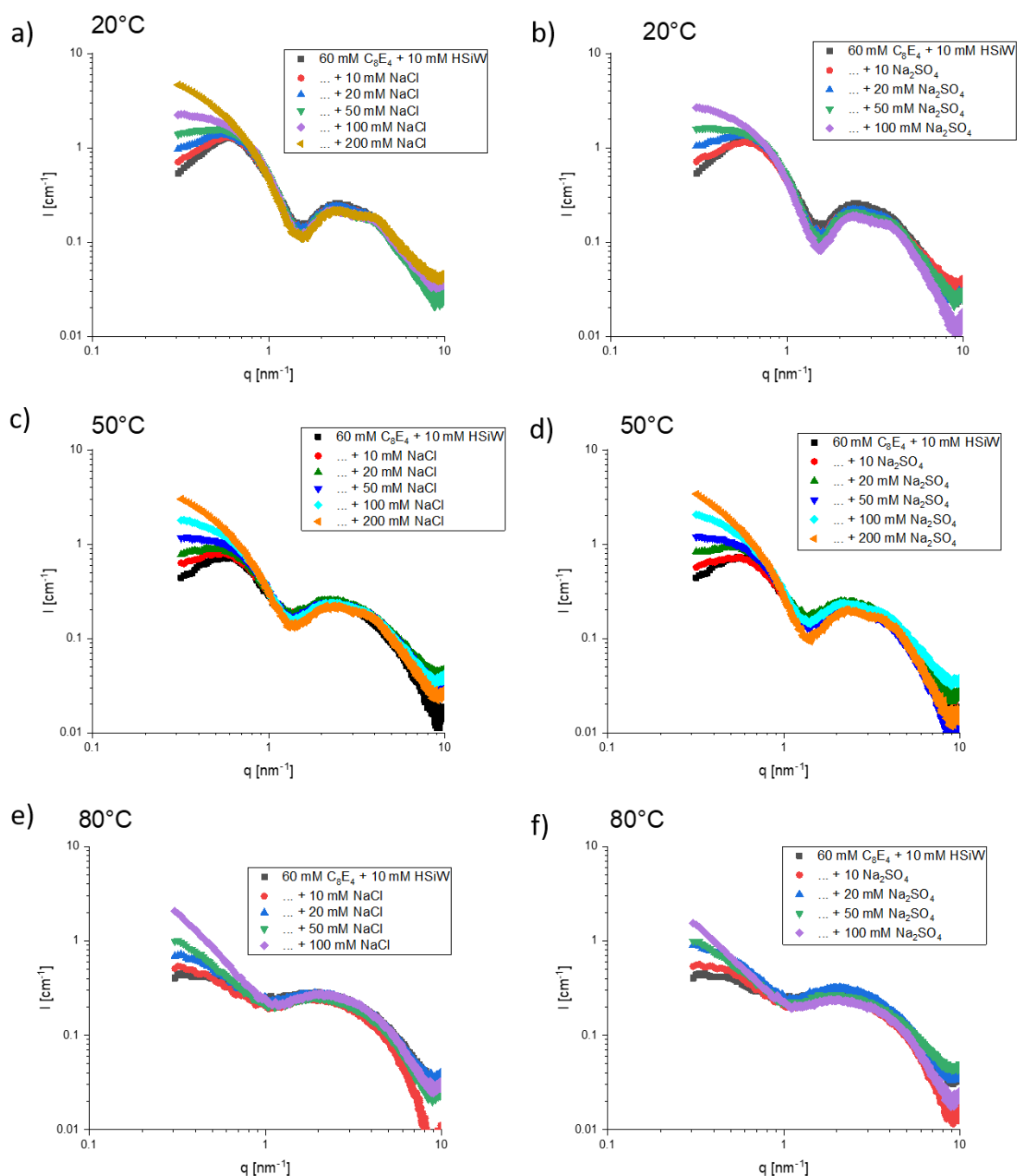


Figure 26: SAXS-spectra of 60 mM  $C_8E_4$  + 10 mM HSiW in the presence of NaCl at a) 20°C, c) 50°C and e) 80°C and in the presence of  $Na_2SO_4$  at b) 20°C, d) 50°C and f) 80°C. The spectra are in absolute scale.

In this section, the effect of electrolyte on SiW-decorated  $C_8E_4$ -micelles was demonstrated. It was observed that upon addition of NaCl, the micelles grew tremendously in length and became more hydrophobic indicated by a pronounced drop of the cloud point, while the adsorption ratio of SiW on the micelles remained strictly unaffected. This result was interpreted in terms of a screening effect by the electrolyte on the repulsive SiW-decorated micelles, which unveils that the  $C_8E_4$ -micelles are dehydrated upon adsorption of SiW. By cloud point measurements, it was further shown for samples containing 60 mM  $C_8E_4$  and HSiW that the nature of the added

electrolyte (kosmotropic or chaotropic) modulates the extent of the CP-drop according to the classical ordering of anions according to the Hofmeister-series: The chaotropic  $\Gamma^-$  caused the weakest CP-decrease, while the kosmotropic  $F^-$  and  $SO_4^{2-}$  caused the strongest CP-drop.

2.3.6. Addendum – Chaotropic POMs in  $C_8E_4$ 

Figure 27 shows the surface tension vs time curves for each sample. Respectively, the last 10 points in each curve were averaged and plotted in Figure 11. The time to reach equilibrium is lower the higher the concentration of the POM and for some samples the air bubble ripped off the capillary before equilibrium (constant surface tension plateau) was reached.

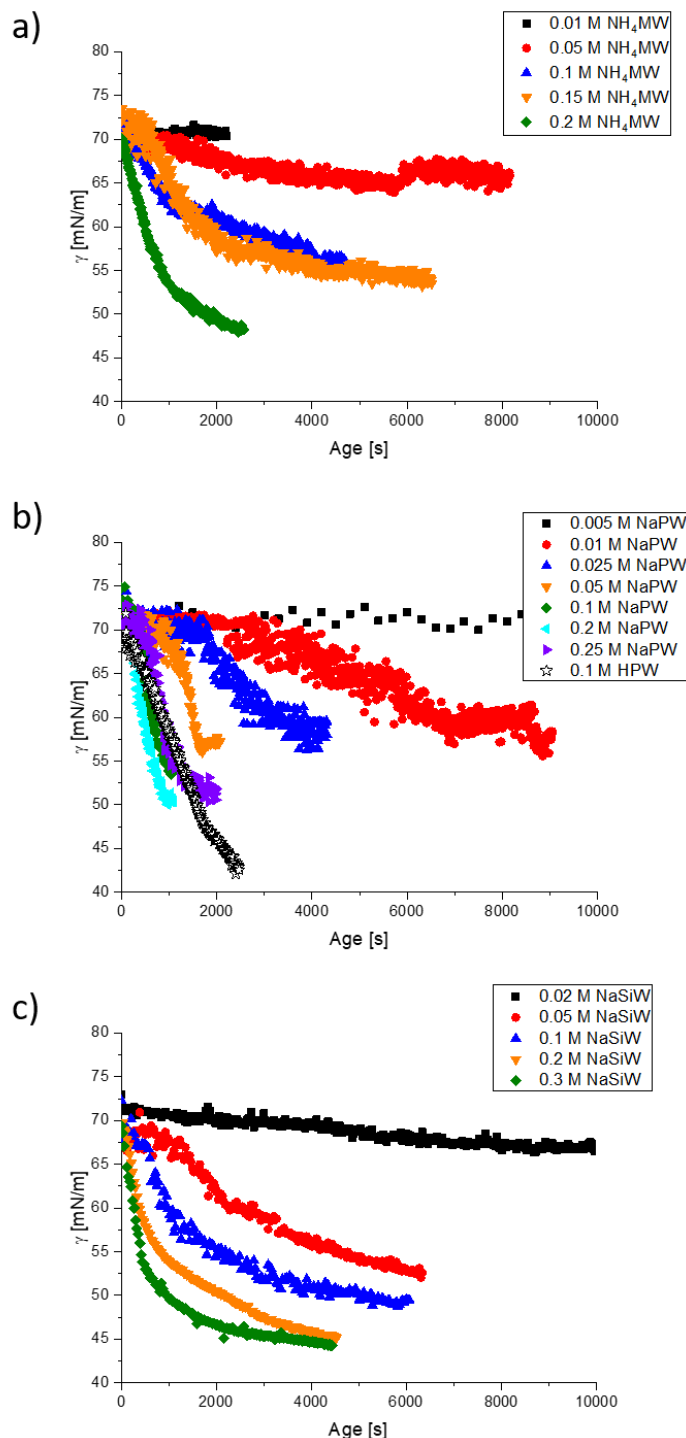


Figure 27: Water/air surface tension vs bubble age for aqueous solutions containing different concentrations of a)  $NH_4MW$  ( $(NH_4)_6H_2W_{12}O_{40}$ ) b)  $NaPW$  ( $Na_3PW_{12}O_{40}$ ) or 0.1 M HPW ( $H_3PW_{12}O_{40}$ ) and c)  $NaSiW$  ( $Na_4SiW_{12}O_{40}$ ).

The SANS and SAXS spectra of 60 mM C<sub>8</sub>E<sub>4</sub> + 1 mM HSiW + 10 mM NaCl were collected at different temperatures and are shown in Figure 28. Upon heating the micelles were found to grow as the CP was approached. Fitting of the spectra allowed for a precise evaluation of the micellar dimensions (from SANS) and for a quantification of the adsorbed SiW. The fitting parameters are shown in Table 9. These data were used in section 2.3.4 to support the van't Hoff plot (Figure 21) in order to determine enthalpy and entropy of the superchaotropic adsorption of SiW on C<sub>8</sub>E<sub>4</sub>-micelles. Most importantly, it was found that the adsorption ratios (and related adsorption equilibrium constants) are unaffected by the presence of 10 mM NaCl, which underlined the robustness of the method.

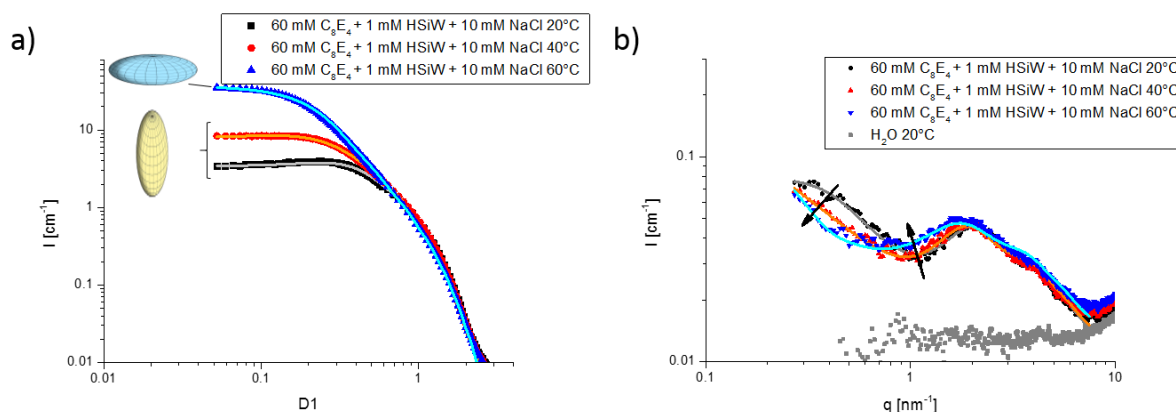


Figure 28: a) SANS- and b) SAXS-spectra of 60 mM C<sub>8</sub>E<sub>4</sub> in D<sub>2</sub>O (H<sub>2</sub>O in SAXS) in the presence of 1 mM HSiW (H<sub>4</sub>SiW<sub>12</sub>O<sub>40</sub>) and 10 mM NaCl at different temperatures. The spectra are in absolute scale and were measured at MLZ. The lines are theoretical fits using ellipsoid form factor models, prolate or oblate as shown with the schemes, coupled with HMSA structure factors in SANS and core-shell ellipsoid form factor models in SAXS. Corresponding fit parameters are listed in section 2.9.

Table 9: Fitting parameters of 60 mM C<sub>8</sub>E<sub>4</sub> + 1 mM HSiW + 10 mM NaCl at increased temperatures including form factor shapes with corresponding dimensions and aggregation numbers from SANS, SiW-adsorption number and ratios from SAXS, and respective charges and salt concentration from the structure factors.

Temperature [°C]	Form factor shape	Micellar dimensions (from SANS)			SiW-shell (from SAXS)		Structure factor (SANS and SAXS)	
		r_eq [nm]	r_pol [nm]	N <sub>Agg</sub>	SiWs per micelle	SiW adsorption ratio <sup>1</sup> , R	Charge, q <sub>e</sub>	Salt [M]
20	Prolate ellipsoid	1.6	9.2	198	2.04	0.69	8	0.003
40	Prolate ellipsoid	1.8	17.5	465	4.26	0.48	18	0.004
60	Oblate ellipsoid	10	1.4	1148	5.67	0.26	none	none

$$^1\text{adsorption ratio } R = \frac{[POM]_{\text{adsorbed}}}{[POM]_{\text{total}}}$$

<sup>2</sup>only determined in SANS as the structure factor peak lies below the investigated q-region in SAXS.

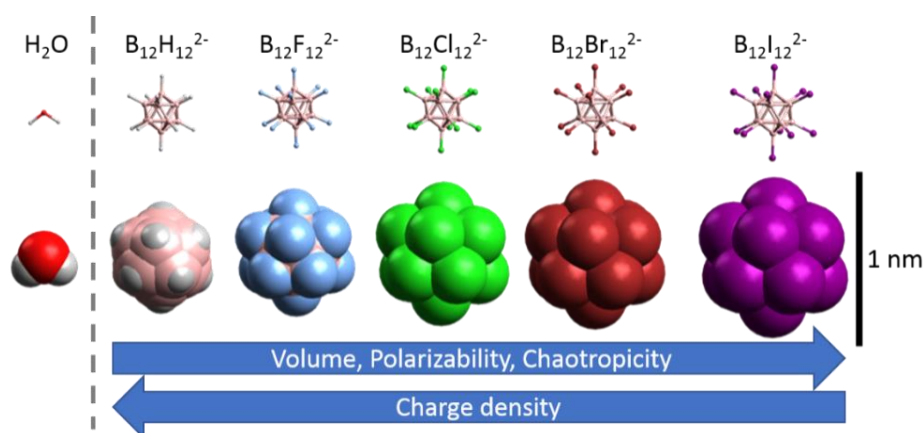
To set the thermodynamic parameters in section 2.3.4 into context, here an overview of all thermodynamic considerations of nano-ion binding to  $\gamma$ -cyclodextrin ( $\gamma$ -CD) is given in comparison to the adsorption of  $\text{SiW}_{12}\text{O}_{40}^{4-}$  to  $\text{C}_8\text{E}_4$ -micelles, see Table 10. As mentioned in the main text, the driving force seems to be rather weak for the binding to  $\text{C}_8\text{E}_4$ -micelles in comparison to the binding of nano-ions to  $\gamma$ -CD.

Table 10: Published Gibbs free energies, Entropies and Enthalpies with association constants for  $\gamma$ -CD/nano-ion association in water at 298 K in comparison to the thermodynamic signature of  $\text{SiW}_{12}\text{O}_{40}^{4-}$  adsorbing to  $\text{C}_8\text{E}_4$ -micelles. The equilibrium constant  $K$  has no unit in the Henry isotherm for SiW on the micelles and has the unit [l/mol] in the  $\gamma$ -CD-binding models.

Authors	Method	Guest	Host	Complex model	$K$ * $10^3$	$\Delta H$ [kJ/mol]	$T\Delta S$ [kJ/mol]	$\Delta G$ [kJ/mol]
Herein	SAXS/SANS	$[\text{SiW}_{12}\text{O}_{40}]^{4-}$	$\text{C}_8\text{E}_4$ -micelle	Henry isotherm	0.0017	-37.2	-35.9	-1.3
Cadot 2020 <sup>161</sup>	ITC	$[\text{H}_2\text{W}_{12}\text{O}_{40}]^{6-}$	$\gamma$ -CD	-	-	-	-	-
Cadot 2020 <sup>161</sup>	ITC	$[\text{BW}_{12}\text{O}_{40}]^{5-}$	$\gamma$ -CD	1:1	1.03	-53.5	-36.3	-17.2
Cadot 2020 <sup>161</sup>	ITC	$[\text{SiW}_{12}\text{O}_{40}]^{4-}$	$\gamma$ -CD	1:1	1.72	-56.4	-32.3	-24.2
Cadot 2020 <sup>161</sup>	ITC	$[\text{SiW}_{12}\text{O}_{40}]^{4-}$	$\gamma$ -CD	1:2	0.46	-55	-39.8	-15.2
Cadot 2020 <sup>161</sup>	ITC	$[\text{PW}_{12}\text{O}_{40}]^{3-}$	$\gamma$ -CD	1:1	2.92	-35.1	-15.3	-19.8
Nau 2015 <sup>3</sup>	NMR-tit	$\text{B}_{12}\text{H}_{11}\text{OH}^{2-}$	$\gamma$ -CD	1:1	0.62			-15.9
Nau 2015 <sup>3</sup>	NMR-tit	$\text{B}_{12}\text{H}_{11}\text{N}(\text{nPr})_3^{2-}$	$\gamma$ -CD	1:1	1.1			-17.4
Nau 2015 <sup>3</sup>	NMR-tit	$\text{B}_{12}\text{H}_{11}\text{NH}_3^{2-}$	$\gamma$ -CD	1:1	1.7			-18.4
Nau 2015 <sup>3</sup>	NMR-tit	$\text{B}_{12}\text{H}_{12}^{2-}$	$\gamma$ -CD	1:1	2			-18.8
Nau 2015 <sup>3</sup>	NMR-tit <sup>[b]</sup> , ITC <sup>[c]</sup>	$\text{B}_{12}\text{H}_{11}\text{SH}^{2-}$	$\gamma$ -CD	1:1	7.8 <sup>[b]</sup> , 9.2 <sup>[c]</sup>	-23.8	-1.3	-22.6
Nau 2015 <sup>3</sup>	ITC	$\text{B}_{12}\text{Cl}_{12}^{2-}$	$\gamma$ -CD	1:1	17	-60.2	-36.0	-24.3
Nau 2015 <sup>3</sup>	ITC	$\text{B}_{12}\text{Br}_{12}^{2-}$	$\gamma$ -CD	1:1	960	-89.5	-55.6	-33.9
Nau 2015 <sup>3</sup>	ITC	$\text{B}_{12}\text{I}_{12}^{2-}$	$\gamma$ -CD	1:1	67	-104.6	-77.0	-27.6
Nau 2015 <sup>3</sup>	ITC	$\text{B}_{12}\text{I}_{11}\text{NH}_3^{2-}$	$\gamma$ -CD	1:1	25			-25.1
Nau 2019 <sup>67</sup>	ITC	$\text{COSAN}^-$	$\gamma$ -CD	1:1	191	-32.2	-1.7	-30.5

## 2.4. Dodecaborates in $C_8E_4$

Dodecaborates are nanometer-sized, icosahedral, anionic borate clusters of the type  $B_{12}X_{12}^{2-}$  with  $X=H, F, Cl, Br, I$ . Due to their high boron content and inertness, such borate clusters find most relevance in medicine in boron neutron capture therapy as a part of cancer treatment.<sup>44,45</sup> Though chemically distinct, these dodecaborate ions share meaningful characteristics with the previously examined Keggin-POMs, that is, delocalized charge, low charge density and nanometric size. Dodecaborates provide an ideal model system to investigate the effect of the size of an ion on its physicochemical properties in solution because they are all chemically exceptionally stable, inert and carry the same charge of -2, while from  $B_{12}H_{12}^{2-}$  to  $B_{12}I_{12}^{2-}$  the size of the dodecaborates increases significantly. As a consequence, their charge densities and the polarizabilities differ systematically, see Scheme 3. Set into scale, their charge densities range from  $B_{12}H_{12}^{2-}$  with a charge density similar to a classical chaotrope (e.g.  $SCN^-$ ) to  $B_{12}I_{12}^{2-}$  with a much lower charge density than the superchaotropic Keggin-POM  $SiW_{12}O_{40}^{4-}$ , see Table 11. Owing to their peculiar physical properties (low charge density, high polarizability), dodecaborates are expected to have strong chaotropic or hydrophobic characters, where the smallest and presumably least chaotropic dodecaborate  $B_{12}H_{12}^{2-}$  was found to adsorb weakly to the air-water interface at  $[B_{12}H_{12}^{2-}] > 1$  M, evidence of a faint hydrophobic nature.<sup>54</sup> Furthermore, dodecaborates were classified as superchaotropic ions as they were found to bind to the hydrophobic cavities of common host-molecules, i.e. cyclodextrins, with unexpectedly high affinities, much higher than other ionic species with thermodynamic signatures reminiscent of classical chaotropic ions, such as  $SCN^-$ .<sup>3</sup> Additionally, dodecaborates were found to interact non-specifically, yet strongly with proteins attributed to hydrophobic interactions.<sup>69-71</sup>



Scheme 3: Ball and stick, and van-der-Waals sphere presentations from smallest to largest for the dodecaborates  $B_{12}H_{12}^{2-}$ ,  $B_{12}F_{12}^{2-}$ ,  $B_{12}Cl_{12}^{2-}$ ,  $B_{12}Br_{12}^{2-}$  and  $B_{12}I_{12}^{2-}$ . For reference, the dodecaborates are juxtaposed with a  $H_2O$ -molecule. With increasing molecular volume, the polarizability and the chaotropy of the dodecaborates is expected to increase, while the volume charge density decreases.

Table 11: Volumes, charges and charge densities of the used dodecaborates  $B_{12}X_{12}^{2-}$  with  $X = H, F, Cl, Br, I$  in comparison to the superchaotropic  $PW_{12}O_{40}^{3-}$  and the classical chaotrope  $SCN^-$ .

	Charge $q_e$	Ionic volume [ $nm^3$ ]	Charge density [ $q_e/nm^3$ ]
$B_{12}I_{12}^{2-}$	2	$0.52^1$	3.9
$B_{12}Br_{12}^{2-}$	2	$0.42^1$	4.8
$B_{12}Cl_{12}^{2-}$	2	$0.33^1$	6.0
$SiW_{12}O_{40}^{4-}$	4	$0.46^2$	8.7
$B_{12}F_{12}^{2-}$	2	$0.18^1$	11.0
$B_{12}H_{12}^{2-}$	2	$0.15^1$	13.2
$SCN^-$	1	$0.07^3$	14.1

<sup>1</sup> Taken from Nau et al.<sup>65</sup>

<sup>2</sup> Taken from Buchecker et al.<sup>92</sup>

<sup>3</sup> Taken from Marcus.<sup>91</sup>

Here, the dodecaborates are investigated as to their general driving force to interact with non-charged environments. To this end, the non-ionic surfactant  $C_8E_4$  and its micelles are used as a probe to pinpoint the effects of these superchaotropic ions. Providing a non-ionic polar (hydrated) interface at the hydrophilic ethoxylated headgroups and a hydrophobic core of the aliphatic  $C_8$ -tail,  $C_8E_4$ -micelles are an ideal and sensitive model system to reveal the preferable interactions of the dodecaborates. In a first step, the cloud point (CP) of 60 mM  $C_8E_4$  was traced as a function of  $B_{12}X_{12}^{2-}$ -concentration, see Figure 29, to examine their impact on the intermicellar interactions.

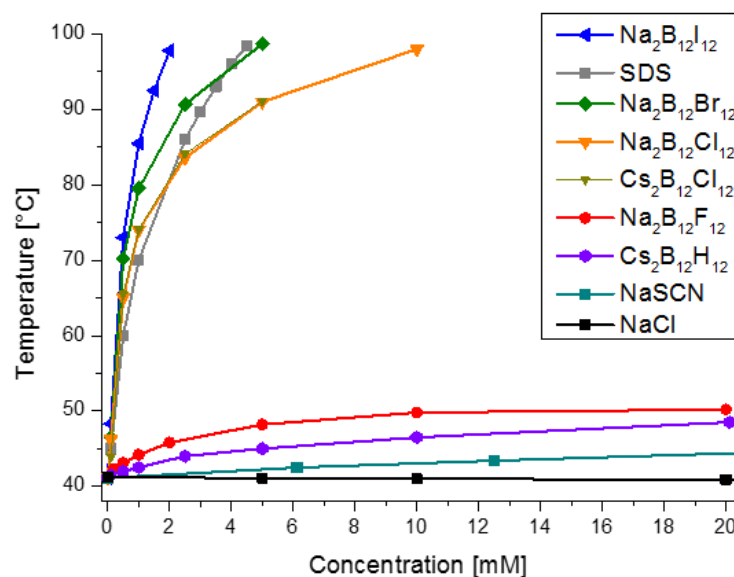


Figure 29: Cloud point evolution of 60 mM  $C_8E_4$  as a function of dodecaborate concentration, NaCl, NaSCN and SDS are added as references. The lines are guides to the eye. For  $Na_2B_{12}I_{12}$  and  $Na_2B_{12}Br_{12}$ , opalescent phases occurred before the cloud point, which will be discussed later and are shown in Figure 36.

Upon addition of the dodecaborates in the millimolar range, the CP of 60 mM  $C_8E_4$  is increased to widely varying extents. Addition of  $B_{12}H_{12}^{2-}$  caused a rather mild CP-increase, while the

heavier analogues  $B_{12}F_{12}^{2-}$ ,  $B_{12}Cl_{12}^{2-}$ ,  $B_{12}Br_{12}^{2-}$  and  $B_{12}I_{12}^{2-}$  exhibited more pronounced effects with increasing size. Ordering the respective shifts of the CP results in a homogeneous series from the smallest to the largest dodecaborate corresponding precisely to their inverse ordering by charge density in Table 11. In comparison with the references,  $B_{12}H_{12}^{2-}$  exceeded merely the classical chaotropic ion  $SCN^-$ , while the largest (lowest charge density) dodecaborates, that is  $B_{12}Br_{12}^{2-}$  and  $B_{12}I_{12}^{2-}$ , even exceeded the effect of the ionic surfactant SDS. The tremendous CP-increase can be attributed to a charging of micelles arising from a strong interaction of the dodecaborate species with the micelles. Here, the iodo- and bromo-dodecaborate are even more efficient than SDS at introducing charges to the micelles, hinting at close to complete partition towards the micelles for  $B_{12}Br_{12}^{2-}$  and  $B_{12}I_{12}^{2-}$ , while for the other dodecaborates ( $B_{12}Cl_{12}^{2-}$ ,  $B_{12}F_{12}^{2-}$ ,  $B_{12}H_{12}^{2-}$ ) the interactions seem to be weaker. Overall, the dodecaborates exhibit varying affinities towards the  $C_8E_4$ -micelles, which seem to be modulated by their sizes and respective charge densities: The lower the charge density, the stronger the cloud point increase, the stronger the interaction with the micelle and the more chaotropic (or possibly also hydrophobic) the dodecaborate. Note that the same trend holds for POMs as pointed out by Buchecker et al. and further corroborated in the previous chapter. Furthermore, it is shown that changing the cation of  $B_{12}Cl_{12}^{2-}$  from  $Na^+$  to  $Cs^+$  has no effect on the CP-evolution, which is expected as dodecaborates are known to be weakly coordinating ions that prohibit counter-ion binding. Merely, a difference in solubility was observed as the Cs-form is insoluble at  $[Cs_2B_{12}Cl_{12}] > 5$  mM, whereas the Na-form remains soluble up to concentrations higher than 100 mM.

To further evidence the interaction of the dodecaborates with the  $C_8E_4$ -micelles on the microscopic level, SAXS was used. As the intensity in SAXS scales with the electron density per scatterer, the lighter dodecaborate analogues  $B_{12}H_{12}^{2-}$ ,  $B_{12}F_{12}^{2-}$  and  $B_{12}Cl_{12}^{2-}$  did not produce any excess scattering in water and only the heaviest dodecaborates  $B_{12}Br_{12}^{2-}$  and  $B_{12}I_{12}^{2-}$  offer satisfactory signals on the SAXS-setup at the ICSM. The corresponding spectra are shown in Figure 30.



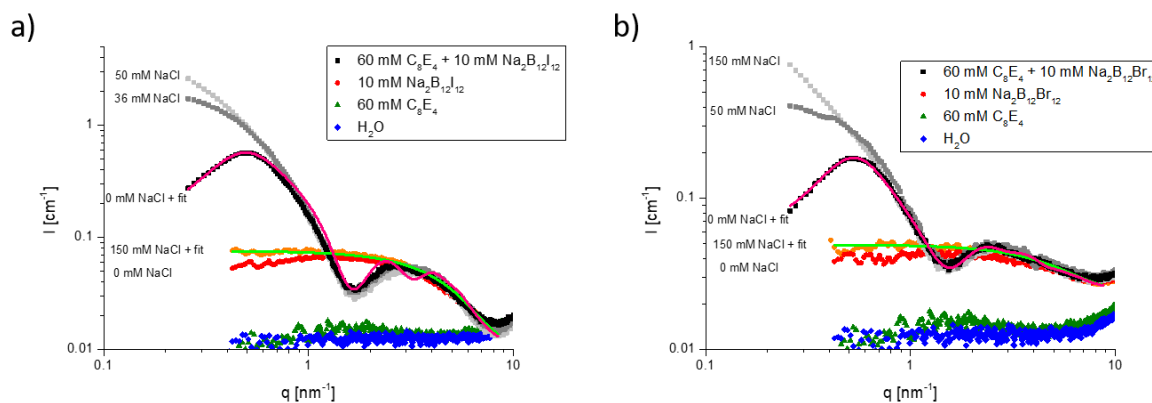


Figure 30: SAXS-spectra of 60 mM  $C_8E_4$  in the presence of a) 10 mM  $NaB_{12}I_{12}$  and b) 10 mM  $Na_2B_{12}Br_{12}$  in absence and presence of the electrolyte NaCl. As references, scattering contributions of water, the surfactant  $C_8E_4$  and the respective dodecaborate in water are shown. The spectra are in absolute scale. The red and green lines are fits respectively using a spherical form factor for the dodecaborates in water and a spherical core-shell form factor for the corresponding dodecaborate in 60 mM  $C_8E_4$ . Corresponding fit parameters are listed in section 2.9.

The SAXS-spectra reveal that the dodecaborates  $B_{12}I_{12}^{2-}$  and  $B_{12}Br_{12}^{2-}$ , respectively at 10 mM in water, produce the classical scattering pattern of spherical scattering objects, which show a slight positive slope at low  $q$  indicative of a structure factor contribution that arises from repulsive Coulomb interactions between the individual dodecaborates. Addition of a screening salt (150 mM NaCl) suppressed the structure factor causing a constant intensity plateau at low  $q$  and fitting (green lines) with spherical form factors resulted in radii of 0.45 nm for  $B_{12}I_{12}^{2-}$  and 0.40 nm for  $B_{12}Br_{12}^{2-}$  in close agreement with simulations by Nau et al.<sup>3</sup> Upon addition of 60 mM  $C_8E_4$  (no scattering in bare water, see green triangles) to 10 mM of either dodecaborate in water, large oscillations appeared giving rise to a core-shell pattern for  $B_{12}I_{12}^{2-}$  as well as  $B_{12}Br_{12}^{2-}$ , which is similar to the preceding sections concerning the POMs (section 2.3). This scattering pattern is characteristic to decorated micelles and evidences directly the strong interaction of these two dodecaborates with the  $C_8E_4$ -micelles. Additionally, the steep positive slopes before the peak at  $q=0.5 \text{ nm}^{-1}$  indicate strong intermicellar repulsion, which arises due to a charging by the dodecaborate ions. Fitting (red curves in Figure 30) was performed on the spectra using spherical core-shell form factors coupled with Hayter-MSA structure factors revealing 6.6 and 5.7 dodecaborates per  $C_8E_4$ -micelle for  $B_{12}I_{12}^{2-}$  and  $B_{12}Br_{12}^{2-}$ , respectively, corresponding to a partition of 78% or 67% towards the micelles. It must be stated that these SAXS-fits exhibit a large window of error, which is why in the previous sections corresponding SANS-spectra were used to make for a more robust collective fitting procedure. Here, auxiliary SANS was unavailable. Furthermore, for  $B_{12}I_{12}^{2-}$  (Figure 30a) an additional artificial minimum arose in the fit at  $q=0.35 \text{ nm}^{-1}$  showing the lacking quality of the fit. Nevertheless, these fits provide insightful feedback on the strong propensity of the dodecaborates to partition to the

$C_8E_4$ -micelles. Further, upon addition of NaCl the structure factor contribution disappeared and the intensity at low  $q$  strongly increased, which hints at micellar growth upon screening of the intermicellar interactions. To showcase the effects of NaCl more systematically, CP-measurements of 60 mM  $C_8E_4$  + 1 mM  $B_{12}X_{12}^{2-}$  as a function of NaCl were performed. The corresponding CP-evolutions are shown in Figure 31. As a reference, the equivalent measurements for bare 60 mM  $C_8E_4$  (no additive curve) and 60 mM  $C_8E_4$ /1 mM SDS are also shown.

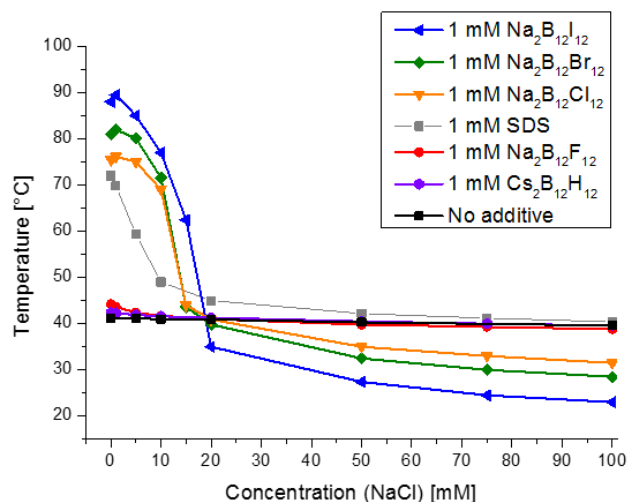


Figure 31: Cloud point evolution of 60 mM  $C_8E_4$  at 1 mM of each dodecaborate, respectively as a function of NaCl-concentration. The lines are guides to the eye. For the chlorinated, brominated, and iodinated dodecaborate opalescent phases occurred before the cloud point, which will be discussed in Figure 36.

Thus, with 1 mM  $B_{12}X_{12}^{2-}$  upon addition of NaCl, the CP drops with varying extents depending on the dodecaborate and inverts from



at low salt contents,  $[NaCl] < 10$  mM, to



at high salt contents,  $[NaCl] > 20$  mM. In all cases, the effect of adding NaCl was more pronounced in the presence of an additive (SDS or  $B_{12}X_{12}^{2-}$ ) than on bare  $C_8E_4$ -micelles (no additive curve). More specifically, the stronger the induced CP-increase at 0 mM NaCl for the respective  $B_{12}X_{12}^{2-}$ , the stronger is the CP-drop upon adding NaCl falling even far below the no-additive curve at high NaCl-concentrations. This drop of the CP below the no-additive curve that appears in the presence of  $B_{12}Cl_{12}^{2-}$ ,  $B_{12}Br_{12}^{2-}$  and  $B_{12}I_{12}^{2-}$  indicates that the micelles have become more hydrophobic than the micelles of bare 60 mM  $C_8E_4$ . In the previous chapter concerning the Keggin-POM SiW, this observation was assigned to a dehydration of the micelles upon adsorption of the superchaotrope, which might also provide an explanation here

regarding the dodecaborates. Thus,  $B_{12}I_{12}^{2-}$  is the most efficient at dehydrating the micelle, followed by  $B_{12}Br_{12}^{2-}$  and  $B_{12}Cl_{12}^{2-}$  according to their ordering of charge densities, see Table 9. The effect of NaCl was then further quantified using SANS for samples containing 60 mM  $C_8E_4$  + 1 mM  $B_{12}Cl_{12}^{2-}$  or 1 mM  $B_{12}Br_{12}^{2-}$  in  $D_2O$  in the presence of NaCl, see Figure 32. Owing to the high contrast between deuterium and hydrogen, the spectra are respectively dominated by the hydrogenated  $C_8E_4$ -micelles (in  $D_2O$ ), while millimolar concentrations of the two dodecaborates exhibit weaker contrasts, cause negligible scattering and are not visible in the spectra. Mathematical fits using ellipsoid form factors coupled with Hayter-MSA structure factors proved to coincide well with the data and provided insight into the micellar dimensions.

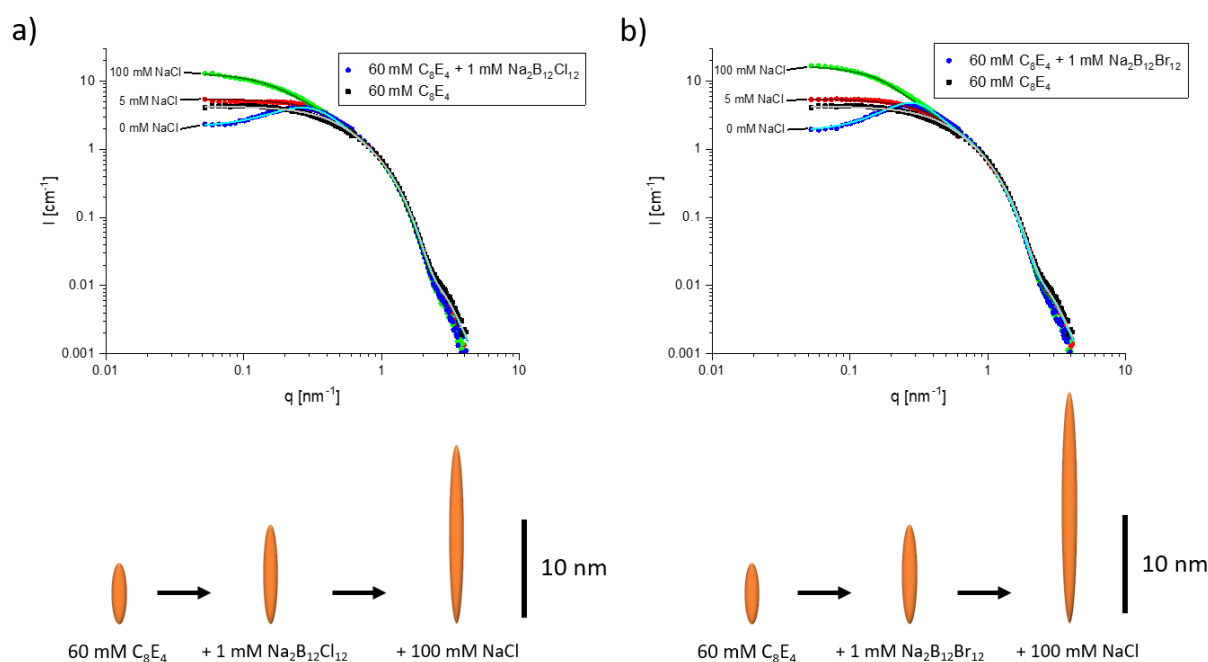


Figure 32: SANS of 60 mM  $C_8E_4$  at a) 1 mM  $Na_2B_{12}Br_{12}$  and b) 1 mM  $Na_2B_{12}Cl_{12}$  at different NaCl-concentrations in  $D_2O$  at 20°C. The lines are theoretical fits using ellipsoid models. Additionally, the growth of the prolate ellipsoidal  $C_8E_4$ -micelles as obtained from fitting is shown with the schemes. The spectra are in absolute scale and were measured at MLZ. Corresponding fit parameters are listed in section 2.9.

The SANS-spectra show that the micelles of 60 mM  $C_8E_4$  exhibit a structure factor peak in the presence of 1 mM  $B_{12}X_{12}^{2-}$  owing to the emergent intermicellar repulsion upon their adsorption, while the shape characteristic steep negative slope at high  $q$  remains unchanged. Addition of NaCl to these repulsive micelles only affected the low  $q$ -region in the spectra as the structure factor peak disappeared already at 5 mM NaCl, while at 100 mM NaCl the scattered intensity at low  $q$  is increased. These two observations can be unambiguously assigned to a screening of the intermicellar repulsion and a growth of the micelles upon addition of NaCl and is in line with the observed CP-drop in Figure 31. Qualitatively, the decorated micelles for 1 mM  $B_{12}Cl_{12}^{2-}$  or  $B_{12}Br_{12}^{2-}$ , show identical responses to NaCl-addition and only slight quantitative differences between the two systems were observed, which became most apparent in the

micellar parameters obtained from the fits. Thus, the ellipsoidal micelles were found to grow in the polar dimension (their length) from a polar radius of 6 nm for bare C<sub>8</sub>E<sub>4</sub>-micelles to 9.5 nm at 1 mM B<sub>12</sub>Cl<sub>12</sub><sup>2-</sup> or 10.2 nm at 1 mM B<sub>12</sub>Br<sub>12</sub><sup>2-</sup>, and addition of 100 mM NaCl caused a respective elongation to polar radii of 17 nm (B<sub>12</sub>Cl<sub>12</sub><sup>2-</sup>) and 22 nm (B<sub>12</sub>Br<sub>12</sub><sup>2-</sup>). An additional experiment was performed with 1 mM B<sub>12</sub>I<sub>12</sub><sup>2-</sup> at 5 mM NaCl, see Figure 38 in the addendum on page 84. Overall, a systematic order was observed: The larger the dodecaborate, the stronger the elongation of the micelle. B<sub>12</sub>I<sub>12</sub><sup>2-</sup> causes the most pronounced elongation followed by B<sub>12</sub>Br<sub>12</sub><sup>2-</sup> and B<sub>12</sub>Cl<sub>12</sub><sup>2-</sup>. This rule seems to hold universally in electrolyte-free as well as in NaCl-containing solution. The latter case is in direct correlation to the CP-decrease upon NaCl-addition and shows that the micelles become longer, presumably due to a dehydration of the micellar head groups in the presence of the dodecaborates. However, the micellar elongation of the C<sub>8</sub>E<sub>4</sub>-micelles upon simply adding B<sub>12</sub>X<sub>12</sub><sup>2-</sup> shows that the micelles become more hydrophobic regardless of the strongly increased CP. This reveals the dual nature of the partition of the superchaotropic (hydrophobic) dodecaborates to the micelles: The charges that are brought to the micelles by the adsorbing ions stabilize strongly the micellar phase, while the individual micelles become more hydrophobic presumably due to a dehydration of the surfactant head groups. Notably, the argument of dehydration was used previously in the chapter concerning the Keggin-POM SiW<sub>12</sub>O<sub>40</sub><sup>4-</sup> (section 2.3), where it was proven that SiW<sub>12</sub>O<sub>40</sub><sup>4-</sup> adsorbs to the micelles without interaction with the micellar core. The same argument is compelling here. However, it seems as if the dodecaborates penetrate into the hydrophobic core of the C<sub>8</sub>E<sub>4</sub>-micelles, which causes an elongation and possibly a disruption of the micelles at elevated dodecaborate concentrations. Such a mechanism, generic to hydrophobic ions<sup>34,35</sup>, would explain the observed micellar growth and would clearly evidence the conjectured hydrophobic nature of the dodecaborates. For this purpose, the lowest charge density (and presumably most hydrophobic) dodecaborate B<sub>12</sub>I<sub>12</sub><sup>2-</sup> was examined as to its concentration-dependent effects on the micelles of 60 mM C<sub>8</sub>E<sub>4</sub> using SAXS. The corresponding spectra are shown in Figure 33b along with the spectra of B<sub>12</sub>I<sub>12</sub><sup>2-</sup> in bare water in Figure 33a. Notably, indeed B<sub>12</sub>I<sub>12</sub><sup>2-</sup> was found to cause precipitation of the micellar phase at [B<sub>12</sub>I<sub>12</sub><sup>2-</sup>]<sup>2-</sup>>60 mM and is therefore only measured in SAXS at inferior concentrations.

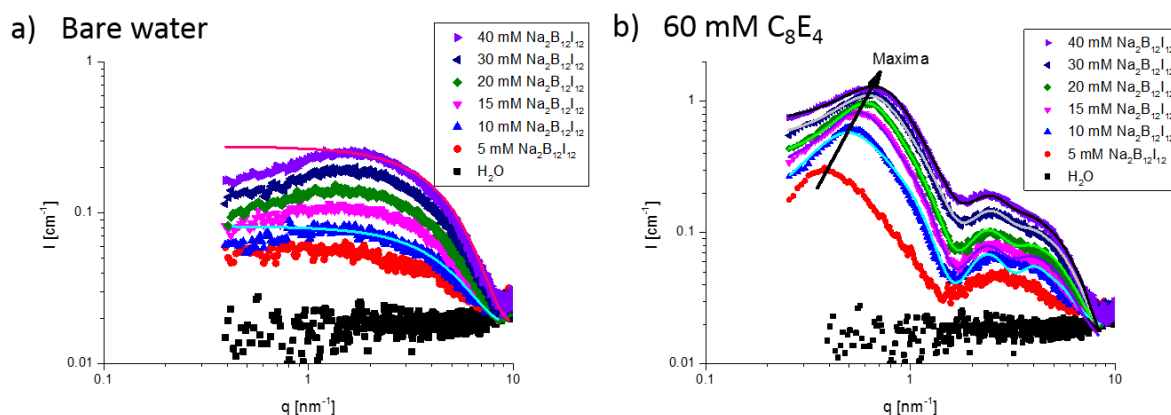


Figure 33: SAXS-spectra of  $\text{Na}_2\text{B}_{12}\text{I}_{12}$  at increasing concentrations at  $20^\circ\text{C}$  in a) bare water and b) 60 mM  $\text{C}_8\text{E}_4$  in water. The full lines in a) are spherical form factor fits to the experimental spectra of 10 mM and 40 mM  $\text{Na}_2\text{B}_{12}\text{I}_{12}$ . The full lines in b) are spherical core-shell form factor fits. The spectra are in absolute scale. The corresponding fit parameters are listed in section 2.9.

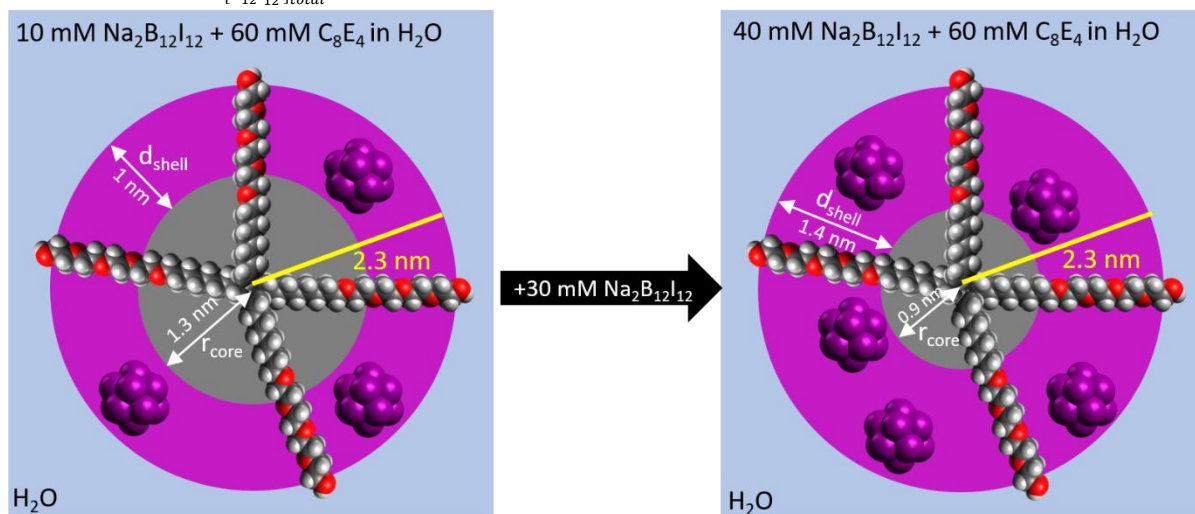
With increasing  $\text{B}_{12}\text{I}_{12}^{2-}$ -concentration the scattered intensity increases in bare water as well as in the presence of 60 mM  $\text{C}_8\text{E}_4$ .  $\text{B}_{12}\text{I}_{12}^{2-}$  in bare water produces at all used concentrations the scattering of individually dispersed, electrostatically repelling spheres with a universal radius of 0.45 nm as exemplified with spherical form factor fits at 10 mM and 40 mM  $\text{Na}_2\text{B}_{12}\text{I}_{12}$  (see Figure 33a, red and blue line). The Coulomb repulsion between the dodecaborates, indicated by the increased slope at low  $q$  before the intensity maximum, could not be modelled with an adequate electrostatic model as the used concentrations were too low. Furthermore, in the presence of 60 mM  $\text{C}_8\text{E}_4$ , at all concentrations the core-shell pattern characteristic to  $\text{B}_{12}\text{I}_{12}^{2-}$ -decorated micelles is observed (Figure 33b). These core-shell patterns were fitted with a simplified model as corresponding SANS-spectra, which would clarify micellar number densities and dimensions, were unavailable. Thus, in this SAXS-fitting procedure the number of micelles was held constant and spherical micellar geometry was assumed. This method provided satisfactory fits only at  $[\text{B}_{12}\text{I}_{12}^{2-}] > 10$  mM, while at lower  $\text{B}_{12}\text{I}_{12}^{2-}$ -concentrations the micelles are of ellipsoidal shape prohibiting fitting with spherical form factors. Using this procedure the number of  $\text{B}_{12}\text{I}_{12}^{2-}$ -molecules per micelle can be obtained by analysis of the obtained shell contrast along with the dimensions of the corresponding core-shell micelles, see Table 12 and Scheme 4. It must be stated that, at  $[\text{Na}_2\text{B}_{12}\text{I}_{12}] \geq 20$  mM, classical spherical form factors (without shell) provided equally good fits of the  $\text{C}_8\text{E}_4/\text{B}_{12}\text{I}_{12}^{2-}$ -micelles. Contrast analysis, however, resulted in identical  $\text{B}_{12}\text{I}_{12}^{2-}$ -numbers per micelle like with the core-shell form factors. For the sake of integrity, core shell form factors were used at all concentrations. A list of all corresponding fitting parameters is given in section 2.9 and the fitting procedure is elaborated in section 7.3.2.

Table 12: Micellar parameters acquired from the fits of the SAXS-spectra of 60 mM C<sub>8</sub>E<sub>4</sub> at different concentrations of Na<sub>2</sub>B<sub>12</sub>I<sub>12</sub> including form factor dimensions, B<sub>12</sub>I<sub>12</sub><sup>2-</sup>-adsorption numbers and ratios.

Sample composition	Form factor shape	Core-Shell dimensions		From contrast analysis	
		inner radius r [nm]	shell thickness d [nm]	B <sub>12</sub> I <sub>12</sub> <sup>2-</sup> - per micelle	B <sub>12</sub> I <sub>12</sub> <sup>2-</sup> - adsorption ratio <sup>1</sup> , R
60 mM C <sub>8</sub> E <sub>4</sub> + 10 mM Na <sub>2</sub> B <sub>12</sub> I <sub>12</sub>	Core-Shell-sphere	1.3	1.1	6.65	0.78
60 mM C <sub>8</sub> E <sub>4</sub> + 15 mM Na <sub>2</sub> B <sub>12</sub> I <sub>12</sub>	Core-Shell-sphere	1.1	1.3	8.41	0.65
60 mM C <sub>8</sub> E <sub>4</sub> + 20 mM Na <sub>2</sub> B <sub>12</sub> I <sub>12</sub>	Core-Shell-sphere	1.1	1.25	8.85	0.52
60 mM C <sub>8</sub> E <sub>4</sub> + 30 mM Na <sub>2</sub> B <sub>12</sub> I <sub>12</sub>	Core-Shell-sphere	1	1.3	10.02	0.39
60 mM C <sub>8</sub> E <sub>4</sub> + 40 mM Na <sub>2</sub> B <sub>12</sub> I <sub>12</sub>	Core-Shell-sphere	0.9	1.4	10.96	0.32
60 mM C <sub>8</sub> E <sub>4</sub> + 60 mM Na <sub>2</sub> B <sub>12</sub> I <sub>12</sub>	Core-Shell-sphere				

**Precipitation**

$$^1\text{adsorption ratio } R = \frac{[B_{12}I_{12}^{2-}]_{\text{adsorbed}}}{[B_{12}I_{12}^{2-}]_{\text{total}}}$$



Scheme 4: Cross-sections of B<sub>12</sub>I<sub>12</sub><sup>2-</sup>-decorated C<sub>8</sub>E<sub>4</sub>-micelles with core-shell patterns in SAXS for 60 mM C<sub>8</sub>E<sub>4</sub> at 10 mM Na<sub>2</sub>B<sub>12</sub>I<sub>12</sub> and 40 mM Na<sub>2</sub>B<sub>12</sub>I<sub>12</sub>, respectively. Van der Waals representations of C<sub>8</sub>E<sub>4</sub> and B<sub>12</sub>I<sub>12</sub><sup>2-</sup> are up to scale.

With increasing Na<sub>2</sub>B<sub>12</sub>I<sub>12</sub>-concentration, the shell was found to become thicker accompanied by a steadily increasing number of adsorbed B<sub>12</sub>I<sub>12</sub><sup>2-</sup>-molecules per micelle. In return, the core of the core-shell object shrinks from 1.3 nm at [Na<sub>2</sub>B<sub>12</sub>I<sub>12</sub>]= 10 mM to 0.9 nm at [Na<sub>2</sub>B<sub>12</sub>I<sub>12</sub>]= 40 mM, where the core radius is even smaller than the extended length of the hydrophobic C<sub>8</sub>H<sub>17</sub>-tail ( $l(\text{C}_8\text{H}_{17})=1.1$  nm). Therefore, the B<sub>12</sub>I<sub>12</sub><sup>2-</sup>-molecules seem to interact partially with the hydrophobic micellar core. However, regardless of the B<sub>12</sub>I<sub>12</sub><sup>2-</sup>-concentration, the overall size ( $r_{\text{core}}+d_{\text{shell}}$ ) of the micelles remained constant at 2.3 nm, which corresponds very well to the extended length of a C<sub>8</sub>E<sub>4</sub>-molecule (2.6 nm). This suggests that the micellar size is limited by the surfactant length. Yet, as more B<sub>12</sub>I<sub>12</sub><sup>2-</sup> loads the micelle, surfactant molecules need to be released presumably leading to an increase in the number of micelles. Regarding the affinity of B<sub>12</sub>I<sub>12</sub><sup>2-</sup> to the C<sub>8</sub>E<sub>4</sub>-micelles, at 10 mM of B<sub>12</sub>I<sub>12</sub><sup>2-</sup> 78% of all dodecaborate molecules are found on the micelles as indicated by an adsorption ratio  $R=0.78$ . Further addition of Na<sub>2</sub>B<sub>12</sub>I<sub>12</sub> causes a decrease in this ratio as the micelles become more saturated and the dodecaborate is

forced into the bulk. By using the same experimental approach, it was shown that the adsorption of the Keggin-POM  $\text{SiW}_{12}\text{O}_{40}^{4-}$  to  $\text{C}_8\text{E}_4$ -micelles can be rationalized by a Langmuir adsorption isotherm, see section 2.3.2.

Here, the behaviors of the two nano-ions  $\text{B}_{12}\text{I}_{12}^{2-}$  and  $\text{SiW}_{12}\text{O}_{40}^{4-}$  are compared using the respective numbers of nano-ion per micelle to evaluate the respective strength of interaction as a function of nano-ion concentration, see Figure 34.

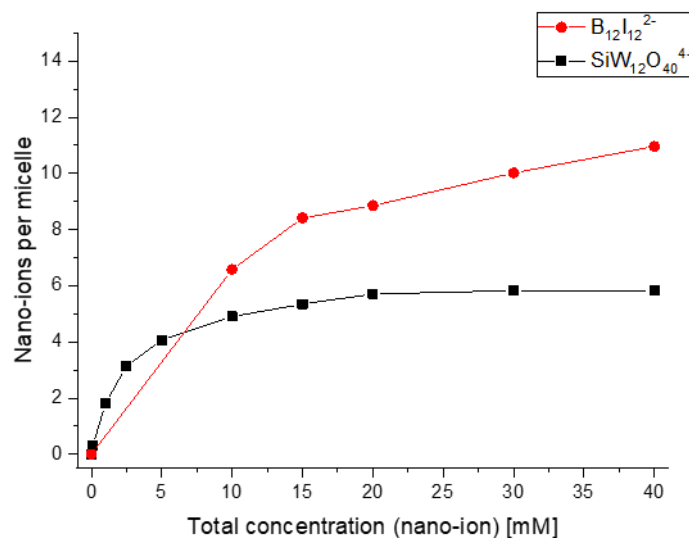


Figure 34: Plot of the number of adsorbed nano-ions per micelle as a function of total nano-ion concentration. The lines are guides to the eye.

Thus, a significantly stronger affinity towards the  $\text{C}_8\text{E}_4$ -micelles is observed for  $\text{B}_{12}\text{I}_{12}^{2-}$  in comparison to  $\text{SiW}_{12}\text{O}_{40}^{4-}$  displayed by the number of adsorbed nano-ions per micelle consistently at all concentrations. Notably, in section 2.3.2, the behavior of  $\text{SiW}_{12}\text{O}_{40}^{4-}$  could be well described using a Langmuir adsorption isotherm. Here, using such a model seems inappropriate because the number of  $\text{B}_{12}\text{I}_{12}^{2-}$  per micelle continues to increase without showing saturation. Therefore, the interaction of  $\text{B}_{12}\text{I}_{12}^{2-}$  with the  $\text{C}_8\text{E}_4$ -micelles does not follow a simple adsorption model. Rather,  $\text{B}_{12}\text{I}_{12}^{2-}$  seems to adsorb to the micelle exterior as well as penetrate deeply in between the surfactant molecules. Therefore,  $\text{B}_{12}\text{I}_{12}^{2-}$  behaves in a more hydrophobic way compared to the superchaotropic  $\text{SiW}_{12}\text{O}_{40}^{4-}$ . This trend can be expected when considering the respective volume charge densities of  $3.85 \text{ qe/nm}^3$  for  $\text{B}_{12}\text{I}_{12}^{2-}$  and  $8.7 \text{ qe/nm}^3$  for  $\text{SiW}_{12}\text{O}_{40}^{4-}$ , that is, the lower the charge per volume the more pronounced becomes the hydrophobic nature. Additionally, at  $[\text{B}_{12}\text{I}_{12}^{2-}] > 60 \text{ mM}$  precipitation of the  $\text{C}_8\text{E}_4$ -micellar phase was observed as would be expected for a hydrophobic (disruptive) ion.<sup>34</sup>

Furthermore, it was shown for decorated micelles of  $\text{SiW}_{12}\text{O}_{40}^{4-}/\text{C}_8\text{E}_4$  in section 2.3.4 that heating induces a significant desorption of the nano-ion from the micelles. This phenomenon seems again interesting for a comparison between  $\text{B}_{12}\text{I}_{12}^{2-}$  and  $\text{SiW}_{12}\text{O}_{40}^{4-}$ . To this end, SAXS-spectra were acquired at increasing temperatures for 60 mM  $\text{C}_8\text{E}_4$  + 10 mM  $\text{Na}_2\text{B}_{12}\text{I}_{12}$ , see Figure 35a and for the reproduced spectra with  $\text{H}_4\text{SiW}_{12}\text{O}_{40}$  see Figure 35b.

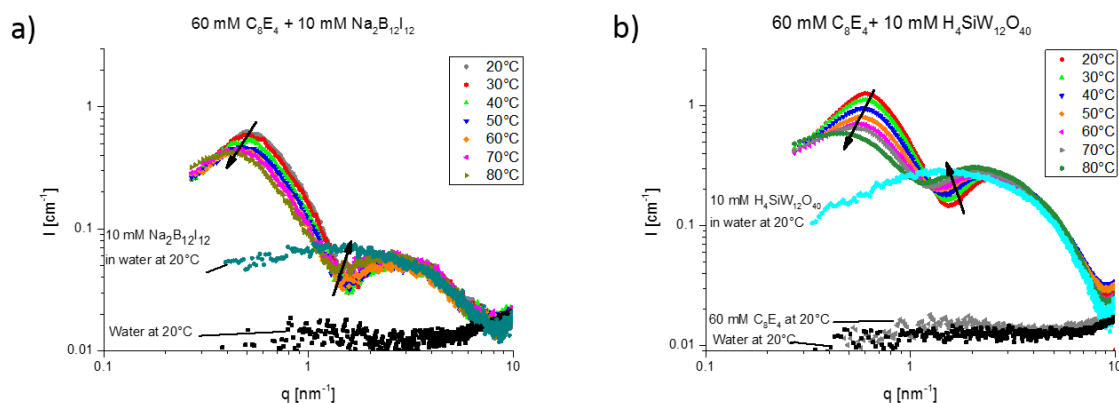


Figure 35: SAXS-spectra of 60 mM  $\text{C}_8\text{E}_4$  as a function of temperature with a) 10 mM  $\text{Na}_2\text{B}_{12}\text{I}_{12}$  and b) 10 mM  $\text{H}_4\text{SiW}_{12}\text{O}_{40}$ . The scattering contributions of the individual components  $\text{H}_2\text{O}$ , 60 mM  $\text{C}_8\text{E}_4$  and 10 mM of the respective nano-ion in water are shown as references. The spectra are in absolute scale.

For both nano-ions, the characteristic core-shell pattern of decorated micelles is observed to change upon heating, that is, the intensity at low  $q$  decreases, while the scattering of the individual nano-ions at high  $q$  remains constant. This trend hints at a desorption of both  $\text{B}_{12}\text{I}_{12}^{2-}$  and  $\text{SiW}_{12}\text{O}_{40}^{4-}$  from the micelles upon heating, which is quantitatively less pronounced for  $\text{B}_{12}\text{I}_{12}^{2-}$ . Therefore,  $\text{B}_{12}\text{I}_{12}^{2-}$  on the  $\text{C}_8\text{E}_4$ -micelles is more persistent and less heat-sensitive than  $\text{SiW}_{12}\text{O}_{40}^{4-}$  and the interaction of  $\text{B}_{12}\text{I}_{12}^{2-}$  with the  $\text{C}_8\text{E}_4$ -micelle is significantly stronger.

In line with the strong interaction,  $\text{B}_{12}\text{I}_{12}^{2-}$  also affected strongly the phase behavior of  $\text{C}_8\text{E}_4$  giving rise to a new bluish opalescent phase before the CP. Interestingly, the same observation was made with  $\text{B}_{12}\text{Br}_{12}^{2-}$  but not with the lighter analogue  $\text{B}_{12}\text{Cl}_{12}^{2-}$  (nor with  $\text{B}_{12}\text{F}_{12}^{2-}$  or  $\text{B}_{12}\text{H}_{12}^{2-}$ ), see Figure 36a-c. Additionally, in the presence of  $\text{NaCl}$  and 1 mM of the dodecaborates  $\text{B}_{12}\text{Cl}_{12}^{2-}$ ,  $\text{B}_{12}\text{Br}_{12}^{2-}$  and  $\text{B}_{12}\text{I}_{12}^{2-}$ , bluish phases preceded the appearance of the CPs, see Figure 36d-f. For the sake of simplicity, these bluish opalescent phases were omitted in the previous discussion of the cloud point evolutions and are considered here.



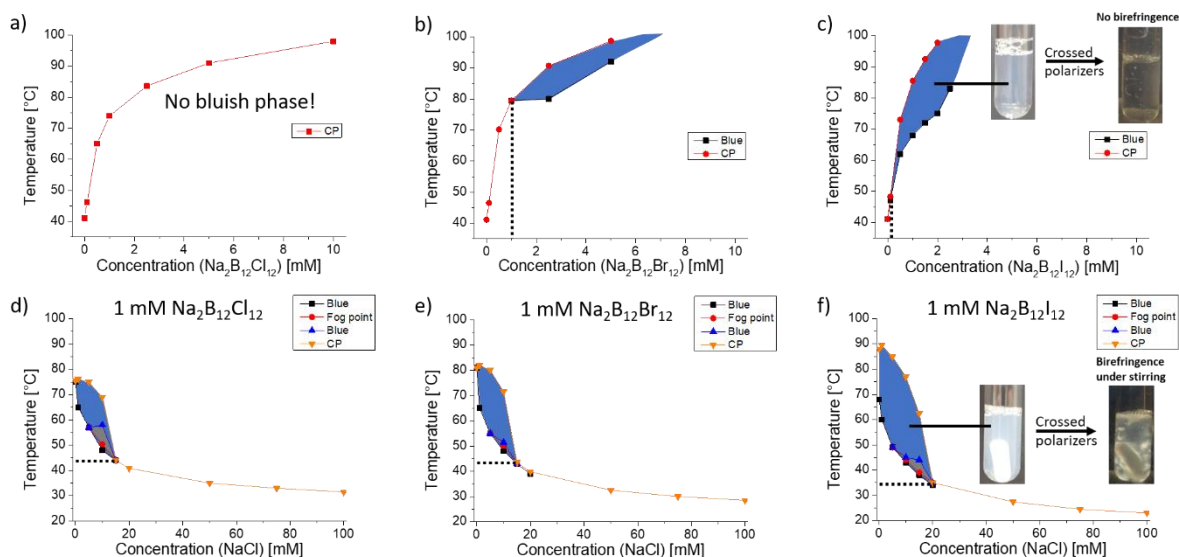


Figure 36: Phase behavior of 60 mM  $C_8E_4$  as a function of the concentration of a)  $Na_2B_{12}Cl_{12}$ , b)  $Na_2B_{12}Br_{12}$  and c)  $Na_2B_{12}I_{12}$  including the bluish opalescent phase regions. The pointed lines display the onset concentration of the bluish phase. Figures d-f) show the blue phases in the phase diagrams of 60 mM  $C_8E_4$  + 1 mM  $Na_2B_{12}X_{12}$  as a function of NaCl-concentration. The pointed lines indicate the minimum temperature of the bluish opalescent phase. Photos of bluish opalescent phases in front of a black backdrop (left photo) and between crossed polarizers (right photo) are additionally shown in figures c and f.

Thus, the CP of 60 mM  $C_8E_4$  is shifted to higher temperatures systematically by the ordering of charge densities of the dodecaborates  $B_{12}I_{12}^{2-} > B_{12}Br_{12}^{2-} > B_{12}Cl_{12}^{2-}$ , see Figure 36a-c and as previously discussed. The appearance of the bluish opalescent phases interestingly follows the same trend, that is,  $B_{12}I_{12}^{2-}$  caused the earliest onset (see pointed lines) and the largest bluish phase region followed by  $B_{12}Br_{12}^{2-}$ , while  $B_{12}Cl_{12}^{2-}$  did not evoke a bluish phase. Additionally, in the presence of NaCl and at 1 mM of dodecaborate, see Figure 36d-f, bluish phases were observed for all three analogues (but not with  $B_{12}F_{12}^{2-}$  or  $B_{12}H_{12}^{2-}$ ), where the size of the phase region and the minimum temperatures (pointed lines) again resulted in the same ordering:  $B_{12}I_{12}^{2-} > B_{12}Br_{12}^{2-} > B_{12}Cl_{12}^{2-}$ .

To identify these phases, the samples were set between crossed polarizers revealing that the bluish phases in Figure 36b and c are non-birefringent and therefore isotropic, while the bluish phases in the presence of NaCl showed birefringence when stirred. This phenomenon is called streaming birefringence and occurs for isotropic phases that get broken into anisotropic fragments upon agitation. Such birefringent behavior is characteristic of so-called sponge phases, which can be described as a random surface of a surfactant bilayer that divides space into two interpenetrating solvent labyrinths.<sup>162</sup> By using SANS, it is easily possible to identify two-dimensional objects (such as bilayers) because they cause a marked  $q^{-2}$ -dependence, which were indeed observed for all bluish phase regions in the presence of NaCl, see Figure 37. At low temperatures, the micellar phase is present, which is characterized by elongated ellipsoidal

objects as previously shown and at high temperatures, in the bluish phase region, a long steep slope of  $q^{-2}$  emerges for the three tested dodecaborates  $B_{12}I_{12}^{2-}$ ,  $B_{12}Br_{12}^{2-}$  and  $B_{12}Cl_{12}^{2-}$ . This is clear evidence of a heat-induced phase transition towards bilayers, which manifest as a sponge-phase as concluded from the observed streaming birefringence. Unfortunately, the bluish phase regions that appear in the absence of NaCl (in Figure 36b and c) were not investigated by SANS though also here a bilayer phase can be expected, which due to the lack of birefringence might be shaped as unilamellar vesicles.

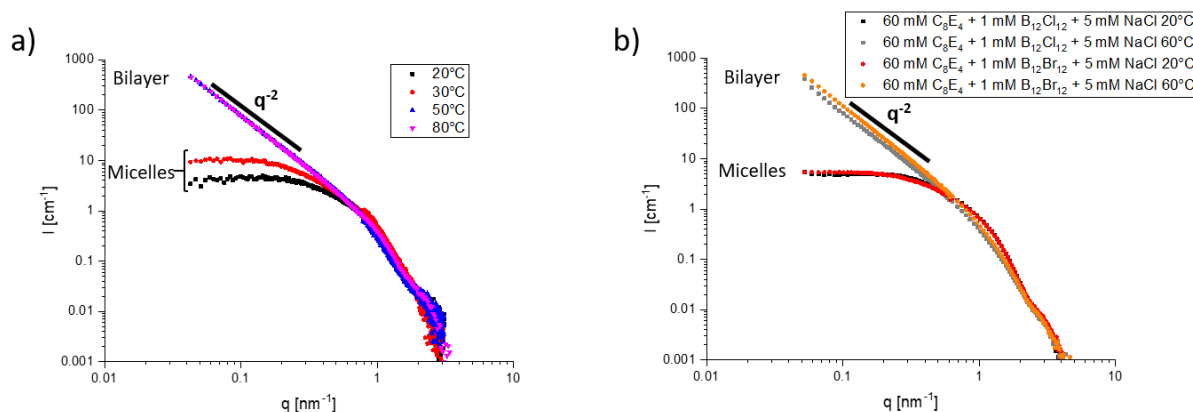


Figure 37: SANS of 60 mM  $C_8E_4$  at a) 1 mM  $Na_2B_{12}I_{12}$  and b) 1 mM  $Na_2B_{12}Br_{12}$  or  $Na_2B_{12}Cl_{12}$  with 5 mM NaCl at different temperatures. The spectra are in absolute scale. Spectra in a) were acquired by TOF-SANS at ILL. Spectra in b) were acquired by SANS at MLZ.

In order to rationalize such a phase transition, the packing in the surfactant/dodecaborate co-assembly has to be considered. As a precondition, it must be stated that  $C_8E_4$ 's geometry allows only for micellar phases, while bilayer phases cannot be formed by  $C_8E_4$  alone.<sup>134</sup> However, as it was shown by SAXS and SANS the dodecaborates adsorb to the micelle and may intercalate deeply between the individual surfactant molecules, which would strongly affect the packing in the micelle. Adsorption of a dodecaborate to the outer periphery or to the ethoxy head groups leads to a supersession of hydration water by the nano-ion and to a spreading apart of the surfactant head groups, which compresses the micelle into spheres at high dodecaborate concentrations. Note that this effect was equivalently observed for the Keggin-ion  $SiW_{12}O_{40}^{4-}$  in section 2.3.2. However, as it was shown here the dodecaborates may also position near the hydrophobic core, which spreads apart the surfactant's  $C_8$ -tails causing an increase in the packing parameter. This effect here seems to be the trigger for the transition of the micelles towards bilayer phases. Therefore, the dodecaborates that induced the formation of these bilayer phases ( $B_{12}Br_{12}^{2-}$ ,  $B_{12}I_{12}^{2-}$ , and  $B_{12}Cl_{12}^{2-}$  in the presence of NaCl) seem to exhibit at least partial hydrophobic characters.

In this section, it was shown that the dodecaborate analogues  $B_{12}H_{12}^{2-}$ ,  $B_{12}F_{12}^{2-}$ ,  $B_{12}Cl_{12}^{2-}$ ,  $B_{12}Br_{12}^{2-}$  and  $B_{12}I_{12}^{2-}$  constitute a continuous scale from chaotropic to superchaotropic ions as concluded from the shifts in the cloud point of the non-ionic surfactant  $C_8E_4$ . These shifts can be traced back to interactions of the dodecaborate ions with the  $C_8E_4$ -micelles causing pronounced electrostatic intermicellar repulsion. The strength of the interaction corresponds with the inverse ordering of the dodecaborates by their volume charge density, that is, the largest (and lowest charge density) dodecaborate  $B_{12}I_{12}^{2-}$  showed consistently the strongest cloud point increase, while the smallest dodecaborate  $B_{12}H_{12}^{2-}$  exhibited the weakest effects. Addition of the electrolyte NaCl screened the emergent intermicellar repulsion and caused a tremendous drop in the cloud point revealing that the  $C_8E_4$ /dodecaborate co-micelles are more hydrophobic than the pure  $C_8E_4$ -micelles presumably due to a dehydration of the hydrophilic surfactant heads. For the strongly interacting dodecaborates  $B_{12}Cl_{12}^{2-}$ ,  $B_{12}Br_{12}^{2-}$  and  $B_{12}I_{12}^{2-}$ , it was further shown by SANS and SAXS that they strongly affect micellar morphology causing an elongation of the micelles at low dodecaborate concentration and a compression into spheres at high dodecaborate concentrations. Additionally, as exemplified for the most superchaotropic  $B_{12}I_{12}^{2-}$ , the interaction of the dodecaborates with the  $C_8E_4$ -micelles cannot be conceptualized with a simple adsorption model. Rather, with increasing concentration,  $B_{12}I_{12}^{2-}$  loads gradually the  $C_8E_4$ -micelles even penetrating deeply into the micellar interior. Thus, the micellar surfactant packing is strongly altered causing the appearance of bluish opalescent bilayer phases especially at elevated temperatures. Such lyotropic phases are uncommon for the surfactant  $C_8E_4$  and these morphological changes on the  $C_8E_4$ -micelles can be attributed to concentration dependent effects by the dodecaborates on the micellar packing parameter linked to the penetration depth of the dodecaborate positioning them either between the hydrophilic surfactant heads or close to the hydrophobic surfactant tails. Consequently, the dodecaborates  $B_{12}Cl_{12}^{2-}$ ,  $B_{12}Br_{12}^{2-}$ ,  $B_{12}I_{12}^{2-}$  exhibit partial hydrophobic characters in addition to their pronounced superchaotropy.

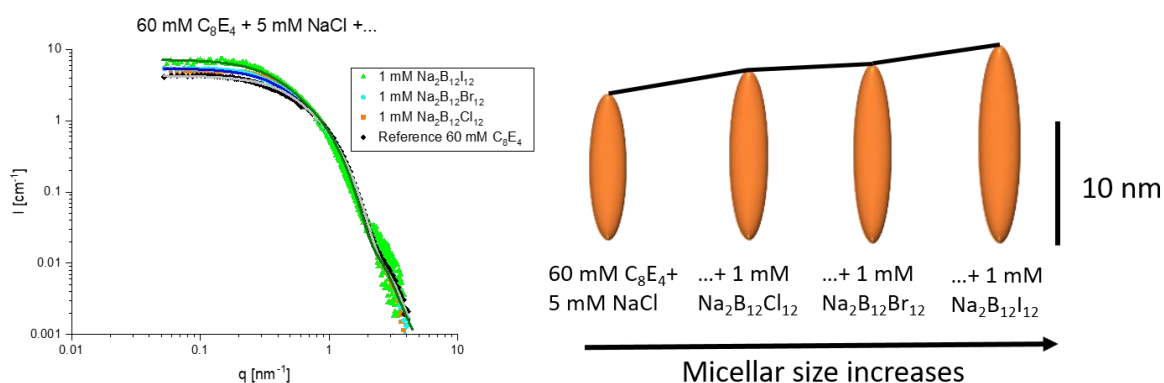
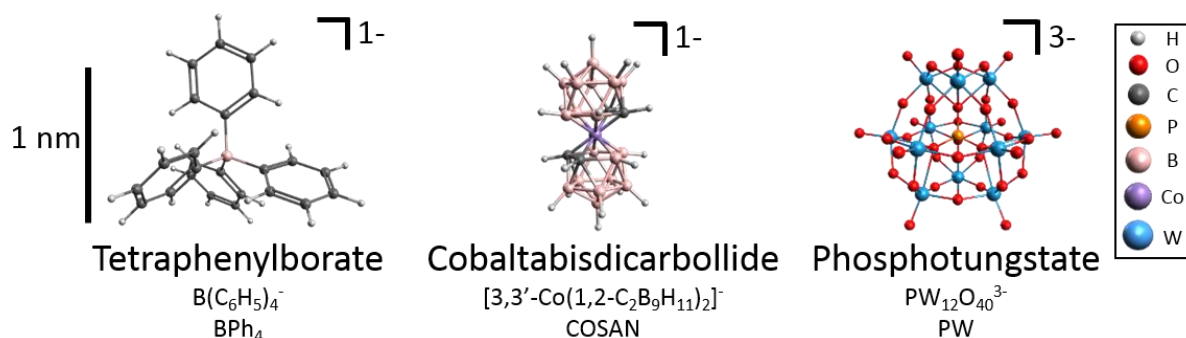
2.4.1. Addendum – Chaotropic dodecaborates in  $C_8E_4$ 

Figure 38: SANS of 60 mM  $C_8E_4$  at 1 mM  $Na_2B_{12}I_{12}$ ,  $Na_2B_{12}Br_{12}$  or  $Na_2B_{12}Cl_{12}$  with 5 mM NaCl at 20°C. The full lines correspond to mathematical fits using ellipsoidal form factors. The spectra are in absolute scale. The received micellar dimensions are shown with the schemes on the right-hand side. Corresponding fit parameters are listed in section 2.9. The spectrum for  $Na_2B_{12}I_{12}$  was acquired by TOF-SANS at ILL and the spectra for  $Na_2B_{12}Br_{12}$  and  $Na_2B_{12}Cl_{12}$  were acquired by monochromatic SANS at MLZ.

The micelles of 60 mM  $C_8E_4$  in the presence of 5 mM NaCl, show higher intensities upon addition of 1 mM of either dodecaborate hinting at micellar growth. To quantify the dimensions fits using ellipsoidal form factor models were used. Thus, the micellar size was largest in the presence of  $B_{12}I_{12}^{2-}$  with a polar radius of 8 nm followed by  $B_{12}Br_{12}^{2-}$  with 7.3 nm and  $B_{12}Cl_{12}^{2-}$  with 7.1 nm. The most superchaotropic dodecaborate  $B_{12}I_{12}^{2-}$  therefore also has the strongest impact on the micellar shape and size.

## 2.5. Disruptive ions ( $\text{BPh}_4^-$ , COSAN, $\text{PW}_{12}\text{O}_{40}^{3-}$ ) in $\text{C}_8\text{E}_4$

Hydrophobic ions, as the name implies, have a strong affinity towards hydrophobic (non-polar) environments because their hydration in water is energetically disfavored.<sup>36,119,120</sup> The by far most studied archetypical hydrophobic ion is tetraphenylborate ( $\text{BPh}_4^-$ ), see Scheme 5 left. Introduction of soft matter, such as non-ionic surfactants, lipids or polymers, to aqueous  $\text{BPh}_4^-$ -solution leads to formation of soft matter-hydrophobic ion contacts driven by the hydrophobic effect. On lipid bilayers, the hydrophobic ion  $\text{BPh}_4^-$  can adsorb to the hydrophilic lipid heads and may intercalate between the hydrophobic lipid tails causing phase changes, while with non-ionic PNiPAM-polymer strong interactions cause precipitation of PNiPAM/hydrophobic ion co-aggregates.<sup>34,35,122</sup> In regards to the effects on the lipid monolayers, the term soft matter disruptor was introduced by Leontidis to describe the behavior of  $\text{BPh}_4^-$  to intercalate deeply between the lipid molecules as an extension of the Hofmeister series beyond chaotropic ions.<sup>34,35</sup> From a different perspective, Bastos-Gonzalez et al. termed  $\text{BPh}_4^-$  as a superchaotropic ion owing to its strong affinity - as an extension to classical chaotropic ions - to hydrophobic colloidal latex particles.<sup>5</sup> Furthermore, in early studies dating back to 1983, experiments on lipid monolayers showed that cobaltabisdicarbollide (COSAN), see Scheme 5 middle, exhibits a strong hydrophobic character similar to  $\text{BPh}_4^-$ .<sup>163</sup> In recent years, it was then further elaborated that COSAN behaves surfactant-like in aqueous solution<sup>55,56,58</sup> and interacts with non-ionic surfactant (octylglucoside,  $\text{C}_8\text{G}_1$ ) micelles driven by either the chaotropic (adsorption to the surfactant heads) or the hydrophobic effect (interaction with the surfactant tail).<sup>164</sup> Additionally, with increasing concentration, COSAN was found to disrupt the  $\text{C}_8\text{G}_1$ -micelles suppressing their formation.<sup>164</sup>



Scheme 5: The three soft matter disruptor nano-ions tetraphenylborate ( $\text{BPh}_4^-$ ), cobaltabisdicarbollide (COSAN) and the Keggin-POM PW ( $\text{PW}_{12}\text{O}_{40}^{3-}$ ).

In the present section, the disruptive natures of  $\text{BPh}_4^-$  and of COSAN are explored on micelles of 60 mM of the non-ionic surfactant  $\text{C}_8\text{E}_4$  in aqueous solution. Additionally, the Keggin-POM phosphotungstate ( $\text{PW}_{12}\text{O}_{40}^{3-}$ , PW, Scheme 5 right) will be discussed, though it has not been

described as a hydrophobic ion and rather as a superchaotropic ion<sup>4,92</sup> or an ionic nanocolloid<sup>96</sup>. Here, PW is set on the same footing with the hydrophobic ions because it induced the appearance of a two-phasic region at low millimolar nano-ion concentrations similarly to  $\text{BPh}_4^-$  and COSAN. This two-phasic region seems to be the only macroscopic observation that sets these three ions apart from the previously discussed superchaotropic Keggin-ions  $\text{BW}_{12}\text{O}_{40}^{5-}$  and  $\text{SiW}_{12}\text{O}_{40}^{4-}$  and the dodecaborates of the  $\text{B}_{12}\text{X}_{12}^{2-}$ -type.

In a first step, the phase behavior of 60 mM  $\text{C}_8\text{E}_4$  was studied as a function of nano-ion concentration. The corresponding phase diagrams with  $\text{BPh}_4^-$ , COSAN and PW are shown in Figure 39a-c.

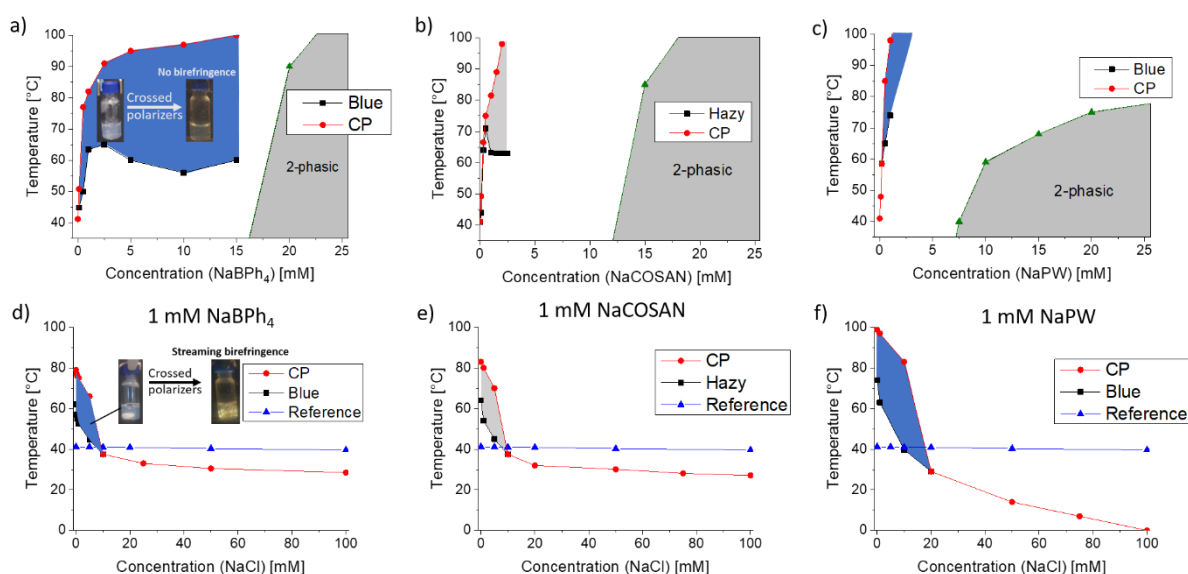


Figure 39: Phase diagrams of  $\text{C}_8\text{E}_4$  with blue/hazy and two-phasic phase regions a-c) without salt for  $\text{NaBPh}_4$ ,  $\text{NaCOSAN}$  and  $\text{NaPW}$  and d-f) as a function of salt for 1 mM  $\text{NaBPh}_4$ ,  $\text{NaCOSAN}$  and  $\text{NaPW}$ , respectively.

Thus, with the hydrophobic ions  $\text{BPh}_4^-$  and COSAN as well as with the Keggin-POM PW as previously discussed, the micellar phase of 60 mM  $\text{C}_8\text{E}_4$  is strongly stabilized as the cloud point (CP) of 60 mM  $\text{C}_8\text{E}_4$  is shifted tremendously to higher temperatures. This marked stabilization can be attributed to a charging of the micelles upon contact formation of the hydrophobic ions with the micelles. At elevated temperatures, this micellar phase transitions into a bluish opalescent vesicle phase in the presence of  $\text{BPh}_4^-$  (as was evidenced by SANS) before phase demixing at the CP. Note that a similarly extensive phase region was observed with COSAN. However, due to the yellow coloring of COSAN-solutions the bluish haze is opposed making the phase appear faint grey. Furthermore, for  $\text{BPh}_4^-$ , COSAN as well as PW, at relatively high nano-ion concentrations a 2-phasic region occurred at low temperatures below the cloud point. Therefore, in the presence of these hydrophobic ions, the phase behavior of  $\text{C}_8\text{E}_4$ , which by

itself forms only a micellar phase in water, is strongly altered. The phase changes are more pronounced than with all previously discussed superchaotropic ions as will be shown in section 2.6, which hints at the disruptive nature of these ions.

To further unravel the origin of these phase changes and test the role of electrostatics in the observed phase sequence, phase diagrams at 60 mM  $C_8E_4$  + 1 mM of each respective nano-ion were traced as a function of the electrolyte NaCl, see Figure 39d-f. Presence of small millimolar amounts of NaCl caused the CP to drop tremendously to low temperatures because the intermicellar repulsion was screened, and below the reference curve of bare  $C_8E_4$ +NaCl for all three tested ions. This pronounced drop clearly shows that the micelles become more hydrophobic in the presence of the hydrophobic ions. Additionally, the vesicle phase transitioned into a sponge phase upon addition of NaCl as exemplified for  $BPh_4^-$  and determined by using SANS. Similar phase changes are expected for the other two-ions though they were not specifically identified by means of SANS.

It is obvious from the phase diagrams that the hydrophobic ions  $BPh_4^-$  and COSAN as well as PW have profound effects on the phase behavior of  $C_8E_4$  already at very low nano-ion concentrations. To examine these effects further on a microscopic level, SANS was performed on the micellar phase of 60 mM  $C_8E_4$  + 1 mM  $NaBPh_4$  at room temperature without and in the presence of NaCl, see Figure 40.

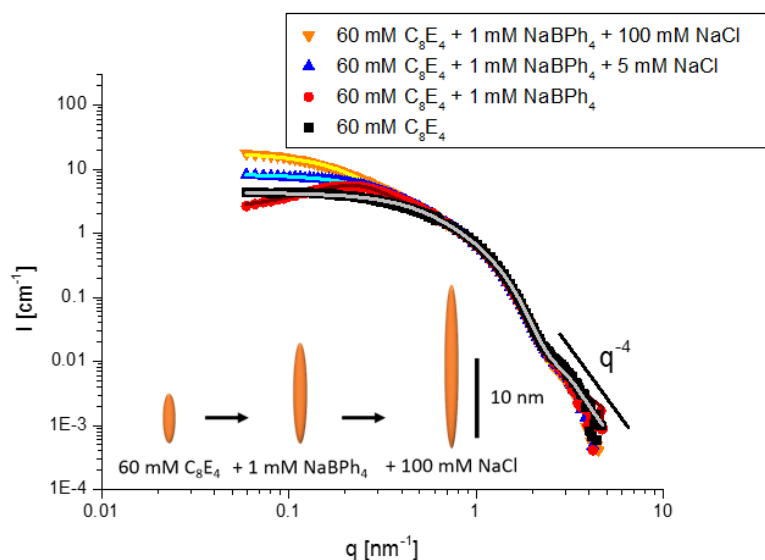


Figure 40: SANS of 60 mM  $C_8E_4$  + 1 mM  $NaBPh_4$  in  $D_2O$  at different NaCl-concentrations at 20°C. The lines are theoretical fits and the inset schemes indicate the micellar dimensions from the fits. The spectra are in absolute scale. The corresponding fit parameters are listed in section 2.9.

Addition of 1 mM  $NaBPh_4$  to micelles of 60 mM  $C_8E_4$  causes the appearance of a structure factor peak (compare red and black curve in Figure 40) owing to the emergent electrostatic

intermicellar repulsion that stabilizes the micellar phase. Fitting further revealed that the prolate ellipsoidal micelles grow significantly in polar radius from 6.0 nm (bare 60 mM  $C_8E_4$ ) to 13.5 nm with 1 mM  $NaBPh_4$ . Addition of  $NaCl$  further leads firstly to a screening of the intermicellar repulsion as the structure factor peak at low  $q$  disappears at  $[NaCl]=5$  mM and secondly to an elongation of the micelles to a polar radius of 22 nm. This behavior explains the observed CP-drop upon  $NaCl$ -addition considering that the CP occurs only when micelles are sufficiently elongated<sup>128</sup> and demonstrates that already 1 mM  $NaBPh_4$  has profound effects on the micellar shape.

Similarly, the emergent bluish opalescent phases in the presence of  $NaBPh_4$  were identified by using SANS. The corresponding spectra are shown in Figure 41.

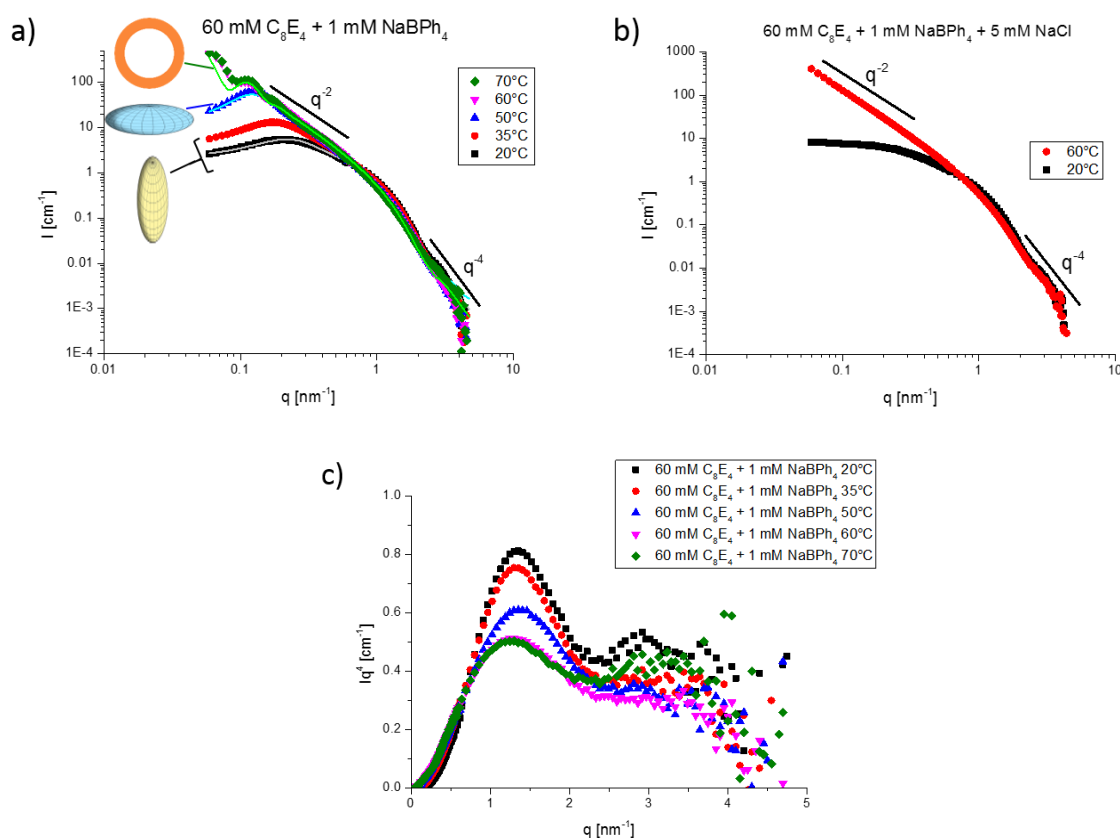


Figure 41: SANS as a function of temperature: a) 60 mM  $C_8E_4$  at 1 mM  $NaBPh_4$  without  $NaCl$  in  $I$  vs  $q$  and  $Iq^4$  vs  $q$  in c) and b) 60 mM  $C_8E_4$  at 1 mM  $NaBPh_4$  with 5 mM  $NaCl$ . In a) schemes are inserted to indicate the shape of the scattering objects: prolate (yellow) or oblate (blue) ellipsoids or vesicles (orange) as identified by fitting. The spectra are in absolute scale. The corresponding fit parameters are listed in section 2.9.

In the absence of salt, the SANS-spectra of 60 mM  $C_8E_4$  + 1 mM  $NaBPh_4$  reveal that, upon heating, the prolate (elongated) ellipsoidal micelles at 20°C and 35°C transition into two-dimensional objects at temperatures above 50°C as indicated by the large  $q^{-2}$ -dependence at low  $q$  with characteristic oscillations appearing at 60°C and 70°C. Fitting of the spectra revealed



the shape of these bilayer phases, namely oblate (disk-like) objects at 50°C and vesicles at 60°C and 70°C, see schemes in Figure 41a. Upon addition of just 5 mM of NaCl and at 60°C, the oscillations of the vesicles at low  $q$  disappear and an extended  $q^{-2}$ -dependence emerges, see Figure 41b, which hints at infinitely large scattering objects characteristic of lamellar or sponge phases. As this phase is birefringent only under stirring it can be clearly identified as a sponge phase.

Furthermore, the two-phasic region was identified using SAXS. As a proxy for the three disruptive ions, the Keggin-POM PW was used as it provides feasible contrast before and in the two-phasic region. To do so, the phase border between the micellar phase and the two-phasic region was approached by increasing NaPW-concentration and one biphasic sample was measured at 10 mM NaPW collecting the scattering of the upper liquid phase as well as of the lower precipitated solid phase, see Figure 42.

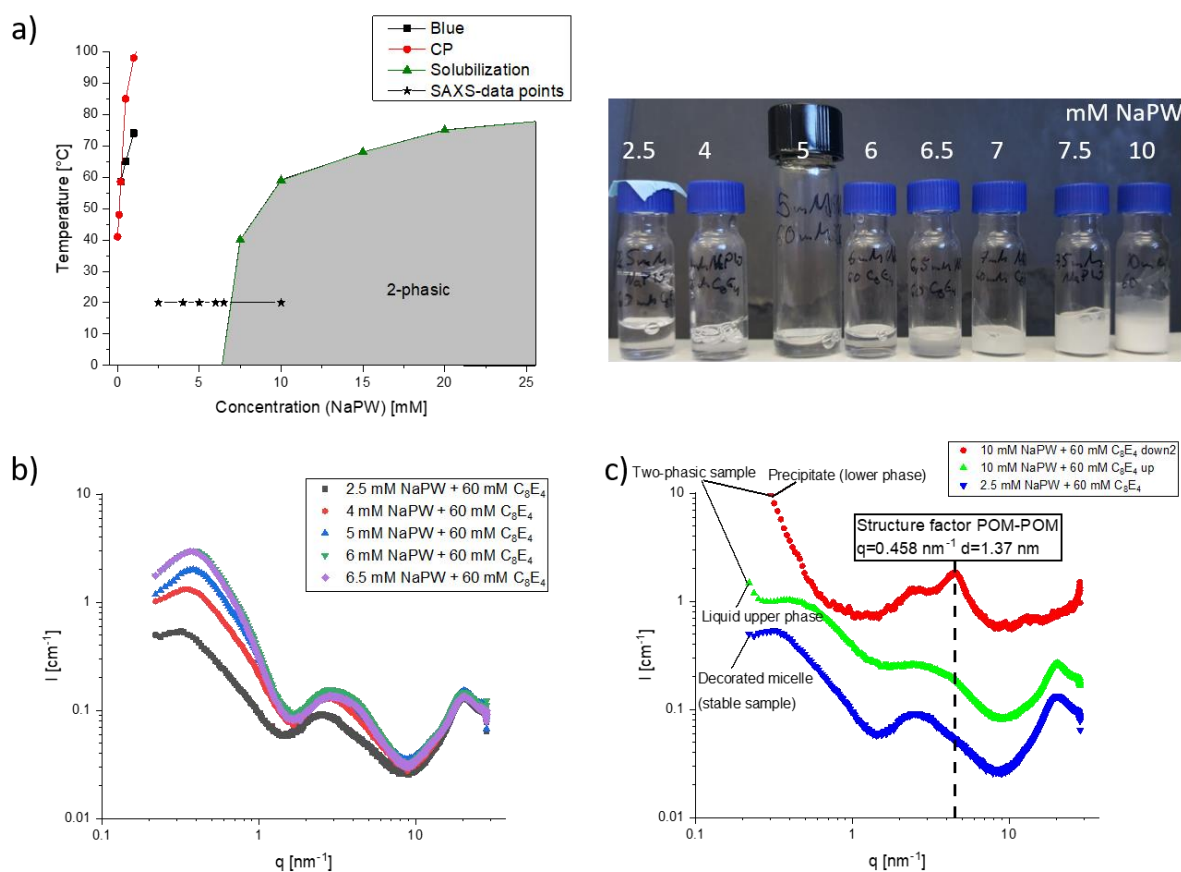


Figure 42: a) Left: Phase diagram of 60 mM C<sub>8</sub>E<sub>4</sub> with indicators for the compositions, where SAXS was measured. Right: Photo of the sample series. b) Normalized SAXS-spectra of 60 mM C<sub>8</sub>E<sub>4</sub> + NaPW before precipitation occurs. c) Two-phasic sample with normalized SAXS-spectra of the upper liquid phase (green curve) and of the precipitated lower phase (red curve) compared to a stable sample at 2.5 mM NaPW (blue curve).

The spectra in the micellar phase at NaPW-concentrations inferior to the precipitation limit show the characteristic fingerprint of classical decorated micelles that increase in intensity with NaPW-concentration. This trend is the known and expected result as more and more PW partition to the C<sub>8</sub>E<sub>4</sub>-micelles and does not hint directly at the upcoming precipitation limit at [NaPW] = 7 mM. For the precipitated samples, the upper phase (green curve) still shows a signature of decorated micelles and therefore still contains a considerable amount of NaPW. Nevertheless, the precipitated solid phase (red curve) has a highly increased scattered intensity and therefore contains mainly NaPW in a condensed state, while the water peak at 20 nm<sup>-1</sup> has completely disappeared showing the “dryness” of the precipitate. The same result is emphasized by the presence of an intense POM-POM structure factor peak at  $q=0.458\text{ nm}^{-1}$ , which is just barely visible on the decorated micelles but protrudes strongly in the spectrum of the precipitate. Translation into direct spacing ( $d=2\pi/q$ ) results in a POM-POM distance of 1.37 nm and points at the condensed organization of PW in this precipitate. Unfortunately, SAXS here does not reveal the mechanism behind this precipitate formation and further research needs to be conducted to understand this phenomenon.

In this section, the hydrophobic ions BPh<sub>4</sub> and COSAN and the Keggin-ion PW were studied as to their effects on the phase behavior of the non-ionic surfactant C<sub>8</sub>E<sub>4</sub>. These hydrophobic ions – sometimes referred to as soft matter disruptors – evinced tremendous changes in the phase sequence of C<sub>8</sub>E<sub>4</sub> due to strong interactions with the surfactant. All three ions produced qualitatively similar effects including a tremendous increase in the cloud point of the micellar phase, the appearance of a bluish opalescent vesicle phase at elevated temperatures and precipitation at millimolar concentrations. The increase in the CP can be attributed to an electric charging of the micelles upon adsorption or incorporation of the hydrophobic ions. By investigating the behavior of BPh<sub>4</sub> in more detail using SANS, it was observed that C<sub>8</sub>E<sub>4</sub>-micelles are significantly elongated in the presence of NaBPh<sub>4</sub> hinting at a positioning of NaBPh<sub>4</sub> between the hydrophobic surfactant tails. Similarly, the emergence of the vesicle phase at high temperatures was confirmed using SANS and can be rationalized by an incorporation of BPh<sub>4</sub> in-between the surfactant tails causing an increase in the packing parameter and driving the transition towards a bilayer phase. Overall, significant evidence of a hydrophobic nature was provided for all three tested ions, that is, BPh<sub>4</sub><sup>-</sup>, COSAN and PW.

## 2.6. Classification of the nano-ions

In the three preceding sections, the behavior of nano-ions ranging from superchaotropic ions to hydrophobic ions in solutions containing the non-ionic surfactant C<sub>8</sub>E<sub>4</sub> was investigated. Firstly, the focus was set deliberately on the Keggin-POM SiW<sub>12</sub>O<sub>40</sub><sup>4-</sup> (sections 2.3.2-2.3.5) due to its moderate superchaotropic character showing strong interaction with C<sub>8</sub>E<sub>4</sub>-micelles, yet leaving the surfactant phase sequence of C<sub>8</sub>E<sub>4</sub> unaffected. Secondly, the dodecaborate B<sub>12</sub>I<sub>12</sub><sup>2-</sup> (section 2.4) was more deeply examined revealing its dual nature comprising superchaotropic as well as a slight disruptive (hydrophobic) traits. The difference to SiW lies in the ability of B<sub>12</sub>I<sub>12</sub><sup>2-</sup> to alter the C<sub>8</sub>E<sub>4</sub>-micellar phase to a bilayer (vesicle) phase and to destabilize the micellar phase at high B<sub>12</sub>I<sub>12</sub><sup>2-</sup>-concentrations. Continuing the series, the presumably more hydrophobic organic ion BPh<sub>4</sub><sup>-</sup> was shown to induce even more pronounced phase changes causing a destabilization of the micellar phase at low BPh<sub>4</sub><sup>-</sup>-concentrations into a biphasic region on top of the emergent bilayer (vesicle) phase, see section 2.5.

In the present section, an ordering and a classification of all studied nano-ions shall be established based on their effects on the phase diagram of 60 mM C<sub>8</sub>E<sub>4</sub>. To this end, the evolution of the cloud point of the C<sub>8</sub>E<sub>4</sub>-micellar phase as a function of nano-ion concentration has served as a reliable indicator in previous studies.<sup>4,92</sup> In particular, it is possible to fit the CP-data with a Langmuir-like model to condense the CP-evolutions into two parameters as proposed by Buchecker et al.<sup>92</sup> This method was applied here and the Langmuir model has the form:

$$CP = CP_{C_8E_4} + \frac{B_{max} * K_A}{1 + K_A * [POM]} \quad 3.10$$

Here,  $CP_{C_8E_4}$  is the CP of bare 60 mM C<sub>8</sub>E<sub>4</sub> in water,  $B_{max}$  is the extent of the cloud point increase and  $K_A$  the initial slope of the CP-increase at low concentrations. This model is merely used to extract the fitting parameters for the sake of comparison as the experimental conditions in the CP-setup do not qualify as a classical Langmuir isotherm experiment. The fitting parameters are listed in Table 13 and the CP-evolutions with corresponding fits are shown in Figure 43. Notably, the ion PF<sub>6</sub><sup>-</sup> is added in the CP-evolutions in Figure 43 though it was not previously discussed. PF<sub>6</sub><sup>-</sup> was discussed by Leontidis et al as a border case between chaotropic and hydrophobic (disruptive) ions.<sup>34,35</sup> To relate to Leontidis' classification PF<sub>6</sub><sup>-</sup> is included here. It shows a stronger CP-increase than the classical chaotrope SCN<sup>-</sup>, yet weaker effects than the previously discussed superchaotropic POMs, boron clusters and organic ions and therefore seems to behave like a strongly chaotropic ion.

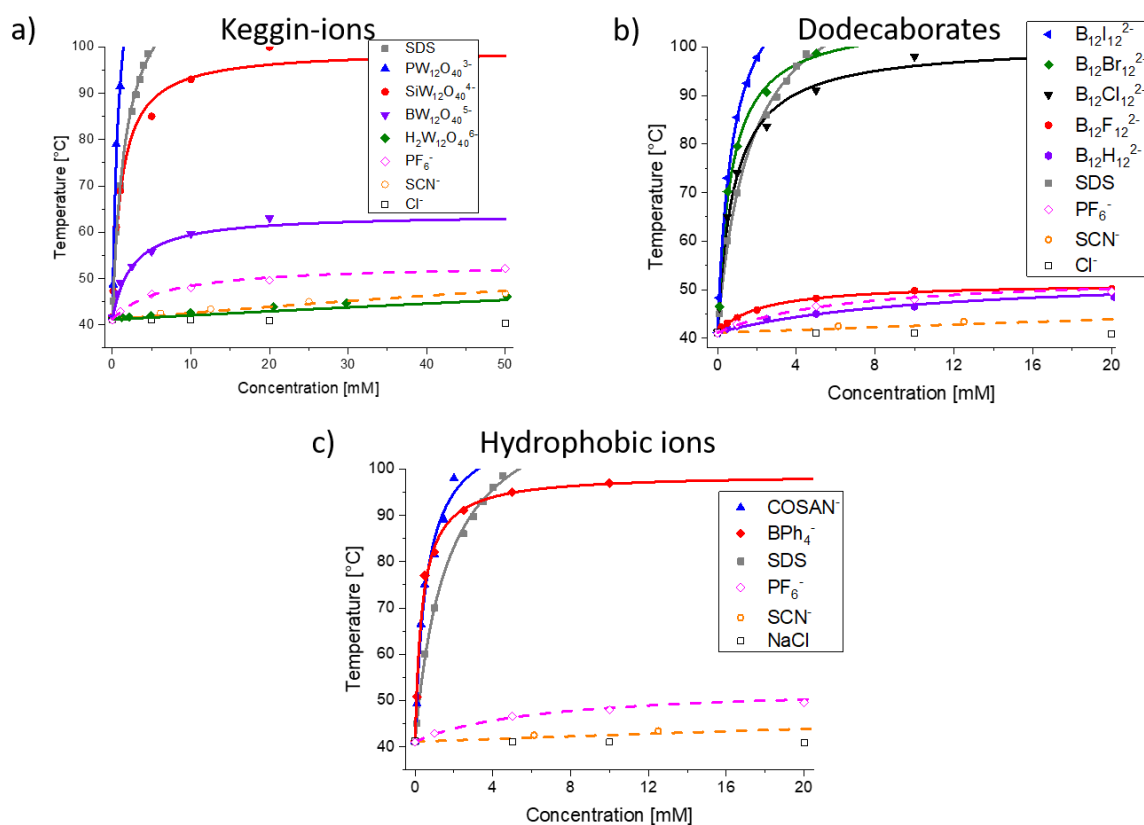
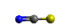

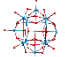
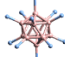
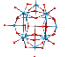
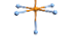
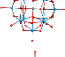
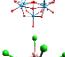
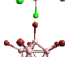
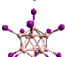
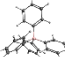
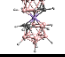




Figure 43: Cloud point evolutions of a) the Keggin-ions b) the dodecaborates and c) the hydrophobic ions. All ions were used in their  $\text{Na}^+$ -form besides  $\text{B}_{12}\text{H}_{12}^{2-}$  ( $\text{Cs}^+$ -form),  $\text{BW}_{12}\text{O}_{40}^{5-}$  ( $\text{K}^+$ -form) and  $\text{H}_2\text{W}_{12}\text{O}_{40}^{6-}$  ( $\text{NH}_4^+$ -form). For reference  $\text{NaCl}$ ,  $\text{NaSCN}$ ,  $\text{NaPF}_6$  and  $\text{SDS}$  are inserted in each figure. The lines are Langmuir fits, see text.

On top of the qualitative evaluation of the CPs by fitting, the secondary phase regions that appear below the CP including bluish opalescent bilayer phases and biphasic regions contain valuable information about the disruptive (hydrophobic) nature of the ions, see Table 13 below. The absence of bluish opalescent phases or of the biphasic region is designated with “no”, while the presence of these phases is denoted with +, ++ or +++ to indicate the extent of the phase. An overview of all bluish opalescent phases or the precipitates in the presence of the nano-ions is given in the addendum to this section on page 97 in Figure 46. Furthermore, in the previous sections and in the literature<sup>92</sup>, it proved pertinent to consider the volume charge density of an ion as a measure of its chaotropicity/hydrophobicity. For this reason, the charge densities were calculated for all ions and Table 13 is ordered from highest to lowest volume charge density from  $\text{SCN}^-$  to  $\text{BPh}_4^-$ .

## 2. Nano-ions in interaction with non-ionic surfactant micelles

Table 13: Ions investigated throughout this chapter from chaotropic classical ions to superchaotropic and hydrophobic ions with their ionic volumes, volume charge densities and macroscopic observations made on the C<sub>8</sub>E<sub>4</sub>-phases including the emergence of bluish opalescent phases and biphasic regions. Additionally, the fitting parameters B<sub>max</sub> and K<sub>A</sub> of the cloud point evolutions are shown.

Chemical class	Molecular formula	Counter-ion	Structure	Charge, q <sub>e</sub>	Ionic radius [nm]	Ionic volume [nm <sup>3</sup> ]	Volume charge density [q <sub>e</sub> /nm <sup>-3</sup> ]	Bluish opalescent phase	Two-phasic region	K <sub>A</sub> [mM <sup>-1</sup> ]	B <sub>max</sub> [°C]
Chaotropic ion	SCN <sup>-</sup>	Na <sup>+</sup>		1	0.21 <sup>a</sup>	0.07 <sup>a</sup>	14.1	no	no	0.02	10.7
Dodecaborate	B <sub>12</sub> H <sub>12</sub> <sup>2-</sup>	Cs <sup>+</sup>		2	0.33	0.15 <sup>b</sup>	13.16	no	no	0.09	12.2
Keggin-POM	H <sub>2</sub> W <sub>12</sub> O <sub>40</sub> <sup>6-</sup> MW	NH <sub>4</sub> <sup>+</sup>		6	0.48	0.46 <sup>c</sup>	13	no	no	0.01	16.4
Dodecaborate	B <sub>12</sub> F <sub>12</sub> <sup>2-</sup>	Na <sup>+</sup>		2	0.35	0.18 <sup>b</sup>	11	no	no	0.45	10.3
Keggin-POM	BW <sub>12</sub> O <sub>40</sub> <sup>5-</sup> BW	K <sup>+</sup>		5	0.48	0.46 <sup>c</sup>	10.87	no	no	0.40	22.8
Chaotropic ion	PF <sub>6</sub> <sup>-</sup>	Na <sup>+</sup>		1	0.25 <sup>a</sup>	0.11 <sup>a</sup>	9.17	no	no	0.15	12.1
Keggin-POM	SiW <sub>12</sub> O <sub>40</sub> <sup>4-</sup> SiW	Na <sup>+</sup>		4	0.48	0.46 <sup>c</sup>	8.7	no	no	0.86	58.3
Keggin-POM	PW <sub>12</sub> O <sub>40</sub> <sup>3-</sup> PW	Na <sup>+</sup>		3	0.48	0.46 <sup>c</sup>	6.52	++	++	1.19	93.9
Dodecaborate	B <sub>12</sub> Cl <sub>12</sub> <sup>2-</sup>	Na <sup>+</sup>		2	0.43	0.33 <sup>b</sup>	6.01	no	no	1.19	59.6
Dodecaborate	B <sub>12</sub> Br <sub>12</sub> <sup>2-</sup>	Na <sup>+</sup>		2	0.46	0.42 <sup>b</sup>	4.81	+	no	1.35	64.9
Dodecaborate	B <sub>12</sub> I <sub>12</sub> <sup>2-</sup>	Na <sup>+</sup>		2	0.5	0.52 <sup>b</sup>	3.85	++	+	1.41	77
Tetraphenylborate	(C <sub>6</sub> H <sub>5</sub> ) <sub>4</sub> B <sup>-</sup> BPh <sub>4</sub>	Na <sup>+</sup>		1	na	0.313 <sup>a</sup>	3.19	+++	+++	2.65	57.8
COSAN	[3,3'-Co(1,2-C <sub>2</sub> B <sub>9</sub> H <sub>11</sub> ) <sub>2</sub> ] <sup>-</sup>	Na <sup>+</sup>		1	na	0.45 <sup>d</sup>	2.22	++	+++	1.68	69.7
SDS	C <sub>12</sub> H <sub>25</sub> SO <sub>4</sub> <sup>-</sup>	Na <sup>+</sup>		1	na	na	na	no	no	0.59	77.4

<sup>a</sup> taken from Marcus.<sup>91</sup>

<sup>b</sup> taken from Nau et al.<sup>65</sup>

<sup>c</sup> taken from Buchecker et al.<sup>92</sup>

<sup>d</sup> taken from Bauduin et al.<sup>56</sup>

It transpires from Table 13 that the lower the charge density of an ion the larger is the extent of the bluish opalescent phase and the more likely it is to find a biphasic region. The Keggin-POM PW<sub>12</sub>O<sub>40</sub><sup>3-</sup> presents the only outlier as it caused the appearance of a bluish opalescent phase and a biphasic region while having an intermediate volume charge density. Overall, it is possible to establish the following classification into phase neutral ions, which leave the phase sequence of C<sub>8</sub>E<sub>4</sub> unaffected, weakly disruptive ions, which cause the emergence of a new phase (bluish

opalescent bilayer phase), and disruptive ions, which cause bluish opalescent bilayer phases and additionally disrupt and destabilize the micellar phase causing a transition into a biphasic region at low temperatures:

Phase-neutral ions:  $\text{SCN}^-$ ,  $\text{PF}_6^-$ ,  $\text{B}_{12}\text{H}_{12}^{2-}$ ,  $\text{H}_2\text{W}_{12}\text{O}_{40}^{6-}$ ,  $\text{B}_{12}\text{F}_{12}^{2-}$ ,  $\text{BW}_{12}\text{O}_{40}^{5-}$ ,  $\text{SiW}_{12}\text{O}_{40}^{4-}$ ,  $\text{B}_{12}\text{Cl}_{12}^{2-}$

Weakly disruptive ions:  $\text{B}_{12}\text{Br}_{12}^{2-}$ ,  $\text{B}_{12}\text{I}_{12}^{2-}$

Strongly disruptive ions:  $\text{PW}_{12}\text{O}_{40}^{3-}$ ,  $\text{B}(\text{C}_6\text{H}_5)_4^-$ ,  $\text{COSAN}^-$

Furthermore, the parameters obtained from the fits of the cloud point evolutions show that both the extent of the CP-increase  $B_{\text{max}}$ , see Figure 44a, as well as the initial slope of the CP-increase  $K_A$ , see Figure 44b, correlate well with the charge density of the tested nano-ion. It should be noted here that the  $B_{\text{max}}$ -value is more error-prone because the Langmuir-like saturation could not be attained for the most superchaotropic ions such as  $\text{B}_{12}\text{I}_{12}^{2-}$ , PW and COSAN, which caused a CP-increase beyond 100°C setting the saturation out of reach. Consequently, the  $K_A$ -parameters seems more reliable to order the nano-ions as to their interaction with the non-ionic micelles. Nevertheless, both parameters are plotted in Figure 44 to highlight the pertinence of the volume charge density as an indicator of a superchaotropic nature. Overall, the generally known trend results: The lower the charge density of an ion, the stronger is its impact on the cloud point and its interaction with the non-ionic surfactant micelles.

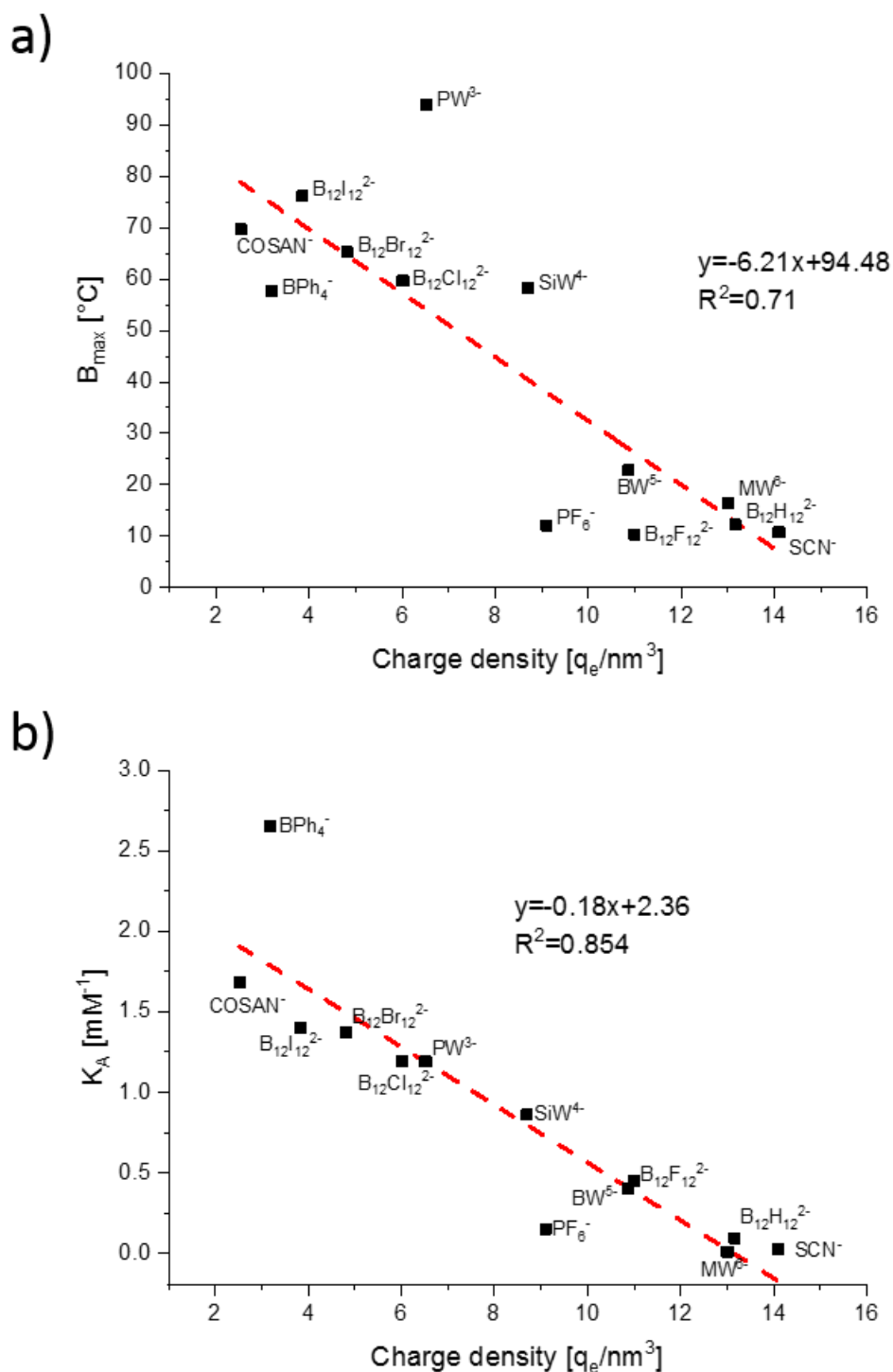
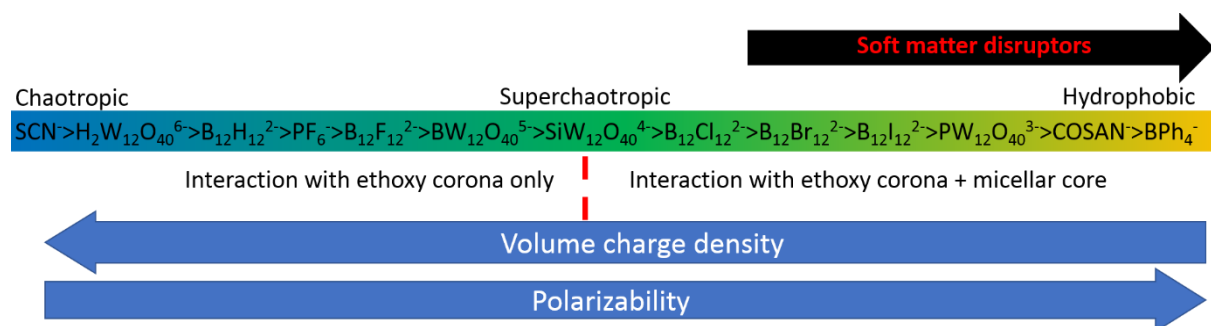


Figure 44: a)  $B_{\max}$ - and b)  $K_A$ -parameters from the Langmuir fits of the CP-curves as a function of charge density of the nano-ions.

Naturally, estimating only the charge density of an ion in order to assess its ionic nature cannot replace any experiment as many other parameters would need to be considered to fully describe an ions behavior including the ions polarizability, the nature of the ion-water contact area, the nature of the surface comprising possible ion-specific interactions, complexation etc.

Nevertheless, an estimation of the volume charge density of an ion seems to serve as a reliable rule of thumb to assess the chaotropic/hydrophobic nature of an ion.

It was shown in this chapter that there exist behavioral differences between chaotropic, superchaotropic and hydrophobic ions. However, the transitions between these ionic species are fluid and ill-defined and may boil down to a question of ions acting in different concentration regimes. Thus, it seems feasible to set all tested nano-ions on the same axis and define superchaotropic ions as the transition region between classical chaotropic and hydrophobic ions as proposed in Scheme 6.



Scheme 6: Ordering of all tested ions from chaotropic to superchaotropic to hydrophobic by their effects on the phase behavior of C<sub>8</sub>E<sub>4</sub> taking into account effects on the CP as well as disruptive behavior and phase changes.

This ordering is based entirely on the experimental observations, i.e. the increase in the CP and the occurrence of phase phenomena such as bluish opalescent phases and precipitates, of which the latter was prioritized. This ordering provides a more detailed picture of the proposed scale by Leontidis<sup>34</sup>, where the chaotropic ion PF<sub>6</sub><sup>-</sup> delimited the transition towards disruptive (hydrophobic) ionic species. Here, a zoom on this transition region is made and superchaotropic ions make up the intermediates between classical chaotropic and hydrophobic ions (soft matter disruptors).



## 2.6.1. Addendum – Classification of the nano-ions

The ordering of the ions by their ability to intercalate between the hydrophobic surfactant tails manifests in the elongation of the  $C_8E_4$ -micelles as is reflected in the SANS spectra of 60 mM  $C_8E_4$  + 1 mM nano-ion, see Figure 45. Figure 45a shows the whole  $q$ -region and Figure 45b zooms in on the low  $q$  region, where the elongation can be observed as an intensity increase indicated by the arrow. The higher the maximum intensity, the more elongated are the  $C_8E_4$ -micelles and the series in Scheme 6 results:  $(SDS\langle)SiW_{12}O_{40}^{4-}\langle B_{12}Cl_{12}^{2-}\langle B_{12}Br_{12}^{2-}\langle BPh_4^-$ .

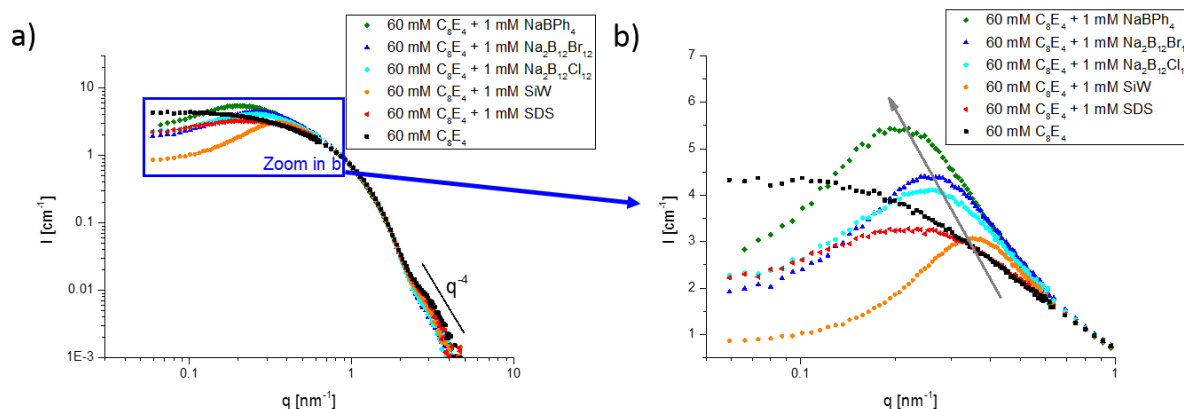


Figure 45: Normalized SANS-spectra of 60 mM  $C_8E_4$  in the presence of 1 mM of each tested nano-ion and 1 mM SDS a) over the whole  $q$ -region and b) a zoom of the low  $q$ -region, which is indicative of the micellar size. The spectra were measured at MLZ.

An overview of all observed bluish opalescent phases is provided in Figure 46.

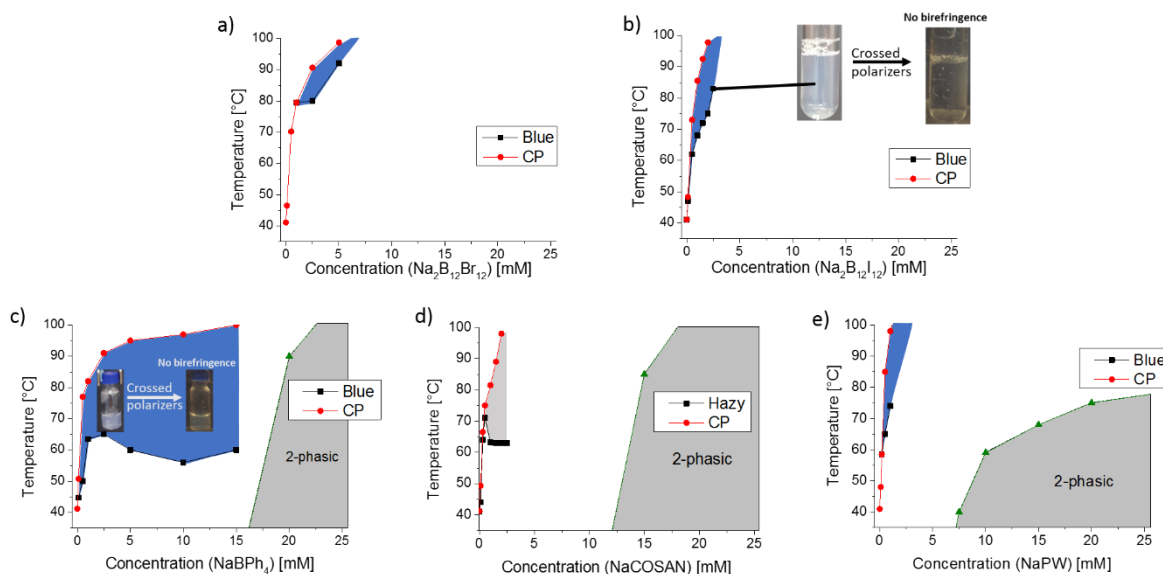


Figure 46: Phase diagrams of 60 mM  $C_8E_4$  indicating the bluish opalescent phase regions (vesicle phases) and the two-phasic regions where precipitation occurred for a)  $Na_2B_{12}Br_{12}$  b)  $Na_2B_{12}I_{12}$  c)  $NaBPh_4$  d)  $NaCOSAN$  and e)  $NaPW$ . For  $Na_2B_{12}I_{12}$ , precipitate formation was observed outside the traced concentration range at  $c(Na_2B_{12}I_{12}) > 60$  mM.

## 2.7. Chapter summary

In this chapter, the phase behavior of the non-ionic surfactant C<sub>8</sub>E<sub>4</sub> was used as a probe to investigate the effects of ionic species ranging from classical chaotropic ions, such as SCN<sup>-</sup>, over superchaotropic nano-ions, such as dodecaborates and Keggin polyoxometalates to large organic ions, such as BPh<sub>4</sub><sup>-</sup>. The micellar phase of the non-ionic surfactant C<sub>8</sub>E<sub>4</sub> exhibits a characteristic cloud point temperature (CP) that is sensitive to the presence of salts and the CP-evolutions as a function of salt concentration result directly in the common Hofmeister ordering of classical ions. Therefore, the behavior of C<sub>8</sub>E<sub>4</sub>-micelles and their macroscopic phase behavior constitute sensible indicators to examine the effects of ions. As it is known that chaotropic ions cause a slight electric charging of the non-ionic surfactant micelles, a reference system that pinpoints the effect of charge was established. To this end, the ionic surfactant sodium dodecylsulfate (SDS) was added in slight amounts to solutions of C<sub>8</sub>E<sub>4</sub>. SDS mixes spontaneously with the non-ionic micelles of C<sub>8</sub>E<sub>4</sub> and thereby renders the micelles partially ionic without affecting the micellar shape and size. The observed stabilization of the micellar phase, reflected in a tremendous CP-increase when SDS is added, were assigned to an electrostatic effect because addition of the electrolyte NaCl caused a screening and drop of the CP back to the CP of pure C<sub>8</sub>E<sub>4</sub>. In the presence of nano-ions (Keggin POMs, boron clusters and large organic ions) CP-shifts to higher temperatures were also observed owing to the emergent micellar charge upon association of the nano-ion with the micelle. The extent of the CP-increase varied strongly from weak effects of chaotropic ions to tremendous effects for the most superchaotropic or hydrophobic nano-ions even affecting profoundly the phase behavior of C<sub>8</sub>E<sub>4</sub>. The effects on the phase behavior of C<sub>8</sub>E<sub>4</sub> were first discussed within each chemical group before comparing all nano-ions among each other.

Thus, the Keggin-POMs H<sub>2</sub>W<sub>12</sub>O<sub>40</sub><sup>6-</sup>, BW<sub>12</sub>O<sub>40</sub><sup>5-</sup>, SiW<sub>12</sub>O<sub>40</sub><sup>4-</sup> and PW<sub>12</sub>O<sub>40</sub><sup>3-</sup> increased the CP of C<sub>8</sub>E<sub>4</sub>, where the lower the charge (density) of the Keggin ion the stronger was the interaction with the C<sub>8</sub>E<sub>4</sub>-micelles and the CP-increase, i.e. H<sub>2</sub>W<sub>12</sub>O<sub>40</sub><sup>6-</sup> < BW<sub>12</sub>O<sub>40</sub><sup>5-</sup> < SiW<sub>12</sub>O<sub>40</sub><sup>4-</sup> < PW<sub>12</sub>O<sub>40</sub><sup>3-</sup>. As a model nano-ion, the focus was set on the Keggin-ion SiW (SiW<sub>12</sub>O<sub>40</sub><sup>4-</sup>), which induced moderate effects on the CP of C<sub>8</sub>E<sub>4</sub> and was previously termed a superchaotropic ion.<sup>4,92</sup> SAXS and SANS on the C<sub>8</sub>E<sub>4</sub>/SiW-system revealed here that SiW strongly adsorbs to non-ionic C<sub>8</sub>E<sub>4</sub>-micelles by inserting between the three exterior ethoxy groups of the hydrophilic surfactant heads. The adsorbed number of SiW-molecules per C<sub>8</sub>E<sub>4</sub>-micelle was found to increase strongly at low SiW-concentrations and to saturate at high SiW-concentrations and was described entirely using a Langmuir isotherm formalism. This study

provided the first complete quantification of the adsorption of a superchaotropic ion onto a soft matter system and revealed that superchaotrope adsorption is governed by the same laws, as is the sorption of gases to solid adsorbents. Furthermore, it was shown that heating has strong effects on the adsorption equilibrium of SiW on the C<sub>8</sub>E<sub>4</sub>-micelles as the adsorbed number of SiW per micelle decreased strongly with temperature. Analysis of these adsorption equilibria via a van't Hoff-plot showed that the superchaotropic adsorption phenomenon is driven by enthalpy accompanied by an entropic penalty. This characteristic thermodynamic signature was previously shown to arise from the binding of superchaotropic ions to the hydrophobic cavity in macrocyclic host molecules resulting in a water structure recovery.<sup>3</sup> The same mechanism is here proposed to be at play for the adsorption of SiW on the C<sub>8</sub>E<sub>4</sub>-micelle. Hydration waters of the ion and the C<sub>8</sub>E<sub>4</sub>-heads are shed upon adsorption and released into the water bulk resulting in a recovery of the bulk water structure. The superchaotropic effect can therefore be seen as a general driving force in any soft matter/nano-ion association phenomena. Upon investigating the SiW-decorated micelles of C<sub>8</sub>E<sub>4</sub> in electrolytic solution, it was observed that the CP dropped far beyond the reference, a phenomenon very different compared to the behavior of mixed C<sub>8</sub>E<sub>4</sub>/SDS-micelles. It was concluded that a superchaotropic ion does not only charge the non-ionic C<sub>8</sub>E<sub>4</sub> micelles but also causes a strong dehydration of the C<sub>8</sub>E<sub>4</sub> surfactant heads, which makes the micelles more hydrophobic and manifests only in the presence of electrolyte as otherwise intermicellar repulsion veils the dehydration effect. Furthermore, it was shown that the presence of electrolyte such as NaCl or Na<sub>2</sub>SO<sub>4</sub> did not affect the adsorption equilibrium of SiW.

Further, nano-ions of the dodecaborate type B<sub>12</sub>H<sub>12</sub><sup>2-</sup>, B<sub>12</sub>F<sub>12</sub><sup>2-</sup>, B<sub>12</sub>Cl<sub>12</sub><sup>2-</sup>, B<sub>12</sub>Br<sub>12</sub><sup>2-</sup> and B<sub>12</sub>I<sub>12</sub><sup>2-</sup> were investigated in solutions of the non-ionic surfactant C<sub>8</sub>E<sub>4</sub> using the same experimental approach (CP-determination, SAXS, SANS). All dodecaborates induced an increase in the CP of C<sub>8</sub>E<sub>4</sub> owing to a charging of the C<sub>8</sub>E<sub>4</sub>-micelles. The extent of the CP-shift increased monotonically from the smallest (highest charge density) to the largest (smallest charge density) dodecaborate, i.e. from B<sub>12</sub>H<sub>12</sub><sup>2-</sup> to B<sub>12</sub>I<sub>12</sub><sup>2-</sup>. The largest dodecaborates B<sub>12</sub>Br<sub>12</sub><sup>2-</sup> and B<sub>12</sub>I<sub>12</sub><sup>2-</sup> additionally evoked the appearance of a lyotropic bilayer phase at elevated temperatures. It was concluded that B<sub>12</sub>Br<sub>12</sub><sup>2-</sup> and B<sub>12</sub>I<sub>12</sub><sup>2-</sup> intercalate partially between the hydrophobic surfactant tails causing a decrease in the curvature of the micelles and a transition towards the bilayer phase upon heating. This deep penetration into the micelles displays the hydrophobic nature of the dodecaborate ions B<sub>12</sub>Br<sub>12</sub><sup>2-</sup> and B<sub>12</sub>I<sub>12</sub><sup>2-</sup>. Furthermore, upon increasing the B<sub>12</sub>I<sub>12</sub><sup>2-</sup>-concentration in the micellar phase present at room temperature, the adsorbed number of B<sub>12</sub>I<sub>12</sub><sup>2-</sup> per micelle increased continuously causing a destabilization of the micellar phase at 60 mM

$B_{12}I_{12}^{2-}$ . This behavior of  $B_{12}I_{12}^{2-}$  cannot be described by a Langmuir isotherm in contrast to the previously discussed superchaotropic SiW. Additionally, it was observed that adsorbed  $B_{12}I_{12}^{2-}$  on the micelles is quite resistant to heating, as it remained on the  $C_8E_4$ -micelles even at high temperatures again in direct contrast to the superchaotropic SiW that desorbed from the  $C_8E_4$ -micelles upon heating. The mentioned results emphasized that  $B_{12}I_{12}^{2-}$  exhibits superchaotropic as well as hydrophobic traits.

On the hydrophobic end of the ionic series, the ions  $BPh_4^-$ , COSAN and  $PW_{12}O_{40}^{3-}$  were discussed. These three ions caused a tremendous increase in the CP of  $C_8E_4$ , the emergence of extensive lyotropic bilayer phases and a destabilization of the micellar phases leading to precipitation at low millimolar nano-ion concentrations ( $c < 20$  mM). These observations are in line with existing literature denoting hydrophobic ions as soft matter disruptors that intercalate between surfactant tails and break the self-assemblies.<sup>34,35</sup>

By comparing all the discussed nano-ion classes, an ordering spanning from classical chaotropic over superchaotropic to hydrophobic ions was established regarding the effects of the nano-ions on the phase behavior of  $C_8E_4$ , including the CP-evolution, the emergence of bilayer phases and precipitation. The established series corresponded well with the inverse ordering of the ions by their volume charge densities and showed the general trend: The lower the charge density, the higher is the superchaotropic or hydrophobic character of an ion.

## 2.8. Résumé du chapitre en français

Dans ce chapitre, le comportement de phase du tensioactif non ionique  $C_8E_4$  a été utilisé comme sonde pour étudier les effets des espèces ioniques allant des ions chaotropes classiques, tels que le  $SCN^-$ , aux nano-ions superchaotropes, tels que les dodécaborates et les polyoxométalates de Keggin, en passant par les grands ions organiques, tels que le  $BPh_4^-$ . La phase micellaire de l'agent de surface non ionique  $C_8E_4$  présente une température de point trouble (PT) caractéristique, sensible à la présence de sels, et les évolutions du PT en fonction de la concentration en sels se manifestent directement dans l'ordre Hofmeister des ions classiques. Par conséquent, le comportement des micelles  $C_8E_4$  et son comportement en phase macroscopique constituent des indicateurs sensibles pour examiner les effets des ions. Comme on sait que les ions chaotropiques provoquent un léger chargement des micelles de tensioactif non ionique, un système de référence permettant de déterminer l'effet de la charge a été établi. À cette fin, le dodécylsulfate de sodium (SDS), un tensioactif ionique, a été ajouté en faibles quantités à des solutions de  $C_8E_4$ . Le SDS se mélange spontanément avec les micelles non-ioniques de  $C_8E_4$  et rend ainsi les micelles partiellement ioniques sans affecter la forme et la taille des micelles. La stabilisation observée de la phase micellaire, qui se reflète dans une formidable augmentation du PT, était attribuée à un effet électrostatique, car l'ajout de l'électrolyte NaCl a provoqué un écrantage et un retour à la stabilité du  $C_8E_4$  pur. En présence de nano-ions (POMs de Keggin, clusters de bore et grands ions organiques), des décalages de PT vers des températures plus élevées ont également été observés en raison de la charge micellaire émergente lors de l'association du nano-ion avec la micelle de  $C_8E_4$ . L'ampleur de l'augmentation du PT varie fortement, allant de faibles effets des ions chaotropiques à des effets considérables pour les nano-ions les plus superchaotropiques ou hydrophobes, modifiant même profondément le comportement de phase de  $C_8E_4$ . Les effets sur le comportement de phase du  $C_8E_4$  ont d'abord été discutés au sein de chaque groupe chimique avant de comparer tous les nano-ions entre eux.

Les POMs de Keggin  $H_2W_{12}O_{40}^{6-}$ ,  $BW_{12}O_{40}^{5-}$ ,  $SiW_{12}O_{40}^{4-}$  and  $PW_{12}O_{40}^{3-}$  ont augmenté le PT de  $C_8E_4$ , où plus la charge (densité) de l'ion de Keggin était faible, plus l'interaction avec les micelles  $C_8E_4$  et l'augmentation du CP étaient fortes :  $H_2W_{12}O_{40}^{6-} < BW_{12}O_{40}^{5-} < SiW_{12}O_{40}^{4-} < PW_{12}O_{40}^{3-}$ . En tant que nano-ion modèle, l'accent a été mis sur l'ion Keggin SiW ( $SiW_{12}O_{40}^{4-}$ ), qui a induit des effets modérés sur le PT de  $C_8E_4$  et était précédemment nommé ion superchaotrope.<sup>4,92</sup> Le SAXS et le SANS ont révélé ici que SiW s'adsorbe fortement sur les micelles non-ioniques de  $C_8E_4$  interagissant principalement avec les trois groupes éthoxy

extérieurs de la tête hydrophile de C<sub>8</sub>E<sub>4</sub>. Le nombre de molécules de SiW adsorbées par micelle s'est avéré augmenter fortement à de faibles concentrations de SiW et saturer à de fortes concentrations de SiW et pourrait être décrit entièrement à l'aide d'un formalisme isotherme de Langmuir. Cette étude a fourni la première quantification complète de l'adsorption d'un ion superchaotropique sur un système de matière molle et a mis en évidence qu'elle est régie par les mêmes paramètres, tout comme la sorption des gaz sur les adsorbants solides. De plus, il a été démontré que le chauffage avait des effets importants sur l'équilibre de l'adsorption de SiW sur les micelles de C<sub>8</sub>E<sub>4</sub>, car le nombre de SiW adsorbé par micelle diminuait fortement avec la température. L'analyse de ces équilibres d'adsorption via un diagramme de van't Hoff a montré que le phénomène d'adsorption superchaotropique est conduit par enthalpie accompagnée d'une pénalité entropique. Il a précédemment été démontré que cette signature thermodynamique caractéristique résulte de la liaison d'ions superchaotropiques à la cavité hydrophobe des molécules hôtes macrocycliques, ce qui entraîne une récupération de la structure de l'eau.<sup>3</sup> Le même mécanisme est en jeu pour l'adsorption de SiW sur la micelle de C<sub>8</sub>E<sub>4</sub>. Les eaux d'hydratation de l'ion et des têtes de C<sub>8</sub>E<sub>4</sub> sont rejetées lors de l'adsorption et vont dans la masse d'eau, ce qui entraîne une récupération de la structure intrinsèque de l'eau. L'effet superchaotropique peut donc être compris comme une force motrice générale dans tout phénomène d'association matière molle/nano-ion. En étudiant les micelles de C<sub>8</sub>E<sub>4</sub> décorées de SiW en solution électrolytique, il est observé que le PT chutait bien au-delà de la référence, un phénomène très différent du comportement des micelles mixtes C<sub>8</sub>E<sub>4</sub>/SDS. Il a été conclu qu'un ion superchaotropique ne charge pas seulement les micelles non-ioniques de C<sub>8</sub>E<sub>4</sub> mais provoque également une forte déshydratation des têtes polaires du C<sub>8</sub>E<sub>4</sub>, ce qui rend les micelles plus hydrophobes et ne se manifeste qu'en présence d'un électrolyte, car sinon la répulsion intermicelle voile l'effet de déshydratation. En outre, il a été démontré que la présence d'électrolyte tel que NaCl ou Na<sub>2</sub>SO<sub>4</sub> n'affecte pas l'équilibre d'adsorption de SiW.

En outre, des nano-ions du type dodécaborate B<sub>12</sub>H<sub>12</sub><sup>2-</sup>, B<sub>12</sub>F<sub>12</sub><sup>2-</sup>, B<sub>12</sub>Cl<sub>12</sub><sup>2-</sup>, B<sub>12</sub>Br<sub>12</sub><sup>2-</sup> et B<sub>12</sub>I<sub>12</sub><sup>2-</sup> ont été étudiés dans des solutions du tensioactif non-ionique C<sub>8</sub>E<sub>4</sub> en utilisant la même approche expérimentale (détermination du PT, SAXS, SANS). Tous les dodécaborates ont induit une augmentation du PT de C<sub>8</sub>E<sub>4</sub> en raison d'un chargement électrique des micelles de C<sub>8</sub>E<sub>4</sub>. L'ampleur du décalage du PT augmente de façon monotone du plus petit (densité de charge la plus élevée) au plus grand (densité de charge la plus faible) dodécaborate, c'est-à-dire de B<sub>12</sub>H<sub>12</sub><sup>2-</sup> à B<sub>12</sub>I<sub>12</sub><sup>2-</sup>. Les dodécaborates de plus grande taille B<sub>12</sub>Br<sub>12</sub><sup>2-</sup> et B<sub>12</sub>I<sub>12</sub><sup>2-</sup> ont en outre évoqué l'apparition d'une phase bicouche lyotrope à des températures élevées. Il a été conclu

que ces dodécaborates s'intercalent partiellement entre les queues hydrophobes de C<sub>8</sub>E<sub>4</sub>, entraînant une diminution de la courbure des micelles et une transition vers la phase bicouche. Cette pénétration en profondeur dans les micelles montre la nature hydrophobe des dodécaborates B<sub>12</sub>Br<sub>12</sub><sup>2-</sup> and B<sub>12</sub>I<sub>12</sub><sup>2-</sup>. De plus, en augmentant la concentration de B<sub>12</sub>I<sub>12</sub><sup>2-</sup> dans la phase micellaire présente à température ambiante, on a constaté que le nombre de B<sub>12</sub>I<sub>12</sub><sup>2-</sup> adsorbé par micelle augmentait continuellement et causait une déstabilisation de la phase micellaire à 60 mM de B<sub>12</sub>I<sub>12</sub><sup>2-</sup>. Ce comportement du B<sub>12</sub>I<sub>12</sub><sup>2-</sup> ne peut pas être décrit par un isotherme de Langmuir, contrairement au SiW superchaotrope dont nous avons parlé précédemment. En outre, le B<sub>12</sub>I<sub>12</sub><sup>2-</sup> adsorbé sur les micelles est très résistant au chauffage car il reste principalement sur les micelles de C<sub>8</sub>E<sub>4</sub>, même à haute température, ce qui contraste encore avec le SiW. Les résultats présentés soulignent que le B<sub>12</sub>I<sub>12</sub><sup>2-</sup> présente des caractéristiques superchaotropiques et hydrophobes.

À l'extrémité hydrophobe de la série ionique, les ions BPh<sub>4</sub><sup>-</sup>, COSAN et PW<sub>12</sub>O<sub>40</sub><sup>3-</sup> ont été examinés. Ces trois ions ont provoqué une augmentation considérable du PT de C<sub>8</sub>E<sub>4</sub>, l'émergence de phases bicouches lyotropes étendues et une déstabilisation des phases micellaires conduisant à des précipitations à de faibles concentrations millimolaires de nano-ions (c<20 mM). Ces observations sont conformes à la littérature existante qui désigne les ions hydrophobes comme des perturbateurs de la matière molle qui s'intercalent entre les queues des agents de surface et brisent les auto-assemblages.<sup>34,35</sup>

Dans l'ensemble, un ordre allant des ions chaotrope classiques aux ions hydrophobes en passant par les ions superchaotropiques a été établi concernant les effets des nano-ions sur le comportement des phases du C<sub>8</sub>E<sub>4</sub>, y compris l'évolution du PT, l'émergence des phases bicouches et la précipitation. Les séries établies correspondent bien à l'ordre inverse des ions selon leur densité de charge volumique et montrent la tendance générale : Plus la densité de charge est faible, plus le caractère superchaotrope ou hydrophobe d'un ion est élevé.

## 2.9. SAXS- and SANS-fit parameters used in this chapter

**SANS:** The SANS-spectra contain exclusively the scattering of the C<sub>8</sub>E<sub>4</sub>-micelles. The fitting procedure is elaborated in section 7.3.1. Generally, a slight polydispersity of around 0.15 was used on the (equatorial) radius.

Table 14: Best fit parameters of ellipsoidal form factors used in the SANS-fits throughout the present chapter. R<sub>eq</sub> and R<sub>pol</sub> are the equatorial and polar radius of the ellipsoidal form factor. ACS=Equivalent averaged curvature sphere

Figure	Sample composition				T [°C]	Φ <sub>mic</sub> [nm <sup>-3</sup> ]	C <sub>8</sub> E <sub>4</sub> -micelle				Hayter-MSA S(q)			
	[C <sub>8</sub> E <sub>4</sub> ] [mM]	nano-ion or SDS	[nano-ion] [mM]	[NaCl] [mM]			Ellipsoidal core-shell P(q)				Hayter-MSA S(q)			
							ρ <sub>mic</sub> *10 <sup>-6</sup> [Å <sup>-2</sup> ]	ρ <sub>H2O</sub> *10 <sup>-6</sup> [Å <sup>-2</sup> ]	R <sub>eq</sub> [nm]	R <sub>pol</sub> [nm]	Φ <sub>mic</sub>	R <sub>HS</sub> [nm]	Charge q <sub>e</sub>	[Salt] [mol/l]
10	60	-	-	0	20	0.016	0.4	6.3	1.6	6	-	-	-	-
9, 10	60	SDS	1	0	20	0.016	0.4	6.3	1.6	6.7	0.016	ACS <sup>1</sup>	3.9	0.001
10	60	SDS	1	0	35	0.016	0.4	6.3	1.7	16.5	0.016	ACS	15	0.001
9, 10	60	SDS	1	0	60	0.016	0.4	6.3	11.5	1.3	0.016	ACS	60	0.001
9, 10	60	SDS	1	100	20	0.016	0.4	6.3	1.6	7.4	-	-	-	-
16	60	SiW	0.1	0	20	0.016	0.4	6.3	1.6	7.8	0.016	ACS	2	0.0001
16	60	SiW	1	0	20	0.016	0.4	6.3	1.6	6.6	0.016	ACS	8	0.0001
16	60	SiW	2.5	0	20	0.016	0.4	6.3	1.8	4.5	0.016	ACS	14	0.001
16	60	SiW	5	0	20	0.016	0.4	6.3	1.6	3.0	0.016	ACS	16	0.001
16	60	SiW	10	0	20	0.016	0.4	6.3	1.7	1.7	0.016	ACS	20	0.006
20	60	SiW	1	0	40	0.016	0.4	6.3	1.7	8.4	0.016	ACS	11	0.0001
20	60	SiW	1	0	60	0.016	0.4	6.3	5.7	1.6	0.016	ACS	11	0.0003
28	60	SiW	1	10	20	0.016	0.4	6.3	1.6	9.2	0.016	ACS	8	0.003
28	60	SiW	1	10	40	0.016	0.4	6.3	1.8	17.5	0.016	ACS	18	0.004
23,28	60	SiW	1	10	60	0.016	0.4	6.3	10	1.4	-	-	-	-
23	60	SiW	1	20	20	0.016	0.4	6.3	1.6	8.0	-	-	-	-
23	60	SiW	1	50	20	0.016	0.4	6.3	1.6	16.8	-	-	-	-
23	60	SiW	1	100	20	0.016	0.4	6.3	1.7	17.3	-	-	-	-



## 2. Nano-ions in interaction with non-ionic surfactant micelles

Continuation Table 14

Figure	Sample composition				T [°C]	$\Phi_{mic}$ [nm <sup>-3</sup> ]	C <sub>8</sub> E <sub>4</sub> -micelle							
	[C <sub>8</sub> E <sub>4</sub> ] [mM]	nano-ion or SDS [mM]	[nano-ion] [mM]	[NaCl] [mM]			Ellipsoidal core-shell P(q)				Hayter-MSA S(q)			
							$\rho_{mic}$ *10 <sup>-6</sup> [Å <sup>-2</sup> ]	$\rho_{H2O}$ *10 <sup>-6</sup> [Å <sup>-2</sup> ]	R <sub>eq</sub> [nm]	R <sub>pol</sub> [nm]	$\Phi_{mic}$ [nm]	R <sub>HS</sub> [nm]	Charge, q <sub>e</sub>	[Salt] [mol/l]
32	60	B <sub>12</sub> Cl <sub>12</sub> <sup>2-</sup>	1	0	20	0.016	0.4	6.3	1.6	9.5	0.016	ACS	11	0.002
32, 38	60	B <sub>12</sub> Cl <sub>12</sub> <sup>2-</sup>	1	5	20	0.016	0.4	6.3	1.6	7.1	-	-	-	-
32	60	B <sub>12</sub> Cl <sub>12</sub> <sup>2-</sup>	1	100	20	0.016	0.4	6.3	1.7	17	-	-	-	-
32	60	B <sub>12</sub> Br <sub>12</sub> <sup>2-</sup>	1	0	20	0.016	0.4	6.3	1.6	10.2	0.016	ACS	16	0.002
32, 38	60	B <sub>12</sub> Br <sub>12</sub> <sup>2-</sup>	1	5	20	0.016	0.4	6.3	1.6	7.3	-	-	-	-
32	60	B <sub>12</sub> Br <sub>12</sub> <sup>2-</sup>	1	100	20	0.016	0.4	6.3	1.7	22	-	-	-	-
38	60	B <sub>12</sub> I <sub>12</sub> <sup>2-</sup>	1	5	20	0.016	0.4	6.3	1.8	8	-	-	-	-
41	60	BPh <sub>4</sub> <sup>-</sup>	1	0	20	0.016	0.4	6.3	1.7	13.5	0.016	ACS	14	0.001
41	60	BPh <sub>4</sub> <sup>-</sup>	1	5	20	0.016	0.4	6.3	1.6	15	-	-	-	-
41	60	BPh <sub>4</sub> <sup>-</sup>	1	0	50	0.016	0.4	6.3	1.4	1.5	0.016	ACS	65	0.001

Table 15: Best fit parameters of flexible cylinder form factors used in the SANS-fits throughout the present chapter. R is the radius of the cylinder, L the length and l<sub>p</sub> the Kuhn length.

Figure	Sample composition				T [°C]	$\Phi_{mic}$ [nm <sup>-3</sup> ]	Flexible cylinder P(q)					Hayter-MSA S(q)			
	[C <sub>8</sub> E <sub>4</sub> ] [mM]	nano-ion or SDS [mM]	[nano-ion] [mM]	[NaCl] [mM]			$\rho_{mic}$ *10 <sup>-6</sup> [Å <sup>-2</sup> ]	$\rho_{H2O}$ *10 <sup>-6</sup> [Å <sup>-2</sup> ]	R [nm]	L [nm]	l <sub>p</sub> [nm]	$\Phi_{mic}$ [nm]	R <sub>HS</sub> [nm]	Charge, q <sub>e</sub>	[Salt] [mol/l]
10	60	-	-	100	35	0.016	0.4	6.3	16	84	9.8	-	-	-	-
10	60	SDS	1	100	35	0.016	0.4	6.3	1.6	113	9.6	-	-	-	-
41	60	BPh <sub>4</sub> <sup>-</sup>	1	100	20	0.016	0.4	6.3	1.6	38	16	-	-	-	-

Table 16: Best fit parameters of the vesicle form factor used in the SANS-fits throughout the present chapter. R is the vesicle radius and d the thickness of the surfactant layer.

Figure	Sample composition				T [°C]	$\Phi_{bilayer}$ [nm <sup>-3</sup> ]	Vesicle P(q)			
	[C <sub>8</sub> E <sub>4</sub> ] [mM]	nano-ion or SDS [mM]	[nano-ion] [mM]	[NaCl] [mM]			$\rho_{bilayer}$ *10 <sup>-6</sup> [Å <sup>-2</sup> ]	$\rho_{H2O}$ *10 <sup>-6</sup> [Å <sup>-2</sup> ]	R [nm]	d [nm]
41	60	BPh <sub>4</sub> <sup>-</sup>	1	0	60	0.016	0.4	6.3	34	2.4

## 2. Nano-ions in interaction with non-ionic surfactant micelles

### SAXS:

As the SAXS-spectra contain the scattering of individual POM-molecules as well as the scattering of decorated micelles the fits comprise two contributions. The fitting procedure is elaborated in section 7.3.2..

Table 17: Best fit parameters used in the SAXS-fits throughout the present chapter.

Figure	Sample composition				T [°C]	$\eta_{mic}$ [nm <sup>-3</sup> ]	Decorated micelle											Nano-ion			
	[C <sub>8</sub> E <sub>4</sub> ] [mM]	nano-ion [mM]	[nano-ion] [mM]	[NaCl] [mM]			Ellipsoidal core-shell P(q)						Hayter-MSA S(q)					Sphere P(q)		Hard sphere S(q)	
							$\rho_{core}$ *10 <sup>-6</sup> [Å <sup>-2</sup> ]	$\rho_{shell}$ *10 <sup>-6</sup> [Å <sup>-2</sup> ]	$\rho_{H_2O}$ *10 <sup>-6</sup> [Å <sup>-2</sup> ]	R <sub>eq</sub> [nm]	R <sub>pol</sub> [nm]	dR [nm]	$\Phi_{mic}$ [nm]	R <sub>HS</sub> [nm]	Charge, q <sub>e</sub>	[Salt] [mol/l]	$\eta_{nano-ion}$ [nm <sup>-3</sup> ]	r [nm]	$\rho_{nano-ion}$ *10 <sup>-6</sup> [Å <sup>-2</sup> ]	$\Phi_{POM}$	R <sub>HS</sub> [nm]
13, 16	0	SiW	10	0	20	-	-	-	-	-	-	-	-	-	-	-	0.006	0.43	74.9	-	-
16	60	SiW	1	0	20	0.00022	9.4	9.93	9.4	1.3	6.2	0.92	0.016	2.7	11	0.001	0.0006	0.43	74.9	0.145	1.41
16	60	SiW	2.5	0	20	0.0003	9.4	10.74	9.4	1.4	3.6	0.92	0.016	2.4	12	0.001	0.0015	0.43	74.9	0.19	1.33
16	60	SiW	5	0	20	0.00042	9.4	11.6	9.4	1.36	2.5	0.92	0.016	2.0	16	0.001	0.003	0.43	74.9	0.165	1.12
16	60	SiW	10	0	20	0.0007	9.4	12.8	9.4	1.46	1.46	0.92	0.016	1.8	20	0.006	0.006	0.43	74.9	0.141	0.86
16	60	SiW	15	0	20	0.0007	9.4	13.15	9.4	1.45	1.45	0.92	0.016	1.75	22	0.013	0.009	0.42	74.9	0.09	0.75
16	60	SiW	20	0	20	0.0007	9.4	13.4	9.4	1.45	1.45	0.92	0.016	1.56	25	0.035	0.012	0.43	74.9	0.09	0.8
16	60	SiW	30	0	20	0.0007	9.4	13.7	9.4	1.4	1.4	0.92	0.016	1.51	25	0.04	0.018	0.43	74.9	0.61	0.8
16	60	SiW	40	0	20	0.0007	9.4	13.7	9.4	1.4	1.4	0.92	0.016	1.45	25	0.05	0.024	0.43	74.9	0.61	0.8
20	60	SiW	1	0	40	0.00015	9.4	9.84	9.4	1.4	7.9	0.92	0.016	2.9	13	0.001	0.0006	0.43	74.9	0.145	1.45
20	60	SiW	1	0	60	0.00007	9.4	9.62	9.4	5.5	1.4	0.92	-	-	-	-	0.0006	0.43	74.9	0.081	1.55
28	60	SiW	1	10	20	0.0002	9.4	9.93	9.4	1.3	7	0.92	0.016	3.5	12	0.01	0.0006	0.43	74.9	0.145	1.4
28	60	SiW	1	10	40	0.00007	9.4	9.85	9.4	1.4	7.9	0.92	-	-	-	-	0.0006	0.43	74.9	0.15	1.52
28	60	SiW	1	10	60	0.00003	9.4	9.74	9.4	5.5	1.4	0.92	-	-	-	-	0.0006	0.43	74.9	0.13	1.6
23	60	SiW	1	20	20	0.00018	9.4	9.98	9.4	1.3	7.5	0.92	-	-	-	-	0.0006	0.43	74.9	0.145	1.4
23	60	SiW	1	50	20	0.00008	9.4	10	9.4	1.35	16.6	0.92	-	-	-	-	0.0006	0.43	74.9	0.145	1.4
23	60	SiW	1	100	20	0.00008	9.4	10	9.4	1.37	16.9	0.92	-	-	-	-	0.0006	0.43	74.9	0.15	1.42

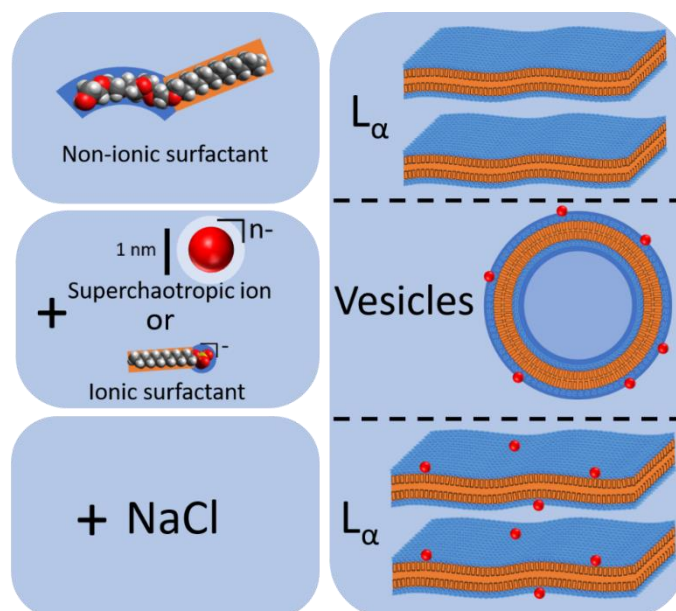
## 2. Nano-ions in interaction with non-ionic surfactant micelles

Continuation Table 17

Figure	Sample composition				T [°C]	$n_{mic}$ [nm <sup>-3</sup> ]	Decorated micelle							Nano-ion							
	[C <sub>8</sub> E <sub>4</sub> ] [mM]	nano-ion [mM]	[nano-ion] [mM]	[NaCl] [mM]			Ellipsoidal core-shell P(q)				Hayter-MSA S(q)			Sphere P(q)		Hard sphere S(q)					
							$\rho_{core}$ *10 <sup>-6</sup> [Å <sup>-2</sup> ]	$\rho_{shell}$ *10 <sup>-6</sup> [Å <sup>-2</sup> ]	$\rho_{H_2O}$ *10 <sup>-6</sup> [Å <sup>-2</sup> ]	$R_{eq}$ [nm]	$R_{pot}$ [nm]	dR [nm]	$\Phi_{mic}$	$R_{HS}$ [nm]	Charge, q <sub>e</sub>	[Salt] [mol/l]	$n_{nano-ion}$ [nm <sup>-3</sup> ]	r [nm]	$\rho_{nano-ion}$ *10 <sup>-6</sup> [Å <sup>-2</sup> ]	$\Phi_{POM}$	$R_{HS}$ [nm]
30	0	B <sub>12</sub> Br <sub>12</sub> <sup>2-</sup>	10	150	20	-	-	-	-	-	-	-	-	-	-	-	0.006	0.42	31.9	-	-
30	60	B <sub>12</sub> Br <sub>12</sub> <sup>2-</sup>	10	0	20	0.0007	9.4	10.8	9.4	1.55	1.55	0.8	0.016	2.1	14	0.001	0.006	0.42	31.9	0.17	0.92
30, 33	0	B <sub>12</sub> I <sub>12</sub> <sup>2-</sup>	10	150	20	-	-	-	-	-	-	-	-	-	-	-	0.006	0.44	37.5	-	-
33	0	B <sub>12</sub> I <sub>12</sub> <sup>2-</sup>	40	0	20	-	-	-	-	-	-	-	-	-	-	-	0.024	0.44	37.5	-	-
30, 33	60	B <sub>12</sub> I <sub>12</sub> <sup>2-</sup>	10	0	20	0.0007	9.4	11.4	9.4	1.3	1.3	1.1	0.016	2.3	13	0.001	0.006	0.44	37.5	0.15	0.59
33	60	B <sub>12</sub> I <sub>12</sub> <sup>2-</sup>	15	0	20	0.0007	9.4	11.75	9.4	1.1	1.1	1.3	0.016	2.1	14	0.001	0.009	0.44	37.5	0.135	0.59
32	60	B <sub>12</sub> I <sub>12</sub> <sup>2-</sup>	20	0	20	0.0007	9.4	12.05	9.4	1.1	1.1	1.25	0.016	2.1	36	0.02	0.012	0.44	37.5	0.113	0.55
33	60	B <sub>12</sub> I <sub>12</sub> <sup>2-</sup>	30	0	20	0.0007	9.4	12.6	9.4	0.98	0.98	1.3	0.016	1.9	38	0.025	0.0018	0.44	37.5	0.077	0.49
33	60	B <sub>12</sub> I <sub>12</sub> <sup>2-</sup>	40	0	20	0.0007	9.4	12.73	9.4	0.9	0.9	1.4	0.016	1.7	30	0.04	0.0024	0.44	37.5	0.054	0.46



### 3. How nano-ions act like ionic surfactants



Scheme 7: Superchaotropic nano-ions and ionic surfactants cause the transition of a non-ionic surfactant lamellar phase towards vesicles. Reversion towards the lamellar phase occurs upon salt addition.

The previous chapter dealt with the effect of nanometric ions on the behavior of the non-ionic surfactant  $C_8E_4$ , which exclusively forms micellar phases in water and, thus, features the simplest possible phase behavior for non-ionic surfactants. A focus was set on the differences between the individual nano-ions based on previous literature by Buchecker and Naskar et al.<sup>4,92</sup> As an extension, in this chapter the effect of the nano-ions is elucidated on a richer surfactant phase behavior. To this end, the non-ionic surfactant pentaethyleneglycol n-dodecylether ( $C_{12}E_5$ , see Figure 47a) was chosen as a model system, as it forms lyotropic bilayer phases in dilute aqueous solution. It will be shown systematically how nano-ions can serve as powerful agents to tune the rich phase behavior of  $C_{12}E_5$  in a fashion similar to classical ionic surfactants. The present chapter aims to harness the superchaotropic property of these nano-ions and presents a steppingstone towards applications that may include inorganic nano-ions as alternatives to organic ionic surfactants.

### 3.1. C<sub>12</sub>E<sub>5</sub> in dilute aqueous solutions

First, the phase characteristics of C<sub>12</sub>E<sub>5</sub> in the absence of nano-ions shall be established. Its behavior in bare water<sup>165</sup> is well known and has served as a rich model system to investigate the effects of additives<sup>143,166,167</sup>. For the purpose of this thesis, the focus is set on the phase behavior of C<sub>12</sub>E<sub>5</sub> in dilute aqueous solution, which for 0.5 – 10 wt-% is shown in Figure 47b.

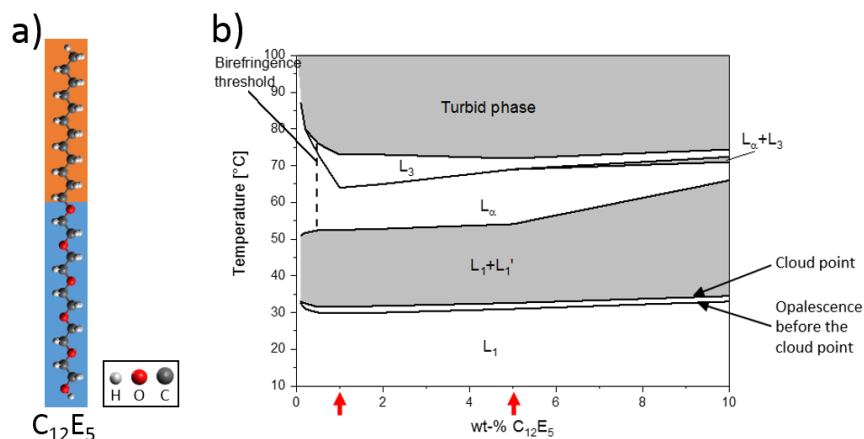


Figure 47: a) Scheme of the molecular structure of the non-ionic surfactant C<sub>12</sub>E<sub>5</sub>; hydrophobic part in orange, hydrophilic part in blue b) Phase diagram of 0.5-10 wt% C<sub>12</sub>E<sub>5</sub> in water. Below 0.5 wt% C<sub>12</sub>E<sub>5</sub>, birefringence of the bilayer phases becomes too weak visually making phase identification impossible. The two red arrows indicate the surfactant concentrations, to which nano-ions were added. Phase assignments: L<sub>1</sub> denotes a micellar phase, L<sub>α</sub> a lamellar phase and L<sub>3</sub> a sponge phase. The turbid phase at high temperatures comprises diverse multiphases involving L<sub>1</sub>, L<sub>α</sub>, L<sub>3</sub> and L<sub>2</sub> (inverse micellar) phases.

C<sub>12</sub>E<sub>5</sub> displays the classical phase sequence of long chain ethoxylated surfactants: At low temperatures, a transparent, non-birefringent micellar L<sub>1</sub>-phase is present. Upon heating, the hydrophilic surfactant heads are gradually dehydrated, which leads to an increase of the packing parameter and drives the morphological transition of spherical micelles into cylindrical ones.<sup>128</sup> In the case of C<sub>12</sub>E<sub>5</sub> micelles, the micelles grow substantially and even become large enough to merge and form an “infinite” connected micellar network, which gives rise to bluish opalescence just before the cloud point (CP).<sup>129,168,169</sup> At the CP at 30°C, the micellar phase separates into a dilute and a concentrated micellar phase, denoted as L<sub>1</sub>+L<sub>1</sub>'. At higher temperatures, above 50°C this two-phasic region then transitions into a lamellar phase, denoted as L<sub>α</sub>. A lamellar phase is a two-dimensional stacking of bilayers. Thus, L<sub>α</sub>-phases are inherently anisotropic, and consequently show birefringence between crossed polarizers. Furthermore, due to the characteristic interlamellar distances they may show bluish opalescence and with increasing surfactant concentration so-called “Schlieren” patterns, i.e. optical inhomogeneities caused by fluctuations of the refractive index in solution. Upon heating of the L<sub>α</sub>-phase, a sponge phase forms, which is denoted as L<sub>3</sub>. According to the definition by D.

Roux, a  $L_3$ -phase is “a spongelike random surface of bilayer that divides space into two interpenetrating solvent labyrinths”.<sup>170</sup> At low  $C_{12}E_5$ -concentrations, the  $L_3$ -phase is bluish opalescent and turns completely colorless at higher concentrations.  $L_3$ -phases are inherently isotropic, however, may show birefringence under stirring because the bilayer network gets temporarily disrupted. Further heating above  $70^\circ\text{C}$  induces phase demixing, which is indicated with the turbid phase at high temperatures. In this turbid region, multiphases exist comprised of  $L_1$ ,  $L_\alpha$ ,  $L_3$  and  $L_2$  phases, which were not further identified.

The described phase behavior is with slight deviations in tune with the phase diagram by Strey et al.<sup>165</sup> The red arrows in Figure 47b indicate the  $C_{12}E_5$ /water compositions to which nano-ions were added. In the following section, the effects of nano-ions on 1 wt%  $C_{12}E_5$  will be discussed and later-on the effects of changing  $C_{12}E_5$ -concentration will be presented.

### 3.2. Nano-ions in dilute $C_{12}E_5$

Nanometer-sized ions span over a wide variety of different molecular architectures involving Keggin polyoxometalates (POMs), diverse boron clusters of the dodecaborate and metallabisdicarbollide type and hydrophobic ions such as tetraphenylborate. All these nano-ions, see Figure 48a, owing to their weak hydration in water<sup>36</sup> exhibit a strong propensity towards environments that are less polar than water. Thus, they have a marked propensity to populate the air water-interface<sup>54,55,118,144</sup> and to assemble with dispersed non-ionic soft matter systems including polymers<sup>104,122</sup>, non-ionic micelles<sup>4,92,164</sup>, hydrophobic cavities in macrocyclic hosts<sup>65–67,109,124</sup> and colloidal latex<sup>5,96</sup> as well as proteins<sup>70,71,123,171</sup>. In all these cases, the nano-ion penetrates into the hydration shell of the soft matter substrate forming close contacts and leading to a release of water molecules from both the substrate and the ion resulting in a bulk water recovery commonly concluded to be driven by the chaotropic effect.<sup>3–5,36,104</sup>

Here, the impact of nano-ions on the dilute phase behavior of the surfactant  $C_{12}E_5$  and its self-assemblies is investigated. Specifically, the composition of 1 wt-%  $C_{12}E_5$  in water was chosen as the phase regions of the bilayer phases  $L_\alpha$  and  $L_3$  are most extensive, see the preceding Figure 47b. Using this composition as a probe, all studied nano-ions (see Figure 48a for their structures) induced qualitatively similar effects as can be seen in section 3.3, besides  $B_{12}H_{12}^{2-}$ , which only exhibits weak chaotropicity. To represent the behavior of the superchaotropic nano-ions the Keggin polyoxometalate  $SiW_{12}O_{40}^{4-}$ , SiW, was chosen as it behaves like a superchaotrope without pronounced hydrophobic character as outline in the preceding chapter. The phase diagram of 1 wt-%  $C_{12}E_5$  as a function of SiW-concentration is shown in Figure 48c.



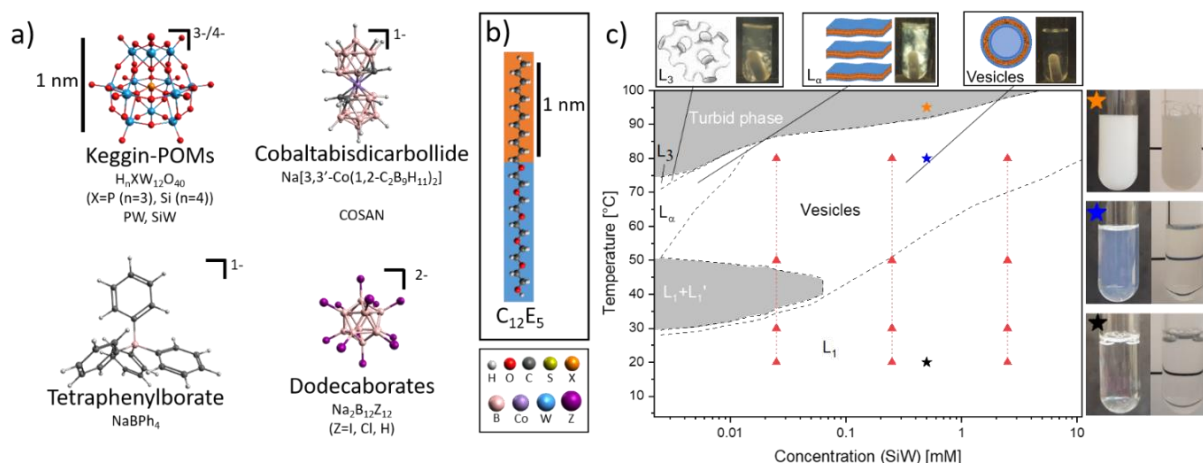


Figure 48: Schemes of the investigated nanometer-sized compounds: The Keggin-POMs silicotungstate (SiW) and phosphotungstate (PW), cobaltabisdicarbollide (COSAN) and the perhalogenated dodecaborates. b) Scheme of the investigated non-ionic surfactant pentaethyleneglycol n-dodecylether,  $C_{12}E_5$ . c) Phase diagram of 1 wt-%  $C_{12}E_5$  (25 mM) in water as a function of the concentration of the Keggin-POM SiW with photos of the macroscopic phases on a white and a black backdrop (right) and between crossed polarizers with schematics of the bilayer phases (top):  $L_3$  is birefringent under stirring (streaming birefringence),  $L_\alpha$  is birefringent, Vesicle phase is non-birefringent. Phase assignments:  $L_1$ -micellar phase,  $L_1'$ -concentrated micellar phase,  $L_\alpha$ -lamellar phase,  $L_3$ -sponge phase. In the turbid phase at high temperatures, different phase separations take place between  $L_3$ -,  $L_\alpha$ -,  $L_1$ - and inverse micellar  $L_2$ -phases. The red triangles indicate the samples measured in SANS and DLS.

At the lowest SiW-concentration ( $[SiW]=2 \mu M$ ), the phase sequence of  $C_{12}E_5$  is equivalent to the phase behavior of bare 1 wt-%  $C_{12}E_5$  in water exhibiting a micellar  $L_1$ -phase below the cloud point at  $30^\circ C$  and a lamellar  $L_\alpha$ -phase from  $50^\circ C$  to  $70^\circ C$  followed by a sponge phase ( $L_3$ ) up to  $75^\circ C$ . Heating above  $75^\circ C$  causes a transition into a turbid phase. Elevation of the SiW-concentration up to  $100 \mu M$  induces tremendous changes in the phase sequence. The micellar phase gets strongly stabilized as the CP is increased, the  $L_3$ -phase vanishes and the  $L_\alpha$ -phase transitions into an extensive vesicle phase. The bilayer phases have clear macroscopic signatures as they all show bluish opalescence to the bare eye. When set between crossed polarizers, however, they can be clearly distinguished because a  $L_\alpha$ -phase is anisotropic and shows strong birefringence. In turn, the  $L_3$ -phase is inherently isotropic and only shows birefringence when temporarily fragmented, e.g. under stirring. For the vesicle phase, no birefringence was observed, which hints at the presence of unilamellar vesicles (ULV) as multilamellar vesicles (MLV) would produce Maltese patterns between crossed polarizers. Photos of the birefringent behavior for the respective phases are shown atop Figure 48c. Additionally, the presence of unilamellar vesicles was confirmed by small angle neutron scattering (SANS). Interestingly, with increasing SiW-concentration, the turbid  $L_1+L_1'$ -phase shrinks and disappears at  $[SiW]=70 \text{ mM}$ . From this concentration on the  $L_1$ -phase transitions directly into the vesicle phase. While the individual ions all caused qualitatively similar effects (except  $B_{12}H_{12}^{2-}$ ), the phase transitions occurred in different concentration regimes. These

quantitative differences are thoroughly discussed in section 3.3 and seem to be related to the ion's volume charge densities. Additionally, this phase sequence is not exclusive to the surfactant  $C_{12}E_5$  and equivalent phase behavior can be observed for any non-ionic surfactant that forms bilayer phases at dilute surfactant concentrations as is shown in the appendix (page 143, section 3.8.8).

SANS was further used to investigate the occurring phase behavior on the microscopic level. Owing to the high sensitivity of neutrons to hydrogenated matter,  $C_{12}E_5$  provides substantial contrast in  $D_2O$ , while SiW produces negligibly low scattering.<sup>106</sup> Therefore, SANS reveals exclusively the alterations to the self-assemblies of  $C_{12}E_5$  upon interaction with SiW. First, the focus is set on the response of  $C_{12}E_5$ -micelles to the presence of SiW at 20°C. The corresponding spectra are shown in Figure 49.

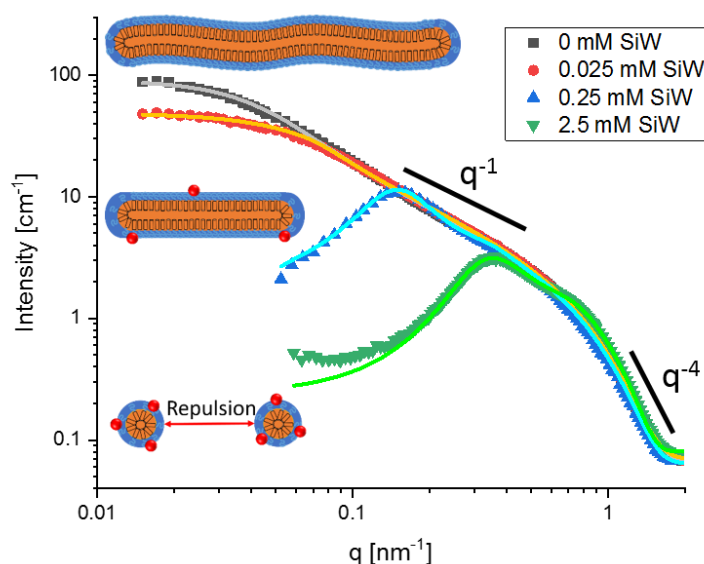


Figure 49: Normalized SANS-spectra of 1 wt-%  $C_{12}E_5$  (25 mM) in  $D_2O$  at 20°C in the micellar  $L_1$ -phase in the presence of SiW ( $SiW_{12}O_{40}^{4-}$ ) (symbols). Full lines represent fits of the data (see text) and the schemes indicate the acquired micellar shapes from flexible cylinders to spheres.

Bare micelles of 1 wt-%  $C_{12}E_5$  in water display a large  $q^{-1}$ -dependence indicating the presence of elongated micelles in tune with literature.<sup>128,129</sup> Upon addition of SiW, the  $q^{-1}$ -dependence shrinks hinting at a shortening of the elongated micelles and a strong intensity decrease arises at low  $q$  that points at emergent intermicellar repulsion. Both phenomena agree with the macroscopically observed CP-increase upon addition of SiW under the pretext that the cloud point always occurs from an aggregation of elongated micelles.<sup>128</sup> Both, the emergent intermicellar repulsion as well as the compression into smaller micelles therefore delay the appearance of the CP. Fitting of the SANS-spectra gave further insight into the micellar dimensions and their interaction potential. The fitting procedure was performed as elaborated

in section 7.3.1 and the used parameters are given in sections 3.8.1-3.8.3. Electrostatically repulsive spherical and flexible (or rigid) cylinder models allowed for a correct fitting of the spectra, see full lines in Figure 49. The micelles of bare  $C_{12}E_5$  in  $D_2O$  have a length of 180 nm with a radius of 2.1 nm. In the presence of SiW, the  $C_{12}E_5$ -micelles are dramatically shortened to a length of 91 and 67 nm at 0.025 mM and 0.25 mM SiW respectively and are compressed into spheres with a radius of 2.4 nm at 2.5 mM SiW. The fitted structure factors of  $C_{12}E_5$ -micelles from 0 mM SiW up to 2.5 mM SiW revealed a continuously increasing micellar charge from 0 to 21  $q_e$ . Analysis of the corresponding SAXS-spectrum at 2.5 mM SiW, supported this notion showing that 6.3 SiW-molecules are adsorbed to each  $C_{12}E_5$ -micelle at 20°C, see below. All parameter used in the SANS fits are shown in section 3.8.

In a second set of SANS experiments, the effect of temperature between 20 and 80°C was investigated on a 1 wt%  $C_{12}E_5$  (25 mM) solution in the presence of 0.025 mM SiW (Figure 59a, page 132), 0.25 mM SiW (Figure 59b, page 132) and 2.5 mM SiW (Figure 50a).

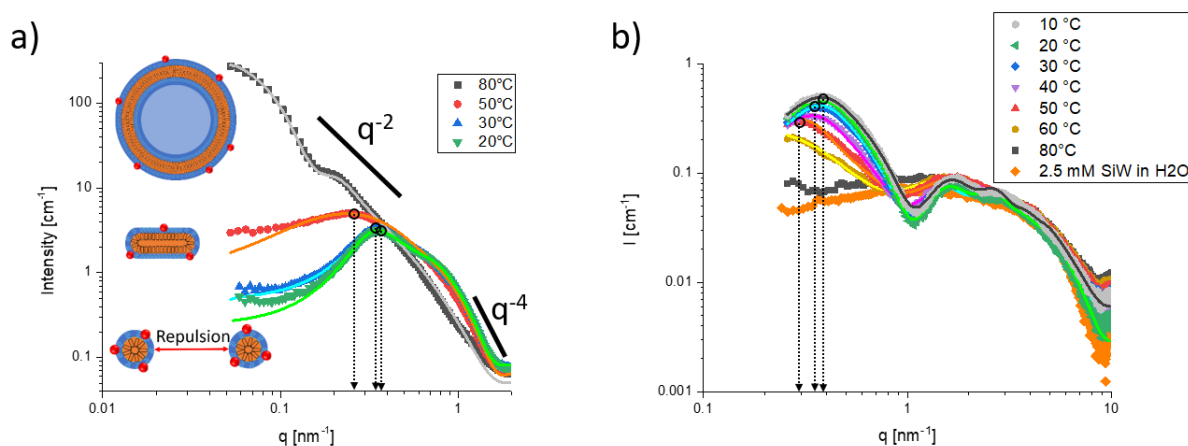


Figure 50: a) SANS-spectra and b) SAXS-spectra of 1 wt-%  $C_{12}E_5$  (25 mM) in  $D_2O$  in SANS and b) in  $H_2O$  in SAXS in the presence of 2.5 mM HSiW at temperatures from 10-80°C. In the SAXS-spectra, the orange diamonds indicate the signal of 2.5 mM HSiW in pure water. The arrows in a) and b) indicate the maxima of the structure factors corresponding to the mean distances between the repelling scatterers for the same respective samples at 20°C, 30°C and 50°C. Intensities are in absolute scale.

Upon heating from 20 to 50°C, the scattered intensity in the low  $q$  range is increased and a  $q^{-1}$ -region arises, indicating that i) the intermicellar repulsive forces decrease and ii) the spherical micelles grow into short cylindrical ones. Therefore, these results suggest that, upon heating, micelles are being dehydrated, and that SiW gradually desorbs from the micelle surface leading to weaker intermicellar repulsions and, hence, to an elongation of the micelles. This interpretation is supported by the fitting results of the SANS spectra and by SAXS (see Figure 50b, discussed below). At 80°C, in the opalescent isotropic phase in the phase diagram, the SANS spectrum is dominated by a  $q^{-2}$ -dependence, indicating the presence of 2D structures,

like the locally planar bilayer of vesicles, and a large oscillation in the low  $q$  range. Here, the fitting of the SANS spectrum with a vesicle model unambiguously confirmed that small unilamellar vesicles (SUVs) with a radius of 18 nm are formed. This value is supported by dynamic light scattering (DLS) yielding a hydrodynamic radius of 27 nm (see section 3.8.6). In contrast to the SANS-spectra, which exclusively reveal the scattering of surfactant  $C_8E_4$ , the SAXS-spectra in Figure 50b contain exclusively the scattering of SiW owing to its high electron density, while the surfactant  $C_{12}E_5$  contributes negligibly to the scattered intensity. Consequently, the SAXS-spectra comprise the scattering of individual SiW-molecules at  $q > 2 \text{ nm}^{-1}$  and the scattering of the SiW-decorated  $C_{12}E_5$ -micelles at  $q < 2 \text{ nm}^{-1}$ . Upon heating the intensity of the decorated micelles at low  $q$  decreases hinting at a gradual desorption of SiW with temperature. Fitting of spectra allows for a precise determination of the number of adsorbed SiW and its adsorption ratio, see section 7.3.2 for the treatment procedure and Table 18 for the acquired parameters. Interestingly, the number of SiW-molecule per micelle is found to increase with temperature. However, as micelles become fewer upon their growth the adsorption ratio of SiW is generally found to decrease with temperature, see Figure 51.

Table 18: Best fit parameters of the SAXS spectra for 25 mM  $C_{12}E_5$  + 2.5 mM HSiW with increasing temperatures using ellipsoidal core-shell form factors.

Temperature [°C]	Number density of micelles $\rho_{mic}$	Core-Shell dimensions			From contrast analysis	
		inner equatorial radius $r_{eq}$ [nm]	inner polar radius $r_{pol}$ [nm]	shell thickness $d$ [nm]	SiW per micelle	SiW adsorption ratio <sup>1</sup> , R
10	0.00017	2.33	2.33	0.9	6.44	0.74
20	0.00017	2.4	2.4	0.9	6.30	0.72
30	0.00015	2.5	2.5	0.9	6.16	0.62
40	0.0001	2.1	4	0.9	6.92	0.46
50	0.00005	2.2	6.8	0.9	9.14	0.33
60	0.00003	2.4	8	0.9	10.96	0.27

$$^1\text{adsorption ratio } R = \frac{[POM]_{adsorbed}}{[POM]_{total}}$$

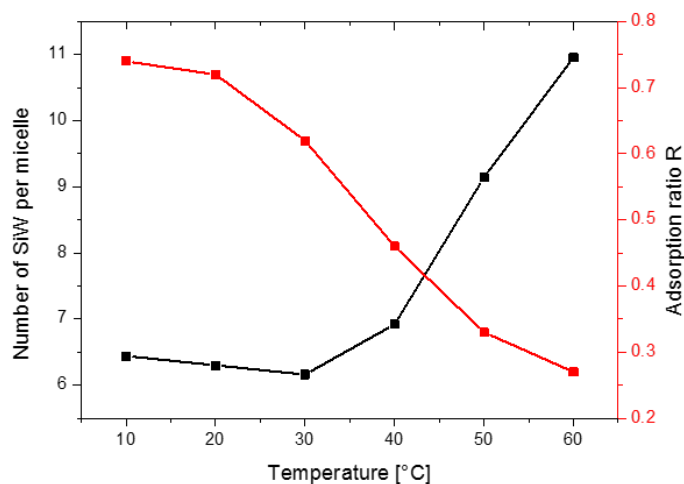


Figure 51: Average number of adsorbed SiW per  $C_{12}E_5$ -micelle and corresponding adsorption ratios obtained from the SAXS-fits of the spectra of 25 mM  $C_{12}E_5$  + 2.5 mM HSiW as a function of temperature in Figure 50b.

Thus, the superchaotropic adsorption of SiW to the  $C_{12}E_5$ -micelles is clearly a reversible phenomenon and depends strongly on the used temperature. These data were already further exploited in section 2.3.4, where it was shown that the adsorption of SiW to ethoxylated micelles is enthalpically driven accompanied by an entropic penalty. This thermodynamic fingerprint was previously demonstrated to arise from the binding of dodecaborates to the hydrophobic cavities in macrocyclic host molecules and provides the general signature of the superchaotropic effect.<sup>3,36</sup> Furthermore, in the vesicle phase at 80°C, only the scattering of the individual SiW-molecules can be observed as the  $q$ -range does not reach low enough to record the scattering of the SiW-decorated vesicles. Nevertheless, SANS has clearly evidenced the formation of vesicles in the presence of SiW here.

Generally, the formation of vesicles out of lamellae requires an energy input to bend the bilayers. This can be done mechanically, for example, by shearing,<sup>172</sup> or chemically with certain additives.<sup>173–175</sup> Dilute lamellar phases of non-ionic surfactants, for example,  $C_{12}E_5$ , turn into vesicles by addition of small amounts of ionic surfactant (chemical method).<sup>143,166,176–178</sup> The transition from the lamellar phase to vesicles was reproduced here by adding the anionic surfactant sodium dodecylsulfate (SDS) to 1 wt-%  $C_{12}E_5$  (see phase diagram in Figure 52) and also at 5 wt-%  $C_{12}E_5$  (see appendix, section 3.4). Interestingly, SDS and nano-ions induce a similar phase evolution.

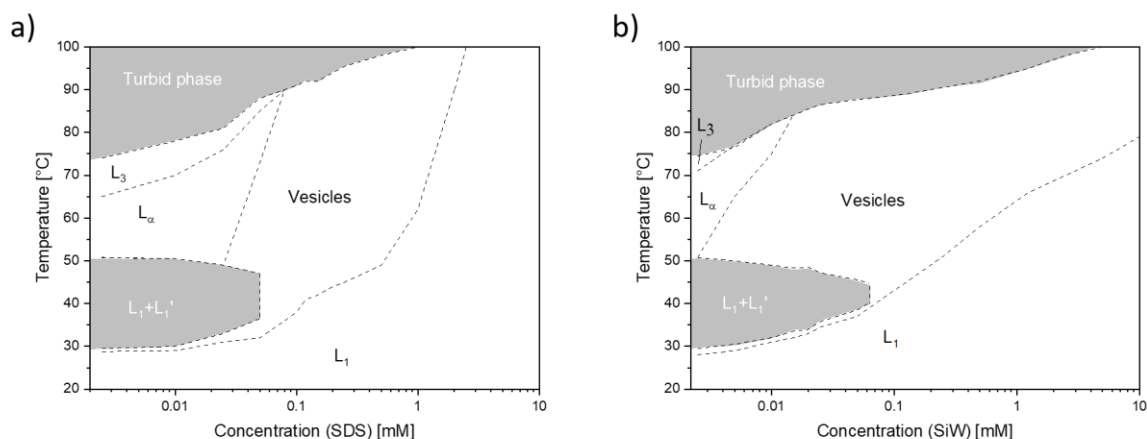


Figure 52: Phase diagram of 1 wt-% C<sub>12</sub>E<sub>5</sub> (25 mM) a) as a function of SDS-concentration and b) as a function of SiW-concentration (identical to Figure 48c).

This result is surprising considering that the purely inorganic POMs are not amphiphilic, that is, without hydrophobic/hydrophilic moieties in stark contrast to (carbon-based) surfactants. It is known that the addition of SDS to elongated C<sub>12</sub>E<sub>5</sub> micelles leads to a decrease of the micellar length down to spherical micelles,<sup>143</sup> similarly to the effect of nano-ions as highlighted herein. Furthermore, the lamellar phase of dilute C<sub>12</sub>E<sub>5</sub> is known to exhibit large thermally induced undulations giving rise to interlamellar Helfrich repulsions<sup>179</sup>, which may lead to huge interlamellar distances up to several hundred nanometers.<sup>165</sup> It was shown that, by addition of SDS, dilute C<sub>12</sub>E<sub>5</sub> lamellae acquire electrical charges by the anchoring of the SDS alkyl chains into the lamella. This charging effect results in a stiffening of the lamella induced by in-plane electrostatic repulsions and, therefore, in the decrease of i) the amplitude of the thermal undulations and ii) the interlamellar distance.<sup>166,180</sup> This phenomenon leads to the destabilization of the lamellar phase and induces a spontaneous transition to an isotropic vesicle phase.<sup>143,180,181</sup> It appears here that the adsorption of nano-ions at the bilayer surface produces an effect similar to the one of ionic surfactants by bringing electrical charges to the nonionic bilayers. As electrostatics dominates the C<sub>12</sub>E<sub>5</sub> phase behavior in the presence of 1 mM SiW and SDS, the phase evolution was studied upon addition of salt (Figure 53) to screen the electrostatic repulsion. Notably, the effect of NaCl on the phase sequence of bare C<sub>12</sub>E<sub>5</sub> (absence of SDS or SiW) is negligible as all phase transitions stay at the same temperatures, see Figure 53a.

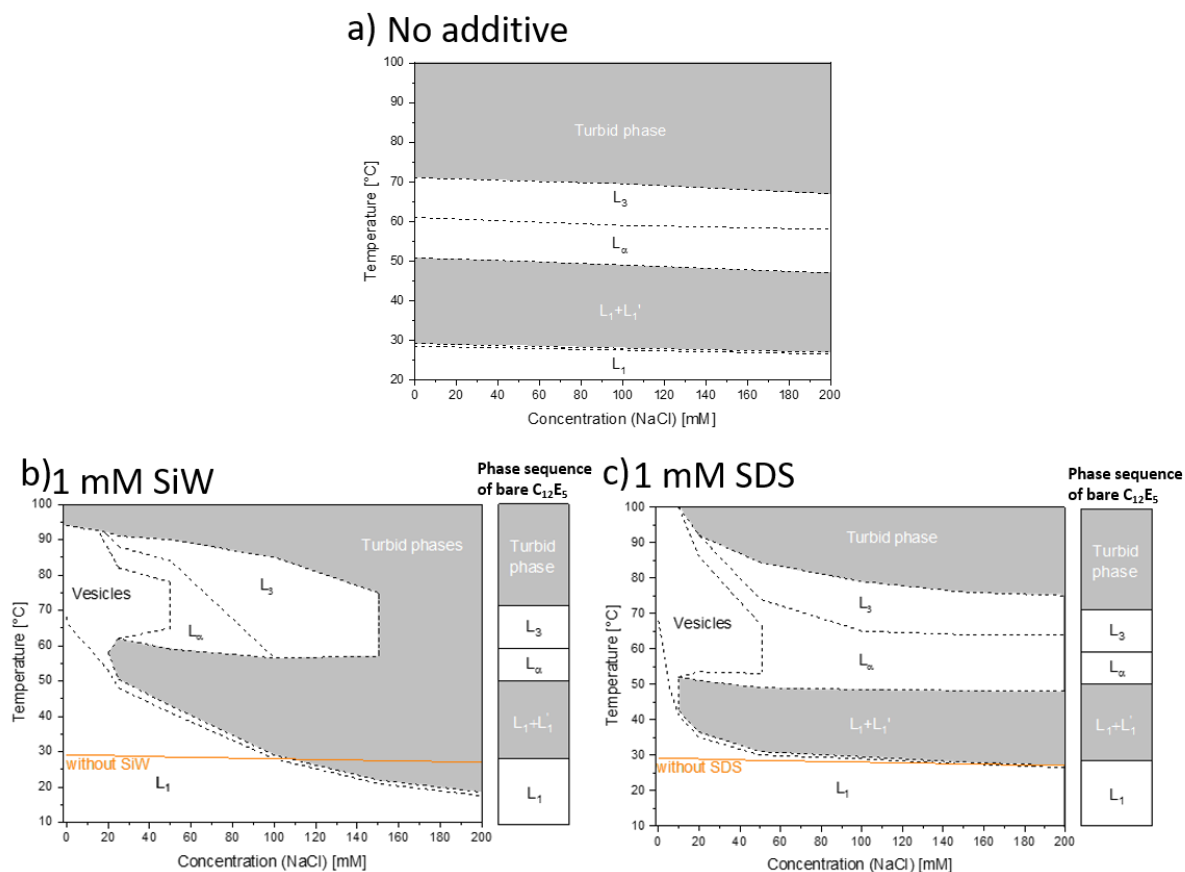


Figure 53: Phase diagram of 1 wt-%  $C_{12}E_5$  as a function of NaCl-concentration a) in absence of nano-ions, b) with 1 mM SiW and c) with 1 mM SDS. Additionally, the cloud point of 1 wt-%  $C_{12}E_5$  as a function of NaCl-concentration is given in b) and c) (orange lines). The side bars show the phase behavior of bare  $C_{12}E_5$  in water (respectively on the right in b) and c)). For SDS, charge screening with NaCl yields a phase behavior similar to the pure surfactant, while for SiW a very different phase behavior arises.

Interestingly, for SDS and SiW, addition of NaCl (at around 50 mM) leads to a reappearance of birefringence, indicating the conversion of vesicles back to a lamellar phase, like for the pure  $C_{12}E_5$ -system in water at 1 wt-%. Therefore, the screening of electrostatic repulsions leads to a softening of the  $C_{12}E_5$  bilayers to the benefit of thermal undulations, which stabilize the dilute lamellar phase. At  $[NaCl] > 50$  mM, SiW and SDS show a strong difference in the phase behavior. For SDS: i) the phase diagram reverts approximately to the temperature-dependent phase sequence of pure 1 wt%  $C_{12}E_5$  (sidebar on the right in Figure 53c) and ii)  $L_\alpha$  and  $L_3$  become insensitive to salt addition and persist at high salinity ( $> 100$  mM). For SiW and at  $50 \text{ mM} < [NaCl] < 150$  mM, the  $L_\alpha$  phase is destabilized in favor of the  $L_3$ -phase. At  $[NaCl] > 150$  mM, the  $L_3$  phase is fully destabilized, leading to phase demixing manifesting as an extensive turbid phase. Furthermore, SDS and SiW show a remarkable difference in the evolution of their cloud points. With SDS (Figure 53c), the CP drops, upon salt addition, down to the exact CP value of the  $C_{12}E_5$  surfactant in the presence of NaCl (orange line in Figure 4b). This behavior is a common result for mixed surfactant micelles in the presence of

electrolyte<sup>135,137,182,183</sup> as it was also shown in the preceding chapter 2. Thus, despite the presence of SDS in the micelles, the C<sub>12</sub>E<sub>5</sub>-SDS system behaves like the pure (neutral) C<sub>12</sub>E<sub>5</sub> micelles when electrostatic repulsions are screened. In the presence of SiW, upon salt addition, the cloud point drops even far below the reference curve, a behavior, which indicates that the SiW- decorated micelles are generally more hydrophobic than the micelles of bare C<sub>12</sub>E<sub>5</sub>. This phenomenon was equally observed in chapter 2 and suggests a dehydration of the hydrophilic surfactant heads upon adsorption of SiW.

The present results show that purely inorganic nano-ions such as POMs and boron clusters can be used as alternatives or substitutes for ionic (organic) surfactants in formulations based on non-ionic surfactants, which are ubiquitous in everyday life products. These nano-ions act like anionic surfactants while they are not ionic surfactants as they neither form micelles in bulk water nor adsorb to the water–air surface, except the special case of COSAN derivatives, which exhibit all properties of surfactants. The addition of nano-ions to nonionic surfactants stands out as a novel method to spontaneously form vesicles, which are commonly used in pharmaceutical formulations as drug-delivery carriers, and highlights the potential of superchaotropic ions for applications.



### 3.3. Comparison of the nano-ions

A variety of different ions was investigated on the phase behavior of 1 wt-% C<sub>12</sub>E<sub>5</sub>. The tested ionic species range from chaotrope-like nano-ions such as B<sub>12</sub>H<sub>12</sub><sup>2-</sup> over superchaotropic ions such as SiW<sub>12</sub>O<sub>40</sub><sup>4-</sup> and B<sub>12</sub>Cl<sub>12</sub><sup>2-</sup> up to more disruptive (superchaotropic/hydrophobic) nano-ions such as B<sub>12</sub>I<sub>12</sub><sup>2-</sup>, PW<sub>12</sub>O<sub>40</sub><sup>3-</sup> and BPh<sub>4</sub><sup>-</sup> according to the proposed ordering of nano-ions in chapter 2. The corresponding phase diagrams are shown below in Figure 54. The classical neutral salt NaCl does not produce any effect in the observed concentration range, see Figure 54a, as the bilayer phases (L<sub>α</sub> and L<sub>3</sub>) at high temperatures as well as the micellar phase remain at the same temperatures. In the presence of the classical chaotropic ions such as B<sub>12</sub>H<sub>12</sub><sup>2-</sup> or SCN<sup>-</sup>, see Figure 54b, the micellar phase is slightly stabilized indicated by a rising cloud point with ion- concentration owing to a slight charging of the non-ionic C<sub>12</sub>E<sub>5</sub>-micelles. Similarly, the L<sub>α</sub>-phase extends slightly to higher temperatures at the expense of the L<sub>3</sub>-phase. Upon using the superchaotropic ions B<sub>12</sub>Cl<sub>12</sub><sup>2-</sup> and SiW<sub>12</sub>O<sub>40</sub><sup>4-</sup> the same effect appears more strongly and additionally a transition from the lamellar phase to a vesicle phase occurs, see Figure 54 c, d as was elucidated by SANS. The emergent vesicle phase expanded strongly to lower temperatures as well as to higher temperatures, while similarly the cloud point increases resulting in a common phase border between the micellar phase and the vesicle phase at high nano-ion concentrations. In the presence of more hydrophobic nano-ions, like PW<sub>12</sub>O<sub>40</sub><sup>3-</sup>, B<sub>12</sub>I<sub>12</sub><sup>2-</sup>, COSAN and BPh<sub>4</sub><sup>-</sup>, the same phenomena arise, while in addition a turbid phase, denoted as insoluble, emerges at low temperatures and high nano-ion concentrations, see Figure 54e-h. The emergence of this multiphasic region results from the particularly strong interaction of these nano-ions with the C<sub>12</sub>E<sub>5</sub>-micelles causing a destabilization and precipitation of the micellar phase. According to these macroscopic observations it is possible to distinguish the nano-ions into chaotropic ions that only cause slight phase changes, superchaotropic ions that interact strongly enough to induce the transition of the lamellar phase into vesicles and disruptive (hydrophobic) ions that interact most strongly and thus additionally lead to a destabilization of the C<sub>12</sub>E<sub>5</sub>-micellar phase:

Phase-neutral ions (chaotropes): SCN<sup>-</sup>, B<sub>12</sub>H<sub>12</sub><sup>2-</sup>

Vesicle makers (superchaotropes): B<sub>12</sub>Cl<sub>12</sub><sup>2-</sup>, SiW<sub>12</sub>O<sub>40</sub><sup>4-</sup>

Vesicle makers + micelle destabilizers (Disruptive ions): B<sub>12</sub>I<sub>12</sub><sup>2-</sup>, PW<sub>12</sub>O<sub>40</sub><sup>3-</sup>, BPh<sub>4</sub><sup>-</sup>, COSAN<sup>-</sup>

This classification is identical to the classification in chapter 2.6 supporting the therein established series of ions.

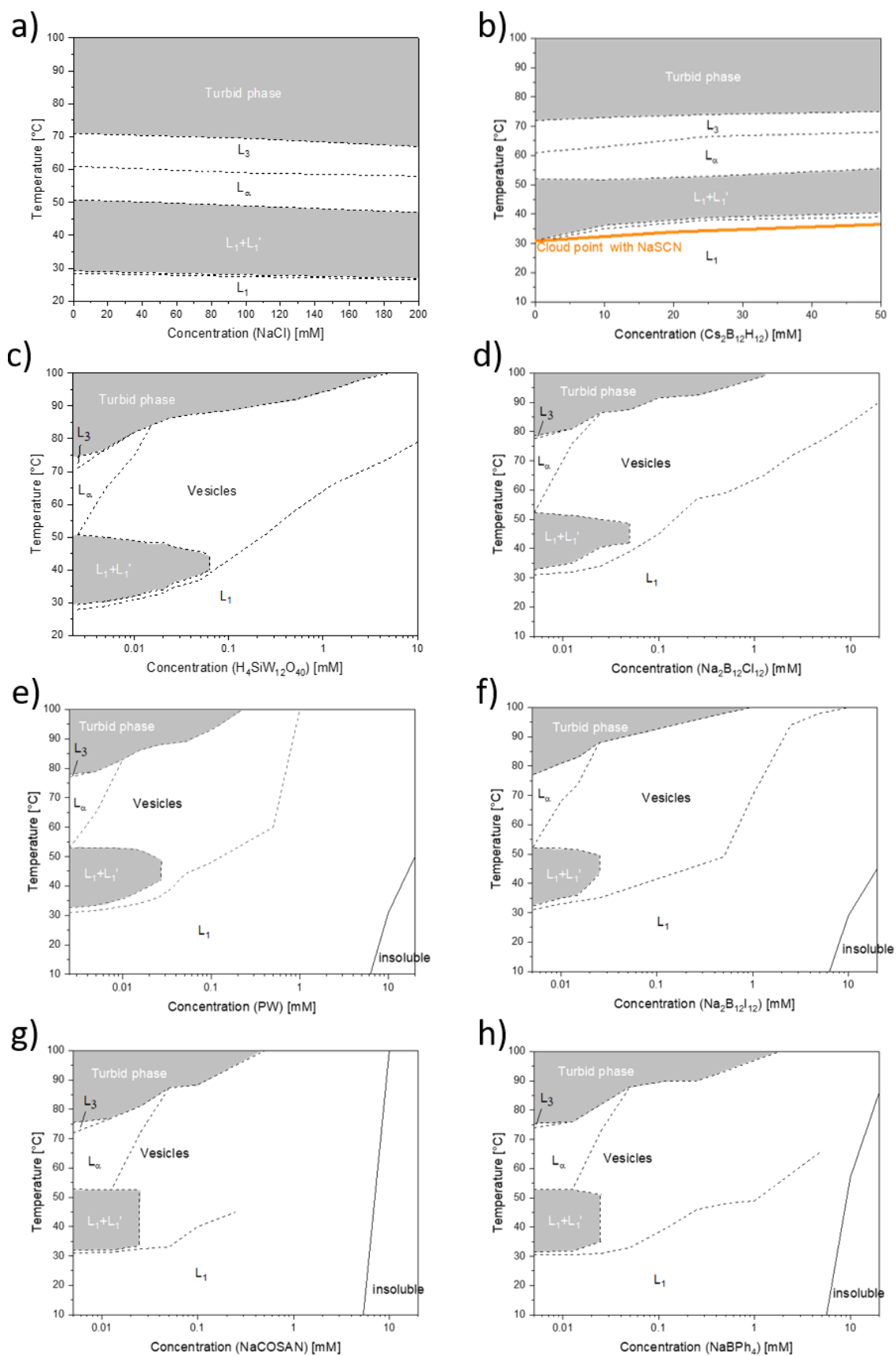


Figure 54: Phase diagrams of 1 wt-% (25 mM)  $C_{12}E_5$  as a function of the concentration of a) NaCl, b)  $Cs_2B_{12}H_{12}$  with added cloud points of NaSCN, c)  $H_4SiW_{12}O_{40}$ , d)  $Na_2B_{12}Cl_{12}$ , e)  $Na_2B_{12}I_{12}$ , f)  $H_3PW_{12}O_{40}$ , g) NaCOSAN and h) NaBPh<sub>4</sub>.

Moreover, the phase transitions in the shown phase diagrams may contain further information about the interactions of the nano-ions with the micelles. In Table 19, the respective transitions of the lamellar to the vesicle phase (loss of birefringence) are listed along with the stability of the micellar phase before appearance of the cloud point or the transition towards vesicles.

Table 19: Characteristic properties of the nano-ions with their charge, volume, charge densities, their classification in terms of superchaotropicity and hydrophobicity along with a listing of the observations made in the phase diagrams: Presence of the insoluble phase, the respective concentration thresholds where the lamellar phase transitions into the vesicle phase and the respective stabilization of the  $L_1$ -phase at 5 mM of nano-ion.

Additive:	SiW (SiW <sub>12</sub> O <sub>40</sub> <sup>4-</sup> )	PW (PW <sub>12</sub> O <sub>40</sub> <sup>3-</sup> )	B <sub>12</sub> I <sub>12</sub> <sup>2-</sup>	B <sub>12</sub> Cl <sub>12</sub> <sup>2-</sup>	B <sub>12</sub> H <sub>12</sub> <sup>2-</sup>	COSAN <sup>-</sup>	BPh <sub>4</sub> <sup>-</sup>	SDS
Charge, e <sup>-</sup>	4	3	2	2	2	1	1	1
Molecular volume [nm <sup>3</sup> ]	0.46	0.46	0.52	0.33	0.15	0.45	0.313 <sup>a</sup>	0.375 <sup>b</sup>
Charge density [charge/nm <sup>3</sup> ]	8.7	6.5	3.9	6.0	13.2	2.2	3.2	2.7
Observations in the phase diagrams								
$L_\alpha$ -vesicle transition* [μM]	2.5-15	2.5-10	5-25	5-25	None	15-50	15-50	25-80
Stability of $L_1$ -phase at c(additive)=5 mM [°C]	75	>100	95	77	33	nd**	65	>100
Insoluble at high c	No	Yes	Yes	No	No	Yes	Yes	No

\*Corresponding minimum (lower temperature) and maximum (higher temperature) threshold concentrations of the  $L_\alpha$ -vesicles transition.

\*\*nd=not determined.

a) Molecular volume of BPh<sub>4</sub> estimated from its simulated molecular structure.

b) Molecular volume of SDS calculated by adding the molecular volumes of C<sub>12</sub>H<sub>25</sub> and SO<sub>4</sub><sup>2-</sup>.

Interestingly, the  $L_\alpha$ -vesicle transition seems to occur earliest for the most charged ions that is for the Keggin-POMs SiW and PW and is consistently shifted to higher concentrations for ions with lower valences. Furthermore, the stability of the micellar phase (at [nano-ion]=5 mM) coincides well with the charge densities of the ions. These results again display the general validity of the concept: The lower the charge density of an ion the higher is its chaotropic/hydrophobic nature and the stronger is its interaction with the non-ionic micelles.

### 3.4. Changing $C_{12}E_5$ -concentration

By increasing the surfactant concentration from 1 wt-%  $C_{12}E_5$  to 5 wt-%  $C_{12}E_5$  (in the absence of additives) the phase behavior shifts only slightly to higher temperatures, see Figure 55, while microscopically the micelles become more crowded and the interlamellar distances in the bilayer phases decrease drastically. Upon addition of  $H_4SiW_{12}O_{40}$ , the emergent phase behavior in the two different concentration regimes shows differing characteristics.

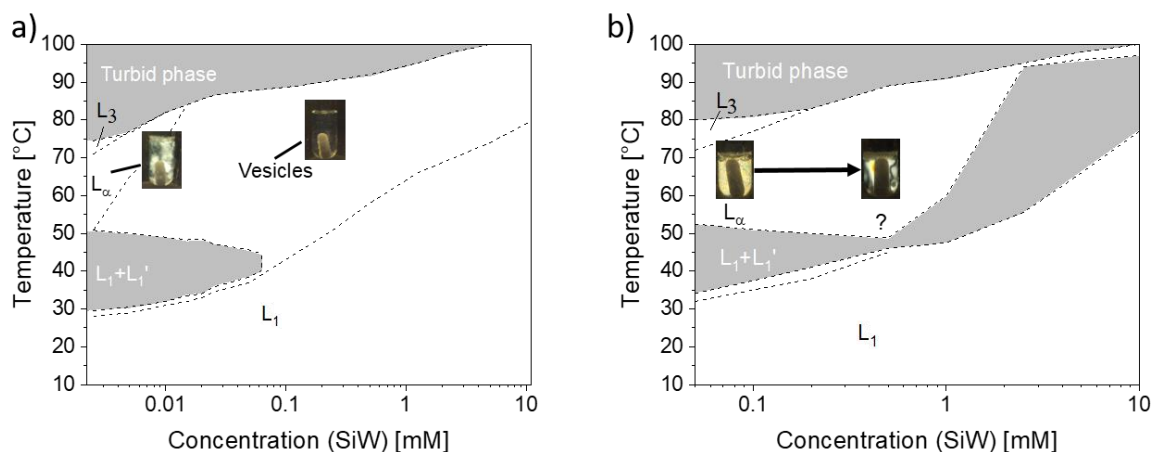


Figure 55: Phase diagram comparison between a) 1 wt-%  $C_{12}E_5$  and b) 5 wt-%  $C_{12}E_5$ , respectively, in the presence of SiW. Photos of the birefringent phases between crossed polarizers are added.

At 1 wt-%  $C_{12}E_5$ , the birefringence of the lamellar phase completely disappears at a threshold concentration of SiW and this non-birefringent vesicle-region then extends to higher concentrations and higher temperatures. At 5 wt-%  $C_{12}E_5$ , the sample remains birefringent upon addition of SiW, while the birefringent patterns change significantly, see Figure 55b. Additionally, this phase was found to be highly viscous. Addition of further SiW causes a destabilization of this birefringent phase into a turbid multiphase positioned on top of the micellar  $L_1$ -phase. The same phase diagram at 5 wt-% was acquired as a function of SDS ( $C_{12}H_{25}SO_4^{2-}$ ), see Figure 56.

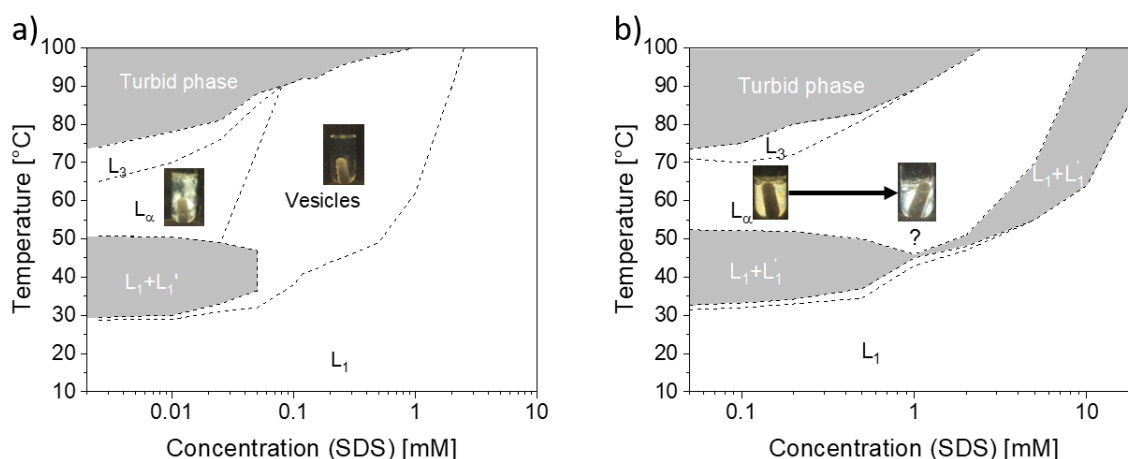


Figure 56: Phase diagram comparison between a) 1 wt-%  $C_{12}E_5$  and b) 5 wt-%  $C_{12}E_5$ , respectively, in the presence of SDS. Photos of the birefringent phases between crossed polarizers are added.

Again, SDS produces a qualitatively identical phase evolution as SiW confirming that SiW acts in this system like an ionic surfactant. The peculiar birefringence pattern observed was similar for SiW and SDS and was also observed by Glatter et al. in a related surfactant system<sup>182</sup>, where the birefringence was proposed to stem from multilamellar vesicles (MLVs). Considering that here from the lamellar phase of 1 wt-%  $C_{12}E_5$  unilamellar vesicles are produced, the production of MLVs out of the more concentrated lamellar phase of 5 wt-%  $C_{12}E_5$  seems to be a compelling assumption. In order to identify this phase more clearly, further investigation would be necessary including a study of the rheologic behavior.

### 3.5. Remarks on vesicle stability

Often vesicle phases exhibit kinetic stability as they are produced as metastable intermediates by mechanical methods for example by shearing a lamellar phase<sup>172</sup>, while by chemical spontaneous vesiculation methods thermodynamically stable vesicles may result.<sup>177</sup> Herein, vesicles were produced by ionizing a dilute non-ionic surfactant lamellar phase using small amounts of superchaotropic nano-ions or ionic surfactants. Among these two techniques the vesicle formation induced by the nano-ions stands out as a novel method to form vesicles in solution and it is an interesting endeavor to investigate the resulting vesicle stability. Thus, in the vesicle phase of 25 mM C<sub>12</sub>E<sub>5</sub> + 2.5 mM HSiW dynamic light scattering was performed to trace the vesicle size as a function of time, see Figure 57.

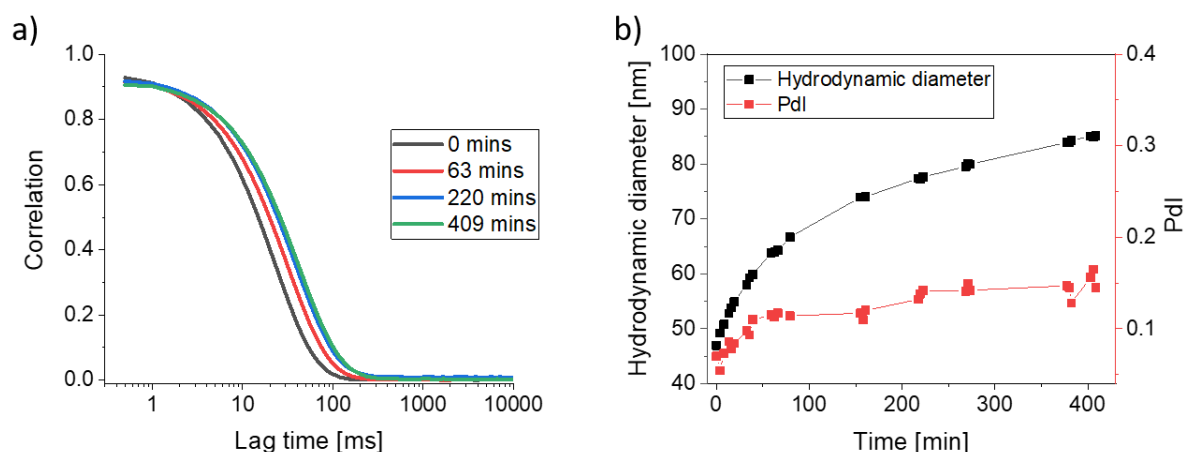


Figure 57: a) DLS correlation functions of 25 mM C<sub>12</sub>E<sub>5</sub> + 2.5 mM HSiW at 80°C as a function of time for vesicle phases with different ages. b) Corresponding hydrodynamic diameters and PDIs.

The correlation functions in Figure 57a show a clear shift towards higher lag times with sample age indicating a significant growth of the vesicles with time. Upon calculation of the corresponding vesicle size, a monotonous increase was observed in the hydrodynamic diameters from 46 nm at an age of 0 min to 83 nm after 400 mins accompanied by a slight increase in polydispersity (PDI). The continuous increase in vesicle size may hint at an inherent instability of this vesicle phase, while it may be possible that the vesicle phase has not yet reached its thermodynamically stable state. Therefore, it was necessary to examine the vesicle stability on a larger time scale. The experiment was performed macroscopically using a furnace set to 80°C. The sample of 25 mM C<sub>12</sub>E<sub>5</sub> + 2.5 mM HSiW was checked regularly regarding phase separation and between crossed polarizers to confirm the absence of birefringence (characteristic of unilamellar vesicles). Thus, it was found that the vesicle phase remains stable at 80°C for seven days until phase separation occurs. This result points at a limited kinetic stability of the formed vesicles. However, it should be noted that ethoxylated surfactants, such

as C<sub>12</sub>E<sub>5</sub> are known to be susceptible to slow thermal degradation at elevated temperatures.<sup>184</sup> The formed degradation products in turn may have enormous effects on the phase behavior and might induce the observed phase separation. Indeed, upon testing with NMR identical samples of 25 mM C<sub>12</sub>E<sub>5</sub> + 1 mM HSiW (without and with heat exposure) significant side peaks of degradation products were observed for the heated sample, see Appendix (section 3.8.7).

Overall, it was shown that the vesicle phase of 1 wt-% C<sub>12</sub>E<sub>5</sub> in the presence of HSiW exhibits long term stability. However, as this vesicle phase exists only at elevated temperatures (T>60°C) problems with thermal degradation of the non-ionic surfactant were encountered making it impossible to draw conclusions on whether the investigated vesicle phase is kinetically or thermodynamically stabilized.

### 3.6. Chapter summary

By means of phase diagrams and SANS it was shown that superchaotropic nano-ions can take the role of a co-surfactant and tailor the properties of a non-ionic surfactant system just like an ionic surfactant. To come to this conclusion, the Keggin-POM  $\text{SiW}_{12}\text{O}_{40}^{4-}$  (SiW) was used as an archetypical superchaotropic ion. It induced tremendous changes in the phase behavior of the non-ionic surfactant  $\text{C}_{12}\text{E}_5$  in water. Driven by the chaotropic effect, SiW adsorbs strongly on the  $\text{C}_{12}\text{E}_5$  self-assemblies conveying its charge to the electrically neutral surfactant aggregate and compressing the elongated  $\text{C}_{12}\text{E}_5$ -micelles into spherical ones. Thus, dilute  $\text{C}_{12}\text{E}_5$  micelles (1 wt-%) become ionic and electrostatically repulsive resulting in a strong stabilization of the micellar  $L_1$ -phase up to elevated temperatures. By contrast, the dilute bilayer phases (lamellar  $L_\alpha$  and sponge  $L_3$ ) of 1 wt-%  $\text{C}_{12}\text{E}_5$  present at high temperatures are destabilized upon adsorption of SiW. Here, the arising electrostatics (in-plane repulsions) cause a rigidification of the bilayers antagonizing the high fluctuation dynamics in the  $L_3$  and the  $L_\alpha$ -phase. The electrostatic suppression of the stabilizing Helfrich undulations causes first a vanishing of the  $L_3$ -phase and a spontaneous transition of the  $L_\alpha$ -phase into a vesicle phase. The formed vesicle phase exhibited long-term stability (one week), while experiments to determine its kinetic or thermodynamic stability were inconclusive as thermally induced  $\text{C}_{12}\text{E}_5$  degradation affected strongly the vesicle stability. It was further shown that the ionic surfactant sodium dodecyl sulfate (SDS) induces a qualitatively identical phase behavior on 1 wt-%  $\text{C}_{12}\text{E}_5$  as SiW owing to the same electrostatic mechanism. However, fundamentally, SDS and SiW interact very differently with the  $\text{C}_{12}\text{E}_5$  self-assemblies as was shown by working in electrolytic (NaCl)-solutions. On the one hand, owing to the hydrophobic effect on the aliphatic dodecyl tail, SDS anchors in between  $\text{C}_{12}\text{E}_5$ -molecules forming mixed surfactant assemblies. The mixed SDS/ $\text{C}_{12}\text{E}_5$ -assemblies were found to act exactly like pure  $\text{C}_{12}\text{E}_5$  when electrostatics are screened. On the other hand, SiW interacts preferably with the polar surfactant heads of  $\text{C}_{12}\text{E}_5$  driven by the chaotropic effect commonly conceived as a thermodynamically favored bulk water structure recovery upon shed of hydration water of both SiW and the polar surfactant heads.<sup>3,36</sup> The occurring dehydration of the  $\text{C}_{12}\text{E}_5$ -assemblies upon adsorption of SiW was reflected in the phase behavior of  $\text{C}_{12}\text{E}_5/\text{SiW}$  by a decreased cloud point and destabilized bilayer phases when electrostatics are screened in direct contrast to the SDS/ $\text{C}_{12}\text{E}_5$ -system. Overall, SiW acts like an ionic surfactant in the  $\text{C}_{12}\text{E}_5$  system without necessitating a surfactant tail or a typical amphiphilic structure. Consequently, superchaotropic inorganic nano-ions constitute an innovative alternative to organic ionic surfactants in surfactant-based



formulations. Additionally, the herein demonstrated nano-ion-assisted vesiculation out of a dilute non-ionic lamellar phase provides a novel method to form vesicles.

Furthermore, the whole range of ionic species from classical neutral ions and chaotropes over superchaotropes to hydrophobic species was investigated regarding their effects on the phase behavior of 1 wt-% C<sub>12</sub>E<sub>5</sub>. The obtained results are fully consistent with the classification of the ions in chapter 2, section 2.6. Thus, chaotropic ions like SCN<sup>-</sup> and B<sub>12</sub>H<sub>12</sub><sup>2-</sup> induced only slight changes to the phase sequence of C<sub>12</sub>E<sub>5</sub> owing to their weak interaction with the non-ionic surfactant assemblies. The superchaotropic ions SiW<sub>12</sub>O<sub>40</sub><sup>4-</sup> and B<sub>12</sub>Cl<sub>12</sub><sup>2-</sup>, in turn, showed much stronger interaction leading to tremendous phase changes including spontaneous vesiculation and an immense stabilization of the micellar phase as outlined above. Further, the ions situated at the hydrophobic side PW<sub>12</sub>O<sub>40</sub><sup>3-</sup>, B<sub>12</sub>I<sub>12</sub><sup>2-</sup>, COSAN and BPh<sub>4</sub><sup>-</sup> manifested even stronger interaction causing the same phase sequence at low nano-ion concentrations and the appearance of an insoluble precipitate at high nano-ion concentrations. Hence, again the disruptive nature of these hydrophobic ions is demonstrated.

### 3.7. Résumé en français

En utilisant les diagrammes de phase et la SANS, il a été démontré que les nano-ions superchaotropiques peuvent jouer le rôle d'un co-tensioactif et adapter les propriétés d'un système de tensioactif non ionique tout comme un tensioactif ionique. Pour arriver à cette conclusion, le Keggin-POM  $\text{SiW}_{12}\text{O}_{40}^{4-}$  (SiW) a été utilisé comme un ion superchaotrope archétypique. Il a induit d'énormes changements dans le comportement de phase du tensioactif non-ionique  $\text{C}_{12}\text{E}_5$  dans l'eau. Sous l'effet de l'effet chaotrope, le SiW s'adsorbe fortement sur les auto-assemblages du  $\text{C}_{12}\text{E}_5$ , transmettant sa charge à l'agrégat tensioactif électriquement neutre et comprimant les micelles allongées du  $\text{C}_{12}\text{E}_5$  en micelles sphériques. Ainsi, les micelles  $\text{C}_{12}\text{E}_5$  diluées (1 % en masse) deviennent ioniques et électrostatiquement répulsives, ce qui entraîne une forte stabilisation de la phase micellaire  $L_1$  jusqu'à des températures élevées. En revanche, les phases bicouches diluées (lamellaire  $L_\alpha$  et éponge  $L_3$ ) de 1 % en masse de  $\text{C}_{12}\text{E}_5$  présentes à haute température sont déstabilisées par l'adsorption de SiW. Dans ce cas, l'électrostatique résultante (répulsions dans le plan) entraîne une rigidification des bicouches, ce qui s'oppose à la dynamique de fluctuation importante dans la phase  $L_3$  et la phase  $L_\alpha$ . La suppression électrostatique des ondulations stabilisatrices de Helfrich provoque d'abord une disparition de la phase  $L_3$  et une transition spontanée de la phase  $L_\alpha$  vers une phase vésicule. La phase vésicule formée a montré une stabilité à long terme (une semaine), tandis que les expériences visant à déterminer sa stabilité cinétique ou thermodynamique n'ont pas été concluantes car la dégradation de  $\text{C}_{12}\text{E}_5$  induite thermiquement a eu un impact important sur la stabilité des vésicules. Il a en outre été démontré que l'agent tensioactif ionique dodécylsulfate de sodium (SDS) induit un comportement de phase qualitativement identique à celui du SiW sur  $\text{C}_{12}\text{E}_5$ , en raison du même mécanisme électrostatique. Cependant, fondamentalement, le SDS et le SiW interagissent très différemment avec les auto-assemblages de  $\text{C}_{12}\text{E}_5$ , comme l'a montré le travail en solutions électrolytiques (NaCl). D'une part, en raison de l'effet hydrophobe sur la queue du dodécyle aliphatique, le SDS s'ancre entre les molécules de  $\text{C}_{12}\text{E}_5$  pour former des assemblages de tensioactifs mixtes. Les assemblages SDS/ $\text{C}_{12}\text{E}_5$  mixtes se sont avérés agir exactement comme du  $\text{C}_{12}\text{E}_5$  pur lorsque les électrostatiques sont filtrés. D'autre part, le SiW interagit de préférence avec les têtes de tensioactifs polaires du  $\text{C}_{12}\text{E}_5$ , sous l'effet chaotrope communément conçu comme une récupération de la structure de l'eau en vrac favorisée thermodynamiquement par la libération d'eau d'hydratation à la fois du SiW et des têtes de tensioactifs polaires.<sup>3,36</sup> La déshydratation des assemblages  $\text{C}_{12}\text{E}_5$  lors de l'adsorption de SiW se reflète dans le comportement de phase du  $\text{C}_{12}\text{E}_5/\text{SiW}$  par une diminution du point de trouble

et une déstabilisation des phases bicouches lorsque l'électrostatique est écranté en contraste direct avec le système SDS/C<sub>12</sub>E<sub>5</sub>.

Dans l'ensemble, le SiW agit comme un tensioactif ionique dans le système C<sub>12</sub>E<sub>5</sub> sans nécessiter de queue hydrophobe ou de structure amphiphile typique. En conséquence, les nano-ions inorganiques superchaotropes constituent une alternative innovante aux tensioactifs ioniques organiques dans les formulations à base d'agents de surface. En outre, la vésiculation assistée par nano-ion démontrée ici à partir d'une phase lamellaire non ionique diluée fournit une nouvelle méthode pour former des vésicules.

En outre, toute la gamme des espèces ioniques, des ions neutres classiques aux chaotropes en passant par les superchaotropes et les espèces hydrophobes, a été étudiée en ce qui concerne leurs effets sur le comportement de la phase de 1 % en masse de C<sub>12</sub>E<sub>5</sub>. Les résultats obtenus sont tout à fait conformes à la classification des ions du chapitre 2, section 2.6. Ainsi, les ions chaotropes comme le SCN<sup>-</sup> et le B<sub>12</sub>H<sub>12</sub><sup>2-</sup> n'ont induit que de légères modifications de la séquence de phase de C<sub>12</sub>E<sub>5</sub> en raison de leur faible interaction avec les assemblages de tensioactif non-ionique. Les ions superchaotropiques SiW<sub>12</sub>O<sub>40</sub><sup>4-</sup> et B<sub>12</sub>Cl<sub>12</sub><sup>2-</sup>, à leur tour, ont montré une interaction beaucoup plus forte, entraînant d'énormes changements de phase, notamment une vésiculation spontanée et une immense stabilisation de la phase micellaire, comme indiqué ci-dessus. En outre, les ions situés du côté hydrophobe PW<sub>12</sub>O<sub>40</sub><sup>3-</sup>, B<sub>12</sub>I<sub>12</sub><sup>2-</sup>, COSAN et BPh<sub>4</sub><sup>-</sup> ont manifesté une interaction encore plus forte, provoquant la même séquence de phases à de faibles concentrations en nano-ions et l'apparition d'un précipité insoluble à des concentrations élevées en nano-ions. Ainsi, la nature perturbatrice de ces ions hydrophobes est à nouveau démontrée.

## 3.8. Appendix

### 3.8.1. Remaining SANS-spectra

For the purpose of contrast, D<sub>2</sub>O was used as a solvent in all SANS-experiments. In comparison to H<sub>2</sub>O, this led to negligible changes in the phase diagram (a downshift of around 1°C for all transitions in D<sub>2</sub>O), see Figure 58.

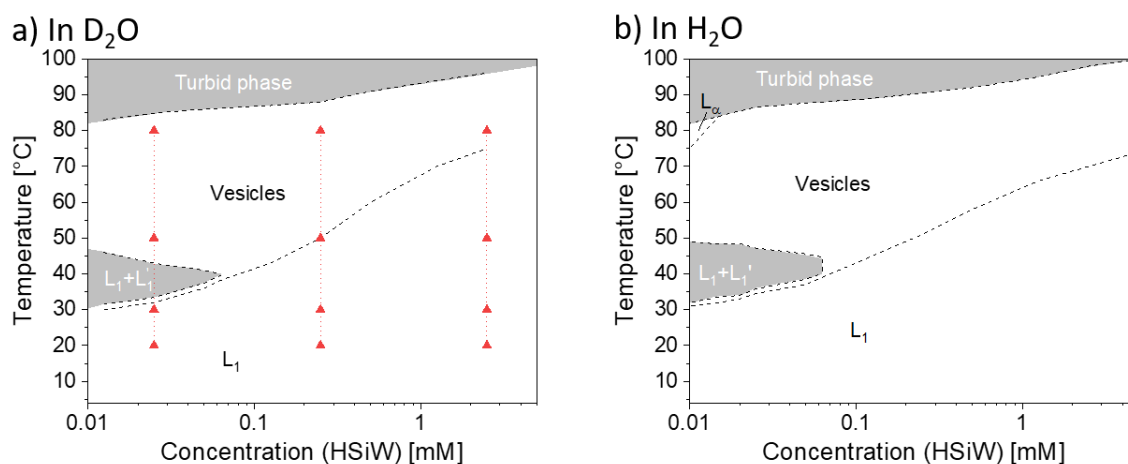


Figure 58: Comparison between the phase diagrams of 1 wt-% C<sub>12</sub>E<sub>5</sub> (25 mM) in the presence of HSiW (H<sub>4</sub>SiW<sub>12</sub>O<sub>40</sub>) a) in D<sub>2</sub>O and b) in H<sub>2</sub>O. The red triangles show the samples investigated by SANS.

The red triangles in Figure 58a indicate the investigated samples in SANS, of which the composition containing 2.5 mM HSiW was discussed in the main text (section 3.2). Here, the remaining spectra containing 25 mM C<sub>12</sub>E<sub>5</sub> + 0.025 mM HSiW or +0.25 mM HSiW shall be examined. The corresponding SANS-spectra are shown in Figure 59 a and b, respectively.

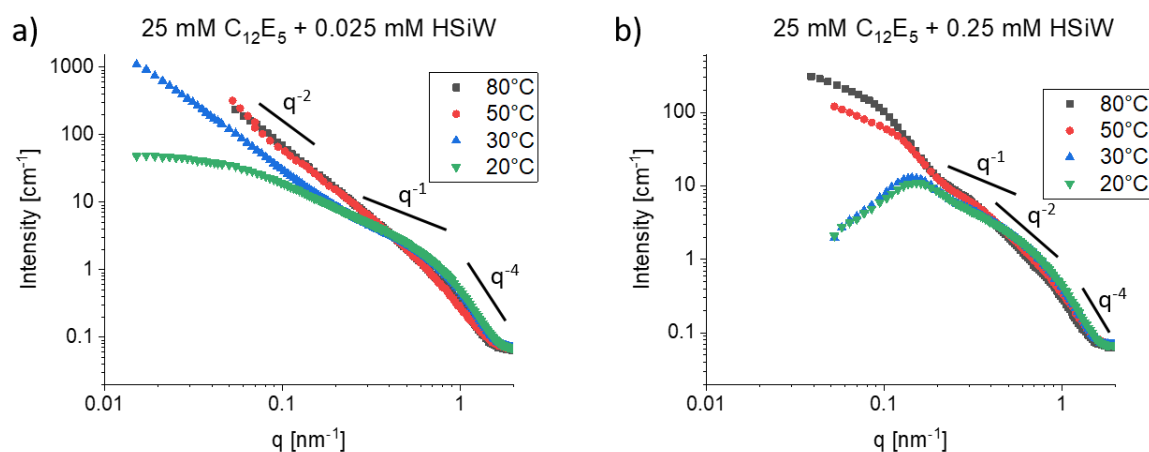


Figure 59: SANS-spectra of 1 wt-% C<sub>12</sub>E<sub>5</sub> at different temperatures in the presence of a) 0.025 mM HSiW (H<sub>4</sub>SiW<sub>12</sub>O<sub>40</sub>) and b) 0.25 mM HSiW. Intensities are in absolute scale.

At 0.025 mM HSiW (Figure 59a), the SANS-spectra show the scattering of elongated micelles with an extensive  $q^{-1}$ -dependence at 20°C. The sample at 30°C is very close to the cloud point in the bluish opalescent so-called “preclouding” region<sup>169</sup> and exhibits this criticality as a steep

slope in the low  $q$ -region, which can be attributed to the formation of an extended micellar network before the occurrence of the CP.<sup>128</sup> When entering into the bilayer phase above 50°C, the dominating slope shifts into a  $q^{-2}$ -dependence indicating the presence of bilayer objects. As no further oscillations occur in these spectra, the presence of vesicles can be excluded at this sample composition.

At 0.25 mM HSiW, the C<sub>12</sub>E<sub>5</sub>-micelles at 20°C and at 30°C, exhibit marked intermicellar repulsion caused by their emergent ionic nature upon adsorption of SiW. At the transition towards the vesicle phase at 50°C, again a marked  $q^{-2}$ -dependence emerges displaying the presence of bilayer structures. Additionally, at 0.2 nm<sup>-1</sup> a minimum occurs together with a maximum at 0.15 nm<sup>-1</sup>. This pattern can be interpreted as the onset of the vesicle phase, which can be clearly identified at 2.5 mM HSiW, see section 3.2.

## 3.8.2. Flexible vs rigid cylindrical micelles (form factor fits)

It has been shown in previous studies that dilute micelles of  $C_{12}E_5$  are elongated and feature a certain flexibility. This flexibility is included into the model by the so-called Kuhn length, which represents the distance over which a part of the flexible cylinder can be considered as a rigid rod. In Figure 60, the difference between the form factor fits for the experimental spectra for 25 mM  $C_{12}E_5$  with 0 mM and 0.025 mM SiW at 20°C are compared for the flexible and rigid cylinder model.

Table 20: Best fit parameters for 25 mM  $C_{12}E_5$  in the presence of 0 mM SiW and 0.025 mM SiW at 20°C. Comparison between (rigid) cylinder and flexible cylinder fits.

Parameter	Description	Units	25 mM $C_{12}E_5$ + 0 mM SiW at 20°C		25 mM $C_{12}E_5$ + 0.025 mM SiW at 20°C	
			Flexible Cylinder form factor	Cylinder form factor	Flexible Cylinder form factor	Cylinder form factor
scale	Approximates volume fraction	None	0.0095	0.001	0.0095	0.01
background	Intensity (background noise+D2O)	$\text{cm}^{-1}$	0.058	0.058	0.058	0.058
sld_scatterer	Approximates SLD of $C_{12}E_5$	$10^{-6}\text{\AA}^{-2}$	0.1	0.1	0.1	0.1
sld_solvent	SLD of $D_2O$	$10^{-6}\text{\AA}^{-2}$	6.34	6.34	6.34	6.34
length	Length of the flexible cylinder	$\text{\AA}$	1800	1800	910	750
kuhn_length	Kuhn length of the flexible cylinder	$\text{\AA}$	410	-	440	-
radius	Radius of the flexible cylinder	$\text{\AA}$	20.7	20	21	19.8
PdI of radius	Polydispersity index	None	0.18	0.2	0.18	0.16

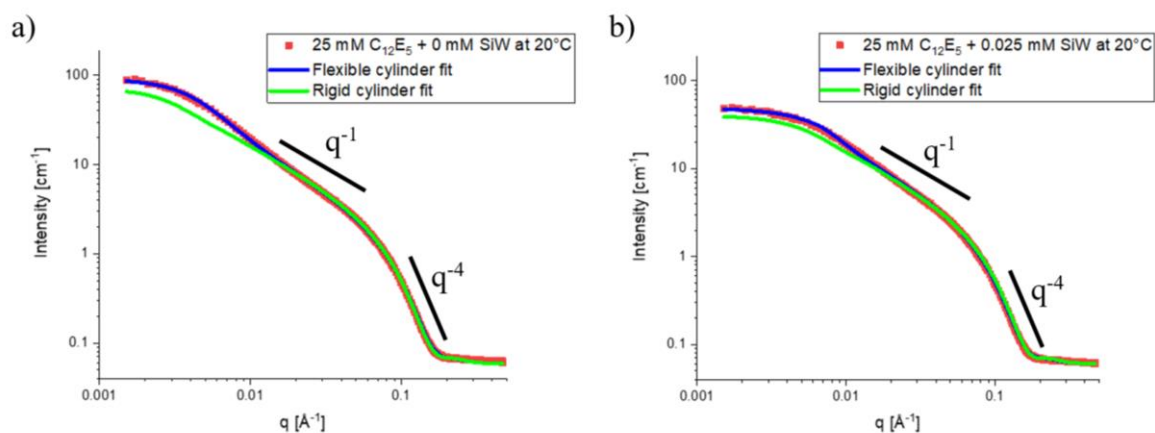


Figure 60: SANS-spectra of 25 mM  $C_{12}E_5$  at 20°C with 0 mM SiW (a) and 0.025 mM SiW (b), respectively with fits of the rigid and flexible cylinder model. The flexible cylinder model fits the data precisely over the whole  $q$ -region for both spectra.

### 3.8.3. Repelling cylindrical and spherical micelles (form and structure factor fits)

As the concentration of SiW is increased further to 0.25 mM and 2.5 mM, the micelles shrink, loose their flexibility and intermicellar repulsions become significant, which induces long-range ordering. Hence, the structure factor must be considered in the fitting procedure. For this purpose, the Hayter-MSA (mean spherical approximation) structure factor model was used. It calculates the long-range ordering of identical, charged colloidal spheres in a dielectric medium. For cylindrical scattering objects, spheres of equivalent volume are considered. Furthermore, as the concentration of SiW is in the low millimolar range, screening effects of potentially free (non-adsorbed) SiW are insignificant and neglected in the fits. The fits and corresponding SANS-spectra are shown in Figure 61.

Table 21: Best fit parameters for 25 mM C<sub>12</sub>E<sub>5</sub> with 0.25 mM SiW at 20°C and 2.5 mM SiW at 20°C and at 50°C.

Parameters	Description	Units	25 mM C <sub>12</sub> E <sub>5</sub> + 0.25 mM SiW at 20°C	25 mM C <sub>12</sub> E <sub>5</sub> + 2.5 mM SiW at 20°C	25 mM C <sub>12</sub> E <sub>5</sub> + 2.5 mM SiW at 30°C
			Cylinder form factor	Sphere form factor	Sphere form factor
<b>scale</b>	Scaling=1 means no scaling	None	1	1	1
<b>background</b>	Background intensity (noise+D <sub>2</sub> O)	cm <sup>-1</sup>	0.055	0.059	0.055
<b>sld_scatterer</b>	Approximates SLD of C <sub>12</sub> E <sub>5</sub>	10 <sup>-6</sup> Å <sup>-2</sup>	0.1	0.1	0.1
<b>sld_solvent</b>	SLD of D <sub>2</sub> O	10 <sup>-6</sup> Å <sup>-2</sup>	6.34	6.34	6.34
<b>length</b>	Length of the flexible cylinder	Å	670	-	-
<b>radius</b>	Radius of the flexible cylinder	Å	20.4	24	25.5
<b>PdI of radius</b>	Polydispersity index of radius	None	0.17	0.18	0.15
			<b>Hayter-MSA structure factor</b>	<b>Hayter-MSA structure factor</b>	<b>Hayter-MSA structure factor</b>
<b>radius_effective</b>	Radius of charged sphere	Å	Equivalent volume sphere	27	28
<b>Vofraction</b>	Volume fraction	None	0.009	0.01	0.01
<b>Temperature</b>	Temperature	K	293.15	293.15	303.15
<b>Charge</b>	Charge of the sphere	e	29	21	26
<b>concentration_salt</b>	Screening salt concentration	mol/L	0	0	0.022
<b>Dielectric constant</b>	Dielectric constant of water	None	81	81	81

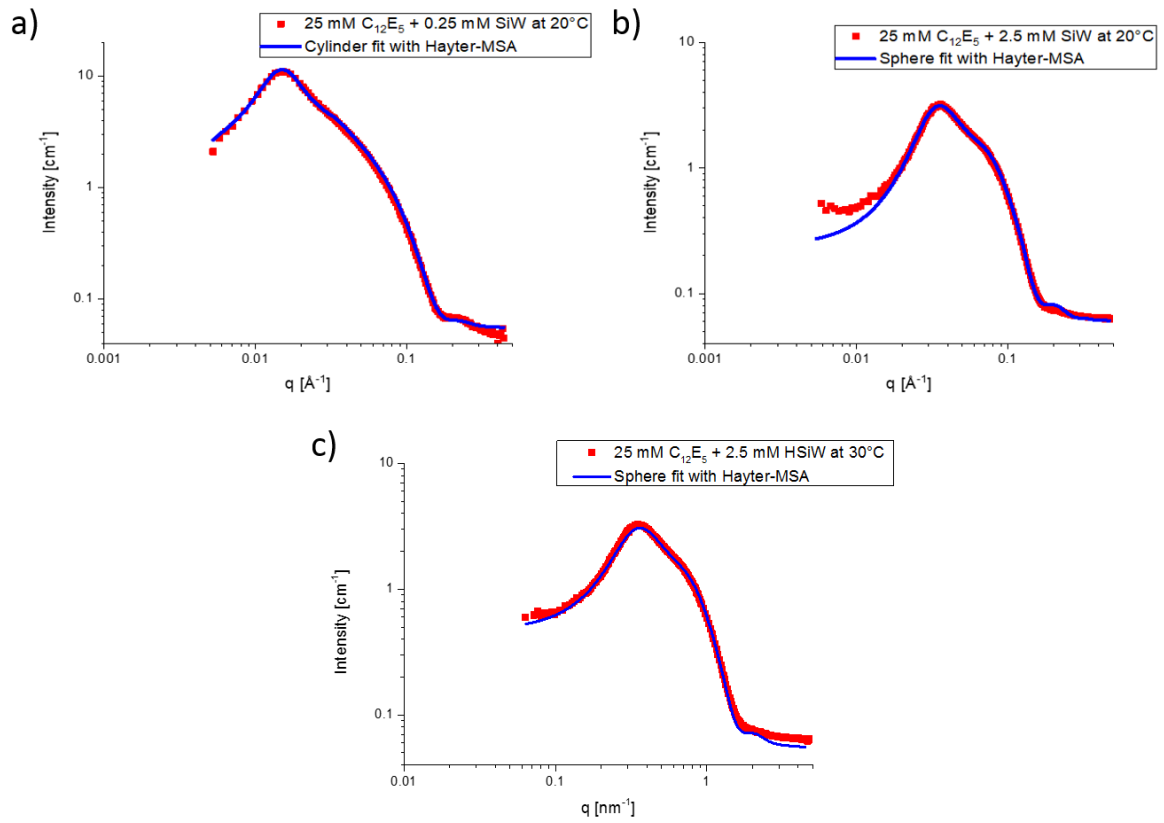


Figure 61: SANS-spectra of 1 wt-%  $\text{C}_{12}\text{E}_5$  (25 mM) with a) 0.25 mM SiW and b) 2.5 mM SiW at 20°C and c) 2.5 mM SiW at 30°C, with fits using cylinder or sphere form factors and Hayter-MSA structure factors.



### 3.8.4. Ellipsoidal fits of SAXS and SANS upon heating

In order to fit accurately the SAXS-spectra an ellipsoid form factor fit was used for the SANS-fit of 25 mM C<sub>12</sub>E<sub>5</sub> + 2.5 mM HSiW at 50°C (Figure 50). Thus, readily available core-shell ellipsoids can be used in SAXS-fitting (while cylinder core-shells complicate the fitting procedure) in order to calculate the number of adsorbed POMs per micelle. It should be noted that the fit quality is equally good when exchanging cylinders for ellipsoid form factors.

Table 22: Best fit parameters for the SANS-spectrum of 25 mM C<sub>12</sub>E<sub>5</sub> + 2.5 mM SiW at 50°C.

			25 mM C <sub>12</sub> E <sub>5</sub> + 2.5 mM SiW at 50°C
Parameters	Description	Units	Ellipsoid form factor
scale	Scaling=1 means no scaling	None	1
background	Background intensity (noise+D2O)	cm <sup>-1</sup>	0.054
sld_scatterer	Approximates SLD of C <sub>12</sub> E <sub>5</sub>	10 <sup>-6</sup> Å <sup>-2</sup>	0.1
sld_solvent	SLD of D <sub>2</sub> O	10 <sup>-6</sup> Å <sup>-2</sup>	6.25
polar radius	polar radius of the ellipsoid	Å	83
equatorial radius	Radius of the flexible cylinder	Å	23
PdI of equatorial radius	Polydispersity index of radius	None	0.1
PdI of polar radius	Polydispersity index of radius	None	0
			Hayter-MSA structure factor
radius_effective	Radius of charged sphere	Å	Equivalent volume sphere
Volfraction	Volume fraction	None	0.01
Temperature	Temperature	K	323.15
Charge	Charge of the sphere	e	22
concentration_salt	Screening salt concentration	mol/L	0.004
Dielectric constant	Dielectric constant of water	None	60

### 3. How nano-ions act like ionic surfactants

Table 23: Best fit parameters used in the SAXS-fits in this chapter.

Figure	Sample composition			T [°C]	$n_{mic}$ [nm <sup>-3</sup> ]	Decorated micelle										Nano-ion				
	[C <sub>12</sub> E <sub>3</sub> ] [mM]	nano-ion [mM]	[nano-ion] [mM]			Ellipsoidal core-shell P(q)						Hayter-MSA S(q)				Sphere P(q)		Hard sphere S(q)		
						$\rho_{core}$ *10 <sup>-6</sup> [Å <sup>-2</sup> ]	$\rho_{shell}$ *10 <sup>-6</sup> [Å <sup>-2</sup> ]	$\rho_{H2O}$ *10 <sup>-6</sup> [Å <sup>-2</sup> ]	$R_{eq}$ [nm]	$R_{pol}$ [nm]	dR [nm]	$\Phi_{mic}$ [nm]	$R_{HS}$ [nm]	Charge, $q_e$ [mol/l]	[Salt] [mol/l]	$n_{nano-ion}$ [nm <sup>-3</sup> ]	r [nm]	$\rho_{nano-ion}$ *10 <sup>-6</sup> [Å <sup>-2</sup> ]	$\Phi_{POM}$	$R_{HS}$ [nm]
50	25	SiW	2.5	20	0.00017	9.4	11.6	9.4	2.33	2.33	0.9	0.01	2.5	16	0.001	0.0015	0.43	74.9	0.11	1
50	25	SiW	2.5	20	0.00017	9.4	11.45	9.4	2.4	2.4	0.9	0.01	2.5	17	0.001	0.0015	0.43	74.9	0.1331	1
50	25	SiW	2.5	20	0.00015	9.4	11.27	9.4	2.5	2.5	0.9	0.01	2.5	17	0.001	0.0015	0.43	74.9	0.1331	1
50	25	SiW	2.5	20	0.0001	9.4	11.28	9.4	2.1	4	0.9	0.01	2.8	20	0.002	0.0015	0.43	74.9	0.129	1.4
50	25	SiW	2.5	20	0.00005	9.4	11	9.4	2.2	6.8	0.9	0.01	3.2	28	0.002	0.0015	0.43	74.9	0.088	1.45
50	25	SiW	2.5	20	0.00003	9.4	10.95	9.4	2.4	8	0.9	0.016	-	-	-	0.0015	0.43	74.9	0.075	1.6

### 3.8.5. Vesicles (form factor fit)

The employed  $q$ -range did not reach low enough to probe the long-range ordering of the vesicles. However, a contribution of the structure factor is expected at lower  $q$  (below  $0.005 \text{ \AA}^{-1}$ ), as nano-ions must be sufficiently adsorbed to the vesicles in order to justify the curvature discrepancy between the outer and inner envelope of the vesicle. The fit below accounts for the form factor only. For reference, the vesicle fit is compared with a fit for infinite lamellae.

Table 24: Best fit parameters for 25 mM  $C_{12}E_5$  with 2.5 mM SiW at  $80^\circ\text{C}$ .

Parameters	Description	Units	25 mM $C_{12}E_5$ + 2.5 mM SiW at $80^\circ\text{C}$	
			Vesicle form factor	Lamella form factor
scale	Scaling=1 means no scaling	None	1	1
background	Background intensity (noise+D2O)	$\text{cm}^{-1}$	0.05	0.05
sld_scatterer	Approximates SLD of $C_{12}E_5$	$10^{-6}\text{\AA}^{-2}$	0.1	0.1
sld_solvent	SLD of $D_2O$	$10^{-6}\text{\AA}^{-2}$	6.34	6.34
Volfraction	Volume fraction of the shell	None	0.0072	0.0072
radius	Radius of the inner envelope	$\text{\AA}$	145	-
thickness	Thickness of the double-layer	$\text{\AA}$	34	34
PdI of radius	Polydispersity index of radius	None	0.35	-
PdI of thickness	Polydispersity index of thickness	None	0	0

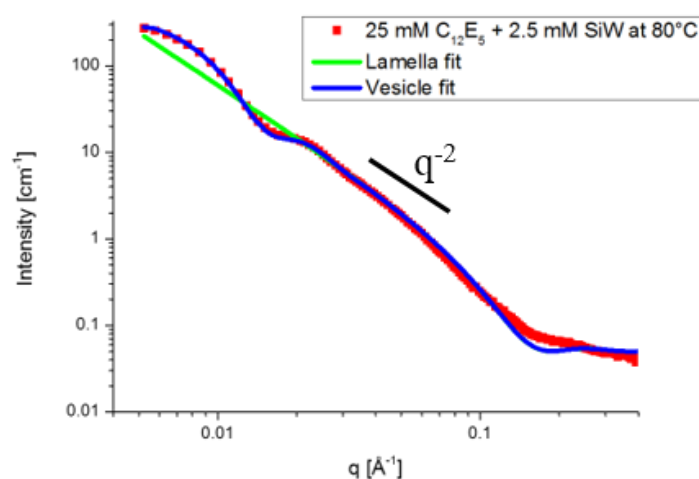


Figure 62: SANS-spectrum of 1 wt-%  $C_{12}E_5$  (25 mM) with 2.5 mM SiW at  $80^\circ\text{C}$  with fits for lamella and vesicle models.

### 3.8.6. DLS of SANS samples

Dynamic light scattering was performed across the phase diagram of 25 mM  $C_{12}E_5$  as a function of  $H_4SiW_{12}O_{40}$  (HSiW) concentration similarly to SANS. The investigated compositions are shown in Figure 63 and the corresponding correlation functions are shown in Figure 64.

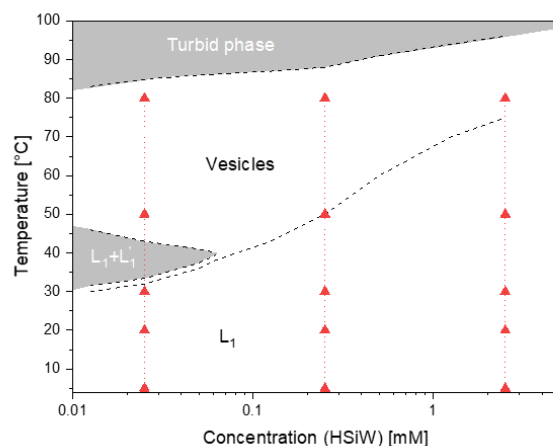


Figure 63: Phase diagram of 1 wt%  $C_{12}E_5$  (25 mM) in  $D_2O$  as a function of SiW-concentration. The red triangles indicate the investigated samples by DLS.

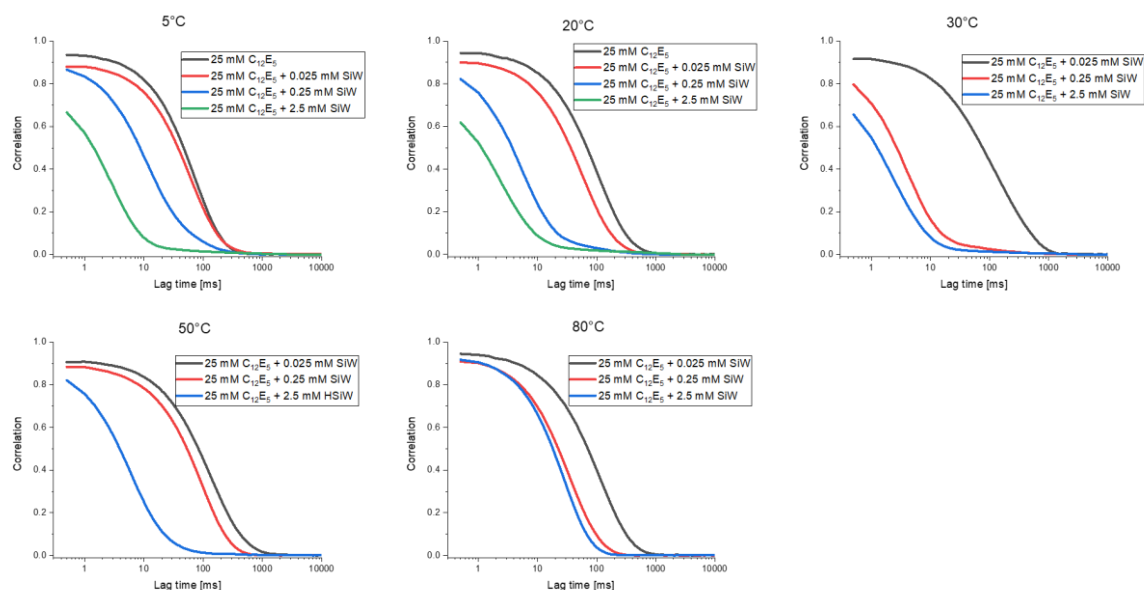


Figure 64: DLS-autocorrelation functions of 25 mM  $C_{12}E_5$  in the presence of 0 mM, 0.025 mM, 0.25 mM, 2.5 mM HSiW at 5°C, at 20°C, at 30°C, at 50°C and at 80°C.

The DLS-correlation functions consistently display monomodal shape at all measured temperatures indicating the presence of only one scattering species in solution. At all measured temperatures, the onset of the exponential decrease is shifted to lower lag times with increasing SiW-concentration. Consequently, the diffusion speed of the scattering objects is generally higher for SiW-decorated micelles (or bilayers) than for the bare  $C_{12}E_5$  self-assemblies.

Generally, the diffusion speed of an object in solution depends on the dispersant medium, the size of the object as well as the forces between diffusing objects. As micelles become more and more electrostatically repulsive upon SiW-adsorption the diffusion speed is generally expected to increase with SiW-concentration. The same concept seems to hold true in the bilayer phase, while for example in a lamellar phase diffusion is anisotropic and only upon generation of finite bilayer objects, such as vesicles, the diffusion coefficient contains valuable information of the scattering object. For the autocorrelation functions of 25 mM C<sub>12</sub>E<sub>5</sub> + 2.5 mM HSiW at 20°C and at 80°C (respectively, spherical micelles and vesicles as identified by SANS) hydrodynamic diameter were extracted according to the procedure in section 7.4. The received dimensions are shown in Table 25 along with the dimensions obtained from SANS-fitting. Overall, the two methods are in decent agreement.

Table 25: Summary of the acquired dimensions from DLS and SANS for the sample containing 1% C<sub>12</sub>E<sub>5</sub>+2.5 mM SiW.

		DLS Hydrodynamic diameter [nm]	SANS “Real” diameter [nm]
1% C <sub>12</sub> E <sub>5</sub> + 2.5 mM SiW at 20°C	spherical micelle	2.0	4.8
1% C <sub>12</sub> E <sub>5</sub> + 2.5 mM SiW at 80°C	vesicle	54	36

3.8.7. NMR: C<sub>12</sub>E<sub>5</sub>-stability

Long time exposure to heat induced degradation of the C<sub>12</sub>E<sub>5</sub>-surfactant as indicated by the emergence of side peaks after storing a sample containing 25 mM C<sub>12</sub>E<sub>5</sub> + 1 mM HSiW (H<sub>4</sub>SiW<sub>12</sub>O<sub>40</sub>) at 80°C for a week, see Figure 65. The degradation products were not further identified.

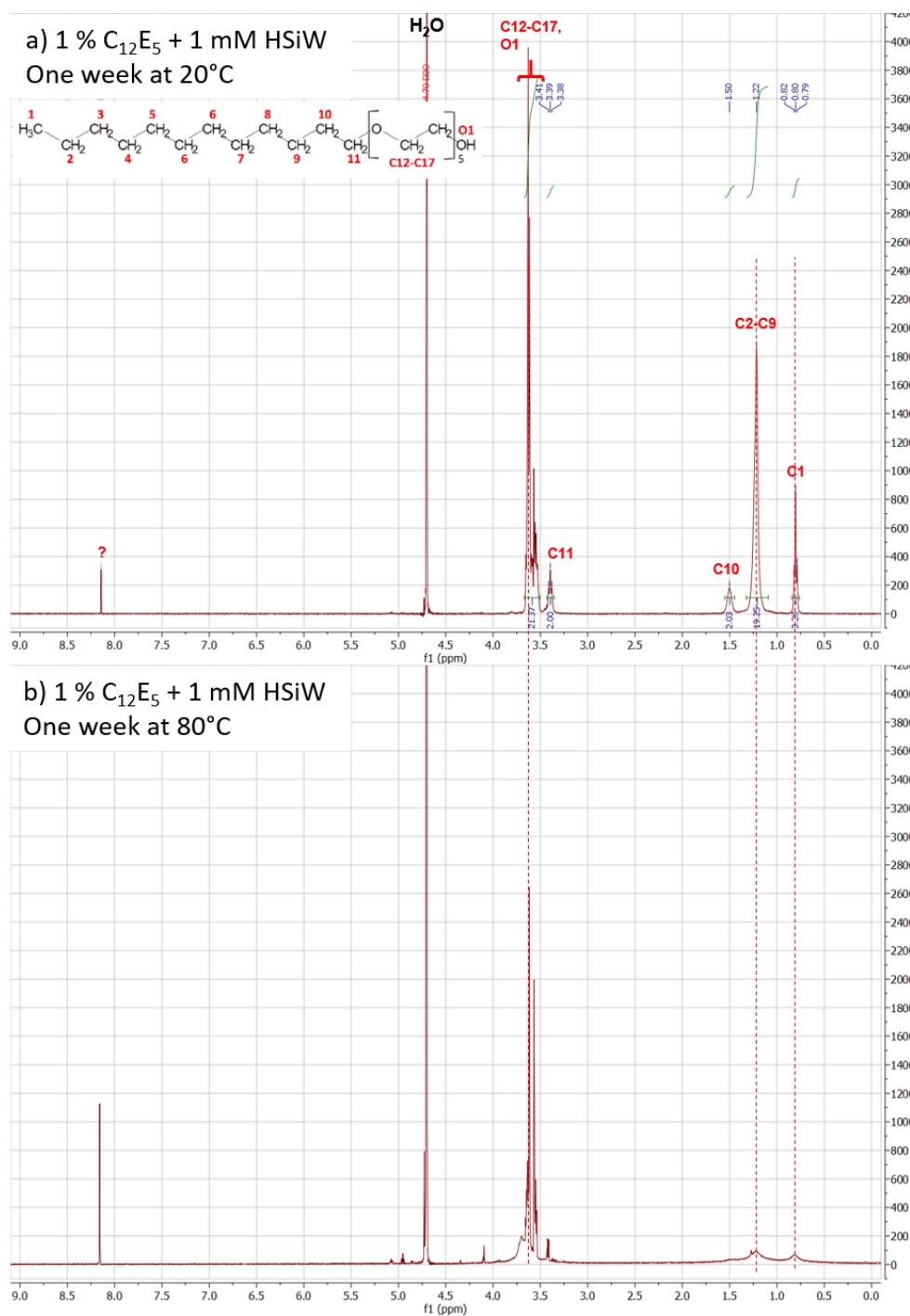


Figure 65: <sup>1</sup>H-NMR spectra of 25 mM C<sub>12</sub>E<sub>5</sub> + 1 mM HSiW after one week at a) 20°C and b) 80°C. Peaks of degradation products appear for the sample exposed to 80°C. The peaks in a) are assigned to the respective carbon atoms enumerated in the upper left molecular formula.

### 3.8.8. Vesicles of another non-ionic surfactant - BrijO10

Here, it shall be shown that the observed phase behavior with  $C_{12}E_5$  can be extended to a variety of non-ionic surfactants that form bilayer phases. For this purpose, the commercial surfactant BrijO10 was chosen, which is a mixture of several surfactants differing only in length of the polymerized hydrophilic head. The main fraction of BrijO10 is composed of  $C_{18:1}E_{10}$  and its phase diagram in water is shown in Figure 66a.

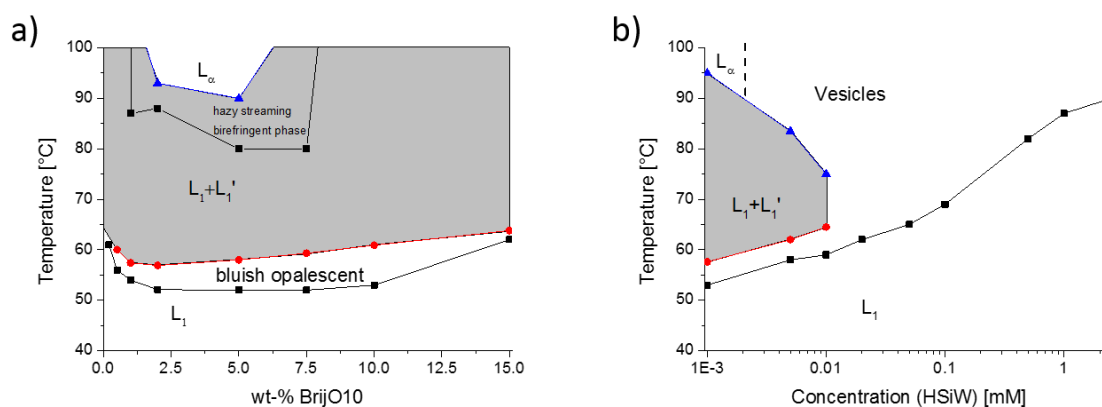


Figure 66: a) Phase diagram of the non-ionic surfactant BrijO10 in water and b) phase diagram of 1 wt-% BrijO10 (14 mM) as a function of HSiW ( $H_4SiW_{12}O_{40}$ ) concentration.

BrijO10 in water forms a micellar phase at low temperatures, which becomes bluish opalescent just before the cloud point at 57°C at 1 wt-% BrijO10. Upon further heating above 90°C a strongly birefringent lamellar phase is formed, which exists only between 1 and 5 wt-% surfactant. When HSiW is added to 1 wt-% BrijO10 the typical phase evolution results like with 1 wt-%  $C_{12}E_5$ , see Figure 66b. The micellar phase at low temperatures becomes stabilized extending to higher temperatures and the birefringent lamellar phase at above 90°C transitions into a vesicle phase (non-birefringent), which stretches out to lower temperatures creating a common phase border with the micellar phase. The origin of these phase transitions was thoroughly discussed on the example of  $C_{12}E_5$  in section 3.2.





## 4. Nano-ions in non-ionic surfactant foams

Superchaotropic ions have been shown to interact strongly with non-ionic surfactant assemblies in solution as well as at the air-water interface covered by surfactants.<sup>4</sup> The impact of the nano-ions is revealed in the previous chapters 2 and 3, where the physical changes (micellar shape and interactions) in non-ionic surfactant phases of micelles and bilayers in the presence of such superchaotropic ions were revealed. In particular, arising electrostatics as well as the dehydration of the surfactant head upon adsorption of the nano-ion were demonstrated to have tremendous effects on the properties of the non-ionic surfactant phases. Naskar et al. further provided clear evidence using flotation experiments that superchaotropic ions, such as the Keggin polyoxometalates  $\text{PW}_{12}\text{O}_{40}^{3-}$  and  $\text{SiW}_{12}\text{O}_{40}^{3-}$ , have a strong affinity towards non-ionic surfactant foams.<sup>4</sup> Generally, foams provide a large surface for possible adsorbates such as superchaotropic ions and constitute therefore an interesting substrate to investigate the impact of superchaotropic ions. The following study represents the first investigation of non-ionic surfactant foams spontaneously loaded with inorganic polyoxometalates driven by the chaotropic effect. First, the reader shall be introduced to the general topic of foams.

## 4.1. Introduction to foams

According to the definition by IUPAC, foams are “A dispersion in which a large proportion of gas by volume in the form of gas bubbles, is dispersed in a liquid, solid or gel. The diameter of the bubbles is usually larger than 1  $\mu\text{m}$ , but the thickness of the lamellae between the bubbles is often in the usual colloidal size range. The term froth has been used interchangeably with foam. In particular cases froth may be distinguished from foam by the fact that the former is stabilized by solid particles (as in froth flotation) and the latter by soluble substances.”<sup>3</sup>

Foams are ubiquitous in everyday life products, such as food or beverages or in cosmetics, where they are desired components in particular due to their smooth silky feel when consumed or applied to the skin. Foams also appear frequently in nature, for example at seashores where natural surface-active substances are agitated by waves and entrain wind leading to the formation of bubbles and subsequently the foam. Similarly, wastewaters often foam indicating industrial pollution with surface-active substances. Furthermore, foams find numerous applications in firefighting, detergency, as thermal isolators, in flotation and separation processes, in the textile industry etc.<sup>185–187</sup> Generally, foams must be formulated and their properties fine-tuned to fulfil the specific requirements (generation, stability, etc.) of the mentioned applications, spawning high interest in understanding foams on a fundamental level. For the purpose of this thesis, the focus is set on aqueous liquid foams.<sup>187</sup> As bubbles generated from pure water rupture immediately owing to the high water/air surface tension and corresponding high interfacial energy, it is necessary to add surfactants in order to decrease the energetic cost of creating the bubble interface and to counterbalance the gravitational pull on the liquid.<sup>187</sup> This can be done using any surface-active component such as proteins, polymers or nanoparticles, while herein exclusively aqueous surfactant foams shall be discussed along their lifetime reaching from their generation over their aging and finally to their collapse.

Thus, in order to generate a foam out of a surfactant solution, gas must be entrained into bubbles, which is possible by a plethora of methods including whisking, whipping, shaking or, as done in this thesis, by sparging gas through a microporous plate into the foaming solution.<sup>186</sup> The used conditions including pore size, the choice of the gas, the foaming agent's concentration, gas flux, temperature or the size of the foam container have significant impact on the resulting nature of the foam. The generated foam can then be classified according to the dispersed inter-bubble liquid volume fraction  $\Phi_L$  as a wet foam, when  $5\% < \Phi_L < 30\%$ , or a dry

---

<sup>3</sup> taken from <https://goldbook.iupac.org/terms/view/F02467>

foam, when  $\Phi_L < 5\%$ .<sup>187,188</sup> Dispersions with liquid fractions above 30% are called bubbly liquids. Figure 67 left provides an example of the aging of a typical wet foam with a liquid volume fraction of  $\Phi_L = 15\%$  to a dry foam with a liquid fraction of  $\Phi_L < 1\%$ .

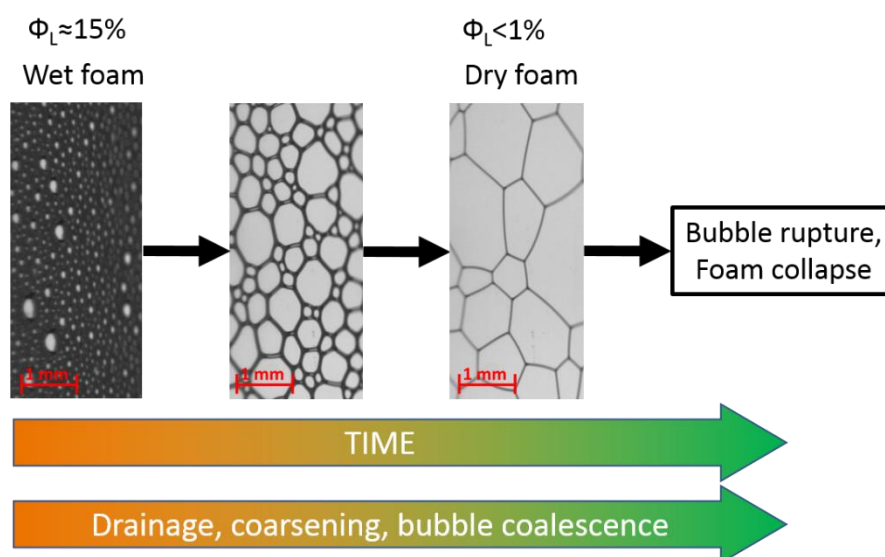


Figure 67: Aging of a foam over time from a wet foam to a dry foam. The pictures represent foam bubbles in contact with a glass wall and depict the evolution of spherical bubbles towards polyhedral ones with decreasing liquid volume fraction.

As the foam is subject to gravity, the dispersed liquid in the films separating the bubbles will move downwards, known as foam drainage. Consequently, the thick liquid films between spherical bubbles at high volume fractions (wet foam) become thinner over time resulting in direct bubble contacts and a transition to polyhedral bubbles at low liquid volume fractions (dry foam), shown for  $\Phi_L < 1\%$  in Figure 67 right. The formed contact regions between the bubbles are referred to as foam films (between two bubbles), plateau borders (between three adjacent bubbles) and vertices (between four adjacent bubbles), see Figure 68. In dry foams, the thickness of thin films is generally in the colloidal range scale spanning from a few up to hundred nanometers, while plateau borders and vertices are characterized by thicknesses in the high micrometer range and can be seen with the naked eye as in Figure 67. Consequently, in dry foams the liquid is almost fully located in the plateau borders and their intersections (vertices), and not in the thin films.

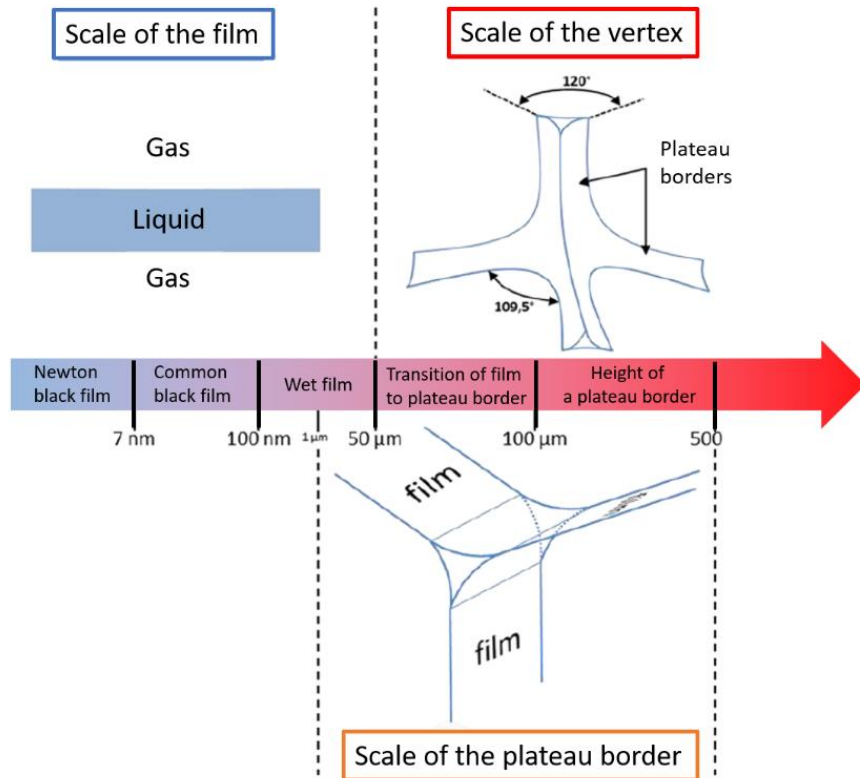


Figure 68: Multi-scale structure in dry foams showing a foam film, a plateau border and a vertex with corresponding length scales. Adapted from the PhD-thesis of Cyril Micheau.<sup>188</sup>

#### 4.1.1. Thin foam films

The properties of a foam depend strongly on the physics and chemistry of the foam films, which are discussed in the following. As is shown in Figure 68 upper left, a foam film is a liquid layer sandwiched in between two gas layers, where surfactant molecules stabilize the interfaces. Foam films are always curved in order to achieve a minimization of surface energy and their curvature depends on the pressure difference  $\Delta P$  between the gas and the liquid phase and the interfacial tension  $\gamma$  according to the Young-Laplace equation.

$$\Delta P = |P_{liq} - P_{gas}| = \gamma \left( \frac{1}{R_1} - \frac{1}{R_2} \right) = \gamma H \quad (5.1)$$

With  $P_{liq}$  and  $P_{gas}$  being the pressure in the liquid and gas phase respectively,  $R_1$  and  $R_2$  the principal radii of curvature and  $H$  the curvature of the foam film. As a direct consequence of this equation, a liquid foam film is a biconcave object. The stability of such a foam film is linked to the balance of transversal attractive and repulsive forces in the film. This force balance is called the disjoining pressure  $\Pi$  and indicates whether a foam film becomes thicker ( $\Pi$  is positive) or thinner ( $\Pi$  is negative) until its eventual rupture. As, however, foam films are

virtually flat and thus exhibit lower curvature than plateau borders/vertices there is a difference in pressure between the two according to the Young-Laplace equation (equation 5.1). This difference results in the so-called capillary pressure  $P_c$ , which causes a stream of liquid out of the thin films towards the vertices.<sup>187</sup>

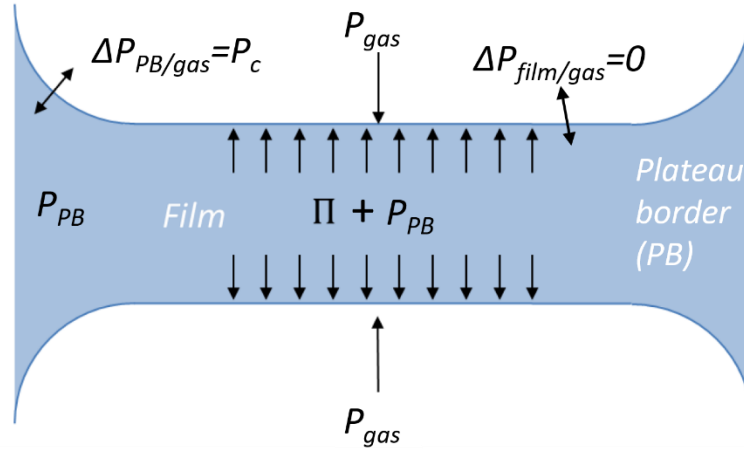


Figure 69: Plane equilibrium foam film, where the disjunction pressure is equal to the capillary pressure  $P_c = P_{liq} - P_{gas}$  defining the stability of the foam. Adapted from the PhD-thesis of Cyril Micheau.<sup>188</sup>

Thus, in order to stabilize a film and its parent foam, the repulsion between the film interfaces needs to compensate the pressure of the gas as well as the capillary pressure. In the simplified case of a plane equilibrium film, see Figure 69, the pressure balance according to the Young-Laplace equation is expressed as:

$$\Delta P_{film/gas} = |P_{gas} - P_{film}| = |P_{gas} - P_{PB} + \Pi| = 0 \quad \Rightarrow P_c = \Pi \quad (5.2)$$

With  $\Delta P_{film/gas}$  the difference between the pressure of the film  $P_{film}$  and the pressure of the gas  $P_{gas}$ .

In general, the thinning of the films has to be inhibited in order to lengthen the lifetime of a foam. According to equation 5.2, this can be accomplished by decreasing the capillary pressure or by increasing the disjoining pressure. On the one hand, the capillary pressure depends on the foaming conditions and its decrease can be achieved by diminishing the surface tension by adding more surfactant or by increasing the liquid fraction to make bubbles more spherical to mitigate the curvature discrepancy between films and plateau borders. Notably, addition of surfactant affects the surface tension in a meaningful way only up to its critical micellar concentration, where the air/water surface is completely covered, and surface tension stays almost constant upon addition of further surfactant. Consequently, foaming conditions are usually best at the CMC of the surfactant.<sup>187</sup>

On the other hand, the disjoining pressure depends on the interactions between the film interfaces and is expressed by:

$$\Pi = \Pi_{\text{elec}} + \Pi_{\text{vdW}} + \Pi_{\text{steric}} + \Pi_{\text{supra}} \quad (5.3)$$

With  $\Pi_{\text{elec}}$  representing electrostatic forces,  $\Pi_{\text{vdW}}$  London-van der Waals dispersion forces,  $\Pi_{\text{steric}}$  describing steric short-range forces and  $\Pi_{\text{supra}}$  denoting forces arising from supramolecular structuring. The electrostatic and the van der Waals terms hereby represent the classical interaction forces in colloidal dispersions considered in the DLVO-theory. In foams, electrostatic interactions within films are always repulsive as opposing interfaces are identical in composition and charge. The range of these electrostatic interactions depends strongly on the ionic strength in the liquid as is expressed by the Debye screening length  $\kappa^{-1}$ .

$$\kappa^{-1} = \sqrt{\frac{\varepsilon_r \varepsilon_0 k_B T}{2 * 10^3 N_A e^2 I}} \quad (5.4)$$

With  $\varepsilon_r$  the relative permittivity of the medium,  $\varepsilon_0$  the permittivity of the vacuum,  $k_B$  the Boltzmann constant,  $T$  the temperature,  $N_A$  the Avogadro constant,  $e$  the elementary charge and the ionic strength  $I = \frac{1}{2} \sum_i c_i * z_i^2$  for an electrolyte composed of ions  $i$  with concentrations  $c_i$  and ionic charge  $z_i$ . The Debye length indicates that the more electrolyte is present in the medium surrounding an electric charge the lower will be the range of the electrostatic force. In turn, in salt-free solutions electrostatic interactions act on the largest length scale compared to the other terms in equation 5.3. Furthermore, van der Waals interactions are generally attractive dipol-dipol interactions that act on a smaller length scale than electrostatics, commonly resulting in overall attractive interaction potentials between very thin films in the low nanometer range. The reason why such thin films do not merge into another is due to the steric requirement (repulsion between “touching” molecules) of the surfactant molecules at the interface. Additionally, some foam films are subject to so-called supramolecular forces that arise from structuring of surfactant self-assemblies in the liquid between the interfaces. These forces are generally of repulsive nature and are common for surfactant foams made of micellar (or lamellar) solutions, where the surfactant micelles form layers between the film interfaces and slide out layer by layer upon film thinning (so-called stratification). All mentioned force contributions depend on the chemistry of the interfaces as well as the interstitial liquid thus providing a rich playing field to modify the properties of a foam by formulation. More details on disjoining pressure and the individual force contributions can be found in von Klitzing, Stubenrauch 2003 and Bergeron 1999.<sup>189,190</sup>

Furthermore, as liquid foams are constantly evolving inhomogeneous systems the water/air interface needs to be deformable upon mechanical stress to prevent film rupture and increase foam stability. This is expressed using the dilatational elasticity modulus  $E$ . If further relaxation occurs after an elastic response this modulus is expressed as a complex number constituted of an elastic term  $E'$  and a viscous term  $E''$ .<sup>186,187,191</sup>

$$E = \frac{d\gamma}{d\ln A} \quad (5.5)$$

$$E^* = E' + iE'' \quad (5.6)$$

with  $\gamma$  the surface tension and  $A$  the interfacial area. The higher the elasticity modulus of a foam film the faster the interface can self-heal and prevent foam rupture. Generally, surfactants that quickly reach surface tension equilibrium are preferred to form stable foams as they quickly equate local differences in surface tension. However, it is also possible to stabilize foams with very resilient and rigid interfaces that simply resist appearing stress halting any deformation. Such stabilization occurs in cationic surfactant foams or in particle-stabilized foams where foam film dynamics are exceptionally slow.<sup>192</sup>

The viscosity of the interface (expressed by  $E''$ ) also has significant effects on the flow of the interstitial liquid. At high interfacial viscosities, e.g. in rigid foam films, liquid flow is retarded close to the interfaces resulting in so-called Poiseuille flow, while for films with low interfacial viscosities the liquid flows at a homogeneous speed together with the interior of the film, so-called plug flow, see Figure 70.<sup>188</sup>

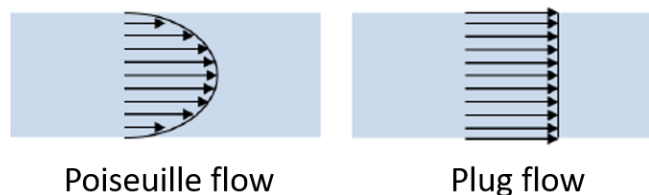


Figure 70: Poiseuille flow appearing in foams with viscous interfaces and plug flow appearing in foams with less viscous interfaces. Adapted from the PhD-thesis of Cyril Micheau.<sup>188</sup>

### 4.1.2. Aging phenomena in foams

Foams are inherently unstable soft matter structures that evolve towards thermodynamic equilibrium by decreasing their overall surface area over time. To reach this goal, foam bubbles interact permanently via gas diffusion through the liquid phase causing a growth of larger bubbles at the expense of smaller ones. This phenomenon is called Ostwald ripening and arises from the pressure difference between small (high pressure, high curvature) and large (low pressure, low curvature) bubbles according to the Young-Laplace equation. The speed of the inter-bubble gas exchange is connected to the solubility of the diffusing gas in the liquid and, therefore, the choice of the gas can have significant effects on foam stability. Furthermore, in very dry foams adjacent bubbles directly exchange gas through the thin interstitial liquid films by the shortest diffusion pathway. Here, the number of faces of a bubble and thus, the number of its neighbors plays a crucial role, as the diffused gas is proportional to the surface around a bubble. Thus, larger bubbles generally exhibit accelerated growth as they are surrounded by more neighbors than small ones. This phenomenon is known as foam coarsening.<sup>186,192,193</sup>

Furthermore, when films become thinner upon drainage, they become unstable. Thus, slight mechanical stress or thinning beyond their stability limit leads ultimately to a film rupture. In foams, initial rupture events entail coalescence of adjacent bubbles, which does not affect the total foam volume at first. However, each rupture event causes a reorganization of surrounding bubbles (mechanical stress) and may trigger a rupture avalanche. Thus, dry foams may collapse entirely over time. It is also possible to trigger foam rupture by adding hydrophobic agents, so-called antifoamers, which penetrate the interface driving the stabilizing surfactant molecules apart causing rapid thinning and collapse of the films. In turn in order to prevent film rupture, foam drainage must be inhibited to ensure a stable minimum thickness of the foam films. This can be done by changes in the composition, which may increase the dispersed liquids viscosity or controls the stabilizing mechanisms in the films discussed in section 4.1.1.



## 4.2. Non-ionic foam films subjected to superchaotropic ions

Superchaotropic ions, like the Keggin polyoxometalate  $\text{SiW}_{12}\text{O}_{40}^{4-}$ , interact strongly with any kind of soft matter in water including non-ionic surfactant self-assemblies in solution<sup>4,92</sup> and at the air water-interface<sup>4</sup>, non-ionic polymers<sup>104</sup>, small organic molecules<sup>105,106</sup> and proteins.<sup>171</sup> As emphasized in the preceding chapters on the example of non-ionic surfactant assemblies, the effects induced by these superchaotropic ions are tremendous and involve strong electrostatics along with a dehydration of the host surface upon adsorption of the nano-ion. The surface of surfactant self-assemblies in water has striking similarities to the air/water interface in surfactant foams and the difference lies exclusively in the surrounding of the hydrophobic surfactant tails. For surfactant assemblies in water, the hydrophobic surfactant tails form an inner liquid hydrophobic core, while in foams the hydrophobic tails constitute the outermost liquid phase border to the gaseous phase (air). For the nano-ion of interest here,  $\text{SiW}_{12}\text{O}_{40}^{4-}$  (SiW), which is classified as a purely superchaotropic ion according to chapter 2, section 2.6, interaction is only expected to occur with the polar hydrated surfactant heads on the aqueous side of the foam, whereas interaction with the hydrophobic surfactant tail can be excluded. Under this pretext, this chapter aims to elucidate the effects of the superchaotropic ion SiW on foams of a non-ionic surfactant. The foam here is stabilized by the non-ionic surfactant BrijO10, a commercial surfactant mixture of polymerized ethoxylated surfactants centered on the main fraction  $\text{C}_{18:1}\text{E}_{10}$ , of which the chemical structure is shown in Figure 71. Owing to its double bond, which perturbs the 2D-packing of the surfactant molecules, BrijO10 forms foam films with high elasticity that exhibit relatively high stability when dry, in comparison to surfactants without double bonds.

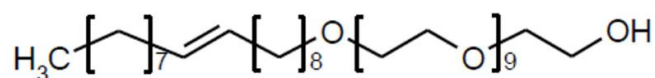


Figure 71: Chemical structure of the main fraction of BrijO10,  $\text{C}_{18:1}\text{E}_{10}$ .

Here, the foams of BrijO10 are probed using small angle neutron scattering (SANS). While neutrons have been exploited for the characterization of soft matter in solution for a long time, its usage for the characterization of foams dates back to experiments by Boué et al in 2003<sup>194</sup> and has since been further developed by various authors.<sup>195–201</sup> In foams, SANS probes simultaneously the scattering of the plateau borders as well as of the thin films. Thus, in wet foams, thick liquid films and plateau borders scatter neutrons because of the structures present in the dispersed liquid, while in dry foams, where liquid is scarce, oscillations emerge from specular neutron reflectivity on the thin foam films.<sup>194,195,198,199</sup>

The foams herein were produced using a setup developed by Micheau et al.<sup>201</sup>, see Figure 72. The foam is generated in a foam column by sparging air through a microporous sintered glass plate into the BrijO10 solution (using D<sub>2</sub>O instead of H<sub>2</sub>O to amplify contrast) leading to a gradual foam generation atop the foaming solution. A weak constant airflow of 0.5 mL/min was used throughout the SANS-experiments to generate dry foams in their quasi-stationary state, where foam generation and collapse compensate one another. At the used conditions, the generated foams just reach the top of the glass column without overflowing. To probe these foams with neutrons three quartz windows, denoted as LW (lower window), MW (middle window) and UW (upper window), are positioned along the column to allow for SANS-acquisition at different foam heights.

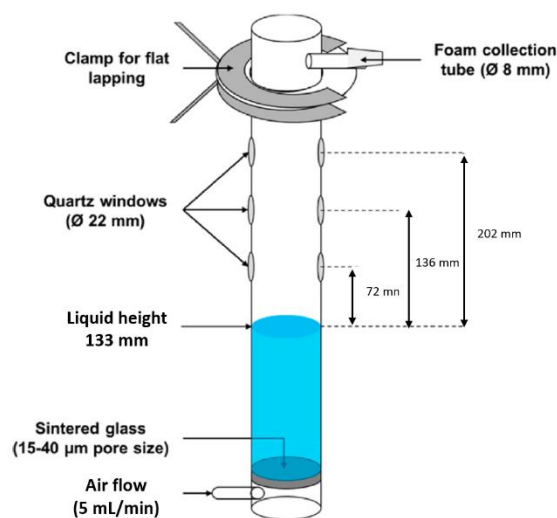


Figure 72: Representation of the SANS-setup. The inner diameter is 24 mm and the foam is retrieved at 422 mm height corresponding to a 289 mm foam column. Adapted from Micheau 2013.<sup>201</sup>

The acquired SANS-spectra of a foam of 0.5 mM BrijO10 with corresponding foam age and for every window are shown in Figure 73. In all spectra, extended  $q^{-4}$ -dependences occur at high and low  $q$  arising from Porod scattering of the large amount of surface present in the foam. In the high  $q$ -region, additionally the scattering of micelles can be expected as 0.5 mM BrijO10 is equivalent to 12.5 times its cmc (cmc=40  $\mu\text{M}$ <sup>202</sup>). Accordingly, micelles are present in the initial foaming solution (SANS on Brij-solution, orange squares in Figure 73a). The presence of micelles in the foams is further evidenced in Appendix 4.3.2 on page 166. Indeed, the scattering acquired in the lower window (wettest part of the foam) shows slight differences in the low  $q$  region over time that can be attributed to the presence of micelles. Notably, this micellar scattering contribution is slight as the micellar phase is highly dilute at 0.5 mM BrijO10 and the foam is dry, i.e. provides low sample thickness and weak scattering. Furthermore, an intensity maximum appears the mid  $q$ -region of the foam SANS-spectra. This maximum

occurred in all measured foam SANS-spectra and will be shown later to correspond to the critical reflectivity angle. Most importantly though, it is shown in Figure 73 that the SANS-spectra overlap well over the examined lifetime of the foam (up to a foam age of 70 minutes) demonstrating that the foam films are in equilibrium and that the so-called quasi-stationary state of the foam is reached immediately after foam generation and persists for more than an hour. It must be noted though that despite constant gas flow ensuring a constant foam height, the lifetime of the foam was limited as gradual collapse occurred at advanced foam age (after 80 mins for the foam of 0.5 mM BrijO10 and after different times for other samples). For this reason, the foam is declared to be in a quasi-stationary state throughout the SANS-measurement.

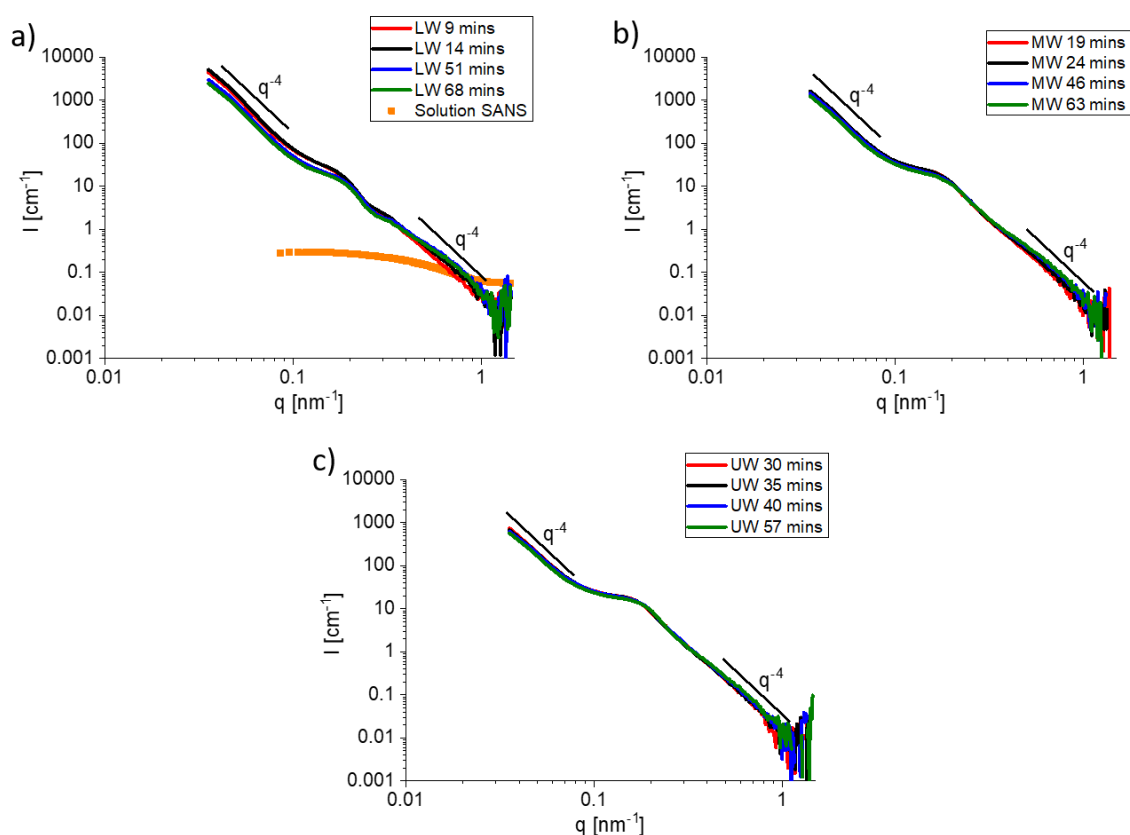


Figure 73: Normalized SANS-spectra of a foam of 0.5 mM BrijO10 at different times after foam generation measured at a) the lower window (LW), b) the middle window (MW) and c) the upper window (UW). In a) additionally the normalized scattering of aqueous 0.5 mM BrijO10 solution is shown.

Equivalently, the scattering spectra of foams of 0.5 mM BrijO10 + 0.5 mM HSiW are presented in Figure 74. Again, the foam evolves very little in the examined timeframe (up to a foam age of 100 minutes) evidencing that the foam is generated in its quasi-stationary state. The, SANS spectra of all windows show the characteristic  $q^{-4}$ -dependence at low and at high  $q$ , where for the lower window, i.e. in the wettest part of the foam, slight deviations are observed at high  $q$  with the foam's age presumably arising from micelles present in the plateau borders and

vertices. In the mid  $q$  region, sizable oscillations occur involving up to five maxima/minima at the middle and upper window.

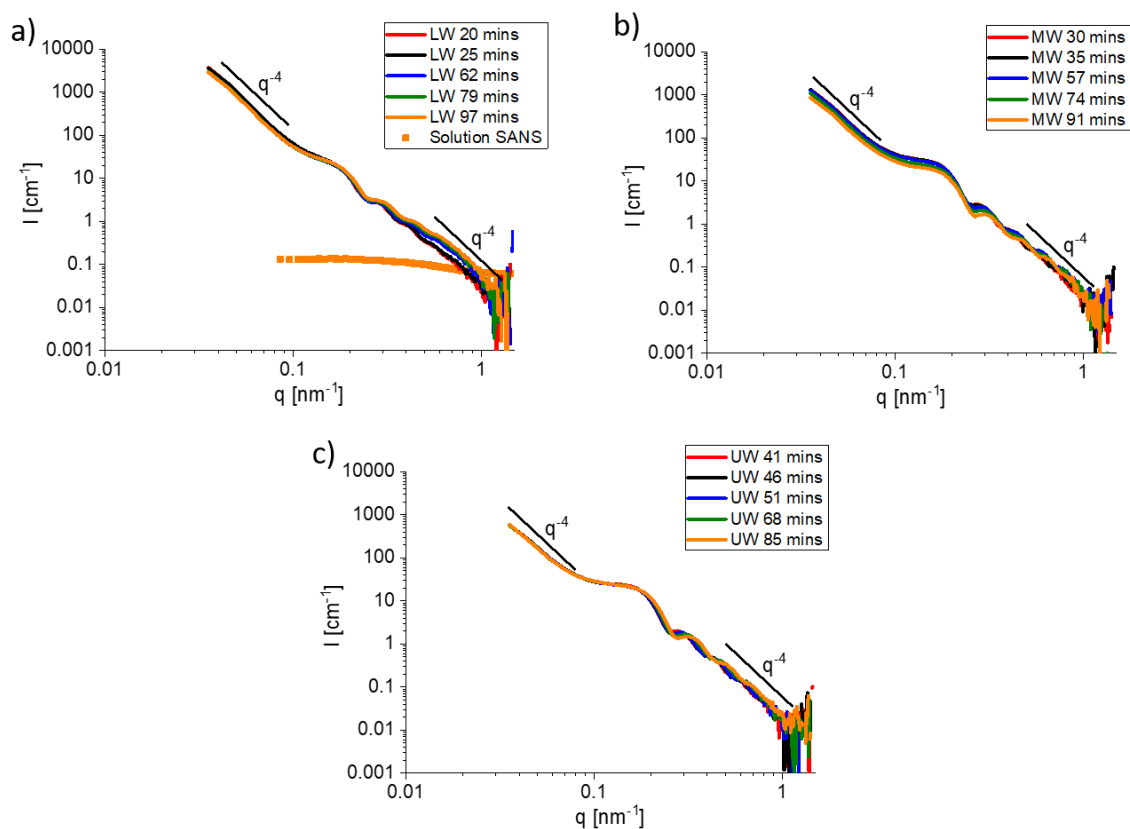


Figure 74: Normalized SANS-spectra of a foam of 0.5 mM BrijO10 + 0.5 mM HSiW ( $\text{H}_4\text{SiW}_{12}\text{O}_{40}$ ) at different times after foam generation measured at a) the lower window (LW), b) the middle window (MW) and c) the upper window (UW). In a) additionally the normalized scattering of aqueous 0.5 mM BrijO10 + 0.5 mM SiW is shown.

These oscillations cannot be attributed to classical structuring observed in SANS. Rather, they result from neutron reflectivity on the thin liquid foam films, i.e. angle-dependent constructive and destructive interferences of reflected neutrons on the outer and inner interface of the films. Here, addition of HSiW causes a tremendous increase in the number of oscillations (up to five) in comparison to the bare BrijO10 foam (one oscillation). This effect reveals that foam films in the presence of SiW are much more monodisperse allowing for multiple extrema in comparison to bare BrijO10 foams. Notably, it is also possible to cause the appearance of these oscillations by injecting SiW into the foaming solution after generation of the foam, see Appendix 4.3.3 on page 168.

Herein, the focus is set on the origin of these oscillations and different foams in their quasi-stationary state need to be compared. For this purpose, foams with advanced ages of 55-70 mins were chosen because at these times the foam films were found to be most stable in terms of film thickness, see Appendix 4.3.1 page 163. Figure 75a shows the corresponding SANS-spectra of foams of BrijO10 with increasing concentrations of the superchaotropic ion SiW. In order to

focus on the mid  $q$ -region, where the reflectivity signal occurs, the spectra are additionally presented in an  $Iq^4$  vs  $q$  plot, the so-called Porod limit, see Figure 75b.

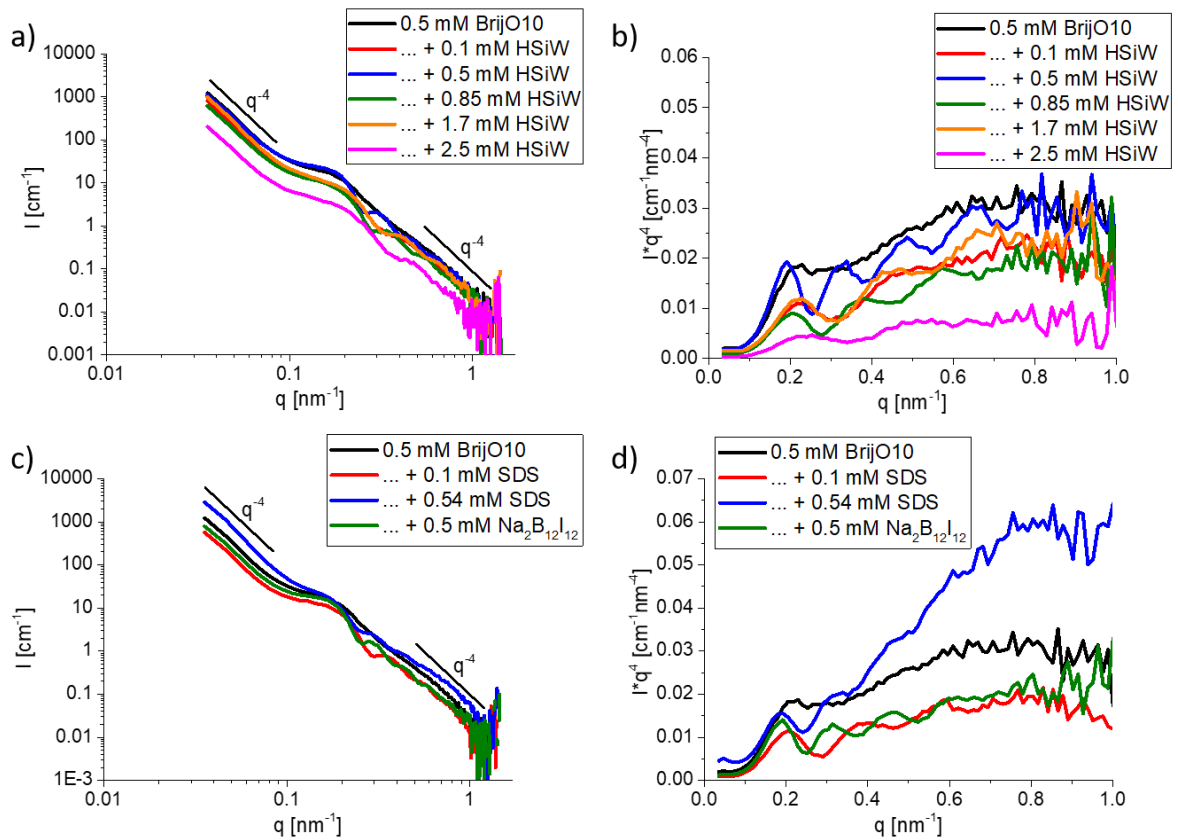


Figure 75: a)Log-log plot of  $I$  vs  $q$  and b)Lin-lin Porod plot of  $Iq^4$  vs  $q$  of the SANS-spectra acquired from the middle window at a foam age of 63-74 minutes for foams of 0.5 mM BrijO10 in the presence of HSiW. c)Log-log plot of  $I$  vs  $q$  and d)Lin-lin Porod plot of  $Iq^4$  vs  $q$  of the SANS-spectra acquired from the middle window at foam age 63-71 minutes for foams of 0.5 mM BrijO10 in the presence of SDS and  $\text{Na}_2\text{B}_{12}\text{I}_{12}$ .

The overall scattered intensities in Figure 75a lie in a similar range from 0-1.7 mM HSiW, while the sample containing 2.5 mM HSiW produced a lower intensity. This difference may arise due to local defects/collapse in the foam, which leads to a smaller liquid fraction or fewer foam films in the neutron beam and may thus cause a decrease in intensity. Such effects are expected for aging foams, of stochastic nature and irrelevant to the performed treatment here, as only the positions of the extrema will be exploited. Furthermore, as mentioned previously upon addition of HSiW large oscillations appear showing that the films become monodisperse in the presence of HSiW. The positions of the extrema and corresponding number of the oscillations are found to depend strongly on the amount of added HSiW, see Figure 75b. Furthermore, similar oscillations were observed for BrijO10 foams upon addition of the ionic surfactant sodium dodecylsulfate (SDS) as well as the superchaotropic dodecaborate  $\text{Na}_2\text{B}_{12}\text{I}_{12}$ , see Figure 75c and d. These oscillations can be fitted using a reflectivity model of a water ( $\text{D}_2\text{O}$ ) film sandwiched between two infinitely thick air layers<sup>199</sup> as illustrated in Figure 76. The first maximum then corresponds to the critical angle, below which total reflection occurs.

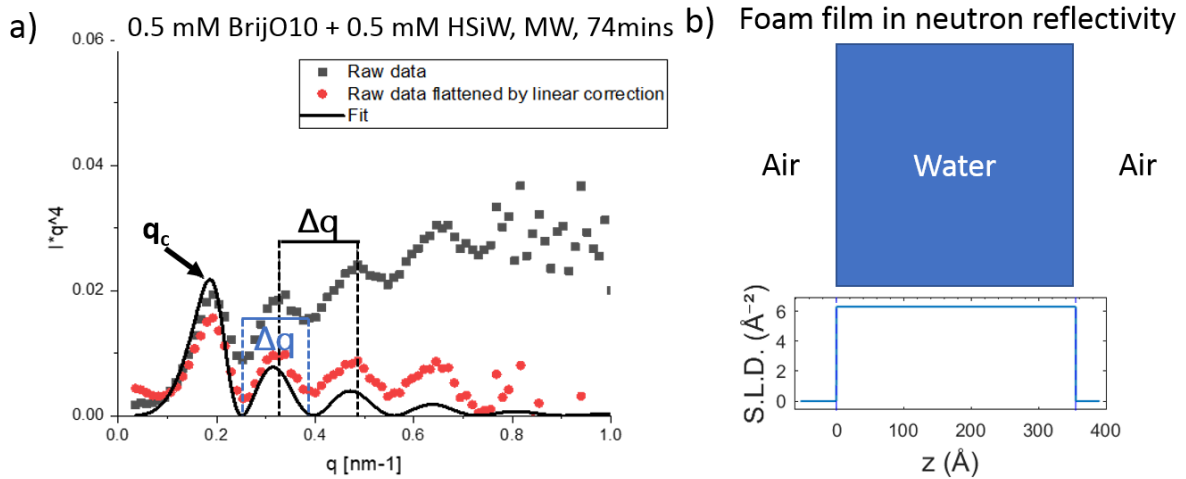


Figure 76: a) Reflectivity fit of the extrema in the scattering of a foam of 0.5 mM BrijO10 + 0.5 mM HSiW (middle window, foam age is 74 mins). b) The used scattering length density (SLD) profile is composed of water (D<sub>2</sub>O) sandwiched between two air layers, where the water layer has a thickness of 355 Å providing the foam film thickness.

Furthermore, it is possible to extract the film thickness  $d$  from the period of the experimental reflectivity extrema by the relation:

$$d = \frac{2\pi}{\Delta q} \quad \text{at } q \gg q_c$$

with  $\Delta q$  being the distance between two adjacent maxima or minima. Herein, only the first oscillations close to the critical angle were observed, where the condition  $q \gg q_c$  does not hold.<sup>203</sup> For this reason, fitting seems a more reliable method and only the thicknesses obtained therefrom are used in the following.

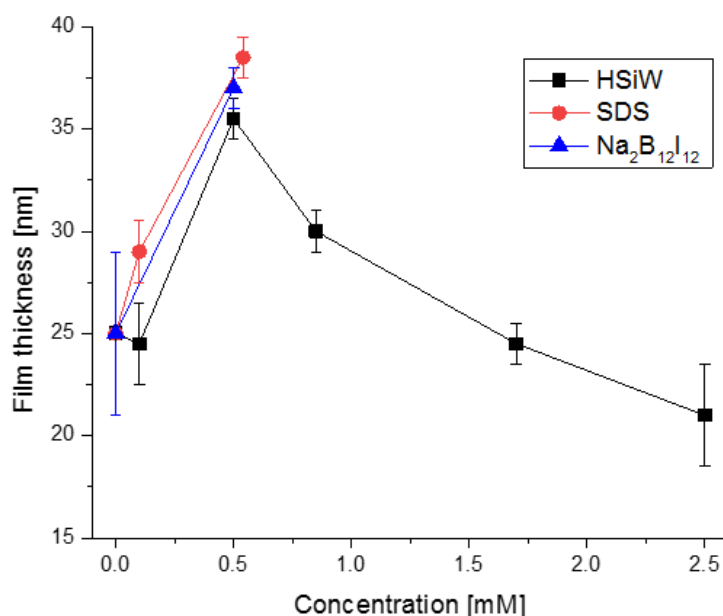


Figure 77: Foam film thicknesses obtained from the reflectivity fits of the SANS-spectra in Figure 75 (0.5 mM BrijO10 foams, MW, foam ages of 55-74 mins). The error bars represent the quality of the respective reflectivity fits and the lines are guides to the eye.

The film thicknesses for foams of 0.5 mM BrijO10 in the presence of Na<sub>2</sub>B<sub>12</sub>I<sub>12</sub>, SDS or HSiW are shown in Figure 77. For the foam of bare 0.5 mM BrijO10 only one maximum (critical angle) and one diffuse minimum are observed making the fitting procedure for this sample quite error prone. The obtained film thickness is therefore quite imprecise resulting in 25±5 nm. In the presence of 0.5 mM Na<sub>2</sub>B<sub>12</sub>I<sub>12</sub>, SDS or HSiW an increase in film thickness takes place up to 36 - 38 nm depending on the additive. Interestingly, for HSiW, further addition leads to a gradual decrease in the film thickness to 22 nm.

Non-ionic ethoxylated (or sugar-based) surfactants like BrijO10 have been shown to produce foam films that are unexpectedly stabilized by electrostatics. The effect, though rather weak, was unanimously attributed by various authors to the presence of “spurious charges” arising from an adsorption of OH<sup>-</sup> ions to the air/water interface.<sup>204–206</sup> Herein, it was observed that 100 mM NaCl caused a complete suppression of the reflectivity signal of a BrijO10 foam (0.5 mM) hinting at an electrolytic mechanism, fully in line with the presence of these surface charges, see Appendix 4.3.4 on page 169. For this reason, BrijO10 foam films can be expected to be thicker than the typical sterically stabilized Newton black films, which for BrijO10 (extended length of 6 nm) would correspond to a thickness of 12 nm. Indeed, we observe thicker foam films (25±5 nm) for 0.5 mM BrijO10 probably due to the presence of these spurious

charges, however, additionally scarcely distributed micelles<sup>4</sup> in the foam films might induce an increase in foam thickness. Nevertheless, the thickening of the foam films upon addition of Na<sub>2</sub>B<sub>12</sub>I<sub>12</sub>, SDS or HSiW can be attributed to arising interfacial electrostatic repulsion. B<sub>12</sub>I<sub>12</sub><sup>2-</sup> and SiW (SiW<sub>12</sub>O<sub>40</sub><sup>4-</sup>) interact with the BrijO10-covered air/water interface driven by the chaotropic effect, while SDS is attracted by the air/water interface driven by the hydrophobic effect on its aliphatic C<sub>12</sub>-tail. In either case, the foam film is equipped with electric charges, which drive apart facing interfaces resulting in an increase of film thickness. The thinning of the foam films upon further addition of HSiW above 0.5 mM cannot be explained in the same lines. At these comparably high HSiW-concentrations, the film interfaces might be fully occupied with SiW and SiW might act as a self-screening agent, i.e. SiW in the interstitial liquid screens the repulsions between adsorbed SiW-molecules at the interfaces. In order to test this hypothesis, foams of 0.5 mM BrijO10 + 0.5 mM HSiW were generated in the presence of increasing amounts of the electrolyte NaCl. Notably, classical inorganic salts like NaCl generally have negligible effects on non-ionic surfactant foam properties up to 100 mM.<sup>207</sup> Here, we stay well below this limit using a maximum NaCl-concentration of 20 mM. The respective SANS-spectra are shown in Figure 78. It is observed that the oscillations dampen and stretch out gradually with NaCl-concentration, see Figure 78a and b. Therefore, addition of NaCl causes the foam films to become more polydisperse causing a weakening in the overall reflectivity signal as well as a substantial effect on the foam film thickness. By fitting of the reflectivity extrema, corresponding foam thicknesses were acquired. As we are interested in a screening effect here, the film thicknesses are plotted as a function of the ionic strength in Figure 78c. For NaCl, a monovalent electrolyte, the ionic strength is equal to its concentration and both Cl<sup>-</sup> and Na<sup>+</sup>-ions contribute to the screening effect. For HSiW, the situation is much less clear as in section 2.3.2, it was shown that the screening effect is surprisingly weak for a quadrivalent electrolyte like HSiW (1xSiW<sub>12</sub>O<sub>40</sub><sup>4-</sup>, 4xH<sup>+</sup>). It was concluded that screening is mostly due to the four H<sup>+</sup>-ions, while the presence of SiW<sub>12</sub>O<sub>40</sub><sup>4-</sup> does not seem to reinforce the screening effect. Here, we test this result by calculating the ionic strength of HSiW in two ways: i) considering only H<sup>+</sup>-ions (red dots) and ii) taking into account both H<sup>+</sup>- as well as SiW<sub>12</sub>O<sub>40</sub><sup>4-</sup>-ions (cyan dots).

---

<sup>4</sup> For BrijO10, 0.5 mM corresponds to twelve times its critical micellar concentration (cmc=40 μM). Therefore, the presence of micelles is expected in the foams. Assuming that micelles in the foam films are equally abundant and shaped as in the bulk (from fitting of solution SANS: ellipsoidal with r<sub>pol</sub>=5.8 nm; r<sub>eq</sub>=2.9 nm) it is possible to calculate their distribution in the foam film. Thus, in the foam film with a thickness of 25 nm, these micelles would be distributed in a plane square mesh with micelle-micelle distances of 160 nm. Therefore, micelles are expected to be scarce and only a slight effect of these micelles can be expected on the equilibrium film thickness. The corresponding SANS-fit is given in Appendix 4.3.2.



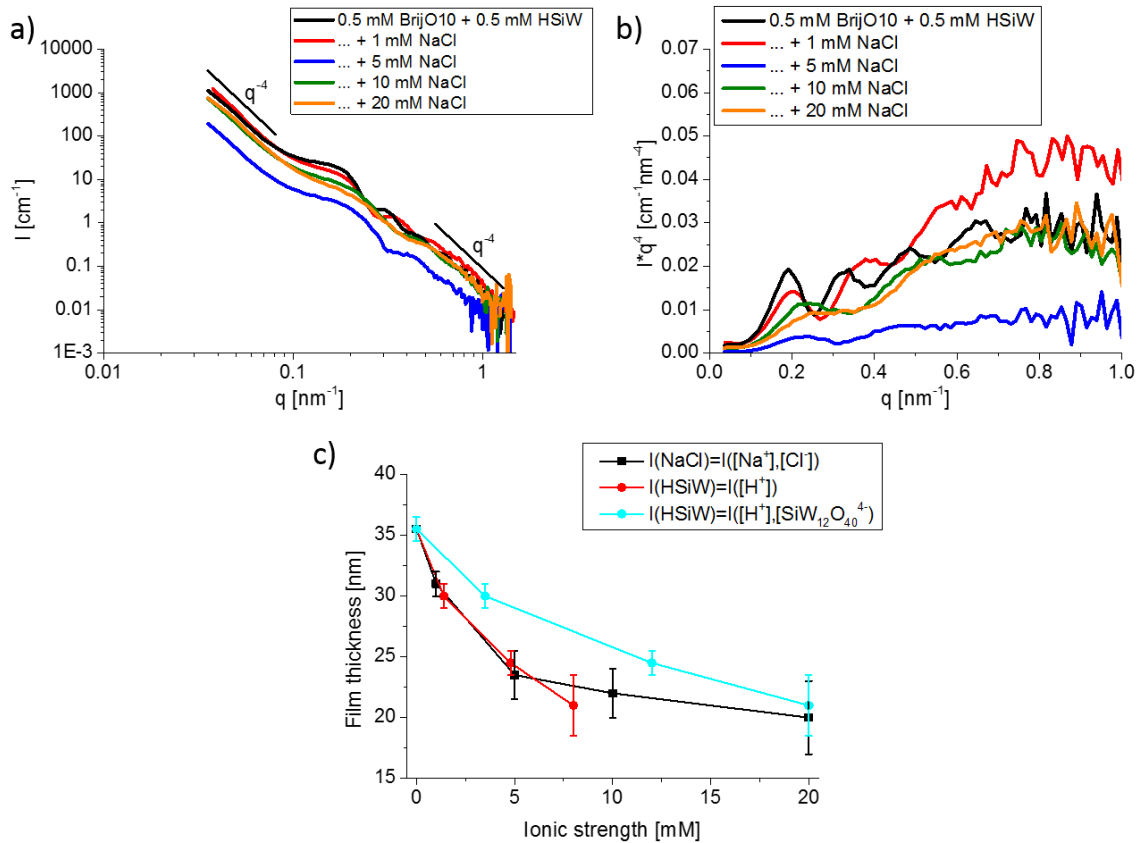


Figure 78: a) Log-log plot of  $I$  vs  $q$  and b) Lin-lin Porod plot of  $Iq^4$  vs  $q$  of the SANS-spectra acquired from the middle window at a foam age of 63-74 minutes for foams of 0.5 mM BrijO10 + 0.5 mM HSiW in the presence of NaCl. c) Foam film thicknesses obtained from the reflectivity fits of the SANS-spectra plotted against the added ionic strength. The data obtained for NaCl are compared with the data obtained for  $c(\text{HSiW}) > 0.5$  mM. The ionic strength of HSiW was calculated in two ways. Red dots: considering only the  $\text{H}^+$ -concentration. Cyan dots: considering  $\text{SiW}_{12}\text{O}_{40}^{4-}$  and  $\text{H}^+$ -concentrations. The error bars indicate the quality of the fits and the lines are guides to the eye. The sample at  $I=0$  mM contains a constant ionic strength due to 0.5 mM HSiW, which is disregarded here.

Thus, addition of NaCl causes a monotonous decrease in the film thickness from 35.5 nm at 0 mM NaCl to 20 nm at 20 mM NaCl (foams of 0.5 mM BrijO10 + 0.5 mM HSiW) and can be interpreted as a reversion to the foam film thickness of a bare BrijO10 foam (at  $25 \pm 8$  nm). This effect confirms that the increase in foam film thickness is indeed due to electrostatics arising from adsorbed SiW at the film interfaces. When comparing the effect of NaCl with the presumed auto-screening effect of HSiW, a strong correlation is observed when considering exclusively the ionic strength of the  $\text{H}^+$ -ions. In turn, taking into consideration both  $\text{SiW}_{12}\text{O}_{40}^{4-}$  as well as  $\text{H}^+$ -ions seems to produce an overestimate of the ionic strength. Therefore, here we come to the same conclusions as in section 2.3.2, i.e. the screening of HSiW is entirely due to the presence of  $\text{H}^+$ -ions while the presence of  $\text{SiW}_{12}\text{O}_{40}^{4-}$ -ions must be disregarded. This result contributes to the debate, whether POMs like  $\text{SiW}_{12}\text{O}_{40}^{4-}$  can be considered as large ions or as small ionic colloids.<sup>95,96</sup> In this context, Malinenko et al. classified the Keggin-ions as hybrids with colloidal as well as ionic character. The former because POMs in solution mutually interact

like colloids and the latter due to their chaotrope-like behavior in the presence of non-ionic polar interfaces.<sup>95</sup> Furthermore, Faraudo et al concluded from stability measurements on colloidal latex particles in the presence of  $\text{PW}_{12}\text{O}_{40}^{3-}$  that such Keggin-POMs are charged nano-colloids without ionic character.<sup>96</sup> Herein, we come to the conclusion that  $\text{SiW}_{12}\text{O}_{40}^{4-}$  behaves like a colloid in terms of its lacking electrolytic properties.

Overall, the superchaotropic Keggin-ion  $\text{SiW}_{12}\text{O}_{40}^{4-}$  has shown remarkable effects on dry foam films stabilized by the non-ionic surfactant BrijO10. Due to its chaotropic nature, SiW adsorbs to the polar surfactant heads on the interior of the foam films equipping them with electrical charges and causing electrostatic repulsion between facing interfaces. In SANS, this effect entails the appearance of multiple oscillations arising from neutron reflectivity on the thin foam films, which directly evidences that the films become highly monodisperse when subjected to electrostatic forces. Thus, the non-ionic surfactant foam films of bare BrijO10, which are mostly sterically stabilized (and presumably by weak electrostatics arising from “spurious” charges), become thicker by addition of HSiW up to equimolarity (0.5 mM BrijO10/0.5 mM HSiW). However, upon further increase of the HSiW-concentration, the film thickness is found to decrease, which was attributed to a screening effect that occurs when the film interfaces are saturated and SiW-molecules are forced into the interstitial liquid between the interfaces. By comparing the induced thinning with HSiW to the screening effect of NaCl, it was demonstrated that  $\text{SiW}_{12}\text{O}_{40}^{4-}$  does indeed not exhibit electrolytic properties and exclusively the four equivalents of  $\text{H}^+$  induce a weakening of the electrostatic repulsion.

Generally, the properties of the foam films determine the behavior of the macroscopic foam. Therefore, it is expected that the induced effects of HSiW have significant effects on macroscopic properties of the BrijO10 foam, in particular due to electrostatic forces that arise in the foam films upon adsorption of the superchaotropic ion. These macroscopic effects were examined in the next section.

## 4.3. Appendix

### 4.3.1. Quasi-stationary foams

For each foam, the SANS-spectra evolved slightly over time showing that the investigated foams are indeed non-equilibrium structures. By fitting the respective reflectivity signals, it is possible to trace the evolving film thickness as is shown in Figure 79.

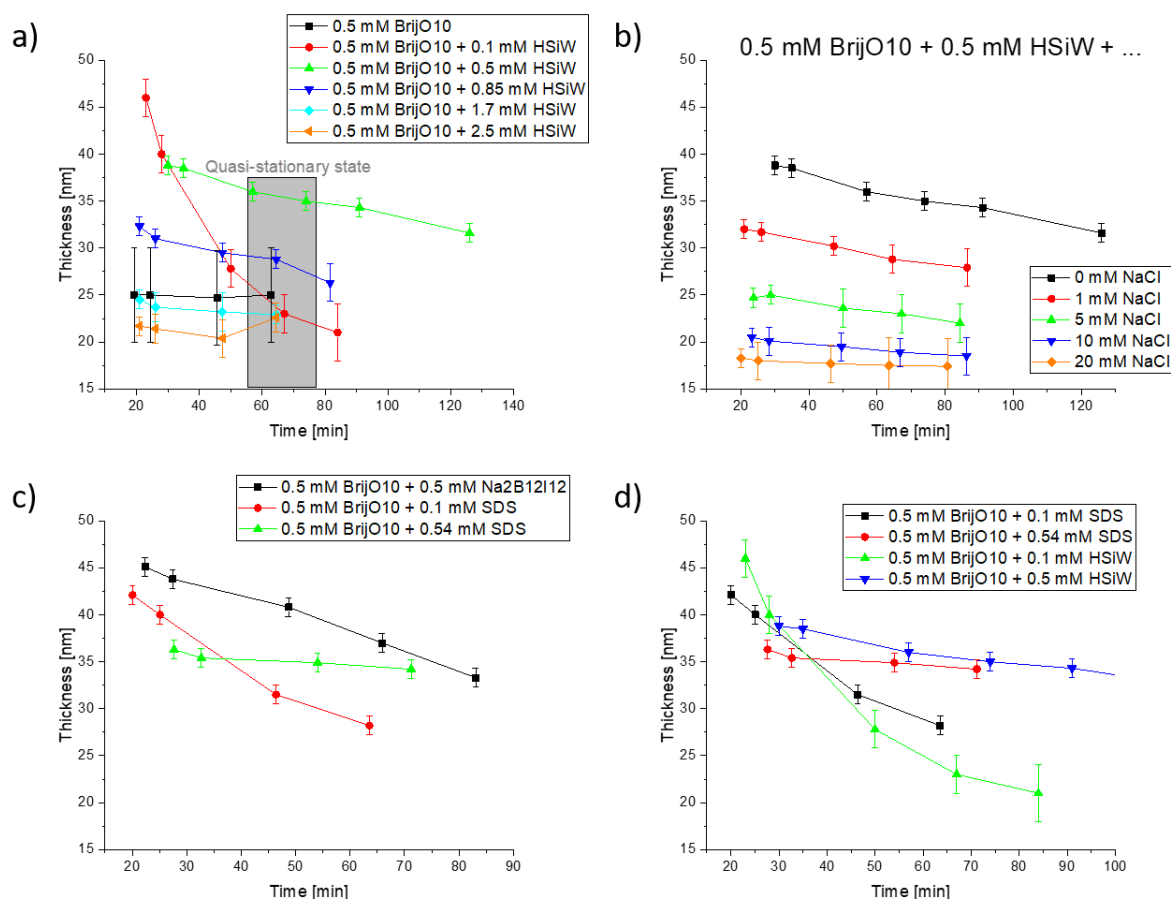


Figure 79: Foam film thicknesses obtained from reflectivity fitting of SANS acquired at the middle window for foams of 0.5 mM BrijO10 in the presence of a) HSiW b) 0.5 mM HSiW and NaCl c) SDS and Na<sub>2</sub>B<sub>12</sub>I<sub>12</sub> and d) comparing SDS and HSiW.

Thus, for most samples a slight thinning of the foam films is observed upon aging of the foam. However, for foams of 0.5 mM BrijO10 + 0.1 mM HSiW (or SDS) the foam film thickness seemed to evolve strongly with foam age as reflected in a strong decrease in foam film thickness from 45 nm (or 42 nm) at 20 minutes to around 22 nm (or 27 nm) at 60 minutes. These strong relaxation effects were by far the most pronounced for these two samples, where electrostatic stabilization is expected to be rather weak as concentrations of the ionic compounds SDS and SiW are low. Because of these effects the foams in the main text are compared at high foam ages (i.e. 55-75 mins), where all foams are expected to have attained their quasi-stationary state

and the foam films are closest to equilibrium. The corresponding SANS-spectra that were exploited to obtain these data are shown in the next pages, Figure 80-Figure 82.

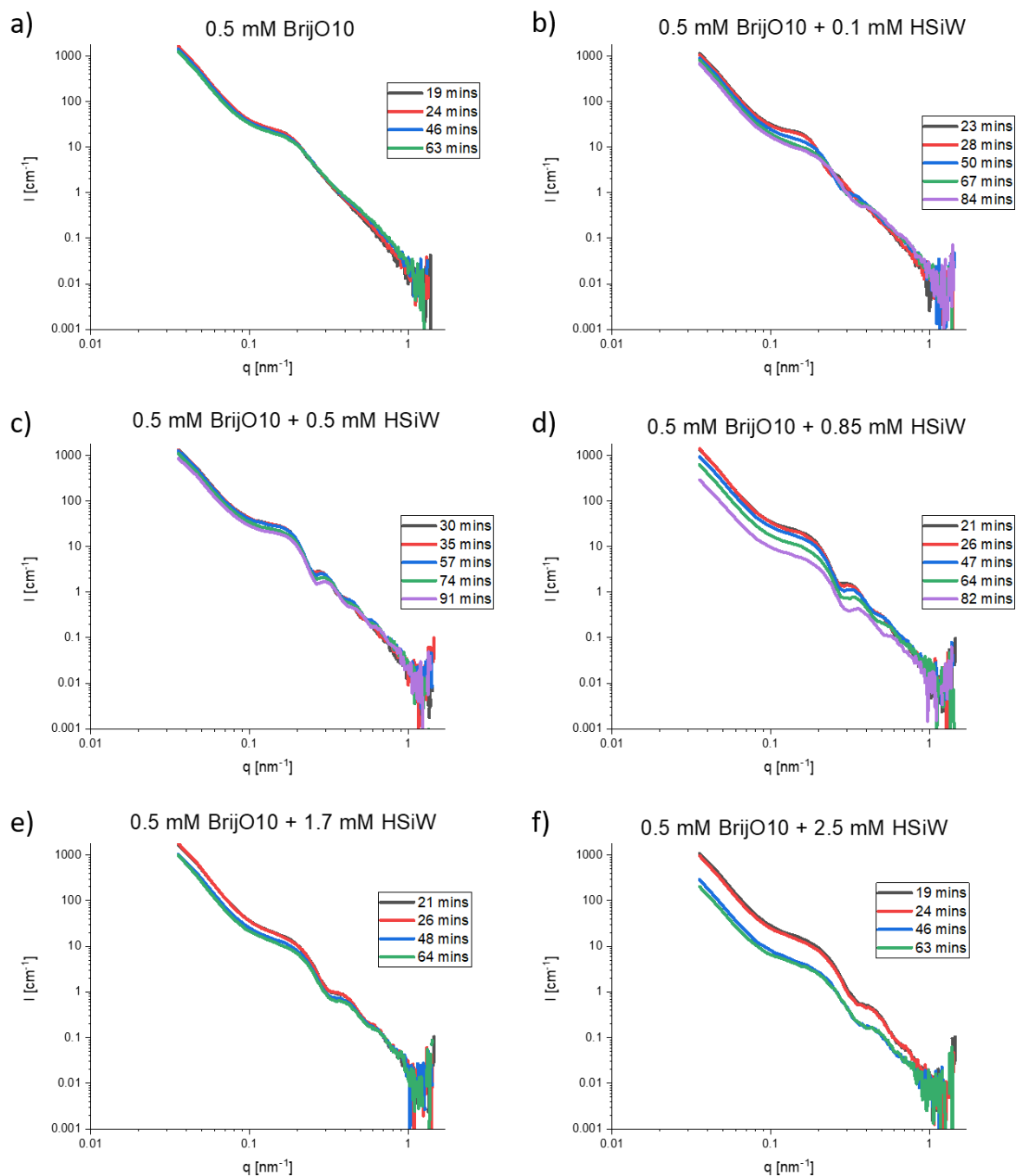


Figure 80: Normalized SANS-spectra acquired at the middle window of foams of a) 0.5 mM BrijO10 b) 0.5 mM BrijO10 + 0.1 mM HSiW c) 0.5 mM BrijO10 + 0.5 mM HSiW d) 0.5 mM BrijO10 + 0.85 mM HSiW e) 0.5 mM BrijO10 + 1.7 mM HSiW and f) 0.5 mM BrijO10 + 2.5 mM HSiW.

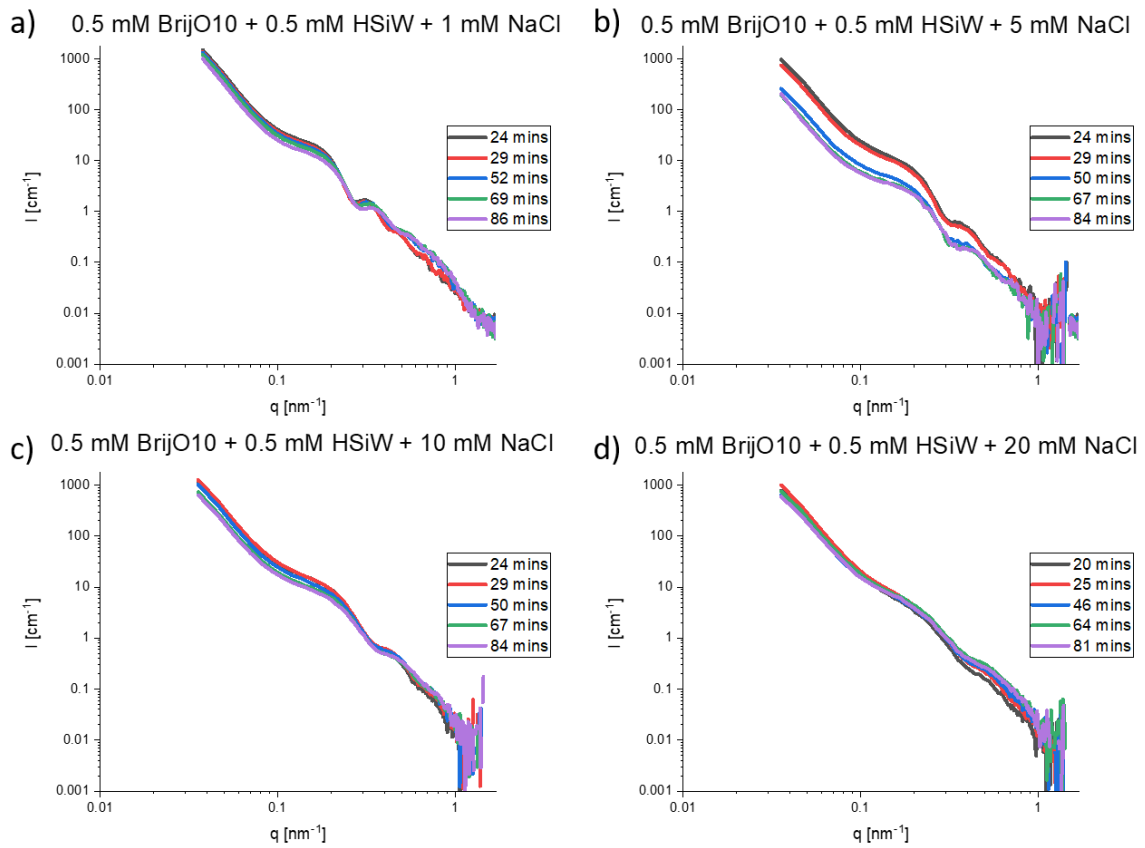


Figure 81: Normalized SANS-spectra acquired at the middle window of foams of a) 0.5 mM BrijO10 + 0.5 mM HSiW + 1 mM NaCl b) 0.5 mM BrijO10 + 0.5 mM HSiW + 5 mM NaCl c) 0.5 mM BrijO10 + 0.5 mM HSiW + 10 mM NaCl d) 0.5 mM BrijO10 + 0.5 mM HSiW + 20 mM NaCl.

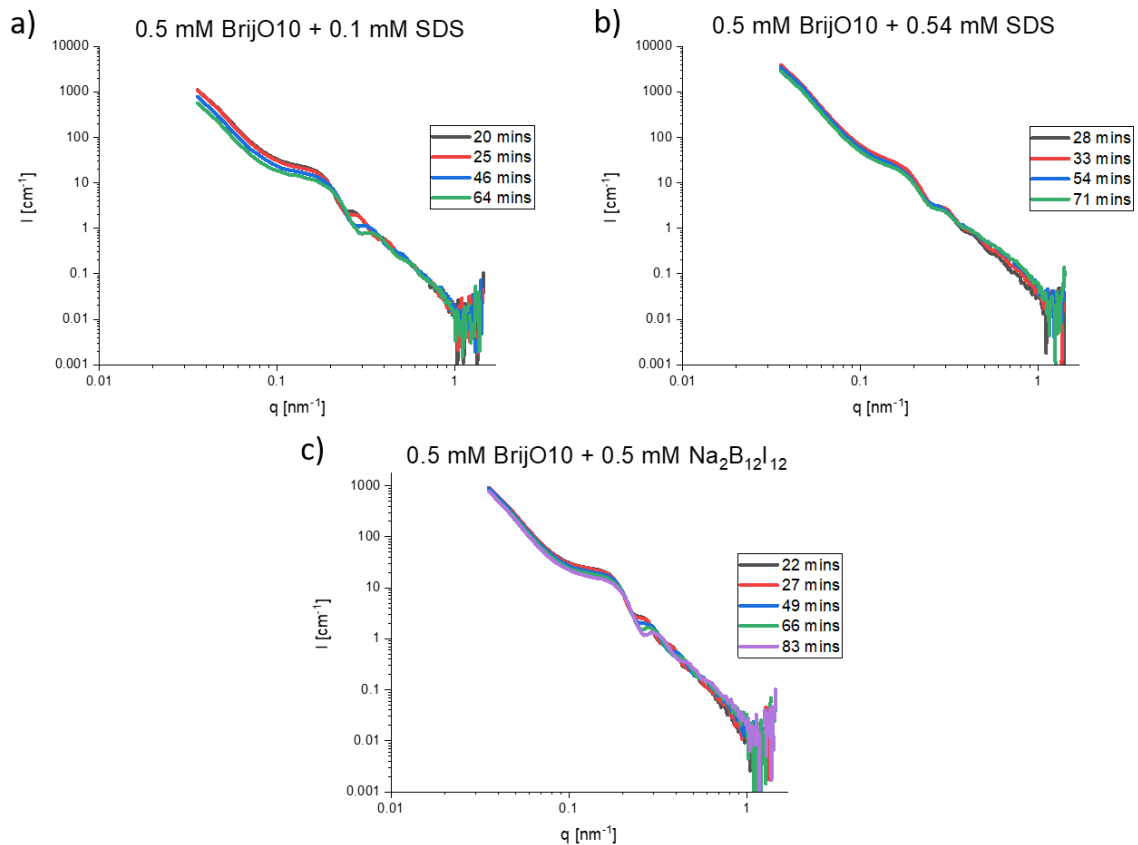


Figure 82: Normalized SANS-spectra acquired at the middle window of foams of a) 0.5 mM BrijO10 + 0.1 mM SDS b) 0.5 mM BrijO10 + 0.54 mM SDS and c) 0.5 mM BrijO10 + 0.5 mM  $\text{Na}_2\text{B}_{12}\text{I}_{12}$ .

### 4.3.2. Micelles in the foams

BrijO10 forms micelles in solution above its cmc at 0.040 mM.<sup>202</sup> Herein, foams were generated from BrijO10-solutions with concentrations above its cmc and, and thus micelles are expected to be found in the plateau borders and vertices as they contain the major liquid volume fraction of the foam. By comparing SANS of foams and solutions of 0.1 mM, 0.5 mM and 1.5 mM BrijO10 we evidence the presence of BrijO10-micelles in the foam here. SANS-spectra of foams with ages of around 65 minutes (acquired at the middle window) are shown in Figure 83 a and b and SANS-spectra of foams with ages of 15 minutes (acquired at the lower window) are shown in Figure 83 c and d.

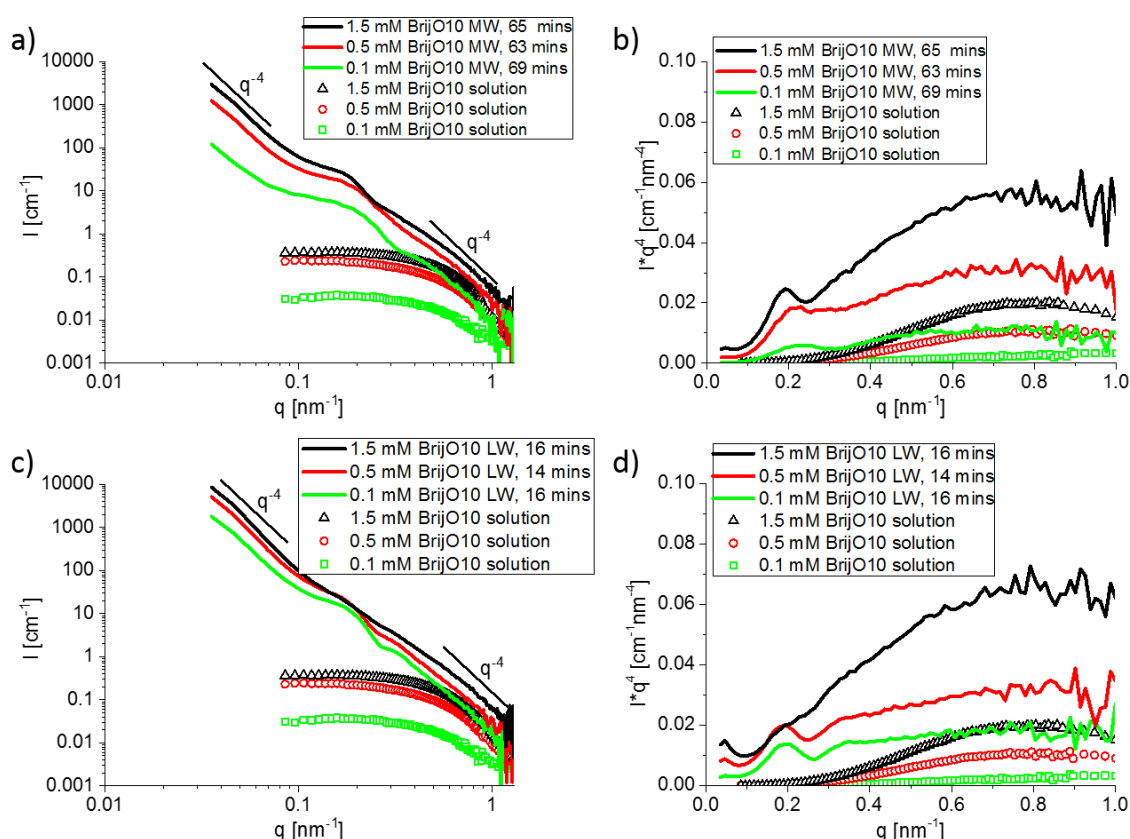


Figure 83: Log-log plots of  $I$  vs  $q$  and Lin-lin Porod plots of  $Iq^4$  vs  $q$  of the SANS-spectra acquired from the foaming solutions (data points) and foams (lines) of 0.1 mM, 0.5 mM or 1.5 mM BrijO10. For the foams the scattering was acquired at the middle window at foam ages of 63-69 mins for a) and b), and at the lower window for a foam age of 14-16 mins for c) and d).

Thus, regardless of foam age or foam height (lower window or middle window) the scattered intensities of the foams increase with BrijO10-concentration. The same trend is clearly observed in the spectra of the respective foaming solutions owing to the higher abundance of BrijO10 micelles. Characteristically, these non-ionic micelles produce a constant intensity at  $q < 0.4 \text{ nm}^{-1}$  demonstrating their non-ionic non-interactive nature, while in the  $q$ -region at  $q > 0.4 \text{ nm}^{-1}$  the scattering intensity increases sharply following a  $q^{-4}$ -dependence, which results

in a plateau in the  $Iq^4$  vs  $q$ -plots in Figure 83 b and d. The foams in these Porod plots, show exactly the same characteristic features as the micellar solutions and additionally the observed intensities coincide well with the concentrations used and therefore seem to scale with the concentration of the BrijO10-micelles. For these reasons, at all used concentrations from 0.1 mM - 1.5 mM, BrijO10-micelles can be expected in the foam and predominantly in the voluminous plateau borders and vertices.

Furthermore, the abundance of micelles was calculated in the foaming solution of 0.5 mM BrijO10 from classical solution SANS. Here, fitting resulted in ellipsoidal micelles with a polar radius of 5.8 nm and an equatorial radius of 2.9 nm, which correspond for the given concentration (surfactant volume fraction) to a number density of the micelles of  $1.57 * 10^{-6} \text{ nm}^{-3}$ . This number was used to estimate the intermicellar distance within the foam films in footnote 4 on page 160.

Table 26: Fitting parameters used for the SANS-spectrum of a solution of 0.5 mM BrijO10.

[BrijO10]	T	$\Phi_{\text{mic}}$	$\rho_{\text{mic}}$	$\rho_{\text{H}_2\text{O}}$	$R_{\text{eq}}$	$R_{\text{pol}}$
[mM]	[°C]	[ $\text{nm}^{-3}$ ]	[ $\text{\AA}^{-2}$ ]	[ $\text{\AA}^{-2}$ ]	[nm]	[nm]
0.5	20	0.00032	0.27	6.2	2.9	5.8

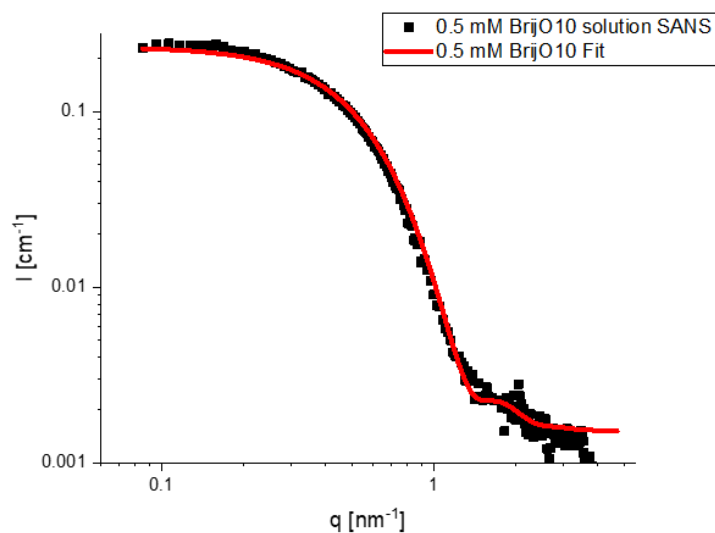


Figure 84: SANS-spectrum of 0.5 mM BrijO10 with ellipsoidal form factor fit.

### 4.3.3. Delayed injection of SiW into the foam

Furthermore, an injection measurement was performed on a foam of 0.5 mM BrijO10 with an age of 63 minutes. A concentrated HSiW-solution was injected into the foaming solution beneath the foam, such that a concentration of 0.5 mM HSiW results. The occurring SiW-concentration gradient between the foam and the solution would then draw SiW-ions into the foam and cause the appearance of the oscillations. This measurement allows for an examination of the foam dynamics.

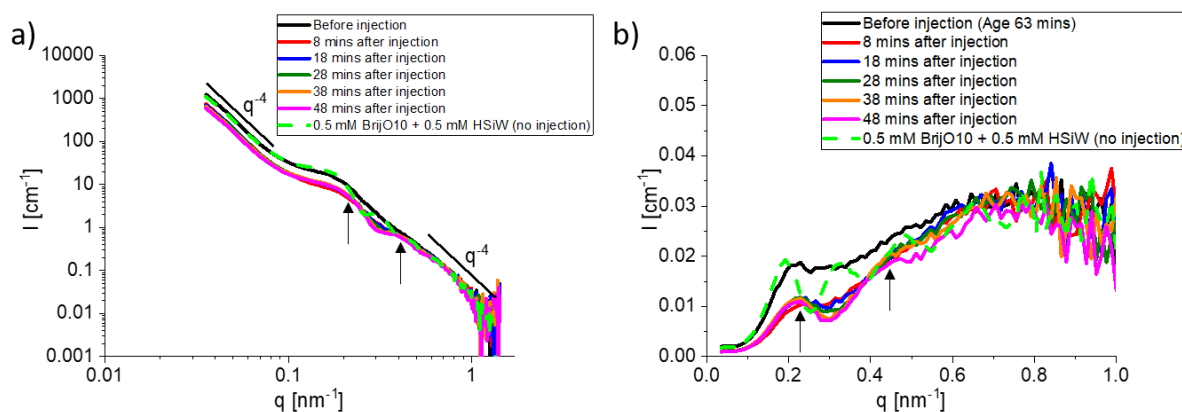


Figure 85: a) Log-log plot of  $I$  vs  $q$  and b) Lin-lin Porod plot of  $Iq^4$  vs  $q$  of the SANS-spectra acquired from the middle window of the following samples. The starting point before injection corresponds to a foam of 0.5 mM BrijO10 at a foam age of 63 minutes. To this foam a concentrated SiW-solution was injected such that the concentration of the resulting foaming solution amounts to 0.5 mM HSiW. The scattering of the foam on top was then traced as a function of time up to 48 minutes after injection. As a reference, the scattering of a foam of 0.5 mM BrijO10+0.5 mM HSiW at an age of 74 mins is shown (green dashed line). The arrows indicate the positions of the maxima.

For the injection, a needle must be introduced into the foam column, which causes local foam collapse around the needle and results in a slight drop in intensity upon injection. Once injected, the oscillations are found to emerge slowly and at 48 minutes after injection, a second maximum can be discerned as SiW migrates into the thin films inducing electrostatic repulsions in the thin foam films. Nevertheless, a much longer equilibration time would be necessary to restore all four oscillations that occur for a foam initially generated from a solution of 0.5 mM BrijO10+0.5 mM HSiW (green dashed line). Nevertheless, this measurement shows that even delayed addition of SiW has strong effects on the foam films as SiW spontaneously (slowly) loads the foams. Importantly, the signal of the micelles present at high  $q$  remains unchanged regardless of added HSiW and therefore here an isolated effect of HSiW on the foam films is demonstrated.



### 4.3.4. The effect of electrolyte in non-ionic BrijO10-foams

The effect of electrolytes on non-ionic foams of 0.5 mM or 1.5 mM BrijO10 was investigated by adding 0.1 M NaCl or 0.1 M HCL ( $\approx$  pH 1). In the presence of either electrolyte, the peak of the critical angle disappears entirely indicating that the foam films become so polydisperse that the reflectivity signal is fully suppressed, see Figure 86. This effect hints at the fact that the foam films of bare BrijO10 are possibly stabilized by electrostatic forces beyond steric ones despite the lack of charging additives (no SiW or SDS). Indeed, it was shown by several authors that the air/water interface covered by non-ionic surfactant holds spurious charges arising from adsorbed  $\text{OH}^-$ .<sup>204–206,208</sup>

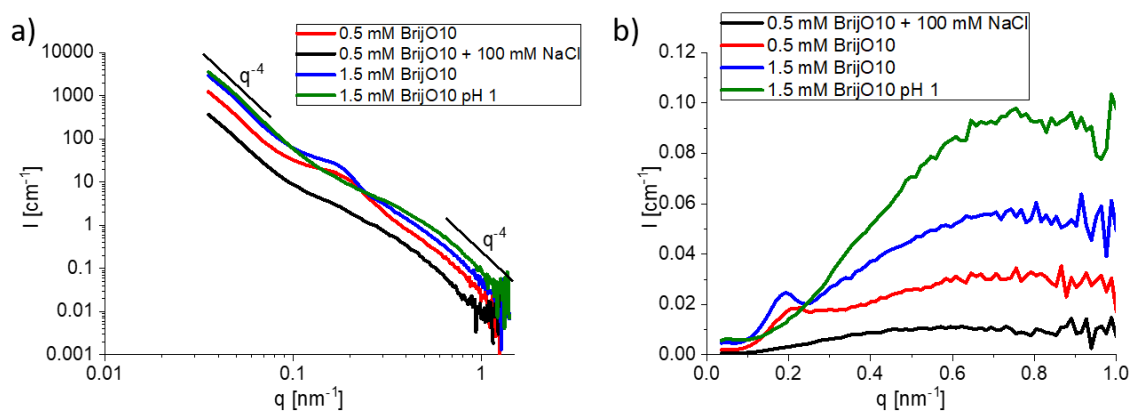


Figure 86: a) Log-log plot of  $I$  vs  $q$  and b) Lin-lin Porod plot of  $Iq^4$  vs  $q$  of the SANS-spectra acquired from the middle window of foams of 0.5 mM or 1.5 mM BrijO10 respectively with 100 mM NaCl or at pH 1 at foam ages of 63-66 minutes.

## 4.4. Lifetime of non-ionic surfactant foams in the presence of superchaotropic ions

It was shown in this thesis that superchaotropic ions can act like ionic surfactants on dilute bilayer phases of a non-ionic surfactant because they electrically charge non-ionic surfactant self-assemblies similarly to ionic surfactants (chapter 3). Likewise, induced electrostatics by superchaotropic ions affected strongly non-ionic surfactant foam films (section 4.2), where it was mentioned that qualitative differences in the foam stability of the investigated quasi-stationary foams were observed. The present section intends to quantify the corresponding macroscopic foam properties of BrijO10/HSiW-foams in the presence and in the absence of the electrolyte NaCl under free drainage conditions. For this purpose, the same foaming solutions as in section 4.2 will be used. For reference purposes, the results will be juxtaposed to equivalent measurements on mixed non-ionic/ionic surfactant foams of BrijO10 and SDS. Thus, the surfactant-like action of the nano-ion  $\text{SiW}_{12}\text{O}_{40}^{4-}$  (SiW) in non-ionic surfactant rich environments shall be further elucidated. It must be noted though that HSiW cannot stabilize aqueous foams by itself because it exhibits only weak surface activity (see section 2.3, Figure 11), in direct contrast to the classical surfactant SDS. Similarly, surface tension measurements showed that the effect of HSiW on 0.5 mM BrijO10 is negligible, while SDS clearly induces strong effects, see appendix 4.4.1 on page 179.

Herein, the foams were generated and analyzed using a FOAMSCAN-device from Teclis. Foam generation was done using an airflow of 50 ml/min through a microporous sintered glass plate resulting in substantial liquid entrainment into a wet foam. When the foam column was completely filled, the airflow was stopped. Two cameras recorded continuously the foam allowing for a simultaneous examination of foam volume and bubble size. Additionally, conductometry enabled to trace liquid drainage over time. Thus, the full lifespan of a foam from generation over drainage to its collapse is surveilled. All samples contained 0.5 mM BrijO10 as the foaming agent, to which the additives HSiW, SDS and NaCl were added systematically to pinpoint their individual effects. BrijO10 in the presence of SDS or HSiW produces ionic foam (films), where addition of the electrolyte NaCl would cause a screening effect as outlined in section 4.2. Notably the maximal concentration of NaCl was 20 mM, which is too low to produce significant effects on the bare non-ionic BrijO10-foam.<sup>207,209,210</sup>

First, photos of the upper part of the investigated foams (at 15 cm above the foaming solution) at identical times are presented in Figure 87 on the next page.

#### 4. Nano-ions in non-ionic surfactant foams

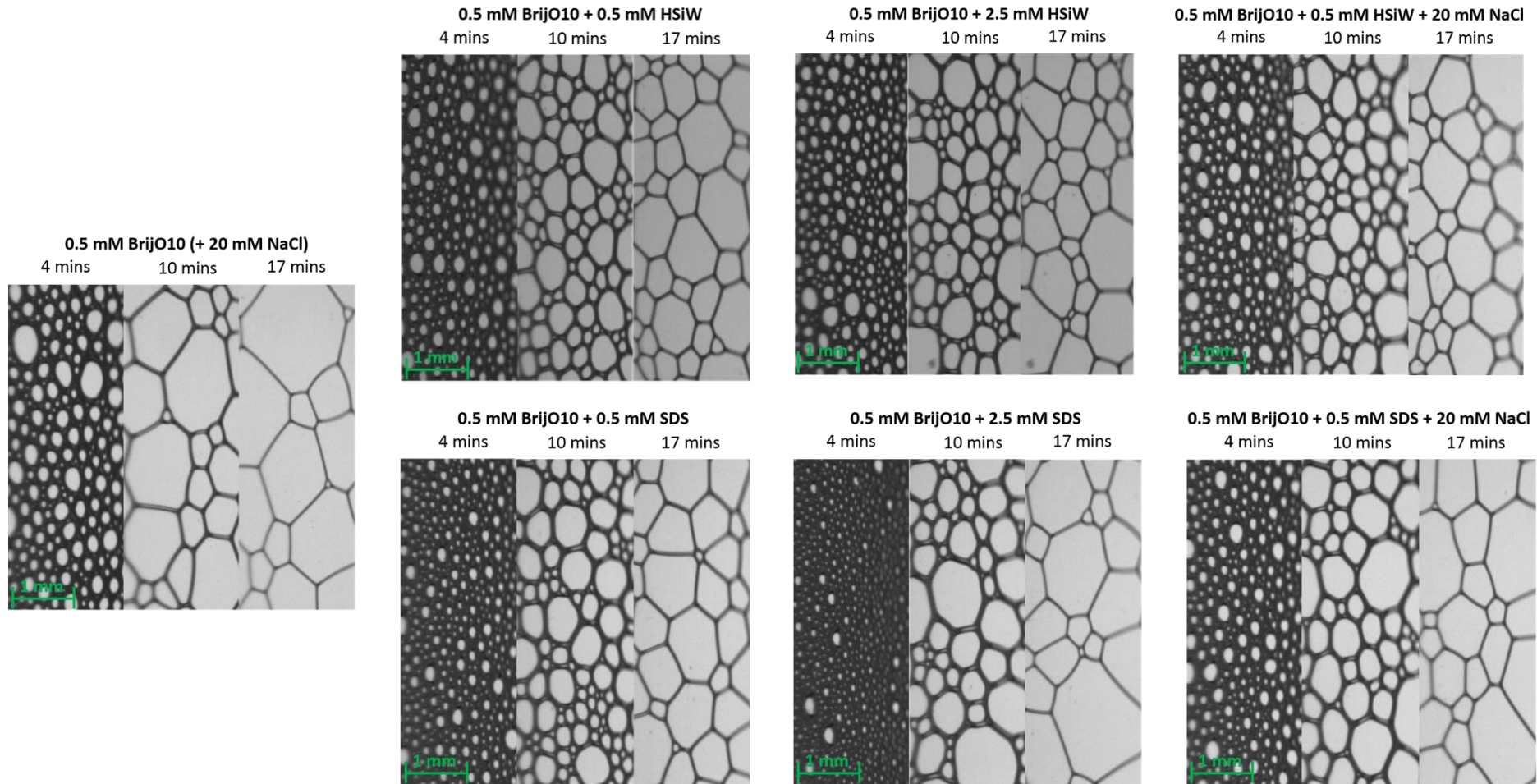


Figure 87: Foams of 0.5 mM BrijO10 in the presence of HSiW, SDS and NaCl. Photos represent foam bubbles in contact with the glass wall taken at the upper part of the foam at a foam column height of 15 cm. The time stamps indicate the foam age after initiation of the gas flow and 4 mins corresponds to the moment, when the foam column is filled, gas flow is stopped, and the free drainage experiment begins. The foaming rate was identical for all samples. Foams of 0.5 mM BrijO10 and 0.5 mM BrijO10 + 20 mM NaCl show identical bubble sizes and are therefore represented by one photo on the left hand side.

All foams initially exhibit small bubbles and hold relatively high liquid volume fractions directly after foam generation (i.e. at 4 minutes), where the foams of 0.5 mM BrijO10 with 0.5 mM and 2.5 mM SDS show the highest liquid volume fractions and smallest bubbles. As the foam age progresses, the liquid drains downwards causing the foam films to become thinner accompanied by a growth in bubble size inducing a transition from spherical to polyhedral bubble shape. The extent of the growth of the bubbles and the drainage times depend strongly on each sample. Thus, to establish a quantitative comparison, bubble sizes were determined for each foam as a function of time by image analysis and are shown in Figure 88.

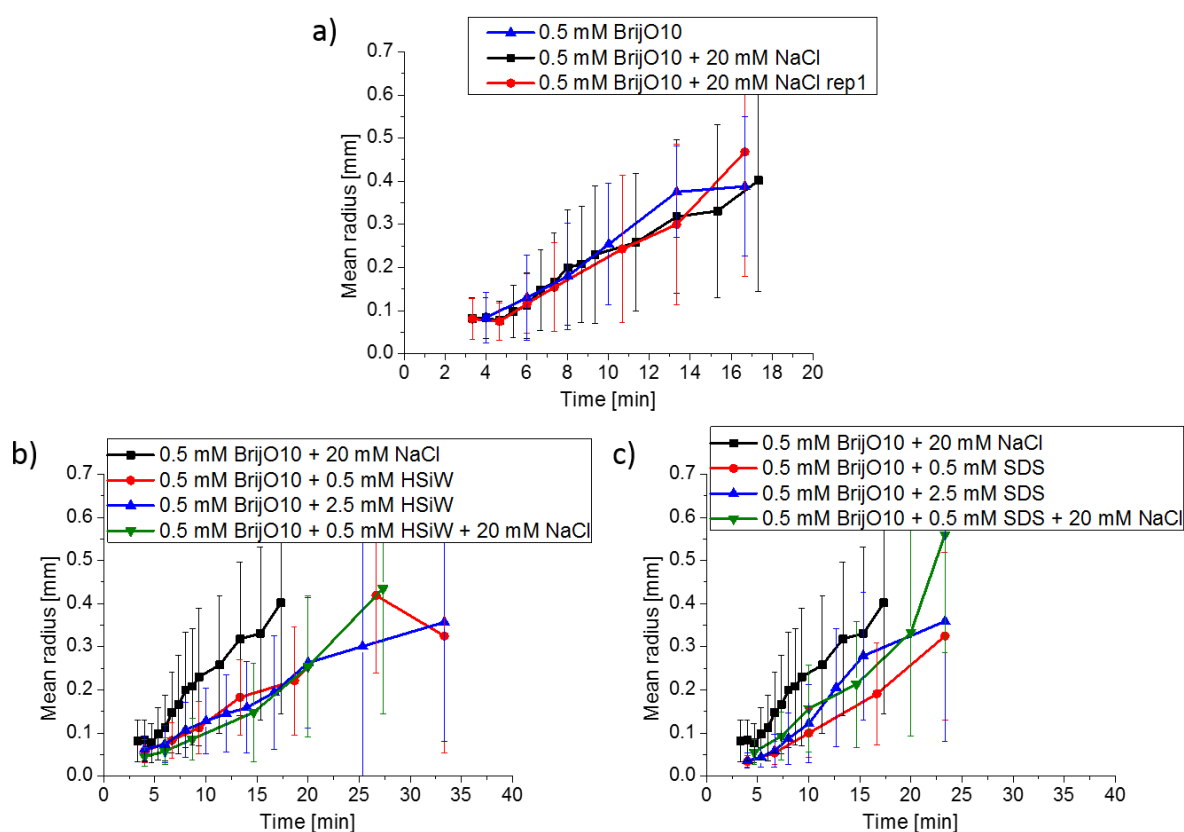


Figure 88: Mean bubble sizes as a function of foam age acquired by image analysis for the foams in Figure 87. The error bars represent standard deviations around the mean bubble radius. The larger the error bar, the more polydisperse are the bubbles.

The bubble size determination is shown to be reliable in Figure 88a, where the sample containing 0.5 mM BrijO10 + 20 mM NaCl is shown twice (from two individual foams) resulting in an identical curve with negligible deviations from each other. In turn, the errors of each curve are high and increase with time indicating that the bubbles become more polydisperse. This effect demonstrates Ostwald ripening, i.e. large bubbles grow at the expense of smaller ones, which is characteristic of aging foams. Furthermore, it is shown that the bubble size of 0.5 mM BrijO10 is unaffected by addition of 20 mM NaCl as the curves overlap well over the investigated timeframe. However, in the presence of HSiW or SDS, respectively Figure

88b and c), the bubble sizes are consistently and significantly smaller than the bubbles of 0.5 mM BrijO10 + 20 mM NaCl. This difference indicates that foams containing SDS or HSiW seem to be less affected by foam coarsening, i.e. bubble growth due to gas diffusion through the thin liquid films between adjacent bubbles, where the larger the bubble the more surface area and the more gas transfer. This aging phenomenon seems to be suppressed in the presence of HSiW or SDS hinting at an increased stability for the corresponding foams. Notably an inhibition of liquid drainage would entail similar effects as the diffusion path for the gas would be much longer in thicker (less drained) foam films. Indeed, already in Figure 87 differences in foam film thickness can be detected in the photos taken at 4 and at 10 minutes, where foams containing SDS have significantly thicker films than the foam of bare BrijO10. The undergoing drainage rates might be significantly different and were determined using conductometry. The corresponding liquid fractions at the bottom (wet foam) and at the top (dry foam) of individual foams are respectively shown as a function of time, see Figure 89.

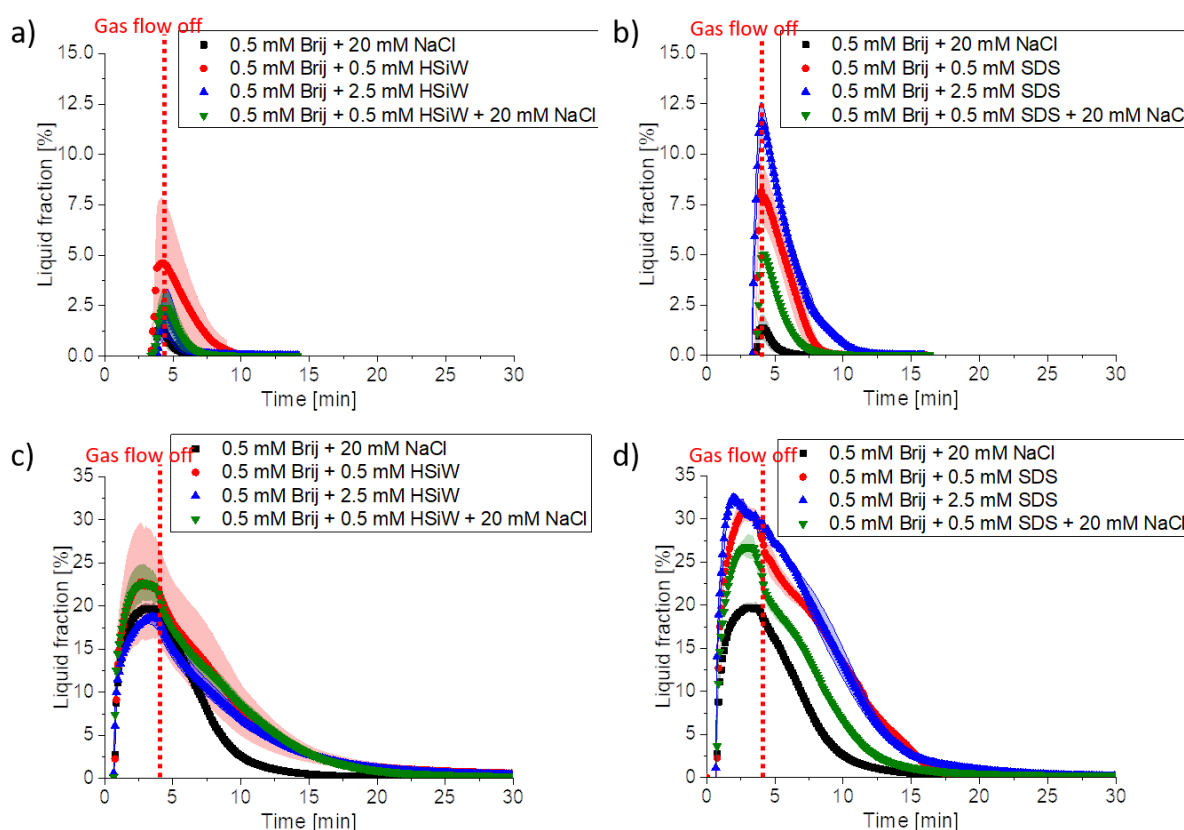


Figure 89: Liquid fraction as a function of time for foams of 0.5 mM BrijO10 containing SiW (left) or SDS (right). a) and b) show the liquid drainage at the top the foam column at a height of 18.5 cm and c) and d) the liquid drainage at the bottom of the foam column at a height of 3 cm above the foaming solution. The light-colored areas below the curves represent standard deviations as each measurement was repeated thrice.

These results illustrate that the produced foams are highly inhomogeneous as they exhibit high liquid fractions at the bottom (wet foam) and low liquid fractions at the top (dry foam) once the

foam generation is stopped (at 4 minutes, pointed lines in Figure 89). It is observed that foams containing SiW or SDS are wetter than foams of bare BrijO10 as their liquid fractions are considerably higher. This effect can be clearly observed with SDS (Figure 89b, d) and seems to be weaker in the presence of HSiW (Figure 89a, c). This is a common result often observed upon increase of the foaming agent's concentration (above the foaming agent's cmc) and is therefore expected upon SDS-addition.<sup>211,212</sup> Notably, the error of the recorded liquid fractions is highest for foams containing 0.5 mM HSiW or 0.5 mM SDS as in these samples the liquid's conductivity is smallest and close to the precision limit of the electrodes. Furthermore, Figure 89c shows that drainage in the presence of HSiW is slowed down, as much longer times are needed to reach low liquid fractions, while the initial liquid fractions are comparable to the foam of bare BrijO10. However, as addition of SDS causes a strong increase in the wetness of the foam, it is unclear whether addition of SDS inhibits liquid drainage, in particular because the drainage rates, represented by the descending slopes in Figure 89d, are very similar for the examined foams BrijO10/SDS-foams. Nevertheless, it is expected that foams of BrijO10 have longer lifetimes in the presence of SDS because the liquid films need more time to reach critical thickness, where rupture may occur. Furthermore, addition of 20 mM NaCl caused the foams to be generally drier, where in the presence of SDS liquid fractions decreased markedly (Figure 89b, d) and in the presence of HSiW only a small decrease is observed in Figure 89a.

These experiments show that SiW and SDS promote the generation of more liquid foams and prolong their lifetime either by generating more liquid foams in the first place (with SDS and HSiW) and by slowing down liquid drainage (with HSiW). Therefore, SiW and SDS are both expected to prolong the BrijO10-foam's lifetime. Thus, long-time experiments were performed to trace the entire life of the foam via image analysis of the foam volume. Figure 90 presents the characteristic aging regimes involving the foam's generation, drainage and collapse. Early on, the foam is generated by a strong airflow (50 ml/min) through the microporous plate into the foaming solution causing a steep increase in foam height up to a foam age of four minutes, where the FOAMSCAN column is completely filled and the airflow is stopped. At this early stage, the foam contains a significant liquid fraction, which drains downwards into the foaming solution. At 50 minutes, the drainage has progressed far enough so that the thin liquid films between bubbles become unstable and start to rupture causing gradual foam collapse. The critical drainage time denoted as  $t_d$ , where foam collapse commences, is characteristic to each sample as drainage rates and film stabilities differ. The foam collapse generally started, where the foam is driest, i.e. on top of the foam column, and then proceeds downwards. Corresponding collapse rates, however, varied between repetitions (each foam sample was generated and

measured thrice and averaged) due to locally inhomogeneous collapse or foam sticking to the column walls causing an erroneous determination of the foam height. These errors between measurements are expressed as an error area, representing standard deviations around the mean.

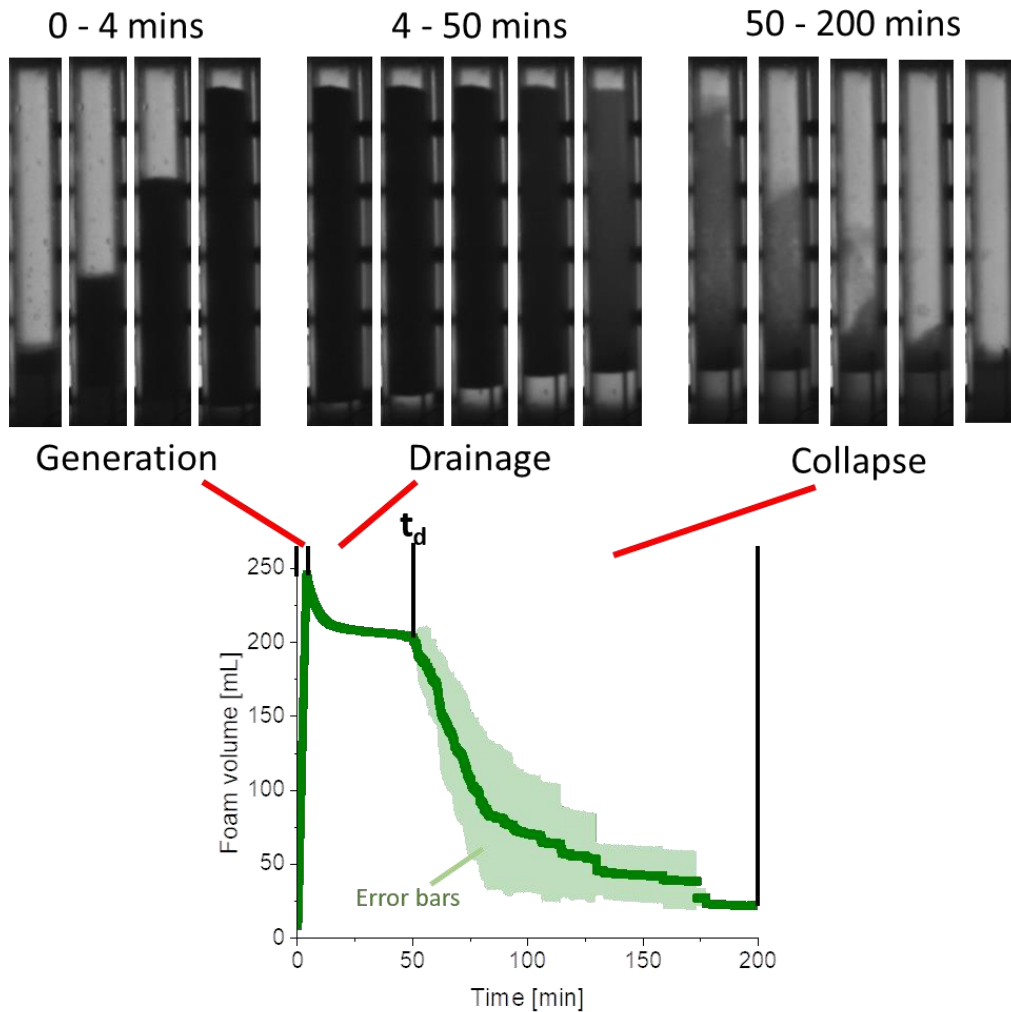


Figure 90: Foam volume over time with characteristic aging regimes including generation, drainage and collapse with corresponding photos. Measurements were performed thrice to allow for a calculation of an average and its corresponding standard deviation, which are shown with the light-green area around the mean. The curve corresponds to measurements of 0.5 mM BrijO10 + 0.5 mM HSiW + 20 mM NaCl.

Thus, now, the measurements of the BrijO10 foams in the presence of SDS and HSiW shall be compared. The results are shown in Figure 91, where a) and b) present the entire lifetimes of the foams and c) and d) focus on the collapse rates of the foams, where the time was normalized by the critical drainage times  $t_d$  respectively for each foam.

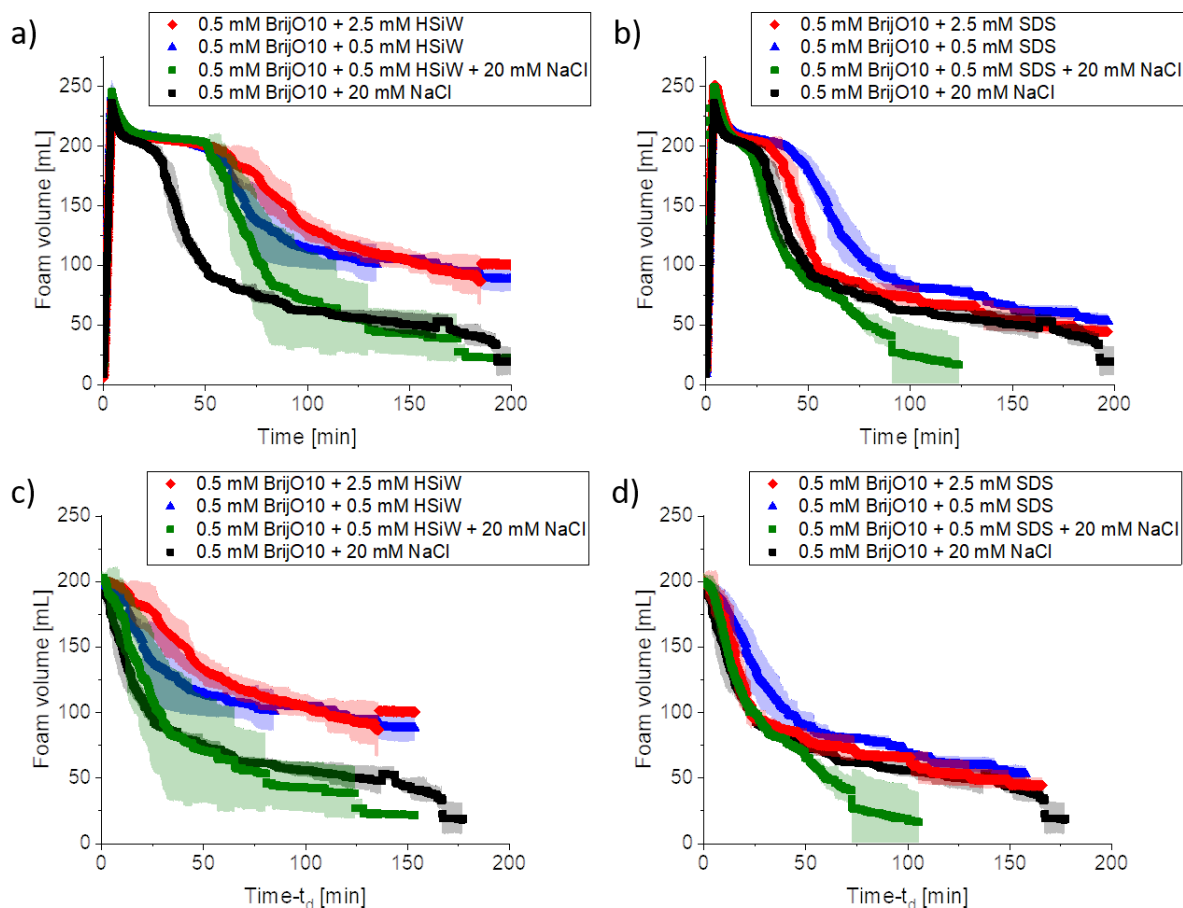


Figure 91: Foam volume vs time for foams of 0.5 mM BrijO10 containing a) HSiW and b) SDS. In c) and d) the foam ages were corrected by the critical drainage time, where foam collapse sets in, allowing for a direct comparison of the collapse rates.

The generation of all measured foams is identical and stopped after four minutes, where the initial maximum foam volumes of the BrijO10-foams are slightly increased in the presence of SDS or HSiW owing to an increased foam wetness. In the subsequent drainage and collapse regimes, significant differences occur between the individual foams. Thus, in the presence of SiW, the transitory drainage regime is strongly expanded in comparison to the bare BrijO10 foam, see Figure 91a. In particular, the onset of the foam collapse, i.e. the critical drainage time  $t_d$ , is shifted to high foam ages of about 50 minutes, indicating that the dry foams with SiW are particularly stable, while the bare BrijO10-foam starts collapsing earlier after 25 minutes. Interestingly, regardless of SiW-concentration or NaCl-addition the drainage regime extends over identical timeframes. Furthermore, the drainage regime also expands to higher foam ages in the presence of SDS see Figure 91b. The effect is less pronounced than with HSiW and the collapse onset time  $t_d$  is maximal (45 minutes) at 0.5 mM SDS, while NaCl- or further SDS-addition seem to destabilize the foams as  $t_d$  decreases. In order to compare the collapse rates of the foams, the foam age was corrected by the critical drainage time  $t_d$ , respectively for each



sample, setting the collapse onset to  $t=0$  min, see Figure 91c and d. At the collapse onset time, all examined foams have drained so that the liquid fractions are below 1% and the stability of the foam originates from the stability of the thin foam films. Here, by comparison with the collapse of the bare BrijO10-foam, it is clear that addition of HSiW decelerates the collapse of the foam, where the higher the HSiW-concentration the more stable the foam (Figure 91c). However, once NaCl is added the foam collapse accelerates and interestingly coincides with the curve of the bare BrijO10-foam. Furthermore, in the presence of SDS (Figure 91d), the foam stability increases upon addition of 0.5 mM SDS and decreases upon further increase to 2.5 mM SDS. Again, NaCl addition causes a marked decrease in foam stability as the lifetime of the salty foam was consistently the shortest.

These foam stabilities (Figure 91c and d) can be directly compared to the results on the thin liquid films of dry quasi-stationary foams, discussed in section 4.2, where the same foam compositions were investigated. Therein, it was observed that the thin liquid film thickness increases up to 0.5 mM HSiW or 0.5 mM SDS. This effect was attributed to arising transversal electrostatic repulsion in the foam films. However, upon further addition of NaCl (or further HSiW) the foam film thickness decreased again due to a screening effect of the interfacial electrostatics. In the present section, it was shown that both 0.5 mM HSiW and 0.5 mM SDS have marked stabilizing effects on the otherwise non-ionic BrijO10 foams. This stability increase can be attributed to the emergent electrostatics in the foam films, which counteract capillary action (suction of liquid from the thin films to the plateau borders) and give rise to higher film thickness and thus disfavor bubble rupture. Accordingly, addition of NaCl to mixed foams of BrijO10/SDS or BrijO10/HSiW entailed a strong decrease in foam stability congruent with an electrostatic screening mechanism that leads to a decrease in foam film thickness facilitating film rupture. However, the foam of BrijO10 + 2.5 mM HSiW exhibited the highest observed foam stability, while SANS in the preceding chapter showed that the foam films are significantly thinner (than for 0.5 mM HSiW), presumably due to a self-screening effect. Conversely, addition of 2.5 mM SDS here caused a decrease in foam stability. Therefore, SDS and HSiW seem to induce opposite effects here that cannot be assigned to mere electrostatics. This result shows that foam stability is an interplay of multiple simultaneous phenomena in the liquid and at the interfaces that constitute the foam films, where the disjoining pressure that includes electrostatic repulsion between the interfaces only plays one (though important) role. In particular, interfacial viscosity and elasticity influence strongly the tendency of a film to rupture or to heal itself, and contribute ineluctably to a foams stability. Here, SiW as well as SDS are expected to have strong effects as both form close contacts with the surfactant

molecules, thus, co-constituting the interface. While SiW forms contacts only with the hydrophilic surfactant heads, SDS anchors deeply into the foam films and thus alters the packing of the BrijO10 surfactant heads as well as hydrophobic chains. Either phenomenon is expected to cause strong effects on the interfacial dynamics. To elucidate such effects film rheology experiments should be performed in the future in order to provide a more complete picture as to the effects of superchaotropic ions on non-ionic surfactant foams. Furthermore, it might be feasible to do equivalent measurements using a classical chaotropic salt like  $\text{SCN}^-$ , although expected effects at the herein used concentrations are expected to be slight<sup>210</sup> and probably negligible in comparison to the superchaotropic SiW.

Either way, herein the superchaotropic Keggin-ion  $\text{SiW}_{12}\text{O}_{40}^{4-}$  (SiW) was shown to have strong effects at millimolar concentrations on the properties of foams of the non-ionic surfactant BrijO10 ( $\text{C}_{18:1}\text{E}_{10}$ ) under free drainage conditions. For the sake of reference, the effects of the ionic surfactant SDS on BrijO10-foams were traced equivalently. Both SiW and SDS are attracted to the non-ionic surfactant foam films, the former driven by the chaotropic effect and the latter driven by the hydrophobic effect on the aliphatic chain, and are therefore expected to equip the non-ionic surfactant foam with ionic charges. However, SDS and HSiW differ fundamentally, i.e. SDS is a classical organic ionic surfactant, exhibits pronounced surface activity and foams in aqueous solution, while HSiW is inorganic without amphiphilic structure, exhibits weak surface activity and cannot stabilize foams by itself. Nevertheless, remarkable parallels can be made between SDS and HSiW in the investigated foams as both caused an increase in wetness of the foams upon generation, reflected in a decreased bubble size and increased liquid fractions in the initial foam. Furthermore, liquid drainage proceeded for longer times without foam collapse in the presence of SDS as well as SiW hinting at an increase in foam stability. The acquisition of the subsequent collapse of the drained (dry) foam over time further showed that HSiW indeed strongly stabilizes the BriO10-foam as the collapse rate was decreased with increasing HSiW-concentration. In turn, SDS induced a stabilizing effect only at low SDS-concentration (0.5 mM), while further addition of SDS (2.5 mM) destabilized the foam. The initial increase in foam stability can be assigned to arising electrostatics in the thin foam films, especially because addition of NaCl caused a marked decrease in the foam stability congruent with a screening effect. However, in order to draw further conclusions, experiments involving a determination of the interfacial viscoelasticity would be necessary and need to be performed in the future.

## 4.4.1. Appendix

Surface tensions were measured with a drop shape analyzer on emergent air bubbles submerged in the aqueous sample. At the used concentrations, HSiW has negligible effects on the surface tension of 0.5 mM BrijO10. In contrast, SDS induces marked alterations to the surface tension of 0.5 mM BrijO10. The plateaus at high bubble ages in Figure 92 allow for a determination of the equilibrium surface tensions, which are listed in Table 27.

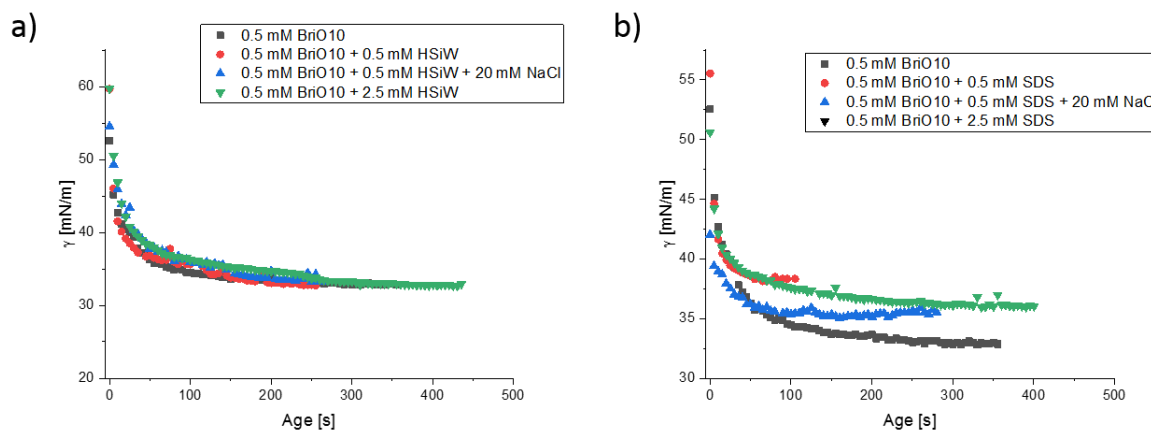


Figure 92: Air/water surface tensions plotted vs bubble age for 0.5 mM BrijO10 in the presence of a) HSiW with or without 20 mM NaCl and b) SDS with or without 20 mM NaCl.

Table 27: Equilibrium water/air surface tensions of the listed samples taken from the constant plateaus at high bubble ages in Figure 92.

0.5 mM BrijO10	0.5 mM BrijO10	0.5 mM BrijO10	0.5 mM BrijO10
	+ 0.5 mM HSiW	+ 2.5 mM HSiW	+ 0.5 mM HSiW
			+ 20 mM NaCl
[mN/m]	[mN/m]	[mN/m]	[mN/m]
32.8	33.4	33.2	33.0

0.5 mM BrijO10	0.5 mM BrijO10	0.5 mM BrijO10	0.5 mM BrijO10
	+ 0.5 mM SDS	+ 2.5 mM SDS	+ 0.5 mM SDS
			+ 20 mM NaCl
[mN/m]	[mN/m]	[mN/m]	[mN/m]
32.8	38.3	36.1	35.5

## 4.5. Chapter summary

The Keggin-ion  $\text{SiW}_{12}\text{O}_{40}^{4-}$  (SiW) – used here in its acid form  $\text{H}_4\text{SiW}_{12}\text{O}_{40}$  (HSiW) – exhibits very limited surface activity and cannot stabilize aqueous foams by itself. Nevertheless, due to its chaotropic nature SiW spontaneously adsorbs to polar soft matter interfaces such as foam films stabilized by non-ionic surfactants. Thus, using electrolytic (NaCl) or NaCl-free foaming solutions containing the non-ionic surfactant BrijO10 ( $\text{C}_{18:1}\text{EO}_{10}$ ) and SiW, mixed BrijO10/HSiW-foams were generated with very different properties. Notably, the concentration of the foaming agent BrijO10 was fixed, while SiW- and NaCl- concentrations were varied systematically. These foams were investigated regarding their foam film thickness using small angle neutron scattering (SANS) and regarding their generation, drainage and stability using conductometry and image analysis via a FOAMSCAN-setup.

In the SANS-experiments, the BrijO10/HSiW-foams were generated using a weak airflow (5 ml/min) resulting in dry foams in their quasi-stationary state, where foam collapse and generation are in equilibrium, and the scattering was acquired as a function of time and as a function of foam height. As the acquired SANS-spectra were found to evolve ever so slightly over time, all measured foams must be considered as non-equilibrium structures. In order to compare these SiW/BrijO10-foams nonetheless, a relatively high foam age (60-75 minutes) was chosen as here the evolution over time was smallest and the foams can be expected to be closest to equilibrium. Each foam SANS-spectrum contained three contributions: i) A  $q^{-4}$ -dependence at low  $q$  arising from Porod scattering of the large amount of surface in the foam, ii) oscillations at mid  $q$  arising from specular neutron reflectivity on the thin foam films and iii) the scattering of the micelles (as BrijO10 is used at concentrations above its cmc) that populate the plateau borders and vertices. Here, the oscillations in the reflectivity were exploited to determine the thickness of the foam films via fitting using a simple reflectivity model. Thus, with increasing SiW-concentration, the oscillations became sharper and more intense up to 0.5 mM SiW and then faded at higher SiW-concentrations up to 2.5 mM HSiW. The emergence of these well-defined oscillations is caused by a decrease in polydispersity of the foam films, i.e. the films show identical film thickness over large distances. By fitting these oscillations, the film thickness was found to increase, pass through a maximum at 0.5 mM SiW and decrease at higher SiW-concentrations up to 2.5 mM. In a similar fashion, the superchaotropic ion  $\text{B}_{12}\text{I}_{12}^{2-}$  and the ionic surfactant SDS respectively caused a comparable thickness increase at low concentrations (up to 0.5 mM respectively). All these species are expected to form direct

contacts with the foam films thereby equipping them with electric charges,  $B_{12}I_{12}^{2-}$  and SiW driven by the chaotropic effect, and the ionic surfactant SDS due to the hydrophobic effect on its aliphatic chain. Consequently, the initially increased film thickness was interpreted as a result of intra-film transversal electrostatic repulsion that arises when SiW (or  $B_{12}I_{12}^{2-}$  or SDS) adsorbs to the otherwise electrically neutral BrijO10-film interfaces. It was further shown that addition of the electrolyte NaCl to foams containing 0.5 mM HSiW (at the thickness maximum) caused a continuous decrease in the film thickness owing to a screening of the electrostatics. This screening effect was further compared with the decrease in film thickness at high SiW-concentrations. It was concluded that HSiW at high concentrations saturates the film interfaces, is forced into the interstitial film liquid and, thus, causes a self-screening effect. Seemingly, only the  $H^+$ -counterions contributed to the screening, while  $SiW_{12}O_{40}^{4-}$  had to be excluded when calculating the ionic strength. Therefore, SiW seems to behave here like an ionic nano-colloid and cannot be considered as a classical ion. The effects of SiW on the thin foam films are expected to affect strongly the disjoining pressure in the films and accordingly the macroscopic properties of the foams.

To examine these macroscopic effects, foams were investigated using a FOAMSCAN device, which allows for a simultaneous acquisition of bubble size and foam height via two cameras along with a conductometric measurement of the foam wetness. In this method, the foams were generated with a strong air flow (50 ml/min), which was turned off once the foam had filled the column, resulting in free drainage of the liquid dispersed in the foam down into the foaming solution. Thus, it was observed that foam generation, drainage as well as foam stability are all strongly affected in the presence of SiW. To provide a reference point, equivalent measurements were performed using SDS and indeed significant parallels between the inorganic SiW and the organic surfactant SDS were observed. Thus, foam generation in the presence of SDS or SiW resulted in smaller bubble sizes and wetter foams in comparison to bare BrijO10-foams, though the effect was more pronounced with SDS. Furthermore, the drainage rate was shown to be significantly slower in the presence of SiW, whereas with SDS drainage also proceeded for longer times owing to a higher liquid fraction in the first place and not due to a decrease in the drainage rate. Dry foams (liquid fraction <1%) resulted after drainage, where addition of SDS and HSiW at low concentrations (0.5 mM respectively) caused a significant slowdown of the subsequent foam collapse. Interestingly, addition of NaCl caused a strong decrease in the drainage rate hinting at an electrostatic stabilization mechanism of the foam consonant with the electrostatic effect on the thin foam films observed in SANS. However, at high SDS and SiW concentrations (2.5 mM respectively in the absence of NaCl)

opposite effects were observed, i.e. with SiW the most stable foams were observed while in the presence of SDS the foam stability was found to strongly decrease. This observation demonstrates that foam stability is a complex interplay of several phenomena, where the disjoining pressure and eventual intra-film electrostatics play only one (though major) role. Principally, it would be necessary to consider interfacial viscoelasticity, which is known to have predominant effects on bubble rupture and the accompanying foam collapse. Expectedly as SDS or SiW take part in the interface, marked effects should appear in their presence. Such measurements are envisaged for the future and will provide a more complete picture of the observed effects.

## 4.6. Résumé en français

L'ion de Keggin  $\text{SiW}_{12}\text{O}_{40}^{4-}$  (SiW) – utilisé ici sous sa forme acide  $\text{H}_4\text{SiW}_{12}\text{O}_{40}$  (HSiW) – présente une activité de surface très limitée et ne peut pas stabiliser les mousses aqueuses par lui-même. Néanmoins, en raison de sa nature chaotrope, le SiW s'adsorbe spontanément sur les interfaces des matières molles polaires telles que les films de mousse stabilisés par des tensioactifs non ioniques. Ainsi, en utilisant des solutions moussantes électrolytiques (NaCl) ou sans NaCl contenant le tensioactif non ionique BrijO10 ( $\text{C}_{18:1}\text{EO}_{10}$ ) et du SiW, des mousses mixtes BrijO10/HSiW ont été générées avec des propriétés très différentes. Notamment, la concentration de l'agent moussant BrijO10 était fixe, tandis que les concentrations de SiW et de NaCl variaient systématiquement. Ces mousses ont été étudiées en ce qui concerne l'épaisseur de leur film de mousse par diffusion de neutrons aux petits angles (SANS) et en ce qui concerne leur génération, leur drainage et leur stabilité par conductimétrie et analyse d'images via un appareil FOAMSCAN.

Dans les expériences SANS, les mousses BrijO10/HSiW ont été générées en utilisant un faible débit d'air (5 ml/min), ce qui a donné des mousses sèches dans leur état quasi-stationnaire, où l'effondrement et la génération de mousse sont en équilibre, et la diffusion a été acquise en fonction du temps et en fonction de la hauteur de la mousse. Comme les spectres SANS acquis se sont avérés évoluer très légèrement dans le temps, toutes les mousses mesurées doivent être considérées comme des structures non équilibrées. Afin de comparer ces mousses SiW/BrijO10, on a néanmoins choisi un âge de mousse relativement élevé (60-75 minutes), car l'évolution dans le temps était plus faible et on peut s'attendre à ce que les mousses soient les plus proches de l'équilibre. Le spectre SANS de chaque mousse contient trois contributions : i) une dépendance  $q^{-4}$  à faible  $q$  due à la diffusion de Porod sur la grande surface de la mousse, ii) des oscillations à  $q$  moyen dues à la réflexion spéculaire des neutrons sur les couches minces de mousse et iii) la diffusion des micelles (comme BrijO10 est utilisé à des concentrations supérieures à son cmc) qui occupent les limites et les sommets du plateau. Ici, les oscillations de la réflectivité ont été exploitées pour déterminer l'épaisseur des films de mousse par fitting en utilisant un modèle simple de réflectivité. Ainsi, avec l'augmentation de la concentration en SiW, les oscillations sont devenues plus nettes et plus intenses jusqu'à 0,5 mM SiW, puis se sont atténuées aux concentrations plus élevées en SiW jusqu'à 2,5 mM HSiW. L'apparition de ces oscillations bien définies est due à une diminution de la polydispersité des films de mousse, c'est-à-dire que les films présentent une épaisseur identique sur de grandes distances. On a constaté que l'épaisseur des films augmentait, passait par un maximum à 0,5 mM SiW et

diminuait à des concentrations plus élevées de SiW jusqu'à 2,5 mM. De la même manière, l'ion superchaotrope  $B_{12}I_{12}^{2-}$  et le tensioactif ionique SDS ont respectivement provoqué une augmentation d'épaisseur comparable à de faibles concentrations (jusqu'à 0,5 mM respectivement). Toutes ces espèces sont censées former des contacts directs avec les films de mousse, les munissant ainsi de charges électriques, le  $B_{12}I_{12}^{2-}$  et le SiW étant entraînés par l'effet chaotrope, et le tensioactif ionique SDS par l'effet hydrophobe sur sa chaîne aliphatique. Par conséquent, l'augmentation initiale de l'épaisseur du film a été interprétée comme le résultat d'une répulsion électrostatique transversale intra-film qui se produit lorsque le SiW (ou le  $B_{12}I_{12}^{2-}$  ou le SDS) s'adsorbe sur les interfaces de film BrijO10, par ailleurs électriquement neutres. Il a en outre été démontré que l'ajout de l'électrolyte NaCl aux mousses contenant 0,5 mM de HSiW (à l'épaisseur maximale) entraînait une diminution continue de l'épaisseur du film en raison d'un blindage de l'électrostatique. Cet effet d'écrantage a été comparé à la diminution de l'épaisseur du film à des concentrations élevées de SiW. Il a été conclu que le HSiW à haute concentration saturait les interfaces des films, était forcé dans le liquide interstitiel du film de mousse et, par conséquent, provoquait un effet d'auto-écrantage. Apparemment, seules les contre-ions  $H^+$  ont contribué à l'écrantage, tandis que le  $SiW_{12}O_{40}^{4-}$  a dû être exclu lors du calcul de la force ionique. Par conséquent, le SiW semble se comporter ici comme un nanocolloïde ionique et ne peut être considéré comme un ion classique. Les effets du SiW sur les films de mousse devraient en outre affecter fortement la pression de disjonction dans les films et par conséquent les propriétés macroscopiques des mousses.

Pour examiner ces effets macroscopiques, les mousses ont été étudiées à l'aide d'un appareil FOAMSCAN, qui permet l'acquisition simultanée de la taille des bulles et de la hauteur de la mousse par deux caméras ainsi qu'une mesure conductimétrique de l'humidité de la mousse. Dans cette méthode, les mousses ont été générées avec un fort débit d'air (50 ml/min), qui a été arrêté une fois que la mousse a rempli la colonne, ce qui a permis de drainer librement le liquide dispersé dans la mousse vers la solution moussante. Ainsi, il a été observé que la génération de mousse, le drainage ainsi que la stabilité de la mousse sont tous fortement affectés en présence de SiW. Pour fournir un point de référence, des mesures équivalentes ont été effectuées à l'aide de SDS et des parallèles significatifs entre le SiW inorganique et le SDS tensioactif organique ont été observés. Ainsi, la formation de mousse en présence de SDS ou de SiW a donné lieu à des bulles plus petites et à des mousses plus humides par rapport aux mousses nues de BrijO10, bien que l'effet ait été plus prononcé avec le SDS. En outre, le taux de drainage s'est avéré plus lent en présence de SiW, alors qu'avec le SDS, le drainage s'est également déroulé sur une plus longue période en raison d'une fraction liquide plus élevée en premier lieu et non pas en raison



d'une diminution du taux de drainage. Des mousses sèches (fraction liquide <1%) se sont formées après le drainage, où l'ajout de SDS et de HSiW à de faibles concentrations (0,5 mM respectivement) a provoqué un ralentissement significatif de l'effondrement de la mousse qui s'en est suivi. Il est intéressant de noter que l'ajout de NaCl a provoqué une forte diminution du taux de drainage, ce qui indique un mécanisme de stabilisation électrostatique de la mousse, en accord avec l'effet électrostatique sur les films minces de mousse observé dans le SANS. Cependant, à des concentrations élevées de SDS et de SiW (2,5 mM respectivement en l'absence de NaCl), des effets opposés ont été observés, c'est-à-dire qu'avec le SiW, les mousses les plus stables ont été observées alors qu'en présence de SDS, la stabilité de la mousse a fortement diminué. Cette observation démontre que la stabilité des mousses est une interaction complexe de plusieurs phénomènes, où la pression de disjonction et les éventuelles électrostatiques intra-film ne jouent qu'un seul rôle (bien que majeur). Principalement, il serait nécessaire de considérer la viscoélasticité interfaciale, dont on sait qu'elle a des effets prédominants sur la rupture des bulles et l'effondrement de la mousse qui l'accompagne. On s'attend à ce que des effets marqués apparaissent en leur présence lorsque des SDS ou des SiW prennent part à l'interface. De telles mesures sont envisagées pour l'avenir et fourniront une image plus complète des effets observés.

## 5. Conclusions

In this thesis, a large variety of ionic species was investigated ranging from classical chaotropic ions like  $\text{SCN}^-$  over superchaotropic nano-ions such as ionic boron clusters and polyoxometalates to nanometric organic ions such as tetraphenylborate. All the nano-ions interact strongly with self-assemblies (micellar and bilayer phases) of non-ionic ethoxylated surfactants causing a charging of the surfactant self-assembly along with a dehydration of the surfactant heads. In electrolyte-free solutions, the emergent electrostatic forces dominate the induced phenomena (e.g. the lamellar phase to vesicle transition in chapter 3 or the increase in foam film thickness in chapter 4) and thus act like ionic surfactants that induce equivalent electrostatics by anchoring into the non-ionic surfactant self-assemblies driven by the hydrophobic effect on the aliphatic surfactant tails. Therefore, though nano-ions are inorganic (besides tetraphenylborate) and globular, and thus fundamentally very different from organic ionic surfactants with amphipathic structure, nano-ions can serve as alternatives to ionic surfactants in surfactant-based formulations. Furthermore, there are subtle differences between all the nano-ions emerging from their chaotropic to hydrophobic characters. To predict their behavior a general rule of thumb seems to apply in order to classify these ions, i.e. the lower the volume charge density of an ion the more chaotropic it becomes, while at very low volume charge densities hydrophobic properties arise. An ion's nature manifests in its effect on the shape of non-ionic surfactant micelles, where chaotropic ions intercalate between the hydrophilic surfactant head groups driving the micelles towards spherical geometries and hydrophobic ions penetrate deeply between the surfactant tails driving towards two-dimensional bilayer geometries. Overall, it was shown that the adsorption of a chaotropic ion to non-ionic surfactant micelle follows a Langmuir isotherm, while hydrophobic ions break up the surfactant assemblies causing destabilization of the self-assemblies leading to precipitation. Accordingly, depending on the choice of the ion it is possible to play on the curvature of a surfactant assembly providing a novel way of tailoring the properties of surfactant phases. Furthermore, it was shown on non-ionic surfactant foams that while SiW induces foam-stabilizing electrostatic effects. The impact of nano-ion adsorption goes beyond the mentioned phenomena (electrostatics, dehydration and packing effects) and for example changes in the viscoelasticity of the non-ionic surfactant layers must appear upon nano-ion adsorption that strongly affect surfactant film stability and behavior. The remarkable behavior of nano-ions – herein on non-ionic surfactant systems – can be extended to any kind of colloidal soft matter system, such as polymers, proteins or nanoparticles. This thesis therefore provides a versatile toolbox for using

nano-ions as novel and powerful candidate components in soft matter materials and applications.

## 6. Perspectives

It was shown herein and previously by other authors<sup>95,96</sup> that some nano-ions behave differently to classical ions and should in some cases rather be referred to as ionic nano-colloids. Additionally, some giant colloidal POMs (several nanometers in size, e.g. Mo<sub>154</sub>-clusters) were shown to exhibit chaotrope-like properties.<sup>110</sup> The question arises here at what size and charge an ion loses its classical (electrolytic) ionic properties and starts behaving like a colloid (not electrolytic). It might be of major interest to investigate and define the ion-ionic colloid transition. The behavior of nano-ions such as POMs could then be linked to the behavior of more classical colloids such as charged nanoparticles. The chaotropic effect might be at play in nanoparticle dispersions and could be interlinked with classical depletion forces between colloids. Related to this, there are current investigations ongoing in collaboration with the group of Regine von Klitzing at TU Darmstadt with the objective to quantify by Debye-Hückel theory the behavior of a chaotropic ion (SiW<sub>12</sub>O<sub>40</sub><sup>4-</sup>) within thin liquid non-ionic surfactant films using thin film liquid balance measurements. This project will allow for a determination of the induced electrostatic effects and the colloidal nature of SiW via ionic strength considerations.

Furthermore, nano-ions were shown to interact strongly with the hydrophobic, non-polar aliphatic or the hydrophilic, polar areas in soft matter dispersions depending on whether an ion is chaotropic or hydrophobic as was shown here on non-ionic surfactant self-assemblies. Particularly, the interaction with the hydrophilic polar moieties provides a novel way to tailor formulations involving soft matter of amphiphilic molecules (surfactants/polymers/proteins). Such nano-ion assisted formulations of every-day life products, especially due to their ionic surfactant-like behavior. Nano-ions here might take the role of a co-surfactant resulting in hybrid inorganic/organic formulations.

Similarly, cationic surfactant mixtures are widely used to form vesicles in medicine as drug carriers. The study of equivalent nano-anion/cationic surfactant mixtures might result in similar vesicular systems and would open a new field of hybrid assemblies.

Some nano-ions such as polyoxometalates are clusters rich in precious metals such as tungsten or molybdenum, which are essential components of metal alloys used, for example in electronic products. Therefore, there is ample industrial interest in developing specific and powerful extraction methods for these metals. In context, the formation of superchaotropic POMs in situ might be a result of a multi-step synthesis procedure or as simple as changing pH (e.g. for

MoO<sub>4</sub><sup>2-</sup>-species<sup>40</sup>). Thus, when a superchaotropic ion forms in solution, it can be extracted specifically by an electrically neutral interface, e.g. as in flotation procedures where the air/water interface covered by non-ionic surfactants in foams serves as the extracting phase. Using such a (non-complexing) method, classical ions would not be extracted resulting in high specificity for the superchaotrope. This thesis serves as a signpost for such superchaotrope extractions foreseeing possible phenomena that might occur in electrolyte-free as well as saline surfactant solutions and foams, and, thus, eventual issues at any point in the extraction procedure can be compared to the results presented herein. Current investigations concerning this topic are conducted as part of the PhD-thesis work of Klaudia Skorzewska at the L2IA.

All phenomena discussed in this thesis were investigated using static methods while the dynamics of nano-ion adsorption were disregarded, as is also the case in the existing literature. It would be of high interest to examine the differences in timescale between chaotropic, superchaotropic and hydrophobic ions and whether the observed time scales can be compared with the dynamics in surfactant self-assembly.



## 7. Materials and methods

### 7.1. Chemicals








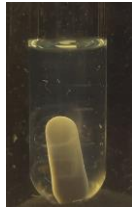
The high purity surfactant pentaethylene glycol monododecyl ether ( $C_{12}E_5$ ,  $C_{22}H_{46}O_6$ ,  $\geq 98\%$ ) was purchased from Sigma Aldrich as well as the commercial surfactant BrijO10. The high purity surfactant tetraethylene glycol mono-octyl ether ( $C_8E_4$ ,  $C_{16}H_{34}O_5$ ,  $\geq 98\%$ ) was purchased from Chem Cruz. The ionic surfactant sodium dodecylsulfate (SDS,  $NaC_{12}H_{25}SO_4$ ,  $\geq 98\%$ ) was purchased from Strem Chemicals. The classical salts sodium chloride ( $NaCl$ ,  $\geq 99.5\%$ ), sodium thiocyanate ( $NaSCN$ ,  $>98\%$ ) and sodium fluoride ( $NaF$ ,  $\geq 99\%$ ) were purchased from Sigma Aldrich. Sodium bromide ( $NaBr$ ,  $\geq 99\%$ ) and sodium iodide ( $NaI$ ,  $\geq 99\%$ ) were purchased from Strem Chemicals. Sodium sulfate ( $Na_2SO_4$ ,  $\geq 99\%$ ) was purchased from Carlo Erba and sodium hexafluorophosphate ( $NaPF_6$ ,  $\geq 99\%$ ) was purchased from Alfa Aesar. The bases sodium hydroxide ( $NaOH$ ,  $>97\%$ ) and potassium hydroxide ( $KOH$ ,  $>85\%$ ) were used in pellet form from Carlo Erba. The Keggin-POMs phosphotungstic acid (HPW,  $H_3PW_{12}O_{40}$ ,  $\geq 99.9\%$ ), sodium phosphotungstate ( $NaPW$ ,  $Na_3PW_{12}O_{40}$ ,  $\geq 99.9\%$ ) tungstosilicic acid ( $HSiW$ ,  $H_4SiW_{12}O_{40}$ ,  $\geq 99.9\%$ ), ammonium metatungstate ( $(NH_4)_6H_2W_{12}O_{40}$ ,  $NH_4MW$ ,  $\geq 99.9\%$ ) were purchased from Sigma Aldrich. Potassium borotungstate ( $K_5BW_{12}O_{40}$ ,  $KBW$ ) was provided by the group of Emanuel Cadot from ILV in Versailles.  $NaCOSAN$  ( $Na^+[3,3'-Co(1,2-C_2B_9H_{11})_2]^-$ ) was purchased in its cesium form from Katchem Chemicals and obtained by ion exchange. The sodium forms of dodecaiodo-/dodecabromo-/dodecachloro-closo dodecaborate ( $Na_2B_{12}I_{12}$ ;  $Na_2B_{12}Br_{12}$ ;  $Na_2B_{12}Cl_{12}$ ) and cesium dodecahydrodo-closo dodecaborate ( $Cs_2B_{12}H_{12}$ ) were purchased from Katchem. Sodium dodecafluoro dodecaborate ( $Na_2B_{12}F_{12}$ ) and cesium dodecachloro dodecaborate ( $Cs_2B_{12}Cl_{12}$ ) were synthesized and provided by the group of Clara Vinãs and Francesc Teixidor at ICMAB in Bellaterra. Sodium tetraphenylborate ( $NaB(C_6H_5)_4$ , p.a., ACS, Reag. Ph Eur) was purchased from Merck. Millipore water was taken from an internal purification system. All chemicals were used without further purification.

## 7.2. Visual methods: Cloud points and phase diagrams

Samples were heated from 10 - 100°C at a rate of 2°C/min in a stirred water bath. All phase transitions were determined by visual inspection against a black backdrop and by setting the samples in between crossed polarizing filters to confirm the presence of lyotropic phases. The corresponding transition temperatures were read from an external precision thermometer. Samples were measured at rest as well as under agitation to confirm the spontaneity of the phase transitions and to exclude side effects of agitation on the phase behavior.

Throughout this thesis non-ionic surfactant concentrations below 5 wt-% were used. In this concentration range, the used surfactants may form micellar, lamellar, sponge and vesicle phases depending on the temperature, surfactant type and additive. In order to clarify the distinction between the phases, some observatory definitions are stated in Table 28

Table 28: Appearance of the different surfactant phases observed in this thesis to the naked eye and between crossed polarizers.

	Micellar phase, $L_1$	Lamellar phase, $L_\alpha$	Sponge phase, $L_3$	(unilamellar) Vesicle phase
With the naked eye	Colorless, clear	Bluish opalescent, clear sometimes hazy with Schlieren patterns	Bluish opalescent, clear	Bluish opalescent, clear
				
Between crossed polarizing filters	No birefringence	Birefringent (no agitation)	Birefringent only under agitation	No birefringence
		 Magnetic bar is still	 Magnetic bar is turning	

The temperature-induced phase-separation of a non-ionic surfactant micellar phase (called the cloud point) is defined as the temperature, where an object behind the sample cannot be seen due to a complete loss of transparence as the sample turns white. The transition is rapid for the used systems, and the estimated error bars are low, i.e.  $\pm 1^\circ\text{C}$ .

In some cases, vesicle phases were formed before the appearance of the cloud point. The transition of a micellar phase into the vesicle phase is difficult to determine visually, as the sole



means for distinction is the onset of opalescence (bluish color). This transition from colorless to a bluish opalescent solution was found to be rather slow and is accelerated with increasing temperature. The  $L_1$ -vesicle transition has large, estimated error bars of around  $\pm 5^\circ\text{C}$ .

The transitions into lamellar phases ( $L_a$ ) and sponge phases ( $L_3$ ) were confirmed by visual inspection upon setting the samples between crossed polarizers. The estimated errors are  $\pm 3^\circ\text{C}$ .

### 7.3. Small angle x-ray (or neutron) scattering (SAXS or SANS)

X-rays are electromagnetic waves with very short wavelengths of  $\lambda_{\text{x-ray}}=0.01\text{-}10$  nm and interact with matter due to electron-density fluctuations within a sample. On the other hand, neutrons are elementary particles (with a spin state) that propagate as waves with wavelength between 0.4 and 2 nm (depending on their temperature), and interact with nuclei and spin states of atoms. Generally, when x-rays or neutrons impinge on a material two different phenomena can occur, i.e. they can be absorbed, which entails x-ray fluorescence, or they can be scattered. Such scattering events can be elastic or inelastic, meaning without or with energy loss of the photon, respectively. In an elastic scattering process, the incident and the outgoing photon have the same energy, i.e. the same wavelength. The thereby scattered waves will interfere with each other giving rise to an interference pattern, which contains information about the structure and shapes of the scattering objects in the sample. Acquired dimensions from such a scattering experiment always represent average values. The measurement of scattering at small angles of x-ray (SAXS) and neutron (SANS) radiation presents a powerful and versatile technique to investigate samples on the nanometer-length scale. The following introduction is based on the annotated references.<sup>213-215</sup>

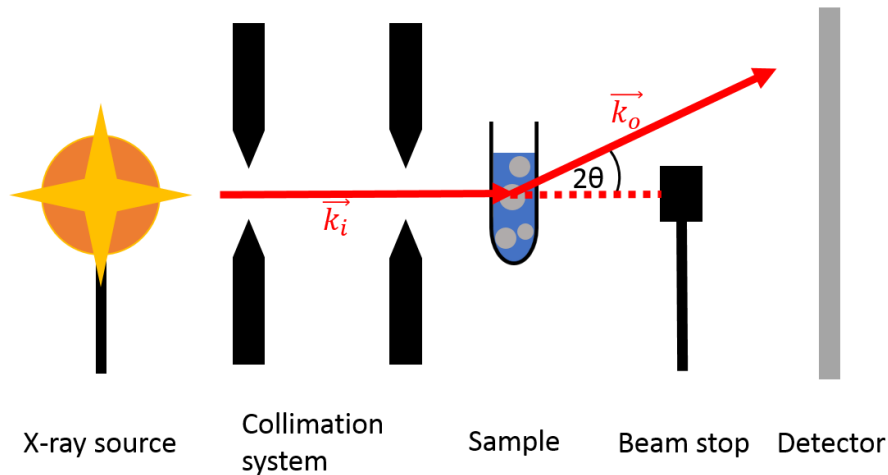
The SAXS(SANS)-experiment

Figure 93: Classical SAXS-setup consisting of x-ray source, collimation system of two slits, sample, beam stop and detector. Incident radiation  $\vec{k}_i$  is scattered at an angle  $2\theta$  resulting in outgoing radiation  $\vec{k}_o$ . Adapted from The SAXS Guide by Anton Paar.

In a small angle scattering experiment, x-rays are emitted from an x-ray source and are collimated by a system of slits to then impinge on the sample. A part of the incident radiation is scattered and then collected by a 2D-detector plate as a function of the scattering angle  $2\theta$ . The X-ray emission spectrum of x-ray sources is never perfectly monochromatic and optical elements such as mirrors, multilayers or single crystal monochromators have to be inserted upstream the collimation to select the needed wavelength and its resolution (width of the selected wavelength and divergence of the beam). Furthermore, as scattering events are rather unlikely, the major part of the incident radiation will be transmitted without interaction with the sample. The transmitted intensity would largely overpower the scattered intensity and can damage the sensible detector. Therefore, a beam stop must be set in front of the detector to cut off the transmitted incident beam with the trade-off that scattering at very low angles cannot be detected. Similar setups are used in neutron scattering experiments. Neutrons are usually produced by a nuclear reactor and then thermalized to select waves with nanometric wavelengths. In comparison to x-rays, neutrons have a mass and at similar wavelengths, the corresponding energies carried by the wave and transferred to the matter is much smaller, typically, around the keV for x-rays and the meV for neutrons, a factor difference of  $10^6$ .

The Bragg condition and reciprocal space

In order to illustrate interference arising from a scattering phenomenon, the Bragg condition will be shortly explained. The Bragg condition accounts for interference of two parallel waves with identical phase that reflect specularly on a crystal lattice of point-scatterers (see Figure 94).

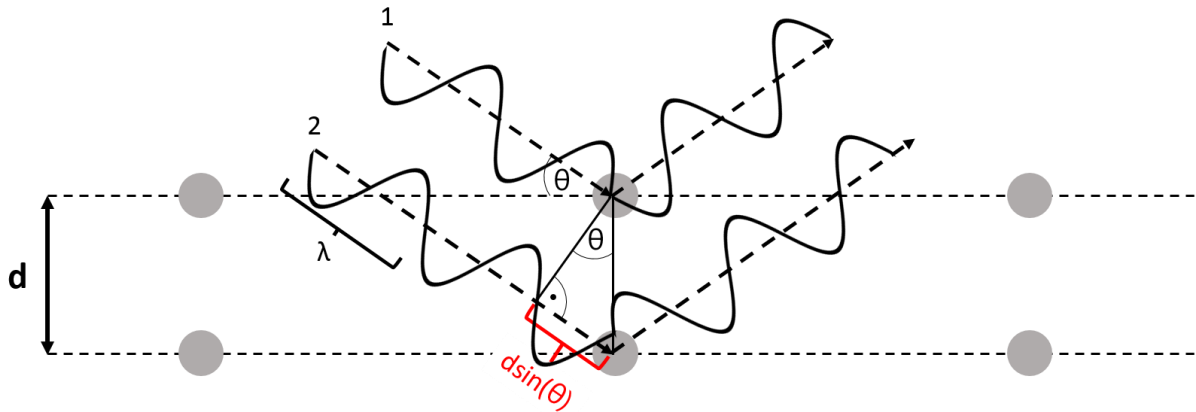


Figure 94: Bragg condition - Constructive superposition of the scattered waves at incident = reflected angle  $\theta$  for a distance between the scatterers  $d$ .

At a reflection angle  $\theta$ , constructive interference of two waves with wavelength  $\lambda$  takes place if the additional path wave 2 must cover is equal  $n\lambda$ . The additional path length is directly linked to the distance  $d$  between the scatterers by the Bragg-condition:

$$n\lambda = 2d\sin(\theta) \quad (8.1)$$

Usually, in a scattering experiment the wavelength is kept constant and, for instance, the Bragg reflexes of a crystal are recorded as a function of the detection angle. As, however, for instance various x-ray sources with different wavelengths are used in practice it is necessary to describe the scattering spectrum of a sample as a function of both the angle of investigation and the wavelength of the x-ray source. This is achieved with the scattering vector  $\vec{q}$ , which is defined as the vector difference between the incident wave  $\vec{k}_i$  and outgoing wave  $\vec{k}_o$  at the scattering angle  $2\theta$ , see Figure 95.

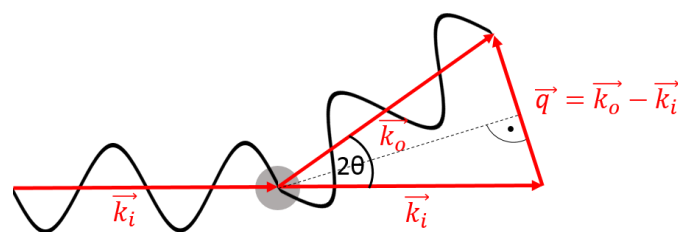


Figure 95: The scattering vector  $\vec{q}$  in a scattering experiment.

The length of the scattering vector  $q$ , also called momentum transfer, is easily calculated (in elastic scattering) using the angular wave numbers  $|\vec{k}_i| = |\vec{k}_o| = \frac{2\pi}{\lambda}$  and is defined as follows:

$$q = |\vec{q}| = |\mathbf{q}| = \frac{4\pi}{\lambda} \sin(\theta) \quad (8.2)$$

The length of the scattering vector has the unit of  $\text{nm}^{-1}$  or  $\text{\AA}^{-1}$  and as scattering spectra are always plotted as a function of  $q$ , they are presented in so-called reciprocal or Fourier space. By combining the Bragg condition and the definition of  $q$ , the relationship of interscatterer distances  $d$  between reciprocal and “real space” becomes apparent:

$$q = \frac{2\pi}{d} \quad (8.3)$$

Using this simple relation characteristic Bragg-distances can be calculated from the peak positions in  $q$ -space, which can give first valuable information about the sample at hand. Every scattering setup is characterized by a certain  $q_{\min}$  and  $q_{\max}$  that define the range of scattering data collection and therefore, according to the Bragg condition, the range of structural information in real space. Experimentally, this  $q$ -window is defined by the sample to detector distance, the size of the beamstop and the size of the detector. On the SWAXS bench at the ICSM, the detector distance is about 750 mm, the beamstop diameter 3 mm and the size of the MAR detector about 340 mm (that is off-centered with respect to the beam direction). On this setup the  $q$ -range lies between  $0.2 \text{ nm}^{-1}$  up to  $30 \text{ nm}^{-1}$ , which corresponds to real space correlation distances of 30 nm to 0.2 nm. This range covers part of the wide-angle scattering range, therefore, the denomination of SWAXS for small AND wide angle scattering. This extension to wide scattering angles enables to acquire information at the molecular scale that can be very useful in correlation to the supramolecular one.

The scattering intensity

Considering a suspension of identical scattering centers  $j$  and  $k$  in a vacuum the time-averaged scattered intensity as a function of the detector angle (or  $q$ -value) is proportional to the sum of all scattered waves.

$$I(q) \propto \sum_{j,k=1}^N \langle b_j b_k \rangle e^{i\mathbf{q} \cdot \mathbf{r}_{jk}} \quad (8.4)$$

where  $b_j$  and  $b_k$  are the scattering lengths and correspond to the amplitude of the scattered wave relative to the incident one. The resulting scattered waves interfere by their respective phase shift  $\Delta\varphi = \mathbf{q} * \mathbf{r}_{jk}$ , which in turn depends on the positions  $\mathbf{r}$  of the scatterers. In x-ray scattering, the expectation value  $\langle b_j b_k \rangle$  is simply  $b^2$  as all electrons interact equally with the incident x-rays ( $b_j=b_k=b$ ) and produce only coherent scattering:

$$I(q)_{SAXS} \propto b^2 \sum_{j,k=1}^N e^{i\mathbf{q} \cdot \mathbf{r}_{jk}} \quad (8.5)$$

In neutron scattering, the situation is slightly different as spin-spin interactions between neutrons and nuclei contribute to the overall scattering and produce an incoherent scattering signal in addition to the coherent one. In particular, the scattering lengths of identical atomic nuclei fluctuate as the neutron-nucleus spin interaction can entail either an increase or a decrease of the overall nucleus+neutron spin-state. Thus, the expectation value of  $\langle b_j b_k \rangle$  must be differentiated for identical and dissimilar scattering lengths:

$$\langle b_j b_k \rangle_{j \neq k} = \langle b \rangle^2 \text{ and } \langle b_j b_k \rangle_{j=k} = \langle b^2 \rangle \quad (8.6)$$

and by combining both terms:

$$\langle b_j b_k \rangle = \langle b \rangle^2 + \delta_{jk} (\langle b^2 \rangle - \langle b \rangle^2) \quad (8.7)$$

with the Kronecker delta  $\delta_{jk}$  which is 0 for  $j \neq k$  and 1 for  $j = k$ .

Therefore, by combining eq. 8.4 and eq. 8.7, the intensity in neutron scattering contains an additional incoherent term:

$$I(q)_{SANS} \propto \langle b \rangle^2 \sum_{j,k=1}^N e^{i\mathbf{q} \cdot \mathbf{r}_{jk}} + N(\langle b^2 \rangle - \langle b \rangle^2) \quad (8.8)$$

The first term here is identical to the coherent scattering intensity in SAXS, see eq.5, with  $\langle b \rangle = b_{coherent}$ . The second term is constant for a given sample, independent of  $q$  and, therefore, contains no structural information. It corresponds to the incoherent part of the scattering with  $\langle b^2 \rangle - \langle b \rangle^2 = b_{incoherent}$ .

As small angle scattering is concerned with nanometer length scales it probes particles and molecules that are much larger than atoms. Thus, it is convenient to use the average scattering length per particle or molecule volume  $v_i$ , which is called the scattering length density  $\rho_i$ :

$$\rho_i = \frac{1}{v_i} \sum_j b_j \quad (8.9)$$

where  $b_j$  represents the coherent scattering lengths of all the atoms inside the particle (or molecule) volume  $v_i$ .

In the case of particles in a medium the excess of scattering length density  $\Delta\rho$  against the solvent must be considered, where we assume the solvent as an incompressible liquid:

$$\Delta\rho = \rho_i - \rho_{\text{solvent}} \quad (8.10)$$

Each atom has a characteristic scattering length, which is tabulated in databases for neutrons and can be easily calculated for x-rays. Throughout the periodic table, the scattering length increases linearly with the atomic number for x-rays, while for neutrons it varies unsystematically. Thus, in x-ray scattering the contrast is fixed (except in anomalous scattering), while in neutron scattering, an adequate isotope substitution enables to enhance the contrast of a sample without affecting its chemistry. This concept is especially useful when using deuterated molecules instead of classical hydrogenated ones as will be exemplified in the worked fitting example in section 7.3.1.

### Fitting of scattering spectra

Detectors in scattering experiments measure the intensity  $I$  of the interference pattern of the scattered radiation, which means that the phase of the detected waves is lost, as  $I(q) = |A(q)|^2$  with the wave amplitude  $A(q)$ . This prohibits a direct holographic reconstruction of the sample in real space and mathematical models are necessary to simulate and reproduce the experimentally observed interference patterns. For this purpose, the form factor  $F(q)$  and the structure factor  $S(q)$  are used that respectively describe mathematically the shape and the higher order arrangement of the scattering objects. Simple geometric bodies, such as spheres and cylinders and many others, are available form factor functions, while the structure factor simulates the interaction potential between the scattering objects, for instance, electrostatic repulsion.

In the simplest case the two functions  $F(q)$  and  $S(q)$  construct a mathematical interference pattern by a simple product, see eq. 8.11, which is physically valid only under the following conditions: i) All scattering objects are identical, ii) the scattering objects are isotropically

distributed and iii) the interactions between scattering objects are independent of their possibly anisotropic shape.

$$I(q) = K * F(q) * S(q) \quad (8.11)$$

The scaling factor  $K$  is fixed by the sample composition and contains the contrast  $\Delta\rho$ , the volume  $v_i$  of the scatterer and its number density  $n_i = \frac{N_i}{V_{total}}$  and, simply stated,  $K$  modulates the number of electrons (or nuclei) that contribute to the x-ray (or neutron) scattering, resulting in the following equation.

$$I(q) = n_i * v_i^2 * \Delta\rho^2 * F(q) * S(q) \quad (8.12)$$

or by using the volume fraction of the scatterers  $\phi_i = \frac{N_i * v_i}{V_{total}}$ :

$$I(q) = \phi_i * v_i * \Delta\rho^2 * F(q) * S(q) \quad (8.13)$$

These two equations are used in this thesis to fit the experimental SANS as well as SAXS data. The resulting best-fit parameters of the form and structure factor can then be related to physical features of the scattering objects such as their geometries and their potential of interaction.

### 7.3.1. Worked fitting example SANS

As an example, an experimental SANS-spectrum of the non-ionic surfactant C<sub>12</sub>E<sub>5</sub> (pentaethyleneglycol monododecylether, C<sub>22</sub>H<sub>46</sub>O<sub>6</sub>) in the presence of the superchaotropic ion SiW (silicotungstate, SiW<sub>12</sub>O<sub>40</sub><sup>4-</sup>) shall be fitted here. C<sub>12</sub>E<sub>5</sub> was used at 25 mM (1 wt-%), SiW concentration was 0.25 mM, and the solvent was D<sub>2</sub>O (instead of H<sub>2</sub>O) to give rise to high contrast between the hydrogenated surfactant and the deuterated solvent and to minimize incoherent scattering, which arises in particular from hydrogenated matter.

The preliminary knowledge of this sample is:

- At the used temperature and concentration, C<sub>12</sub>E<sub>5</sub> forms classical micelles, which are of cylindrical shape.<sup>129</sup>
- The critical micellar concentration of C<sub>12</sub>E<sub>5</sub> is around 50 μM<sup>133</sup> and consequently at the used concentration of 25 mM C<sub>12</sub>E<sub>5</sub> virtually all C<sub>12</sub>E<sub>5</sub>-molecules are found in the micelles.
- SiW adsorbs to the micelles and induces intermicellar repulsion.

Mathematical fitting here helps to quantify the shape and size of the micelles and intermicellar interactions. For this purpose, the scaling factors needed in equation 8.11 shall be determined to then produce fits with physical meaning. First, the scattering length densities  $\rho$  of C<sub>12</sub>E<sub>5</sub> and of D<sub>2</sub>O that give rise to the contrast  $\Delta\rho$  were calculated respectively by using the SLD-calculator in SASView, which uses equation 8.9:

$$\rho_{C_{12}E_5} = \frac{\sum b_i}{v_{C_{12}E_5}} = \frac{\rho'_{C_{12}E_5} * N_A * \sum b_i}{M_{C_{12}E_5}} = \frac{\rho'_{C_{12}E_5} * N_A * (22 * b_C + 46 * b_H + 6 * b_O)}{M_{C_{12}E_5}} = 0.13 * 10^{-6} \text{ \AA}^{-2}$$

$$\rho_{D_2O} = \frac{\sum b_i}{v_{D_2O}} = \frac{\rho'_{D_2O} * N_A * \sum b_i}{M_{D_2O}} = \frac{\rho'_{D_2O} * N_A * (2 * b_D + b_O)}{M_{D_2O}} = 6.38 * 10^{-6} \text{ \AA}^{-2}$$

with  $v_{C_{12}E_5}$ ,  $v_{D_2O}$ ,  $M_{C_{12}E_5}$ ,  $M_{D_2O}$  and  $\rho'_{C_{12}E_5}$ ,  $\rho'_{D_2O}$  respectively being the molecular volume, the molar mass and the mass density of C<sub>12</sub>E<sub>5</sub> or D<sub>2</sub>O, N<sub>A</sub> the Avogadro number, and b<sub>C</sub>, b<sub>H</sub>, b<sub>O</sub> and b<sub>D</sub> the relevant coherent scattering lengths tabulated in reference 216.<sup>216</sup> By using one scattering density value, the scattering length density is assumed homogeneous along the C<sub>12</sub>E<sub>5</sub>-molecule and, thus, throughout the C<sub>12</sub>E<sub>5</sub>-micelles. This assumption neglects the presence of hydration water around the surfactant heads and leads to an underestimation of the micellar size. Yet, this treatment provides the most reliable model and gives rise to so-called “dry” micellar dimensions. Furthermore, it should be stated that SiW does not show significant excess scattering in D<sub>2</sub>O, meaning it is transparent in D<sub>2</sub>O to the neutrons. As a result, owing to the



choice of D<sub>2</sub>O as the solvent, here, SANS exclusively reveals the scattering of the C<sub>12</sub>E<sub>5</sub>-micelles in this experiment.

Additionally, by making the assumption that C<sub>12</sub>E<sub>5</sub>-micelles are completely separated from the solvent, the volume fraction of the micelles can be estimated from the known weight fraction of 1 wt-% (25 mM C<sub>12</sub>E<sub>5</sub>) by using the density of C<sub>12</sub>E<sub>5</sub> ( $\rho_{C_{12}E_5} = 0.961 \text{ g/mol}$ ) resulting in  $\Phi_{SANS} = \Phi_{C_{12}E_5} = 0.0096$ . Thus, the contrast  $\Delta\rho = |\rho_{C_{12}E_5} - \rho_{D_2O}|$  and the volume fraction  $\Phi_{C_{12}E_5}$  are fixed for the fitting procedure and suitable form and structure factors need to be chosen. For the expected dispersion of micelles in D<sub>2</sub>O, spherical, cylindrical and ellipsoidal form factors come to mind. All these mathematical form factors are embedded in the SASView-software<sup>217</sup>, which was used for all SANS-fits in this thesis. The experimental spectrum and corresponding best fits are shown in Figure 96.

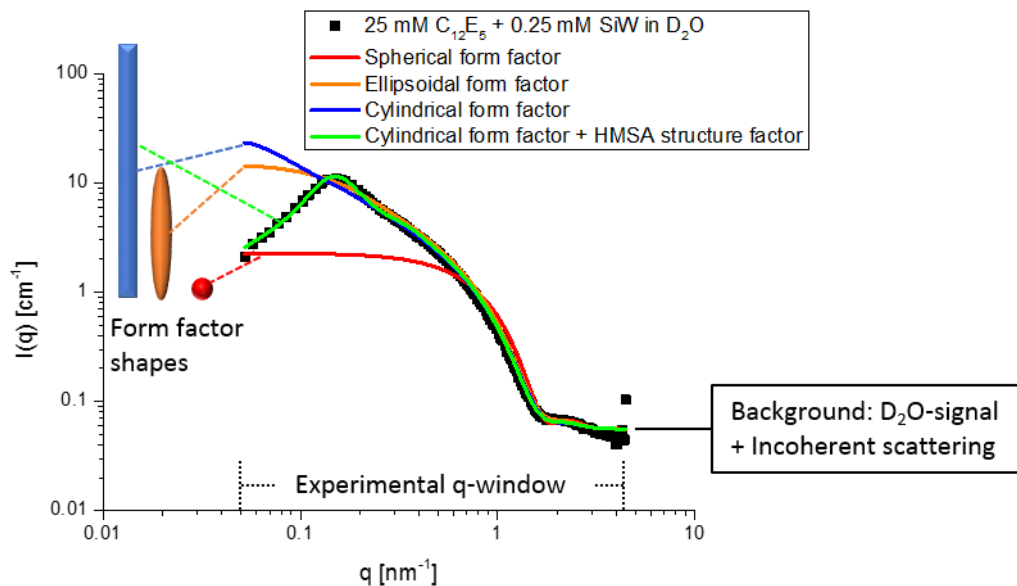


Figure 96: SANS-spectrum of 25 mM C<sub>12</sub>E<sub>5</sub> + 0.25 mM SiW in D<sub>2</sub>O and mathematical fits using spherical, ellipsoidal and cylindrical form factors, as indicated with the schematic bodies. The cylindrical form factor worked best to fit the high  $q$ -region at  $q > 0.3 \text{ nm}^{-1}$  and was thus used in combination with a HMSA structure factor.

The experimental spectrum was collected over the  $q$ -range  $0.05\text{--}5 \text{ nm}^{-1}$  to acquire the excess scattering of the micelles. At high  $q$ -values  $q > 2 \text{ nm}^{-1}$ , the background scattering, which contains the scattering of D<sub>2</sub>O as well as the  $q$ -independent incoherent scattering, swallows the signal of the C<sub>12</sub>E<sub>5</sub>-micelles and is accounted for by a constant background in the fits. Yet, a dampened oscillation is discernable at  $q = 2 \text{ nm}^{-1}$ . At  $q < 2 \text{ nm}^{-1}$ , the scattering intensity increases sharply with a slope that is characteristic for the scattering object's geometry. In this  $q$ -region, the form factor suitability can be assessed. The best fit was achieved with the form factor for a cylinder followed by a prolate ellipsoid, while the sphere produced the worst fit. The respective form factor inputs and resulting dimensions are shown in Table 29. Importantly, micelles in solution

are never perfectly monodisperse, which was accounted for in the form factors by adding a small polydispersity of  $PdI=0.1$  (Gaussian form) of the respective radii giving rise to a small size distribution around the listed values. Furthermore, at  $q=0.2 \text{ nm}^{-1}$  a structure factor peak is observed in the experimental spectrum, which arises from a charging of the  $C_{12}E_5$ -micelles by adsorption of SiW that leads to intermicellar repulsion and a long-range ordering of the micelles. Such a peak can be fitted by using a structure factor that models the electrostatic interaction between charged scattering objects such as the Hayter-Penfold rescaled mean spherical approximation (HMSA), which assumes charged spherical scatterers and a purely electrostatic interscatterer interaction in a dielectric medium. As the cylinder form factor provided the best fit, it was combined with the HMSA-structure factor. The input parameters are shown in Table 29 assuming a charged equivalent volume sphere of the cylinder, which resulted in the green curve in Figure 96. In the HMSA structure factor, the temperature, the dielectric constant of the medium and the salt-concentration are fixed by the experiment. Here, the salt concentration is set at an arbitrary low value as 0.25 mM SiW is expected to fully adsorb onto the micelles of 25 mM  $C_{12}E_5$  and no additional electrolyte was added.

Table 29: Best fit parameters for different form factors and for the cylinder form factor using a HMSA structure factor.

Form factor shape	Sphere	Ellipsoid	Cylinder	Cylinder
Background [ $\text{cm}^{-1}$ ]	0.055	0.055	0.055	0.055
$\Phi_{SANS}$	0.01	0.01	0.01	0.01
$\rho_{D2O}$ [ $10^{-6} \text{ \AA}^{-2}$ ]	6.3	6.3	6.3	6.3
$\rho_{C12E5}$ [ $10^{-6} \text{ \AA}^{-2}$ ]	0.13	0.13	0.13	0.13
radius [nm]	2.4	2.3 <sup>1</sup>	2.1	2.1
polar radius of ellipsoid [nm]	-	17	-	-
length of cylinder [nm]	-	-	66	66
Polydispersity of the radius	0.1	0.1	0.17	0.17
Structure factor	none	none	none	Hayter-MSA
Effective radius of sphere	-	-	-	equivalent volume sphere
Charge, $q_e$	-	-	-	30
Temperature [K]	-	-	-	298.15
Salt concentration [mol/L]	-	-	-	0.0001
Dielectric constant	-	-	-	81

<sup>1</sup> corresponds to the equatorial radius of the ellipsoid.

In conclusion, the investigated sample (25 mM  $C_{12}E_5$ +0.25 mM SiW in  $D_2O$ ) contains cylindrical micelles with a dry radius of 2.1 nm and a length of 66 nm. The radius of the cylinder here, is expectedly lower than the extended length of a  $C_{12}E_5$ -molecule ( $l=3 \text{ nm}$ ) because dry

micelles are assumed (no water between ethoxylate-groups). These non-ionic C<sub>12</sub>E<sub>5</sub> micelles are decorated with SiW-ions, which equips them with a substantial ionic charge (30 charges per micelle, therefore about 8 SiW<sub>12</sub>O<sub>40</sub><sup>4-</sup>-ions per micelle) that induces intermicellar repulsion and long-range ordering.

### 7.3.2. Worked fitting example SAXS (supported by SANS)

Many samples containing nano-ion decorated micelles were measured using both SANS and SAXS in this thesis. The treatment and fitting of the acquired spectra was performed using a global procedure, which is elaborated here on the example of the sample 60 mM C<sub>8</sub>E<sub>4</sub> + 10 mM HSiW. The corresponding SAXS and SANS spectrum along with the corresponding fits are shown in Figure 97. The procedure to acquire the SAXS-fit is elaborated in this section and provides a refinement of the previously proposed fitting procedure in Naskar et al.<sup>4</sup>

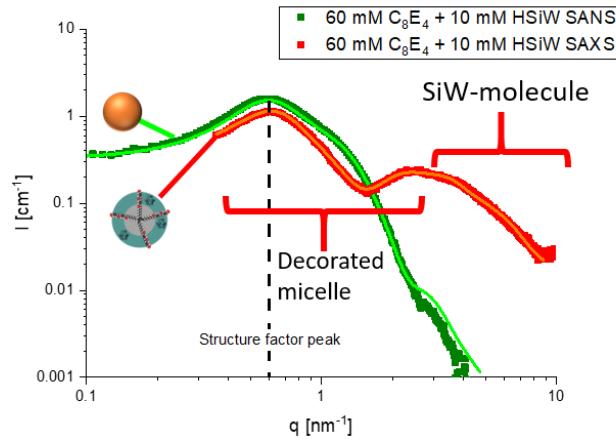


Figure 97: SAXS and SANS-spectrum of 60 mM C<sub>8</sub>E<sub>4</sub> + 10 mM HSiW (in D<sub>2</sub>O in SANS and in H<sub>2</sub>O in SAXS) with corresponding fits. The structure factor peak position is identical in both spectra showing the identity of the samples.

All SAXS-fits in this thesis were performed using SAS-Fit, in which the scattering intensity is generally expressed by

$$I(q) = n_i * v_i^2 * \Delta\rho^2 * P(q) * S(q) \quad (8.14)$$

With  $n_i$  being the number density of the scattering object,  $v_i$  the volume of the scattering object,  $\Delta\rho$  the scattering contrast,  $P(q)$  the form factor and  $S(q)$  the structure factor. In SAXS, the scattering contrast is the difference in electron density of the scattering object  $\rho_i$  and of the surrounding medium  $\rho_{medium}$ . The individual electron density of any scattering object  $i$  can be calculated by

$$\rho_i = \frac{\sum_j b_j}{v_i} * l_{Thomson} \quad (8.15)$$

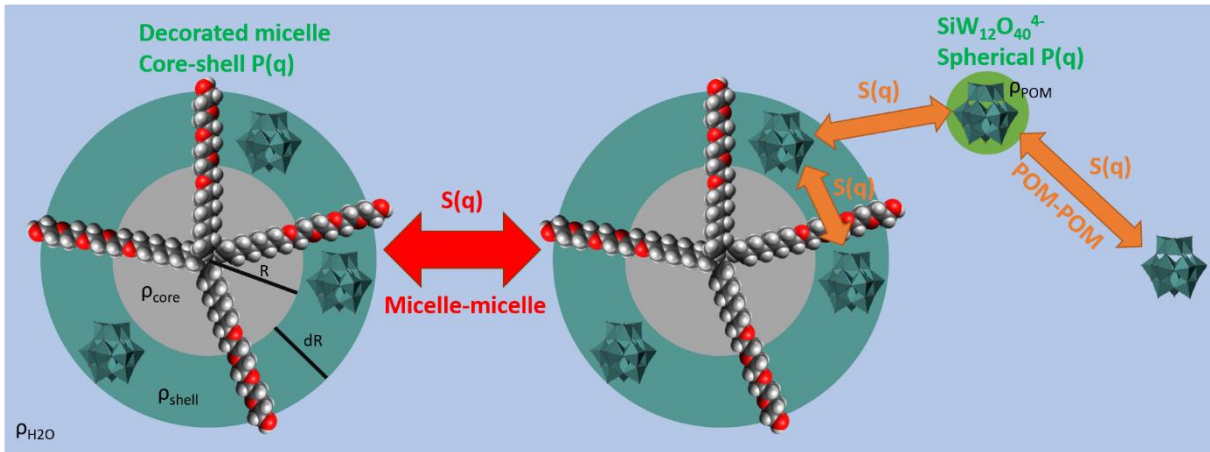
With  $b_j$  being the number of electrons in the  $j$ th atom,  $v_i$  the scattering objects volume and  $l_{Thomson}$  the Thomson length ( $l_{Thomson} = 2.82 \times 10^{-13}$  m).

Furthermore, for mixtures of scattering entities  $i$  the contrast  $\rho_M$  is described by

$$\rho_M = \sum_i \rho_i * \phi_i \quad (8.16)$$

With  $\phi_i$  being the volume fraction of the scattering entity  $i$  in the mixture.

For the sample of interest in this section, which contains  $\text{SiW}_{12}\text{O}_{40}$ -decorated  $\text{C}_8\text{E}_4$ -micelles, the SAXS-spectrum is a sum of several contributions and comprises the scattering of the individual  $\text{SiW}_{12}\text{O}_{40}^{4-}$  Keggin-POM and of the decorated micelles as is shown in Scheme 8. The individual POMs as well as the decorated micelles are charged and therefore repulsive causing them to mutually interact resulting in structure factors.



Scheme 8: Form and structure factor contributions in a typical SAXS-sample including decorated micelles and individual POM ( $\text{SiW}_{12}\text{O}_{40}^{4-}$ ) contributions.

To account for several different scattering objects, the individual contributions including POMs and micelles need to be summed by

$$I(q) = I_{POM} + I_{mic} + Bkg \quad (8.17)$$

With  $Bkg$  being the background scattering intensity.

For the sample of interest comprising the POMs and POM-decorated  $\text{C}_8\text{E}_4$ -micelles (core-shell, CS) the total scattering intensity is expressed as

$$I(q) = n_{POM} * v_{POM}^2 * \Delta\rho_{POM}^2 * P_{POM}(r, q) * S_{POM}(q, r_{HS}, \phi_{POM}) \\ + n_{mic} * P_{CS}(R, dR, \rho_{core}, \rho_{shell}, \rho_{medium}, q) * S_{mic}(q) + Bkg \quad (8.18)$$

Note that equation 8.14 is not valid for core-shell form factors, where  $\Delta\rho_{CS}$  and  $v_{CS}$  are comprised in  $P_{CS}$  as indicated in equation 8.18. The number density of POM  $n_{POM}$  is given by its concentration and the POMs dimensions including the POM-volume and its radius in the spherical form factor are known from literature and are therefore fixed parameters. Similarly, the contrast of the POM in solution is estimated against the surrounding medium (water) by equation 8.15 and is fixed as well. The structure factor  $S_{POM}(q)$  is a convoluted product of electrostatic interactions of POMs on the micelles and free POMs in solution, see Scheme 8.

This situation cannot be described by existing models and was approximated with a hard sphere structure factor. Furthermore, the scattering contribution of the micelles includes the number density of the micelles  $n_{mic}$ , which is fixed from the SANS-fit by

$$n_{mic} = \frac{\phi_{SANS}}{V_{mic\ SANS}} \quad (8.19)$$

with the volume fraction  $\phi_{SANS}$  of the micelles and  $V_{mic\ SANS}$  the volume of one micelle as attained from SANS-fitting (described in section 7.3.1). Likewise, the form factor used in SANS defines the shape of the core-shell scatterer (decorated micelle) in SAXS. For the sample of interest here (60 mM  $C_8E_4$  + 10 mM  $H_4SiW_{12}O_{40}$ ), SANS showed that micelles are spherical with a radius of 1.73 nm and therefore a spherical core-shell form factor is chosen for the fitting in SAXS. Furthermore, the structure factor in SANS corresponds to the micelle-micelle structure factor in SAXS and is therefore fixed.

Consequently, only the parameters that describe the core-shell structure need to be determined in the fitting procedure and amount to the radius of the inner core  $R$ , the thickness of the shell  $dR$  and the respective electron densities  $\rho_{core}$ ,  $\rho_{shell}$  and  $\rho_{H_2O}$ . As an approximation, the electronic density of the micellar core (containing only  $C_8E_4$  surfactant) is set equal to the electronic density of the surfactant and the electronic density of the dispersing medium ( $H_2O$ ) is fixed. Both electron densities were calculated by equation 8.15 and fixed in the fitting procedure. In turn, only the dimensions of the core-shell form factor and the electron density of the shell need to be determined by fitting. Figure 98 shows the individual contributions of the fit and Table 30 lists the acquired parameters.

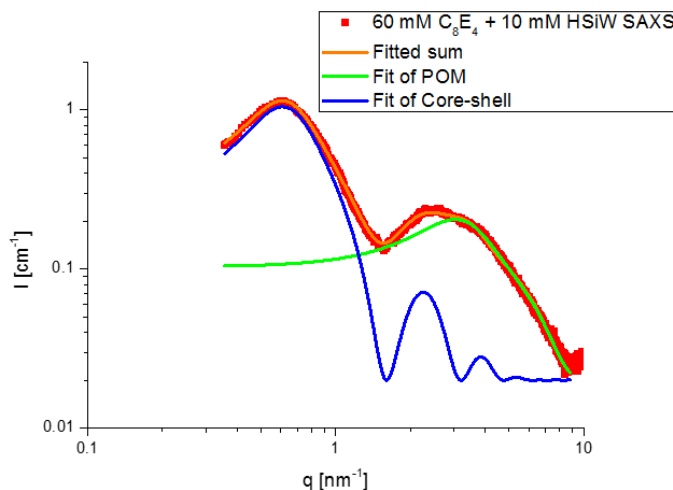


Figure 98: SAXS-spectrum of 60 mM  $C_8E_4$  + 10 mM  $H_4SiW_{12}O_{40}$  (HSiW). The fit of the spectrum (orange line) is comprised of two contributions, namely, the core-shell designating the SiW-decorated  $C_8E_4$ -micelles (blue line) and the individual POM-molecules (green line). A constant background of  $I=0.015\ cm^{-1}$  was used in all shown fits.

Table 30: Best fit parameters used for the sample 60 mM C<sub>8</sub>E<sub>4</sub>+10 mM H<sub>4</sub>SiW<sub>12</sub>O<sub>40</sub>. The parameters that are known from SANS are highlighted with a grey background and fixed parameters in SAXS-fitting are displayed with a yellow background.

Decorated micelle						POM							
$\rho_{mic}$	Spherical core-shell P(q)					Hayter-MSA S(q)			Sphere P(q)		Hard sphere S(q)		
	$\rho_{core}$	$\rho_{shell}$	$\rho_{H2O}$	R	dR	R <sub>HS</sub>	Charge, q <sub>e</sub>	[Salt]	$n_{POM}$	r	$\rho_{POM}$	$\Phi_{POM}$	R <sub>HS</sub>
[nm <sup>-3</sup> ]	*10 <sup>-6</sup> [Å <sup>-2</sup> ]	*10 <sup>-6</sup> [Å <sup>-2</sup> ]	*10 <sup>-6</sup> [Å <sup>-2</sup> ]	[nm]	[nm]	[nm]		[mol/l]	[nm <sup>-3</sup> ]	[nm]	*10 <sup>-6</sup> [Å <sup>-2</sup> ]		[nm]
0.007	9.4	12.8	9.4	1.46	0.92	1.8	20	0.006	0.006	0.43	74.9	0.141	0.86

The shell of the decorated micelle is a mixture of the ethoxylated surfactant head of C<sub>8</sub>E<sub>4</sub>, of hydration water and of adsorbed POM. The electron density of the shell is therefore described using equation 8.16 by:

$$\rho_{shell} = \phi_{POM \text{ in shell}} * \rho_{POMs} + \phi_{H2O \text{ in shell}} * \rho_{H2O} + \phi_{EO \text{ in shell}} * \rho_{EO} \quad (8.20)$$

$$\phi_{POM \text{ in shell}} = \frac{N_{POMs \text{ in shell}} * V_{POM}}{V_{shell}} \quad (8.21)$$

$$\phi_{H2O \text{ in shell}} = \frac{N_{H2O \text{ in shell}} * V_{H2O}}{V_{shell}} \quad (8.22)$$

$$\phi_{EO \text{ in shell}} = \frac{N_{EO \text{ in shell}} * V_{EO}}{V_{shell}} \quad (8.23)$$

with the corresponding volume fractions in the shell  $\phi_{POM \text{ in shell}}$ ,  $\phi_{H2O \text{ in shell}}$  and  $\phi_{EO \text{ in shell}}$ . The contrast of the shell is largely dominated by the Keggin-POM SiW<sub>12</sub>O<sub>40</sub><sup>4-</sup> as its electron density strongly exceeds the one of C<sub>8</sub>E<sub>4</sub> (or its surfactant head E<sub>4</sub>) and of H<sub>2</sub>O, see Table 31. Additionally, C<sub>8</sub>E<sub>4</sub> and H<sub>2</sub>O have a very similar electron density resulting in negligible scattering of bare C<sub>8</sub>E<sub>4</sub>-micelles in H<sub>2</sub>O.

Table 31: Electronic densities and molecular volumes of H<sub>2</sub>O, C<sub>8</sub>E<sub>4</sub>, E<sub>4</sub>, C<sub>12</sub>E<sub>5</sub>, E<sub>5</sub>, SiW<sub>12</sub>O<sub>40</sub><sup>4-</sup> and B<sub>12</sub>I<sub>12</sub><sup>2-</sup>.

	H <sub>2</sub> O	C <sub>8</sub> E <sub>4</sub>	E <sub>4</sub>	C <sub>12</sub> E <sub>5</sub>	E <sub>5</sub>	SiW <sub>12</sub> O <sub>40</sub> <sup>4-</sup>	B <sub>12</sub> I <sub>12</sub> <sup>2-</sup>	B <sub>12</sub> Br <sub>12</sub> <sup>2-</sup>
Molecular volume [nm <sup>3</sup> ]	0.03 <sup>1</sup>	0.525 <sup>1</sup>	0.287 <sup>1</sup>	0.701 <sup>1</sup>	0.352 <sup>1</sup>	0.46 <sup>2</sup>	0.52 <sup>3</sup>	0.42 <sup>3</sup>
Number of electrons	10	170	106	226	130	1226	696	476
$\rho$ [* 10 <sup>-6</sup> Å <sup>-2</sup> ]	9.43	9.13	10.4	7.57	10.4	74.9	37.5	31.9

<sup>1</sup> calculated from the respective pure liquid densities

<sup>2</sup> taken from Buchecker et al.<sup>92</sup>

<sup>3</sup> taken from Nau et al.<sup>65</sup>

Owing to the similarity in electron density of C<sub>8</sub>E<sub>4</sub> and H<sub>2</sub>O, it is possible to make an approximation and simplify equation 8.20 in order to consider only water and the POM neglecting the term of the ethoxylated head.

$$\rho_{shell} = \phi_{POM \text{ in shell}} * \rho_{POMs} + \phi_{H2O \text{ in shell}} * \rho_{H2O} \quad (8.24)$$

$$\phi_{POM \text{ in shell}} = 1 - \phi_{H_2O \text{ in shell}} \quad (8.25)$$

Using this simplification, the number of POMs per micelle (in the shell)  $N_{POMs \text{ in shell}}$  can be calculated from the contrast of the fit by combination of equations 8.24, 8.25 and 8.21:

$$\frac{\rho_{shell} - \rho_{H_2O}}{\rho_{POM} - \rho_{H_2O}} * \frac{V_{shell}}{V_{POM}} = N_{POMs \text{ in shell}} \quad (8.26)$$

By calculating the ratio of the number of POMs per micelle over the maximally possible number of POMs per micelle  $M$ , the adsorption ratio  $R$  can be calculated.

$$M = \frac{n_{POM}}{n_{mic}} \quad (8.27)$$

$$R = \frac{N_{POMs \text{ in shell}}}{M} \quad (8.28)$$

Where  $n_{POM}$  is the number density of POM in solution, and  $n_{mic}$  is the number density of micelles in solution acquired from SANS, see equation 8.19.

For the present sample of 60 mM  $C_8E_4$ +10 mM  $H_4SiW_{12}O_{40}$ , application of this procedure results in a number of 4.9 POMs ( $SiW_{12}O_{40}^{4-}$ ) per micelle amounting to an adsorption ratio of 0.59 (59% of SiW is on the micelles and 41% is dispersed in the bulk). Using this adsorption ratio  $R$ , adsorption constants were calculated in section 2.3.2 and the thermodynamics of the adsorption process of  $SiW_{12}O_{40}$  on ethoxylated micelles was determined in section 2.3.4.



### 7.3.3. List of used form and structure factors

The following section lists the used form factors for the fits in this thesis. The scattering intensity is expressed by:

$$I(q) = n * J(q) * S(q) \quad (8.29)$$

with the number density of the scattering object,  $J(q)$  the scattering intensity of one sole scattering object,  $S(q)$  the structure factor.  $J(q)$  is generally connected to the form factor  $P(q)$  by

$$J(q) = v^2 * \Delta\rho^2 * P(q) \quad (8.30)$$

with  $v$  being the volume of the scattering object and  $\Delta\rho$  the scattering contrast. The following listing is extracted from the SASView and SASFit libraries.<sup>217,218</sup>

#### Spherical Form factor:

$$J_{sphere}(q, R) = K_{sphere}^2(q, R) \quad (8.31)$$

$$K_{sphere}(q, R, \Delta\rho) = \frac{4}{3} * \pi * R^3 * \Delta\rho * 3 \frac{\sin(qR) - QR\cos(qR)}{(QR)^3} \quad (8.32)$$

with  $R$  the radius of the sphere.

#### Spherical core-shell form factor:

$$J_{shell}(q, R, dR, \Delta\rho_{core}, \Delta\rho_{shell}) = [K_1(q, R + dR, \Delta\rho_{shell}) - K_2(q, R, \Delta\rho_{shell} - \Delta\rho_{core})] \quad (8.33)$$

$$K_i(q, R, \Delta\rho) = \frac{4}{3} * \pi * R^3 * \Delta\rho * 3 \frac{\sin(qR) - QR\cos(qR)}{(QR)^3} \quad (8.34)$$

with  $R$  the core radius and  $dR$  the shell thickness.

#### Cylindrical form factor:

$$J_{cyl}(q, \alpha) = \int_0^{\frac{\pi}{2}} K_{cyl}(q, \alpha, L, R)^2 * \sin(\alpha) d\alpha \quad (8.35)$$

$$K_{cyl}(q, \alpha, L, R) = \Delta\rho * V * 2 \frac{\sin\left(\frac{1}{2}qL\cos(\alpha)\right)}{\frac{1}{2}qL\cos(\alpha)} * \frac{B_1(qR\sin\alpha)}{qR\sin\alpha} \quad (8.36)$$

with  $\alpha$  the angle between the axis of the cylinder and  $q$ ,  $V$  the volume of the cylinder and  $B_1$  the first order Bessel function.

Ellipsoidal form factor:

$$J_{\text{ellipsoid}}(q, R_p, R_e, \Delta\rho, \alpha) = \int_0^{\frac{\pi}{2}} K_{\text{ellipsoid}}^2 * \sin\alpha \, d\alpha \quad (8.37)$$

$$K_{\text{ellipsoid}}(q, r) = \Delta\rho * V * 3 \frac{\sin qr - qr \cos(qr)}{(qr)^3} \quad (8.38)$$

for

$$r(R_p, R_e, \alpha) = [R_e^2 \sin^2 \alpha + R_p^2 \cos^2 \alpha]^{\frac{1}{2}} \quad (8.39)$$

with  $\alpha$  the angle between the axis of the ellipsoid and  $q$ ,  $R_p$  being the polar radius and  $R_e$  being the equatorial radius of the ellipsoid.

Ellipsoidal core-shell form factor

$$J_{CS-\text{ellip}}(q, R_p, R_e, \Delta\rho, \alpha) = \int_0^1 K_{CS-\text{ellip}}^2 \, d\mu \quad (8.40)$$

$$K_{CS-\text{ellip}} = (\eta_{\text{core}} - \eta_{\text{shell}}) * V_c \frac{3j_1(x_c)}{x_c} + (\eta_{\text{shell}} - \eta_{\text{solvent}}) V_{\text{total}} \frac{3j_1(x_{\text{total}})}{x_{\text{total}}} \quad (8.41)$$

$$j_1(x) = \frac{\sin(x) - x \cos(x)}{x^2} \quad (8.42)$$

$$x_c = q \sqrt{R_p^2 \mu^2 + R_e^2 (1 - \mu^2)} \quad (8.43)$$

$$x_{\text{total}} = q \sqrt{(R_p + t)^2 \mu^2 + (R_e + t)^2 (1 - \mu^2)} \quad (8.44)$$

with  $\mu = \sin\alpha$  and  $d\mu = \cos\alpha \, d\alpha$ , the volume of the ellipsoidal core  $V_c$ , the total ellipsoid volume  $V_{\text{total}}$  with corresponding polar radius  $R_p$ , equatorial radius  $R_e$  and thickness of the shell  $t$ .

Further, flexible cylinder form factors were used as well as hard sphere and Hayter-MSA structure factors. For information concerning these models the reader is referred to the SASView and SASFit libraries and references therein.<sup>217,218</sup>

### 7.3.4. SAXS-Experimental

SAXS measurements using Mo radiation ( $\lambda=0.071$  nm) were performed at the ICSM on a bench built by XENOCES. The scattered beam was recorded using a large online scanner detector (diameter: 345 mm, from MAR Research). A large  $q$ -range (0.2 to  $40 \text{ nm}^{-1}$ ) was covered with an off-center detection. The collimation was applied using a  $12:\infty$  multilayer Xenocs mirror (for Mo radiation) coupled to two sets of scatterless FORVIS slits providing a  $0.8 \times 0.8$  mm X-ray beam at the sample position. Pre-analysis of data was performed using FIT2D software. The scattered intensities are expressed versus the magnitude of scattering vector  $q = [(4 \pi) / \lambda] \sin(\theta / 2)$ , where  $\lambda$  is the wavelength of incident radiation and  $\theta$  the scattering angle. 2 mm quartz capillaries were used as sample containers, which were set into a metal sample holder for measurements at ambient temperature or into a thermostated furnace for measurements with temperature regulation. Experimental resolution was  $\Delta q/q = 0.05$ . Silver behenate in a sealed capillary was used as the scattering vector calibration standard. The concentration of the non-ionic surfactant and of the nano-ion were chosen to get a reasonable signal by the laboratory SAXS camera.

In order to transfer the SAXS-spectra to absolute scale, usual corrections for background (empty cell and detector noise) subtractions and intensity normalization using a high-density polyethylene film standard were applied by equation 8.45.

$$I_{absolute}(q) = \frac{1}{d_s} * \left( \frac{\frac{I_s(q) - B_{el}}{T_s}}{\frac{T_{EB}}{t_s}} - \frac{\frac{I_{EC}(q) - B_{el}}{T_{EC}}}{\frac{T_{EB}}{t_{EC}}} \right) * NF \quad (8.45)$$

With the sample thickness  $d_s$ , the scattered intensity of the sample  $I_s$  and of the empty cell  $I_{EC}$ , the constant electronic background noise  $B_{el}$ , the transmitted intensity at  $q=0$  of the sample  $T_s$ , of the empty cell  $T_{EC}$  and the empty beam  $T_{EB}$ , the corresponding acquisition times for the scattering of the sample  $t_s$  and of the empty cell  $t_{EC}$  and the normalization factor  $NF$ .

### 7.3.5. SANS-Experimental ILL

SANS-measurements were performed at beamline D33 at the Institut Laue-Langevin (ILL) in Grenoble from July 1 to July 4, 2019.

Time of flight small angle neutron scattering (TOF-SANS) experiments were performed on foams on the D33 spectrometer at Institut Laue-Langevin (ILL) in Grenoble from July 1 to July 4, 2019. The four-chopper system allows to probe the sample with a multi-wavelength neutron beam from 2 up to 20 Å. The sample to “back” detector distance was set to 7 m and the second “front” detector was set at 3 m. Acquisition time was fixed at 300 s. The collimation length was set to 7.8 m and the beam size at the sample position was fixed at 12 mm in diameter with a source size of the neutron guide dimension of 30 mm x 30 mm. Treatment of the time-of-flight spectra and eventual azimuthal averaging of the 2D-data was made using the GRASP software package. In this thesis, only the scattering from the “back” detector is presented as it contains all the exploitable information about the sample, while the front detector merely showed the constant inelastic and background scattering. The SANS-curves were normalized with an arbitrary constant sample thickness of 0.1 cm.

A glass column with three quartz windows was used as sample container. This column was fixed at the same exact position for every sample ensuring reproducibility of the illumination by the neutron beam and of the  $q$ -range. After the background was established and as normalization references were already measured prior, the first sample solution (60 mL) was poured into the column. The foam was then generated by sparging air at a flow of 5 ml/min through the sintered glass plate at the bottom of the column. The measurement protocol started when the foam had filled the first window and comprised two consecutive scans per window (5 minutes per scan), followed by several rounds of scanning the three windows one after the other, followed by a transmission measurement at all three windows. The acquisition was discontinued when the curves for e.g. the 2<sup>nd</sup> or 3<sup>rd</sup> windows overlapped indicating the quasi-stationary state of the foam. The solution was then taken out of the column. If necessary, the empty column was rinsed thoroughly with D<sub>2</sub>O and the next measurement could begin. Furthermore, in order to check the dynamics of the foam an injection measurement was performed, i.e. a volume of HSiW-solution was injected into an already foaming solution of surfactant in D<sub>2</sub>O with a quasi-stationary foam on top. The measurement was performed at the second window. A spectrum was acquired all 5 minutes in order to probe the foam equilibration kinetics.

Additionally, liquid samples were measured using two different measurement modes, i.e. monochromatic ( $\lambda_{\text{neutron}}=0.6$  nm) and time-of-flight (TOF) mode. Detection was done at 2 m and 5 m during the monochromatic and at 7 m and 3 m during TOF mode. Rectangular quartz cuvettes from Helma with thicknesses of 1 mm or 2 mm were used as sample containers. A thermostatic sample rack served as sample holder. Acquisition times were set to 5-20 minutes taking into consideration sample thickness and contrast. The spectra were treated and normalized using the available software on site.

### 7.3.6. SANS-Experimental MLZ

SANS-measurements on liquid samples were performed on beamline SANS-1 at the Heinz Meier-Leibniz Zentrum (MLZ) in Garching, Munich from January 21 to January 22, 2020. Round quartz cuvettes with caps from Helma with thicknesses of 1 or 2 mm were used as sample containers. A thermostated sample rack served as sample holder. The samples were illuminated with a monochromatic neutron beam with a wavelength of 4.5 nm. The scattered beam was measured at sample-detector distances of 2 m and 16 m with acquisition times of 5 min and 15 min, respectively. In between measurement series, the cuvettes were cleaned with water and ethanol. The acquired raw 2D-data were reduced, normalized with respect to the incoherent scattering of H<sub>2</sub>O, radially averaged and merged with BerSANS software.

## 7.4. Dynamic Light Scattering

Dynamic light scattering (DLS) is a widely used technique to investigate the size of nanoparticles. DLS uses visible light emitted by a laser to probe the sample. For visible light, the wavelength  $\lambda$  within a medium, for instance in a liquid sample, differs from the wavelength in the vacuum  $\lambda_0$ , as accounted for by the refractive index  $n = \frac{\lambda}{\lambda_0}$ , which must be respected when considering the length of the scattering vector  $q$ .

$$q = \frac{4\pi n}{\lambda_0} * \sin(\theta) \quad (8.46)$$

In contrast to SANS and SAXS, which are static methods that measure the angular dependence of the time-averaged scattering intensity  $I(q)$ , DLS measures the time-dependent scattered intensity  $I(t)$  at a fixed detector angle.

$$I(t) = I_s \sum_{j,k=1}^N e^{iq(t) \cdot r_{jk}(t)} \quad (8.47)$$

with  $I_s$  denominating the total mean scattered intensity. Due to Brownian motion, the scattering objects in solution move about randomly, which gives rise to changes in the interscatterer distances and, therefore, causes time-dependent shifts in the phase difference  $\Delta\varphi(t) = \mathbf{q}(t) \cdot \mathbf{r}(t)$  of the scattered waves. This results in intensity fluctuations that depend on the diffusion speed of the scattering objects. Generally, these fluctuations are mathematically converted into the intensity auto-correlation function  $G_2(\tau)$ , which quantifies the correlation between the intensity at time  $t$  with the intensity at a time  $t+\tau$ . The increment time  $\tau$  is called the lag time.

$$G_2(\tau) = \lim_{T \rightarrow \infty} \frac{1}{T} \int_0^T I(t)I(t + \tau)dt \quad (8.48)$$

Figure 99 shows a monomodal autocorrelation function, which represents the DLS-output characteristic of a sample containing only one defined scattering species with one specific diffusion coefficient. Autocorrelation functions with more than one mode are observed for samples that contain more than one scattering species, which, however, is irrelevant for this thesis. In the following, the analysis of monomodal autocorrelation functions is described. For a detailed derivation of the underlying physics, see the appended references.<sup>214,219</sup>

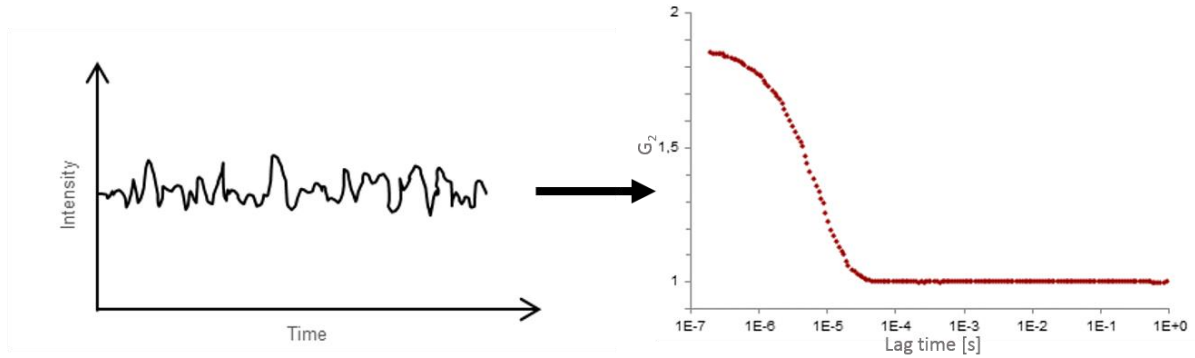


Figure 99: Intensity fluctuations in a DLS-experiment and the corresponding autocorrelation function. Note that in this thesis not  $G_2$ , but rather  $G_2-1$  is used as the y-axis in all presented autocorrelation functions.

To quantify the diffusion coefficient of the scattering objects in solution, the autocorrelation functions must be fitted. This is done with the general form of a monomodal function.

$$f(\tau) = a_0 + a_1 * e^{-2a_2*\tau} \quad (8.49)$$

Here,  $a_0$  is a constant baseline and  $a_1$  is a factor that depends on the experimental geometry. The fitting parameter for the exponential decay  $a_2$  is related to the scattering vector  $q$  and the diffusion coefficient  $D$ .

$$a_2 = D * q^2 \quad (8.50)$$

As  $q$  can be directly calculated from the experimental configuration (wavelength of the laser and the acquisition angle of the detector) and the refractive index of the sample, the diffusion coefficient  $D$  can be determined.

Under the assumption that the scattering objects are of spherical shape the Stokes-Einstein equation can be used to determine the hydrodynamic radius  $r_H$  of the scattering objects.

$$D = \frac{k_B T}{6\pi\eta * r_H} \quad (8.51)$$

with  $k_B$  being the Boltzmann constant,  $T$  the temperature and  $\eta$  the dynamic viscosity of the sample. Notably, the resulting hydrodynamic radius of an object in solution is always larger than its “real” radius because hydration water is dragged along, which decreases the diffusion speed and in turn increases the corresponding hydrodynamic radius.

### 7.4.1. DLS-Experimental

All measurements were performed using a Zetasizer Nano ZS from Malvern Instruments. The samples were illuminated with a 632.8 nm laser and detection was done in backscattering position at an angle of 173°. Disposable plastic cuvettes or glass cuvettes with plastic cap served as sample containers. Once set into the measurement chamber the samples were equilibrated for 300 s at the set temperature before acquisition would start. Count rates and corresponding autocorrelation functions were collected in triplicates for each sample where one measurement consisted of 10 runs of 10 seconds each, which would then be automatically averaged. The autocorrelation functions were fitted as outlined above yielding the corresponding hydrodynamic diameters. Solution densities were measured with a densitometer DSA 5000 from Anton Paar, dynamic viscosities were measured with a rolling-ball viscometer AMVn from Anton Paar and refractive indices were measured with a refractometer RX 7000 $\alpha$  from Atago.



## 7.5. FOAMSCAN

The FOAMSCAN setup from Teclis Scientific was used herein to study foams over their lifetime. The device generates a foam in a round bottom glass column (width=3.5 cm and height=27.5 cm) by sparging air through a microporous plate. Two cameras then record the foam, one focused on the foam column and one zoomed in on one of four prisms on the glass column that lay bare the microscopic foam structure in a plane, see Figure 100. Captured photos of the foam column are analyzed live according to the grey levels tracing the evolution of the foam height (and volume) over time. The photos of the foam bubbles need to be treated by the experimenter after measurement to ensure good sharpness and contrast in image analysis. This is done by feeding the photos into CSA (cell size analysis)-software, which sets the size scale by a pre-measured size standard and determines bubble number and size and corresponding polydispersity by black/white contrast.

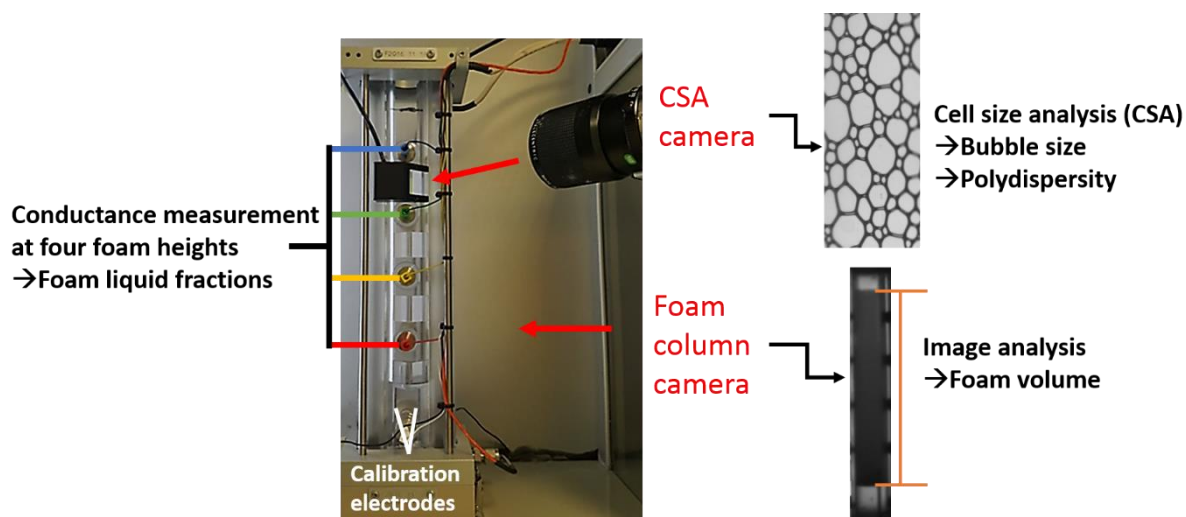


Figure 100: Overview of the foam acquisition modes in the FOAMSCAN setup involving conductometry at four different foam heights and two cameras respectively recording overall foam height and bubble size.

Additionally, the generated foams are measured continuously by conductance electrodes at four different foam heights that allow for a determination of the corresponding liquid fractions over time. For this purpose, the horizontal electrodes need to be calibrated for each foam (the dispersed liquid) prior to measurement, which is done via the vertical electrodes that are immersed in the foaming solution at the bottom of the column.

The liquid fraction  $\varepsilon$  at a specific foam height can then be calculated for any foam regardless of its wetness by the empirical relation

$$\frac{\sigma_{foam}}{\sigma_{liquid}} = \frac{2\varepsilon + 24\varepsilon^2}{6 + 29\varepsilon - 9\varepsilon^2} \quad (8.52)$$

with  $\sigma_{foam}$  and  $\sigma_{liquid}$  being the conductivities of the foam and the foaming solution.<sup>220</sup>

### 7.5.1. FOAMSCAN Experimental

Foam measurements were performed on a FOAMSCAN from Teclis Scientific. The size scale of the CSA-camera was calibrated using a metal ball ( $r=2.499$  mm) suspended in front of the captured window. Then, 50 mL of the foaming solution were injected into the glass column in 10 ml-steps via the inlet at the bottom. After each injection step, the conductance was measured with the calibration electrodes resulting in a linear calibration curve (conductance vs volume liquid). The valve to the inlet was then closed and the measurement was initiated using the FOAMSCAN software. Foam generation was done using a constant gas flow of 50 mL/min through a microporous plate with pore sizes of 16-40  $\mu\text{m}$ . Once the foam had filled completely the glass column, the gas flow was stopped, leaving the foam under free drainage conditions. The foam was recorded continuously by two cameras and measured conductometrically to determine bubble size and polydispersity, foam volume and liquid drainage. Importantly, the opening on top of the glass column was covered with a lid to prohibit air currents from affecting foam collapse. In order to obtain standard deviations of the individual measurement mode each foam was generated from a fresh foaming solution and recorded thrice for 200 minutes. Once the experiment was stopped, the collapsed foam and its foaming solution were sucked out of the column with a vacuum pump and discarded. Before the next measurement, the glass column was rinsed generously with MilliQ-water to avoid pollutant effects on the conductance measurements.

## 7.6. NMR-Experimental

$^1\text{H}$ -NMR spectra were measured at room temperature using a Bruker Avance 400 (400 MHz for  $^1\text{H}$ ) NMR spectrometer. Chemical shifts are reported in  $\delta$ -scale as parts per million [ppm] relative to the solvent residual peak ( $\text{D}_2\text{O}$ ) as the internal standard.

## 7.7. Surface tension experimental

Surface tension measurements were performed on a drop shape analyzer DSA 100 from Krüss. Surface tensions were measured on emergent air bubbles submerged in aqueous samples at room temperature. Corresponding solution densities were determined at 20°C with a densitometer DSA 5000 from Anton Paar. For the samples containing just nano-ion in water, reaching surface tension equilibrium took up to several hours. To allow for such long-time experiments, air bubbles had to be produced with minimal volumes (about 1  $\mu\text{L}$ ) in order to avoid bubble detachment from the capillary.



# Bibliography

1. Gibb, B. C. Abiogenesis and the reverse Hofmeister effect. *Nat. Chem.* **10**, 797–798 (2018).
2. Van Der Vegt, N. F. A., Haldrup, K., Roke, S., Zheng, J., Lund, M. & Bakker, H. J. Water-Mediated Ion Pairing: Occurrence and Relevance. *Chem. Rev.* **116**, 7626–7641 (2016).
3. Assaf, K. I., Ural, M. S., Pan, F., Georgiev, T., Simova, S., Rissanen, K., Gabel, D. & Nau, W. M. Water structure recovery in chaotropic anion recognition: High-affinity binding of dodecaborate clusters to  $\gamma$ -cyclodextrin. *Angew. Chemie Int. Ed.* **54**, 6852–6856 (2015).
4. Naskar, B., Diat, O., Nardello-Rataj, V. & Bauduin, P. Nanometer-Size Polyoxometalate Anions Adsorb Strongly on Neutral Soft Surfaces. *J. Phys. Chem. C* **119**, 20985–20992 (2015).
5. Bastos-González, D., Pérez-Fuentes, L., Drummond, C. & Faraudo, J. Ions at interfaces: The central role of hydration and hydrophobicity. *Curr. Opin. Colloid Interface Sci.* **23**, 19–28 (2016).
6. Hofmeister, F. Zur Lehre von der Wirkung der Salze - Dritte Mitteilung. *Arch. für Exp. Pathol. und Pharmakologie* **25**, 1–30 (1888).
7. Kunz, W., Henle, J. & Ninham, B. W. ‘Zur Lehre von der Wirkung der Salze’ (about the science of the effect of salts): Franz Hofmeister’s historical papers. *Curr. Opin. Colloid Interface Sci.* **9**, 19–37 (2004).
8. Boström, M., Kunz, W. & Ninham, B. W. Hofmeister effects in surface tension of aqueous electrolyte solution. *Langmuir* **21**, 2619–2623 (2005).
9. Jungwirth, P. & Tobias, D. J. Specific ion effects at the air/water interface. *Chem. Rev.* **106**, 1259–1281 (2006).
10. Pegram, L. M. & Record, M. T. Hofmeister Salt Effects on Surface Tension Arise from Partitioning of Anions and Cations between Bulk Water and the Air–Water Interface. *J. Phys. Chem. B* **111**, 5411–5417 (2007).
11. Kunz, W. *Specific ion effects*. (World Scientific, 2009).
12. Leontidis, E. Hofmeister anion effects on surfactant self-assembly and the formation of mesoporous solids. *Curr. Opin. Colloid Interface Sci.* **7**, 81–91 (2002).
13. Taraszewska, J. & Wójcik, J. Complexation of inorganic anions by  $\beta$ -cyclodextrin studied by polarography and  $^1\text{H}$  NMR. *Supramol. Chem.* **2**, 337–343 (1993).

14. Peula-García, J. M., Ortega-Vinuesa, J. L. & Bastos-González, D. Inversion of hofmeister series by changing the surface of colloidal particles from hydrophobic to hydrophilic. *J. Phys. Chem. C* **114**, 11133–11139 (2010).
15. Lo Nostro, P., Ninham, B. W., Lo Nostro, A., Pesavento, G., Fratoni, L. & Baglioni, P. Specific ion effects on the growth rates of *Staphylococcus aureus* and *Pseudomonas aeruginosa*. *Phys. Biol.* **2**, 1–7 (2005).
16. Craig, V. S. J., Ninham, B. W. & Pashley, R. M. Effect of electrolytes on bubble coalescence. *Nature* **364**, 317–319 (1993).
17. Craig, V. S. J., Ninham, B. W. & Pashley, R. M. The effect of electrolytes on bubble coalescence in water. *J. Phys. Chem.* **97**, 10192–10197 (1993).
18. Mazzini, V., Liu, G. & Craig, V. S. J. Probing the Hofmeister series beyond water: Specific-ion effects in non-aqueous solvents. *J. Chem. Phys.* **148**, (2018).
19. Schwierz, N., Horinek, D., Sivan, U. & Netz, R. R. Reversed Hofmeister series—The rule rather than the exception. *Curr. Opin. Colloid Interface Sci.* **23**, 10–18 (2016).
20. Schwierz, N., Horinek, D. & Netz, R. R. Reversed anionic hofmeister series: The interplay of surface charge and surface polarity. *Langmuir* **26**, 7370–7379 (2010).
21. Kunz, W., Lo Nostro, P. & Ninham, B. W. The present state of affairs with Hofmeister effects. *Curr. Opin. Colloid Interface Sci.* **9**, 1–18 (2004).
22. Omta, A. W., Kropman, M. F., Woutersen, S. & Bakker, H. J. Influence of ions on the hydrogen-bond structure in liquid water. *J. Chem. Phys.* **119**, 12457–12461 (2003).
23. Collins, K. D., Neilson, G. W. & Enderby, J. E. Ions in water: Characterizing the forces that control chemical processes and biological structure. *Biophys. Chem.* **128**, 95–104 (2007).
24. Krestov, G. A. *Thermodynamics of solvation*. (Ellis Horwood, 1991).
25. Marcus, Y. Effect of ions on the structure of water: Structure making and breaking. *Chem. Rev.* **109**, 1346–1370 (2009).
26. Stirnemann, G., Wernersson, E., Jungwirth, P. & Laage, D. Mechanisms of acceleration and retardation of water dynamics by ions. *J. Am. Chem. Soc.* **135**, 11824–11831 (2013).
27. Yang, L., Fan, Y. & Gao, Y. Q. Differences of cations and anions: Their hydration, surface adsorption, and impact on water dynamics. *J. Phys. Chem. B* **115**, 12456–12465 (2011).
28. Collins, K. D. The behavior of ions in water is controlled by their water affinity. *Q. Rev. Biophys.* **52**, e11 (2019).

29. Okur, H. I., Hladílková, J., Rembert, K. B., Cho, Y., Heyda, J., Dzubiella, J., Cremer, P. S. & Jungwirth, P. Beyond the Hofmeister Series: Ion-Specific Effects on Proteins and Their Biological Functions. *J. Phys. Chem. B* **121**, 1997–2014 (2017).
30. Jungwirth, P. & Cremer, P. S. Beyond hofmeister. *Nat. Chem.* **6**, 261–263 (2014).
31. Collins, K. D. Ions from the Hofmeister series and osmolytes: Effects on proteins in solution and in the crystallization process. *Methods* **34**, 300–311 (2004).
32. Vlachy, N., Jagoda-Cwiklik, B., Vácha, R., Touraud, D., Jungwirth, P. & Kunz, W. Hofmeister series and specific interactions of charged headgroups with aqueous ions. *Adv. Colloid Interface Sci.* **146**, 42–47 (2009).
33. Kunz, W. Specific ion effects in colloidal and biological systems. *Curr. Opin. Colloid Interface Sci.* **15**, 34–39 (2010).
34. Leontidis, E. Chaotropic salts interacting with soft matter: Beyond the lyotropic series. *Curr. Opin. Colloid Interface Sci.* **23**, 100–109 (2016).
35. Leontidis, E., Christoforou, M., Georgiou, C. & Delclos, T. The ion-lipid battle for hydration water and interfacial sites at soft-matter interfaces. *Curr. Opin. Colloid Interface Sci.* **19**, 2–8 (2014).
36. Assaf, K. I. & Nau, W. M. The Chaotropic Effect as an Assembly Motif in Chemistry. *Angew. Chemie Int. Ed.* **57**, 13968–13981 (2018).
37. Matějčíček, P. Erratic ions: self-assembly and coassembly of ions of nanometer size and of irregular structure. *Curr. Opin. Colloid Interface Sci.* **45**, 97–107 (2020).
38. Bijelic, A. & Rompel, A. The use of polyoxometalates in protein crystallography - An attempt to widen a well-known bottleneck. *Coord. Chem. Rev.* **299**, 22–38 (2015).
39. Botar, B., Ellern, A. & Kögerler, P. Mapping the formation areas of giant molybdenum blue clusters: A spectroscopic study. *Dalt. Trans.* **41**, 8951–8959 (2012).
40. Falaise, C., Moussawi, M. A., Floquet, S., Abramov, P. A., Sokolov, M. N., Haouas, M. & Cadot, E. Probing Dynamic Library of Metal-Oxo Building Blocks with  $\gamma$ -Cyclodextrin. *J. Am. Chem. Soc.* **140**, 11198–11201 (2018).
41. Stock, A. Hydrides of Boron and Silicon. *J. Phys. Chem.* **38**, 714–715 (2002).
42. Stock, A. & Massenez, C. Boron hydrides. *Berichte* **45**, 3539–3568 (1913).
43. King, R. B. Three-dimensional aromaticity in polyhedral boranes and related molecules. *Chem. Rev.* **101**, 1119–1152 (2001).
44. Grimes, R. N. Boron clusters come of age. *J. Chem. Educ.* **81**, 657–672 (2004).
45. Plešek, J. Potential Applications of the Boron Cluster Compounds. *Chem. Rev.* **92**, 269–278 (1992).

46. Axtell, J. C., Saleh, L. M. A., Qian, E. A., Wixtrom, A. I. & Spokoyny, A. M. Synthesis and Applications of Perfunctionalized Boron Clusters. *Inorg. Chem.* **57**, 2333–2350 (2018).
47. Mukherjee, S. & Thilagar, P. Boron clusters in luminescent materials. *Chem. Commun.* **52**, 1070–1093 (2016).
48. Dash, B. P., Satapathy, R., Maguire, J. A. & Hosmane, N. S. Polyhedral boron clusters in materials science. *New J. Chem.* **35**, 1955–1972 (2011).
49. Wang, W., Wang, X., Cao, J., Liu, J., Qi, B., Zhou, X., Zhang, S., Gabel, D., Nau, W. M., Assaf, K. I. & Zhang, H. The chaotropic effect as an orthogonal assembly motif for multi-responsive dodecaborate-cucurbituril supramolecular networks. *Chem. Commun.* **54**, 2098–2101 (2018).
50. Strauss, S. H. The Search for Larger and More Weakly Coordinating Anions. *Chem. Rev.* **93**, 927–942 (1993).
51. Hansen, B. R. S., Paskevicius, M., Li, H. W., Akiba, E. & Jensen, T. R. Metal boranes: Progress and applications. *Coord. Chem. Rev.* **323**, 60–70 (2016).
52. Buades, A. B., Kelemen, Z., Arderiu, V. S., Zaulet, A., Viñas, C. & Teixidor, F. A fast and simple B-C bond formation in metallacarboranes avoiding halometallacarboranes and transition metal catalysts. *Dalt. Trans.* **49**, 3525–3531 (2020).
53. Karki, K., Gabel, D. & Roccatano, D. Structure and dynamics of dodecaborate clusters in water. *Inorg. Chem.* **51**, 4894–4896 (2012).
54. Ďord'ovič, V., Tošner, Z., Uchman, M., Zhigunov, A., Reza, M., Ruokolainen, J., Pramanik, G., Cígler, P., Kalíková, K., Gradzielski, M. & Matějčiček, P. Stealth Amphiphiles: Self-Assembly of Polyhedral Boron Clusters. *Langmuir* **32**, 6713–6722 (2016).
55. Gassin, P. M., Girard, L., Martin-Gassin, G., Brusselle, D., Jonchère, A., Diat, O., Viñas, C., Teixidor, F. & Bauduin, P. Surface activity and molecular organization of metallacarboranes at the air-water interface revealed by nonlinear optics. *Langmuir* **31**, 2297–2303 (2015).
56. Bauduin, P., Prevost, S., Farràs, P., Teixidor, F., Diat, O. & Zemb, T. A theta-shaped amphiphilic cobaltabisdicarbollide anion: Transition from monolayer vesicles to micelles. *Angew. Chemie Int. Ed.* **50**, 5298–5300 (2011).
57. Viñas, C., Tarrés, M., González-Cardoso, P., Farràs, P., Bauduin, P. & Teixidor, F. Surfactant behaviour of metallacarboranes. A study based on the electrolysis of water. *Dalt. Trans.* **43**, 5062–5068 (2014).



58. Brusselle, D., Bauduin, P., Girard, L., Zaulet, A., Viñas, C., Teixidor, F., Ly, I. & Diat, O. Lyotropic lamellar phase formed from monolayered  $\theta$ -shaped carborane-cage amphiphiles. *Angew. Chemie Int. Ed.* **52**, 12114–12118 (2013).
59. Uchman, M., Abrikosov, A. I., Lepšík, M., Lund, M. & Matějčíček, P. Nonclassical Hydrophobic Effect in Micellization: Molecular Arrangement of Non-Amphiphilic Structures. *Adv. Theory Simulations* **1**, 1700002 (2018).
60. Malaspina, D. C., Viñas, C., Teixidor, F. & Faraudo, J. Atomistic Simulations of COSAN: Amphiphiles without a Head-and-Tail Design Display “Head and Tail” Surfactant Behavior. *Angew. Chemie Int. Ed.* **59**, 3088–3092 (2020).
61. Warneke, J., Jenne, C., Bernarding, J., Azov, V. A. & Plaumann, M. Evidence for an intrinsic binding force between dodecaborate dianions and receptors with hydrophobic binding pockets. *Chem. Commun.* **52**, 6300–6303 (2016).
62. Eyrilmez, S. M., Bernhardt, E., Dávalos, J. Z., Lepšík, M., Hobza, P., Assaf, K. I., Nau, W. M., Holub, J., Oliva-Enrich, J. M., Fanfrlík, J. & Hnyk, D. Binary twinned-icosahedral [B<sub>21</sub>H<sub>18</sub>]<sup>-</sup> interacts with cyclodextrins as a precedent for its complexation with other organic motifs. *Phys. Chem. Chem. Phys.* **19**, 11748–11752 (2017).
63. El Anwar, S., Assaf, K. I., Begaj, B., Samsonov, M. A., Růžičková, Z., Holub, J., Bovol, D., Nau, W. M., Gabel, D. & Grüner, B. Versatile, one-pot introduction of nonahalogenated 2-ammonio-decaborate ions as boron cluster scaffolds into organic molecules; host–guest complexation with  $\gamma$ -cyclodextrin. *Chem. Commun.* **55**, 13669–13672 (2019).
64. Diab, M., Floquet, S., Haouas, M., Abramov, P. A., López, X., Landy, D., Damond, A., Falaise, C., Guérineau, V., Touboul, D., Naoufal, D. & Cadot, E. Encapsulation of Chaotropic closo-Decahydrodecaborate Clusters Within Cyclodextrins: Synthesis, Solution Studies, and DFT Calculations. *Eur. J. Inorg. Chem.* **2019**, 3373–3382 (2019).
65. Assaf, K. I., Gabel, D., Zimmermann, W. & Nau, W. M. High-affinity host-guest chemistry of large-ring cyclodextrins. *Org. Biomol. Chem.* **14**, 7702–7706 (2016).
66. Assaf, K. I., Holub, J., Bernhardt, E., Oliva-Enrich, J. M., Fernández Pérez, M. I., Canle, M., Santaballa, J. A., Fanfrlík, J., Hnyk, D. & Nau, W. M. Face-Fusion of Icosahedral Boron Hydride Increases Affinity to  $\gamma$ -Cyclodextrin: closo,closo-[B<sub>21</sub>H<sub>18</sub>]<sup>-</sup> as an Anion with Very Low Free Energy of Dehydration. *ChemPhysChem* 1–7 (2020).

67. Assaf, K. I., Begaj, B., Frank, A., Nilam, M., Mougharbel, A. S., Kortz, U., Nekvinda, J., Grüner, B., Gabel, D. & Nau, W. M. High-Affinity Binding of Metallocarborane Cobalt Bis(dicarbollide) Anions to Cyclodextrins and Application to Membrane Translocation. *J. Org. Chem.* **84**, 11790–11798 (2019).
68. Fox, J. M., Kang, K., Sherman, W., Héroux, A., Sastry, G. M., Baghbanzadeh, M., Lockett, M. R. & Whitesides, G. M. Interactions between Hofmeister anions and the binding pocket of a protein. *J. Am. Chem. Soc.* **137**, 3859–3866 (2015).
69. Goszczyński, T. M., Fink, K., Kowalski, K., Leśnikowski, Z. J. & Boratyński, J. Interactions of Boron Clusters and their Derivatives with Serum Albumin. *Sci. Rep.* **7**, 1–12 (2017).
70. Losytskyy, M. Y., Kovalska, V. B., Varzatskii, O. A., Kuperman, M. V., Potocki, S., Gumienna-Kontecka, E., Zhdanov, A. P., Yarmoluk, S. M., Voloshin, Y. Z., Zhizhin, K. Y., Kuznetsov, N. T. & Elskaya, A. V. An interaction of the functionalized closo-borates with albumins: The protein fluorescence quenching and calorimetry study. *J. Lumin.* **169**, 51–60 (2016).
71. Kuperman, M. V., Losytskyy, M. Y., Bykov, A. Y., Yarmoluk, S. M., Zhizhin, K. Y., Kuznetsov, N. T., Varzatskii, O. A., Gumienna-Kontecka, E. & Kovalska, V. B. Effective binding of perhalogenated closo-borates to serum albumins revealed by spectroscopic and ITC studies. *J. Mol. Struct.* **1141**, 75–80 (2017).
72. Matějíček, P., Zedníky, J., Ušelová, K., Pleštil, J., Fanfrlík, J., Nykänen, A., Ruokolainen, J., Hobza, P. & Procházka, K. Stimuli-responsive nanoparticles based on interaction of metallocarborane with poly ethylene oxide. *Macromolecules* **42**, 4829–4837 (2009).
73. Ďord'ovič, V., Uchman, M., Procházka, K., Zhigunov, A., Pleštil, J., Nykänen, A., Ruokolainen, J. & Matějíček, P. Hybrid nanospheres formed by intermixed double-hydrophilic block copolymer poly(ethylene oxide)- block -poly(2-ethylloxazoline) with high content of metallocarboranes. *Macromolecules* **46**, 6881–6890 (2013).
74. Ďord'ovič, V., Verbraeken, B., Hogenboom, R., Kereiče, S., Matějíček, P. & Uchman, M. Tuning of Thermoresponsivity of a Poly(2-alkyl-2-oxazoline) Block Copolymer by Interaction with Surface-Active and Chaotropic Metallocarborane Anion. *Chem. - An Asian J.* **13**, 838–845 (2018).
75. Vrbata, D., Dord'ovic, V., Seitsonen, J., Ruokolainen, J., Janoušková, O., Uchman, M. & Matějíček, P. Preparation of membrane-mimicking lamellar structures by molecular confinement of hybrid nanocomposites. *Chem. Commun.* **55**, 2900–2903 (2019).

76. Verdiá-Báguena, C., Alcaraz, A., Aguilera, V. M., Cioran, A. M., Tachikawa, S., Nakamura, H., Teixidor, F. & Viñas, C. Amphiphilic COSAN and I2-COSAN crossing synthetic lipid membranes: Planar bilayers and liposomes. *Chem. Commun.* **50**, 6700–6703 (2014).
77. Berzelius, J. The preparation of the phosphomolybdate ion [PMo12O40] 3<sup>-</sup>. *Pogg. Ann* **6**, 369–371 (1826).
78. Keggin, J. F. Structure of the molecule of 12-phosphotungstic acid. *Nature* **131**, 908–909 (1933).
79. Müller, A., Krickemeyer, E., Bögge, H., Schmidtman, M. & Peters, F. Organizational forms of matter: an inorganic super fullerene and keplerate based on molybdenum oxide. *Angew. Chemie Int. Ed.* **37**, 3359–3363 (1998).
80. Müller, A., Krickemeyer, E., Bögge, H., Schmidtman, M., Beugholt, C., Das, S. K. & Peters, F. Giant Ring-Shaped Building Blocks Linked to Form a Layered Cluster Network with Nanosized Channels:[Mo124VIMo28VO429 (μ<sup>3</sup>-O) 28H14 (H<sub>2</sub>O) 66.5] 16<sup>-</sup>. *Chem. Eur. J.* **5**, 1496–1502 (1999).
81. Pope, M. T. & Müller, A. Polyoxometalate chemistry: an old field with new dimensions in several disciplines. *Angew. Chemie Int. Ed.* **30**, 34–48 (1991).
82. Long, D., Tsunashima, R. & Cronin, L. Polyoxometalates: building blocks for functional nanoscale systems. *Angew. Chemie Int. Ed.* **49**, 1736–1758 (2010).
83. Parker, G. A. Analytical chemistry of molybdenum. (1983).
84. Ammam, M. Polyoxometalates: formation, structures, principal properties, main deposition methods and application in sensing. *J. Mater. Chem. A* **1**, 6291–6312 (2013).
85. Hasenknopf, B. Polyoxometalates: introduction to a class of inorganic compounds and their biomedical applications. *Front. Biosci* **10**, 10–2741 (2005).
86. Kortz, U., Mueller, A., van Slageren, J., Schnack, J., Dalal, N. S. & Dressel, M. Polyoxometalates: Fascinating structures, unique magnetic properties. *Coord. Chem. Rev.* **253**, 2315–2327 (2009).
87. Gumerova, N. I. & Rompel, A. Synthesis, structures and applications of electron-rich polyoxometalates. *Nat. Rev. Chem.* **2**, 1–20 (2018).
88. López, X. Effect of protonation, composition and isomerism on the redox properties and electron (de) localization of classical polyoxometalates. *Phys. Sci. Rev.* **2**, (2017).
89. Li, B., Li, W., Li, H. & Wu, L. Ionic complexes of metal oxide clusters for versatile self-assemblies. *Acc. Chem. Res.* **50**, 1391–1399 (2017).

90. King, R. B. Aromaticity in transition metal oxide structures. *J. Chem. Inf. Comput. Sci.* **41**, 517–526 (2001).
91. Marcus, Y. *Ions in Solution and their Solvation*. (John Wiley & Sons, 2015).
92. Buchecker, T., Schmid, P., Renaudineau, S., Diat, O., Proust, A., Pfitzner, A. & Bauduin, P. Polyoxometalates in the Hofmeister series. *Chem. Commun.* **54**, 1833–1836 (2018).
93. Baker, M. C., Lyons, P. A. & Singer, S. J. Velocity ultracentrifugation and diffusion of silicotungstic acid. *J. Am. Chem. Soc.* **77**, 2011–2012 (1955).
94. Kurucsev, T., Sargeson, A. M. & West, B. O. Size and hydration of inorganic macroions from viscosity and density measurements. *J. Phys. Chem.* **61**, 1567–1569 (1957).
95. Malinenko, A., Jonchère, A., Girard, L., Parrès-Maynadié, S., Diat, O. & Bauduin, P. Are Keggin's POMs Charged Nanocolloids or Multicharged Anions? *Langmuir* **34**, 2026–2038 (2018).
96. Drummond, C., Pérez-Fuentes, L. & Bastos-González, D. Can Polyoxometalates Be Considered as Superchaotropic Ions? *J. Phys. Chem. C* **123**, 28744–28752 (2019).
97. Bera, M. K., Qiao, B., Seifert, S., Burton-Pye, B. P., Olvera de la Cruz, M. & Antonio, M. R. Aggregation of heteropolyanions in aqueous solutions exhibiting short-range attractions and long-range repulsions. *J. Phys. Chem. C* **120**, 1317–1327 (2016).
98. Antonio, M. R. & Bera, M. K. pH-Dependent Interactions between Keggin Heteropolyanions in Dilute Solutions. *Eur. J. Inorg. Chem.* **2019**, 367–373 (2019).
99. Chaumont, A. & Wipff, G. Polyoxometalate Keggin anions at aqueous interfaces with organic solvents, ionic liquids, and graphite: a molecular dynamics study. *J. Phys. Chem. C* **113**, 18233–18243 (2009).
100. Liu, T., Diemann, E., Li, H., Dress, A. W. M. & Müller, A. Self-assembly in aqueous solution of wheel-shaped Mo 154 oxide clusters into vesicles. *Nature* **426**, 59–62 (2003).
101. Liu, T. An unusually slow self-assembly of inorganic ions in dilute aqueous solution. *J. Am. Chem. Soc.* **125**, 312–313 (2003).
102. Liu, G., Liu, T., Mal, S. S. & Kortz, U. Wheel-shaped polyoxotungstate [Cu<sub>20</sub>Cl(OH)<sub>24</sub>(H<sub>2</sub>O)<sub>12</sub>(P<sub>8</sub>W<sub>48</sub>O<sub>184</sub>)]<sup>25-</sup> macroanions form supramolecular “Blackberry” structure in aqueous solution. *J. Am. Chem. Soc.* **128**, 10103–10110 (2006).
103. Yin, P., Li, D. & Liu, T. Solution behaviors and self-assembly of polyoxometalates as models of macroions and amphiphilic polyoxometalate–organic hybrids as novel surfactants. *Chem. Soc. Rev.* **41**, 7368–7383 (2012).

104. Buchecker, T., Schmid, P., Grillo, I., Prevost, S., Drechsler, M., Diat, O., Pfitzner, A. & Bauduin, P. Self-assembly of short chain poly-n-isopropylacrylamid induced by superchaotropic keggin polyoxometalates: From globules to sheets. *J. Am. Chem. Soc.* **141**, 6890–6899 (2019).
105. Girard, L., Naskar, B., Dufrêche, J.-F., Lai, J., Diat, O. & Bauduin, P. A thermodynamic model of non-ionic surfactants' micellization in the presence of polyoxometalates. *J. Mol. Liq.* **293**, 111280 (2019).
106. Buchecker, T., Le Goff, X., Naskar, B., Pfitzner, A., Diat, O. & Bauduin, P. Polyoxometalate/Polyethylene Glycol Interactions in Water: From Nanoassemblies in Water to Crystal Formation by Electrostatic Screening. *Chem. Eur. J.* **23**, 8434–8442 (2017).
107. Wen, T., Qiu, L., Zheng, Z., Gong, Y., Yuan, J., Wang, Y., Huang, M. & Yin, P. Inclusion Crystallization of Silicotungstic Acid and Poly (ethylene oxide) and Its Impact on Proton Conductivities. *Macromolecules* **53**, 1415–1421 (2020).
108. Jing, B., Ferreira, M., Gao, Y., Wood, C., Li, R., Fukuto, M., Liu, T. & Zhu, Y. Unconventional Complex Coacervation between Neutral Polymer and Inorganic Polyoxometalate in Aqueous Solution via Direct Water Mediation. *Macromolecules* **52**, 8275–8284 (2019).
109. Wu, Y., Shi, R., Wu, Y.-L., Holcroft, J. M., Liu, Z., Frasconi, M., Wasielewski, M. R., Li, H. & Stoddart, J. F. Complexation of polyoxometalates with cyclodextrins. *J. Am. Chem. Soc.* **137**, 4111–4118 (2015).
110. Moussawi, M. A., Haouas, M., Floquet, S., Shepard, W. E., Abramov, P. A., Sokolov, M. N., Fedin, V. P., Cordier, S., Ponchel, A. & Monflier, E. Nonconventional three-component hierarchical host–guest assembly based on Mo-blue ring-shaped giant anion,  $\gamma$ -cyclodextrin, and Dawson-type polyoxometalate. *J. Am. Chem. Soc.* **139**, 14376–14379 (2017).
111. Moussawi, M. A., Leclerc-Laronze, N., Floquet, S., Abramov, P. A., Sokolov, M. N., Cordier, S., Ponchel, A., Monflier, E., Bricout, H. & Landy, D. Polyoxometalate, cationic cluster, and  $\gamma$ -cyclodextrin: from primary interactions to supramolecular hybrid materials. *J. Am. Chem. Soc.* **139**, 12793–12803 (2017).

112. Ivanov, A. A., Falaise, C., Abramov, P. A., Shestopalov, M. A., Kirakci, K., Lang, K., Moussawi, M. A., Sokolov, M. N., Naumov, N. G. & Floquet, S. Host–Guest Binding Hierarchy within Redox-and Luminescence-Responsive Supramolecular Self-Assembly Based on Chalcogenide Clusters and  $\gamma$ -Cyclodextrin. *Chem. Eur. J.* **24**, 13467–13478 (2018).
113. Ivanov, A. A., Falaise, C., Laouer, K., Hache, F., Changenet, P., Mironov, Y. V, Landy, D., Molard, Y., Cordier, S. & Shestopalov, M. A. Size-Exclusion Mechanism Driving Host–Guest Interactions between Octahedral Rhenium Clusters and Cyclodextrins. *Inorg. Chem.* **58**, 13184–13194 (2019).
114. Ivanov, A. A., Falaise, C., Landy, D., Haouas, M., Mironov, Y. V, Shestopalov, M. A. & Cadot, E. Tuning the chaotropic effect as an assembly motif through one-electron transfer in a rhenium cluster. *Chem. Commun.* **55**, 9951–9954 (2019).
115. Breibeck, J., Bijelic, A. & Rompel, A. Transition metal-substituted Keggin polyoxotungstates enabling covalent attachment to proteinase K upon co-crystallization. *Chem. Commun.* **55**, 11519–11522 (2019).
116. Kobayashi, D., Nakahara, H., Shibata, O., Unoura, K. & Nabika, H. Interplay of hydrophobic and electrostatic interactions between polyoxometalates and lipid molecules. *J. Phys. Chem. C* **121**, 12895–12902 (2017).
117. Chandler, D. Interfaces and the driving force of hydrophobic assembly. *Nature* **437**, 640–647 (2005).
118. Winkler, R., Buchecker, T., Hastreiter, F., Touraud, D. & Kunz, W. PPh 4 Cl in aqueous solution—the aggregation behavior of an antagonistic salt. *Phys. Chem. Chem. Phys.* **19**, 25463–25470 (2017).
119. Sadakane, K., Onuki, A., Nishida, K., Koizumi, S. & Seto, H. Multilamellar structures induced by hydrophilic and hydrophobic ions added to a binary mixture of D<sub>2</sub>O and 3-methylpyridine. *Phys. Rev. Lett.* **103**, 167803 (2009).
120. Sadakane, K. & Seto, H. Membrane formation in liquids by adding an antagonistic salt. *Front. Phys.* **6**, 26 (2018).
121. Onuki, A., Yabunaka, S., Araki, T. & Okamoto, R. Structure formation due to antagonistic salts. *Curr. Opin. Colloid Interface Sci.* **22**, 59–64 (2016).
122. Pérez-Fuentes, L., Bastos-González, D., Faraudo, J. & Drummond, C. Effect of organic and inorganic ions on the lower critical solution transition and aggregation of PNIPAM. *Soft Matter* **14**, 7818–7828 (2018).

123. Pérez-Fuentes, L., Drummond, C., Faraudo, J. & Bastos-González, D. Interaction of organic ions with proteins. *Soft Matter* **13**, 1120–1131 (2017).
124. Nhujak, T. & Goodall, D. M. Comparison of binding of tetraphenylborate and tetraphenylphosphonium ions to cyclodextrins studied by capillary electrophoresis. *Electrophoresis* **22**, 117–122 (2001).
125. Israelachvili, J. N., Mitchell, D. J. & Ninham, B. W. Theory of self-assembly of hydrocarbon amphiphiles into micelles and bilayers. *J. Chem. Soc. Faraday Trans. 2 Mol. Chem. Phys.* **72**, 1525–1568 (1976).
126. Lindman, B., Medronho, B. & Karlström, G. Clouding of nonionic surfactants. *Curr. Opin. Colloid Interface Sci.* **22**, 23–29 (2016).
127. Naqvi, A. Z. Clouding phenomenon in amphiphilic systems: A review of five decades. *Colloids Surfaces B Biointerfaces* **165**, 325–344 (2018).
128. Glatter, O., Fritz, G., Lindner, H., Brunner-Popela, J., Mittelbach, R., Strey, R. & Egelhaaf, S. U. Nonionic micelles near the critical point: micellar growth and attractive interaction. *Langmuir* **16**, 8692–8701 (2000).
129. Bernheim-Groswasser, A., Wachtel, E. & Talmon, Y. Micellar growth, network formation, and criticality in aqueous solutions of the nonionic surfactant C12E5. *Langmuir* **16**, 4131–4140 (2000).
130. Schott, H. Lyotropic numbers of anions from cloud point changes of nonionic surfactants. *Colloids and Surfaces* **11**, 51–54 (1984).
131. Schott, H. Effect of inorganic additives on solutions of nonionic surfactants. *J. Colloid Interface Sci.* **189**, 117–122 (1997).
132. Zhang, Y., Furyk, S., Bergbreiter, D. E. & Cremer, P. S. Specific ion effects on the water solubility of macromolecules: PNIPAM and the Hofmeister series. *J. Am. Chem. Soc.* **127**, 14505–14510 (2005).
133. Hinze, W. L. & Pramauro, E. A critical review of surfactant-mediated phase separations (cloud-point extractions): theory and applications. *Crit. Rev. Anal. Chem.* **24**, 133–177 (1993).
134. Mitchell, D. J., Tiddy, G. J. T., Waring, L., Bostock, T. & McDonald, M. P. Phase behaviour of polyoxyethylene surfactants with water. Mesophase structures and partial miscibility (cloud points). *J. Chem. Soc. Faraday Trans. 1 Phys. Chem. Condens. Phases* **79**, 975–1000 (1983).
135. Marszall, L. Cloud point of mixed ionic-nonionic surfactant solutions in the presence of electrolytes. *Langmuir* **4**, 90–93 (1988).

136. Gu, T., Qin, S. & Ma, C. The effect of electrolytes on the cloud point of mixed solutions of ionic and nonionic surfactants. *J. Colloid Interface Sci.* **127**, 586–588 (1989).
137. Gu, T. & Galera-Gomez, P. A. Clouding of Triton X-114: the effect of added electrolytes on the cloud point of Triton X-114 in the presence of ionic surfactants. *Colloids Surfaces A Physicochem. Eng. Asp.* **104**, 307–312 (1995).
138. Panchal, K., Desai, A. & Nagar, T. Physicochemical behavior of mixed nonionic-ionic surfactants in water and aqueous salt solutions. *J. Dispers. Sci. Technol.* **27**, 33–38 (2006).
139. Mata, J. P. Hydrodynamic and clouding behavior of triton X-100+ SDS mixed micellar systems in the presence of sodium chloride. *J. Dispers. Sci. Technol.* **27**, 49–54 (2006).
140. Vora, S., George, A., Desai, H. & Bahadur, P. Mixed micelles of some anionic-anionic, cationic-cationic, and ionic-nonionic surfactants in aqueous media. *J. Surfactants Deterg.* **2**, 213–221 (1999).
141. Kekicheff, P., Grabielle-Madelmont, C. & Ollivon, M. Phase diagram of sodium dodecyl sulfate-water system: 1. A calorimetric study. *J. Colloid Interface Sci.* **131**, 112–132 (1989).
142. Kelkar, V. K., Mishra, B. K., Rao, K. S., Goyal, P. S. & Manohar, C. Transition from a nonionic to an ionic micelle. *Phys. Rev. A* **44**, 8421 (1991).
143. Douglas, C. B. & Kaler, E. W. Bilayer phases in aqueous mixtures of dodecylpentaoxyethylene glycol monoether (C12E5) and sodium decyl sulfonate (C10SO<sub>3</sub>Na). *J. Chem. Soc. Faraday Trans.* **90**, 471–477 (1994).
144. Bera, M. K. & Antonio, M. R. Aggregation of Heteropolyanions Implicates the Presence of Zundel Ions Near Air-Water Interfaces. *ChemistrySelect* **1**, 2107–2112 (2016).
145. Misra, A., Kozma, K., Streb, C. & Nyman, M. Beyond Charge Balance: Counter-Cations in Polyoxometalate Chemistry. *Angew. Chemie Int. Ed.* **59**, 596–612 (2020).
146. Pradeep, C. P., Long, D. L. & Cronin, L. Cations in control: Crystal engineering polyoxometalate clusters using cation directed self-assembly. *Dalt. Trans.* **39**, 9443–9457 (2010).
147. Stoyanov, E. S., Stoyanova, I. V. & Reed, C. A. The unique nature of H<sup>+</sup> in water. *Chem. Sci.* **2**, 462–472 (2011).
148. Reed, C. A. Myths about the proton. The nature of H<sup>+</sup> in condensed media. *Acc. Chem. Res.* **46**, 2567–2575 (2013).



149. Bajuk-Bogdanović, D., Holclajtner-Antunović, I., Todorović, M., Mioč, U. B. & Zakrzewska, J. A study of 12-tungstosilicic and 12-molybdophosphoric acids in solution. *J. Serbian Chem. Soc.* **73**, 197–209 (2008).
150. Jürgensen, A. & Moffat, J. B. The stability of 12-molybdosilicic, 12-tungstosilicic, 12-molybdophosphoric and 12-tungstophosphoric acids in aqueous solution at various pH. *Catal. Letters* **34**, 237–244 (1995).
151. Custer, G. S., Xu, H., Matysiak, S. & Das, P. How Hydrophobic Hydration Destabilizes Surfactant Micelles at Low Temperature: A Coarse-Grained Simulation Study. *Langmuir* **34**, 12590–12599 (2018).
152. Dong, R. & Hao, J. Complex fluids of poly(oxyethylene) monoalkyl ether nonionic surfactants. *Chem. Rev.* **110**, 4978–5022 (2010).
153. Sato, T., Akahane, T., Amano, K., Hyodo, R., Yanase, K. & Ogura, T. Scattering and Spectroscopic Study on the Hydration and Phase Behavior of Aqueous Alcohol Ethoxylate and Methyl Ester Ethoxylate: Effects of Terminal Groups in Hydrophilic Chains. *J. Phys. Chem. B* **120**, 5444–5454 (2016).
154. Tse-Ve-Koon, K., Tremblay, N., Constantin, D. & Freyssingeas, É. Structure, thermodynamics and dynamics of the isotropic phase of spherical non-ionic surfactant micelles. *J. Colloid Interface Sci.* **393**, 161–173 (2013).
155. Sato, T., Sakai, H., Sou, K., Buchner, R. & Tsuchida, E. Poly(ethylene glycol)-conjugated phospholipids in aqueous micellar solutions: hydration, static structure, and interparticle interactions. *J. Phys. Chem. B* **111**, 1393–1401 (2007).
156. Schrödle, S., Hefter, G., Kunz, W. & Buchner, R. Effects of nonionic surfactant C12e5 on the cooperative dynamics of water. *Langmuir* **22**, 924–932 (2006).
157. Ensing, B., Tiwari, A., Tros, M., Hunger, J., Domingos, S. R., Pérez, C., Smits, G., Bonn, M., Bonn, D. & Woutersen, S. On the origin of the extremely different solubilities of polyethers in water. *Nat. Commun.* **10**, 1–8 (2019).
158. Daley, K. R. & Kubarych, K. J. An ‘iceberg’ Coating Preserves Bulk Hydration Dynamics in Aqueous PEG Solutions. *J. Phys. Chem. B* **121**, 10574–10582 (2017).
159. Bruce, E. E. & Van Der Vegt, N. F. A. Molecular Scale Solvation in Complex Solutions. *J. Am. Chem. Soc.* **141**, 12948–12956 (2019).
160. Bruce, E. E., Bui, P. T., Rogers, B. A., Cremer, P. S. & Van Der Vegt, N. F. A. Nonadditive Ion Effects Drive Both Collapse and Swelling of Thermoresponsive Polymers in Water. *J. Am. Chem. Soc.* **141**, 6609–6616 (2019).

161. Yao, S., Falaise, C., Ivanov, A. A., Leclerc, N., Hohenschutz, M., Haouas, M., Landy, D., Shestopalov, M. A., Bauduin, P. & Cadot, E. Hofmeister Effect in the Keggin-type Polyoxotungstate Series. *Inorg. Chem. Front.* (2020).
162. Hervé, P., Roux, D., Bellocq, A.-M., Nallet, F. & Gulik-Krzywicki, T. Dilute and concentrated phases of vesicles at thermal equilibrium. *J. Phys. II* **3**, 1255–1270 (1993).
163. Davion van Mau, N., Isaaurat, B. & Amblard, G. Adsorption of hydrophobic anions on phospholipid monolayers. *J. Colloid Interface Sci.* **101**, 1–9 (1984).
164. Merhi, T., Jonchère, A., Girard, L., Diat, O., Nuez, M., Viñas, C. & Bauduin, P. Highlights on the binding of cobalta-bis-(dicarbollide) with glucose units. *Chem. – A Eur. J.* (2020).
165. Strey, R., Schomäcker, R., Roux, D., Nallet, F. & Olsson, U. Dilute lamellar and L3 phases in the binary water-C12E5 system. *J. Chem. Soc. Faraday Trans.* **86**, 2253–2261 (1990).
166. Schomäcker, R. & Strey, R. Effect of ionic surfactants on nonionic bilayers: Bending elasticity of weakly charged membranes. *J. Phys. Chem.* **98**, 3908–3912 (1994).
167. Jonströmer, M. & Strey, R. Nonionic bilayers in dilute solutions: Effect of additives. *J. Phys. Chem.* **96**, 5993–6000 (1992).
168. McCarroll, M. E., Toerne, K. & Von Wandruszka, R. Preclouding in mixed micellar solutions. *Langmuir* **14**, 6096–6100 (1998).
169. Toerne, K., Rogers, R. & Von Wandruszka, R. Fluctuating clouding behavior in mixed micellar solutions. *Langmuir* **16**, 2141–2144 (2000).
170. Roux, D., Coulon, C. & Cates, M. E. Sponge phases in surfactant solutions. *J. Phys. Chem.* **96**, 4174–4187 (1992).
171. Solé-Daura, A., Poblet, J. M. & Carbó, J. J. Structure–Activity Relationships for the Affinity of Chaotropic Polyoxometalate Anions towards Proteins. *Chem. - A Eur. J.* **26**, 5799–5809 (2020).
172. Gentile, L., Rossi, C. O., Olsson, U. & Ranieri, G. A. Effect of shear rates on the MLV formation and MLV stability region in the C12E5/D2O System: Rheology and Rheo-NMR and Rheo-SANS experiments. *Langmuir* **27**, 2088–2092 (2011).
173. Oberdisse, J., Couve, C., Appell, J., Berret, J. F., Ligoure, C. & Porte, G. Vesicles and onions from charged surfactant bilayers: A neutron scattering study. *Langmuir* **12**, 1212–1218 (1996).

174. Oberdisse, J. & Porte, G. Size of microvesicles from charged surfactant bilayers: Neutron scattering data compared to an electrostatic model. *Phys. Rev. E - Stat. Physics, Plasmas, Fluids, Relat. Interdiscip. Top.* **56**, 1965–1975 (1997).
175. Lasic, D. D., Joannic, R., Keller, B. C., Frederik, P. M. & Auvray, L. Spontaneous vesiculation. *Adv. Colloid Interface Sci.* **89–90**, 337–349 (2001).
176. Grillo, I. & Penfold, J. Self-assembly of mixed anionic and nonionic surfactants in aqueous solution. *Langmuir* **27**, 7453–7463 (2011).
177. Marques, E. F. Surfactant Vesicles: Formation, Properties, and Stability. *Encycl. Surf. Colloid Sci. Third Ed.* 7190–7209 (2016).
178. Dubois, M. & Zemb, T. Swelling limits for bilayer microstructures: The implosion of lamellar structure versus disordered lamellae. *Curr. Opin. Colloid Interface Sci.* **5**, 27–37 (2000).
179. Helfrich, W. Steric Interaction of Fluid Membranes in Multilayer Systems. *Zeitschrift fur Naturforsch. - Sect. A J. Phys. Sci.* **33**, 305–315 (1978).
180. von Berlepsch, H. & de Vries, R. Weakly charged lamellar bilayer system: Interplay between thermal undulations and electrostatic repulsion. *Eur. Phys. J. E* **1**, 141–152 (2000).
181. Jung, H. T., Coldren, B., Zasadzinski, J. A., Iampietro, D. J. & Kaler, E. W. The origins of stability of spontaneous vesicles. *Proc. Natl. Acad. Sci. U. S. A.* **98**, 1353–1357 (2001).
182. Zou, A., Hoffmann, H., Freiburger, N. & Glatter, O. Influence of ionic charges on the bilayers of lamellar phases. *Langmuir* **23**, 2977–2984 (2007).
183. Marszall, L. The effect of electrolytes on the cloud point of ionic-nonionic surfactant solutions. *Colloids and surfaces* **25**, 279–285 (1987).
184. Blute, I., Svensson, M., Holmberg, K., Bergh, M. & Karlberg, A. T. Solution behaviour of a formate capped surfactant-the oxidation product of an alcohol ethoxylate. *Colloids Surfaces A Physicochem. Eng. Asp.* **160**, 229–236 (1999).
185. Prud'homme, R. *Foams: theory: measurements: applications.* (Routledge, 2017).
186. Gochev, G., Ulaganathan, V. & Miller, R. in *Ullmann's Encycl. Ind. Chem.* 1–31 (Wiley-VCH, 2016).
187. Bikerman, J. J. *Foams.* **10**, (Springer Science & Business Media, 2013).
188. Micheau, C. Tensioactif carboxylique polyéthoxylé pour la flottation ionique : étude fondamentale de la solution à la mousse. (2013).
189. Stubenrauch, C. & Von Klitzing, R. Disjoining pressure in thin liquid foam and emulsion films - New concepts and perspectives. *J. Phys. Condens. Matter* **15**, (2003).

190. Bergeron, V. Forces and structure in thin liquid soap films. *J. Phys. Condens. Matter* **11**, (1999).
191. Langevin, D. Aqueous foams: A field of investigation at the Frontier between chemistry and physics. *ChemPhysChem* **9**, 510–522 (2008).
192. Rio, E., Drenckhan, W., Salonen, A. & Langevin, D. Unusually stable liquid foams. *Adv. Colloid Interface Sci.* **205**, 74–86 (2014).
193. Hilgenfeldt, S., Koehler, S. A. & Stone, H. A. Dynamics of coarsening foams: Accelerated and self-limiting drainage. *Phys. Rev. Lett.* **86**, 4704–4707 (2001).
194. Axelos, M. A. V. & Boué, F. Foams as viewed by small-angle neutron scattering. *Langmuir* **19**, 6598–6604 (2003).
195. Mikhailovskaya, A., Zhang, L., Cousin, F., Boué, F., Yazhgur, P., Muller, F., Gay, C. & Salonen, A. Probing foam with neutrons. *Adv. Colloid Interface Sci.* **247**, 444–453 (2017).
196. Arnould, A., Cousin, F., Salonen, A., Saint-Jalmes, A., Perez, A. & Fameau, A. L. Controlling Foam Stability with the Ratio of Myristic Acid to Choline Hydroxide. *Langmuir* **34**, 11076–11085 (2018).
197. Yada, S., Shimosegawa, H., Fujita, H., Yamada, M., Matsue, Y. & Yoshimura, T. Microstructural Characterization of Foam Formed by a Hydroxy Group-Containing Amino Acid Surfactant Using Small-Angle Neutron Scattering. *Langmuir* **36**, 7808–7813 (2020).
198. Etrillard, J., Axelos, M. A. V., Gantat, I., Artzner, F., Renault, A., Weiss, T., Delannay, R. & Boué, F. In situ investigations on organic foam films using neutron and synchrotron radiation. *Langmuir* **21**, 2229–2234 (2005).
199. Terriac, E., Emile, J., Axelos, M. A. V., Grillo, I., Meneau, F. & Boué, F. Characterization of bamboo foam films by neutron and X-ray experiments. *Colloids Surfaces A Physicochem. Eng. Asp.* **309**, 112–116 (2007).
200. Schmidt, I., Novales, B., Boué, F. & Axelos, M. A. V. Foaming properties of protein/pectin electrostatic complexes and foam structure at nanoscale. *J. Colloid Interface Sci.* **345**, 316–324 (2010).
201. Micheau, C., Bauduin, P., Diat, O. & Faure, S. Specific salt and pH effects on foam film of a pH sensitive surfactant. *Langmuir* **29**, 8472–8481 (2013).
202. Liu, F., Wang, Z., Sun, D., Wei, X., Zhou, W., Li, G. & Zhang, G. Adsorption kinetics of Brij 97 at the air/solution interface. *J. Dispers. Sci. Technol.* **27**, 657–663 (2006).

- 
203. Cubitt, R. & Fragneto, G. Neutron Reflection: Principles and Examples of Applications (Chapter 2.8.3). *Scattering* 1198–1208 (2002).
  204. Karraker, K. A. & Radke, C. J. Disjoining pressures, zeta potentials and surface tensions of aqueous non-ionic surfactant/electrolyte solutions: Theory and comparison to experiment. *Adv. Colloid Interface Sci.* **96**, 231–264 (2002).
  205. Hänni-Ciunel, K., Schelero, N. & von Klitzing, R. Negative charges at the air/water interface and their consequences for aqueous wetting films containing surfactants. *Faraday Discuss.* **141**, 41–53 (2009).
  206. Stubenrauch, C., Schlarmann, J. & Strey, R. A disjoining pressure study of n-dodecyl- $\beta$ -D-maltoside foam films. *Phys. Chem. Chem. Phys.* **4**, 4504–4513 (2002).
  207. Bournival, G., Du, Z., Ata, S. & Jameson, G. J. Foaming and gas dispersion properties of non-ionic surfactants in the presence of an inorganic electrolyte. *Chem. Eng. Sci.* **116**, 536–546 (2014).
  208. Pugh, R. J. & Yoon, R. H. Hydrophobicity and rupture of thin aqueous films. *J. Colloid Interface Sci.* **163**, 169–176 (1994).
  209. Castro, S., Miranda, C., Toledo, P. & Laskowski, J. S. Effect of frothers on bubble coalescence and foaming in electrolyte solutions and seawater. *Int. J. Miner. Process.* **124**, 8–14 (2013).
  210. Karakashev, S. I. & Manev, E. D. Frothing behavior of nonionic surfactant solutions in the presence of organic and inorganic electrolytes. *J. Colloid Interface Sci.* **235**, 194–196 (2001).
  211. Theander, K. & Pugh, R. J. Synergism and foaming properties in mixed nonionic/fatty acid soap surfactant systems. *J. Colloid Interface Sci.* **267**, 9–17 (2003).
  212. Zawala, J., Wiertel-Pochopien, A., Larsen, E. & Kowalczyk, P. B. Synergism between Cationic Alkyltrimethylammonium Bromides (CnTAB) and Nonionic n-Octanol in the Foamability of Their Mixed Solutions. *Ind. Eng. Chem. Res.* **59**, 1159–1167 (2020).
  213. Schnablegger, H. & Singh, Y. The SAXS guide: getting acquainted with the principles. *Austria Ant. Paar GmbH* 1–124 (2011).
  214. Glatter, O. *Scattering methods and their application in colloid and interface science.* (Elsevier, 2018).
  215. Roe, R. J. *Methods of X-ray and neutron scattering in polymer science.* (Oxford University Press New York, 2000).
  216. <https://www.ncnr.nist.gov/resources/n-lengths/>.

217. Doucet, M., Cho, J. H., Alina, G., Bakker, J., Bouwman, W., Butler, P., Campbell, K., Gonzales, M., Heenan, R. & Jackson, A. SasView Version 4.1. *Zenodo* <http://www.sasview.org> (2017).
218. Breßler, I., Kohlbrecher, J. & Thünemann, A. F. SASfit: a tool for small-angle scattering data analysis using a library of analytical expressions. *J. Appl. Crystallogr.* **48**, 1587–1598 (2015).
219. Øgendal, L. Light Scattering Demystified. *Theory Pract.*
220. Feitosa, K., Marze, S., Saint-Jalmes, A. & Durian, D. J. Electrical conductivity of dispersions: From dry foams to dilute suspensions. *J. Phys. Condens. Matter* **17**, 6301–6305 (2005).